Genetic control of bacterial morphogenesis

Antoine Vigouroux

To cite this version:

Antoine Vigouroux. Genetic control of bacterial morphogenesis. Biological Physics [physics.bio-ph]. Université Sorbonne Paris Cité, 2019. English. NNT : 2019USPCB041 . tel-03131336

HAL Id: tel-03131336
https://theses.hal.science/tel-03131336v1

Submitted on 4 Feb 2021

Université Paris Descartes
École Doctorale 474 Frontières du Vivant

Genetic control of bacterial morphogenesis

par Antoine Vigouroux

Thèse de doctorat de biophysique
Dirigée par David Bikard et Sven van Teeffelen

Présentée et soutenue publiquement le 27 mai 2019, devant un jury composé de :

David Bikard	Directeur	Institut Pasteur
Sven van Teeffelen	Directeur	Institut Pasteur
Meriem El Karoui	Rapporteuse	University of Edinburgh
Johannes Hohlbein	Rapporteur	Wageningen University
Olivier Tenaillon	Examinateur	Université Paris Diderot
Lydia Robert	Examinatrice	Université Pierre et Marie Curie
Ivan Matic	Examinateur	Université Paris Descartes

Résumé

Depuis la découverte de l'ADN, notre compréhension de la morphogénèse bactérienne a beaucoup progressé mais aussi donné lieu à de nouvelles questions. La bactérie Escherichia coli est capable de maintenir une forme de bâtonnet de façon robuste, mais son génome ne contient aucun de plan de construction précis. La forme des cellules est déterminée dynamiquement par les enzymes qui synthétisent la paroi cellulaire, un polymère rigide qui entoure la cellule. Pour étudier quantitativement comment la biogénèse de la paroi et la forme des cellules dépend des concentrations des enzymes essentielles, nous utilisons un dérivé sans activité nucléase de CRISPR/Cas9 pour bloquer partiellement la transcription. Cette méthode n'ayant pas été utilisée avant, nous avons étudié ses propriétés en détail sur des rapporteurs fluorescents. Cela nous a conduit à des découvertes surprenantes: on considérait auparavant que la répression dépendait de la fréquence de fixation de dCas9 à sa cible. Nous avons démontré un mécanisme différent: la complémentarité guide/cible détermine la probabilité que la RNA polymérase déplace activement dCas9 lors de la transcription. Cela conduit à des propriétés désirables: la force de répression ne dépend pas du niveau d'expression natif de la cible, et n'ajoute pas de bruit extrinsèque à l'expression. Armés de cet outil, nous avons pour objectif de comprendre globalement comment les différents composants de la machinerie de synthèse de la paroi cellulaire sont articulés entre eux. Pour polymériser la paroi cellulaire, qui donne sa forme à la cellule, deux groupes d'enzymes ont été décrits: le complexe Rod et les PBP de classe A. Nous avons créé des souches exprimant ces deux catégories d'enzymes à des niveaux variables et caractérisé leurs phénotypes par différents moyens biophysiques (résistance mécanique, diffusion de molécules uniques, sensibilité à des antibiotiques...). Nous avons pu mettre en évidence que des enzymes avec des activités biochimiques similaires peuvent provoquer des réponses complètement différentes lorsque leurs niveaux sont changés. Ces travaux ont permis de mieux comprendre comment ces différents mécanismes sont coordonnés pour maintenir l'intégrité de la paroi à de multiples échelles.

Abstract

Since the discovery of DNA, our understanding of the morphogenesis of bacterial cells has made great advance and also gave rise to new questions. Even though the bacterium Escherichia coli is able to maintain rod shape robustly, the genome does not encode any internal blueprint of what the cell should look like. Rather, cell shape is dynamically determined by the enzymes synthesizing the cell-wall, a rigid polymer that surrounds the cell. To quantitatively study the dependence of cell-wall biogenesis and cell shape on levels of essential cell-wall synthesis proteins, we use a nuclease-deficient CRISPR/Cas9 to partially block transcription. As this method had no been put into practice before, we thoroughly investigated its properties on a model system using fluorescent reporters. This led us to surprising findings: it was previously assumed that decreased levels of guide RNA complementarity would decrease repression strength by virtue of reduced occupancy of the target. We demonstrated a different mechanism: complementarity determines the probability that RNA polymerase kicks out dCas9 during the transcription attempt, while the rate of spontaneous dCas9 unbinding is negligibly small. If dCas9 levels are high enough to saturate the target this mechanism alone determines repression strength. This leads to desirable properties: First, relative repression strength is independent of native expression levels. Second, repression does not add any extrinsic noise to gene expression. Armed with this tool, we aim get a global understanding of the interplay between the different components of the cell-wall machinery. To polymerize the cell wall , which gives its shape to the cell, two groups of enzymes were described: the Rod Complex and class A PBPs. We created strains expressing this two categories of enzyme at variable levels, then characterized their phenotypes by different biophysical means (mechanical resistance, single-molecule diffusion, antibiotic sensitivity...). This way, we could show that enzymes that share similar biochemical activities can elicit very different responses when their levels are changed. This work allowed to better understand how these different mechanisms are coordinated to maintain cell wall integrity at multiple scales.

Genetic control of bacterial morphogenesis

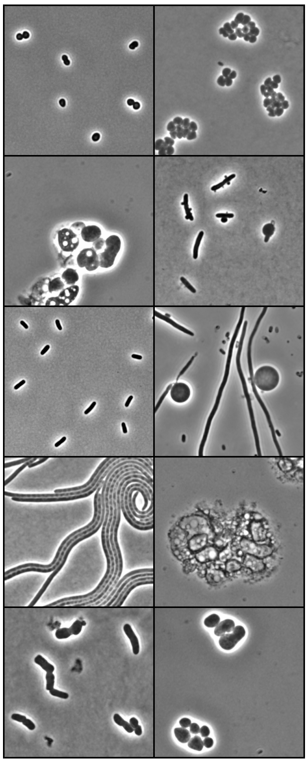

Remerciements

First of all, I would like to thank my advisors David and Sven, for guiding me during these 3.5 years and always putting me back on track. Thanks to the members of my Thesis Advisory Committee, Ivo Boneca and Pascal Hersen, for their precious advice and support. I also thank the jury for taking the time to examine this work.

A big thank to all the people who directly participated in the projects discussed in this thesis: Baptiste Cordier, Lun Cui, Alicia Calvo-Villamañan, Gizem Özbaykal, François Simon, Enno Oldewurtel, Richard Wheeler and Martin Sachse, and my two interns, Lucas and Dimitrije.

For bearing with me during all these years, I address special thanks to the past and present members of my two labs. I met so many exceptional people here. Aude, Élise, Gizem, Alicia, Yuki, François, François, it was great to share the PhD experience with you. You'd better not forget me in your acknowledgements after I'm gone.

Mes parents, même si l'on ne s'est pas vus si souvent, merci pour le réconfort, l'aide inestimable et les trucs bons. Diane, Augustin, on s'est tous retrouvés à travailler dur en même temps, vers la fin. Heureusement que vous étiez là.

Lyam, Florian, Eugénie, Julien et Corentin, merci pour l'élévation philosophique et l'illumination spirituelle que leur sagesse et leur érudition m'ont apportées. Mes confères de pharma, Julien, Éric, William, Reynald, Quentin, vous m'avez tout appris. Merci à l'Ernestophone, ma fanfare, pour cette joie débordante et pour m'avoir fait me sentir à ma place. Mention particulière pour le personnel de la vigoumobile, le feat est lourd, vous êtes la peufra. Ma team iGEM, que des numéros dix. L'an 2015 est passé, mais l'équipe reste. Thanks CRI friends, Miza, Guillermo, Roberta, Anna, Olga, Aamir, Juliette and all others. To Pasteur people, Marisaõ, Corentin, Christiane, Dariusz, Lukas, Mélanie, Sarah, the RSG lab, and so many more. To my former neighbors from Cité U, you were the best neighbors I ever had and our crêpes were unrivaled. Merci aux acrimoines, qui ne trouveront jamais cette dédicace. Thanks to the developers of LaTeX and R, my unsung heroes. Please don't blame me too much if I forgot you, I did not sleep so much during the last few days.

Contents

List of Figures

List of Tables

Chapter 1

How can bacteria be so large?

1.1 Introduction

The question of morphogenesis was settled by natural philosopher and theologian Nicolas Malebranche in 1680. Microscopes had recently been introduced to biologists by Antonie van Leeuwenhoek, revealing the existence of creatures so small the naked eye could not see them. As there were no reasons, at the time, think that there was lower limit to the size of living creatures, Malebranche suggested that there were, in fact, infinitely small creatures so that one could always discover new species by building better microscopes. This solved the problem of the origin of organisms: animals simply carry miniature versions of themselves in their body, which in turn carry even smaller versions of themselves, and so forth *ad infinitum*. This way, all past, present and future living organisms were already imbricated there, waiting for their turn since the time God created the Universe[1].

However, this theory was still obscured by two clouds. The first cloud was that it was not entirely clear whether these infinite lineages of animals were stored in male or female gonads (figure 1.1), a debate that would enrage natural philosophers for decades. The second cloud was that, in the following centuries, the development of atomic theory put quite a hard limit on the minimal size of living bodies. On top of that, the theory of natural selection and evolution cast some doubt on the hypothesis that God created the living realm. Eventually, it was found that all living organisms had one thing in common: instructions about how to build an entire organism are stored inside each cell, in the form of long molecules of DNA.

This information includes morphological traits [1], as mutants can have different morphologies.

How can DNA, a one-dimensional, structure-less molecule that is hundreds of times smaller than the full organism, describe such complex shapes?

---

[1] Nicolas Malebranche, *Traité de la nature et de la grâce*, 1680.

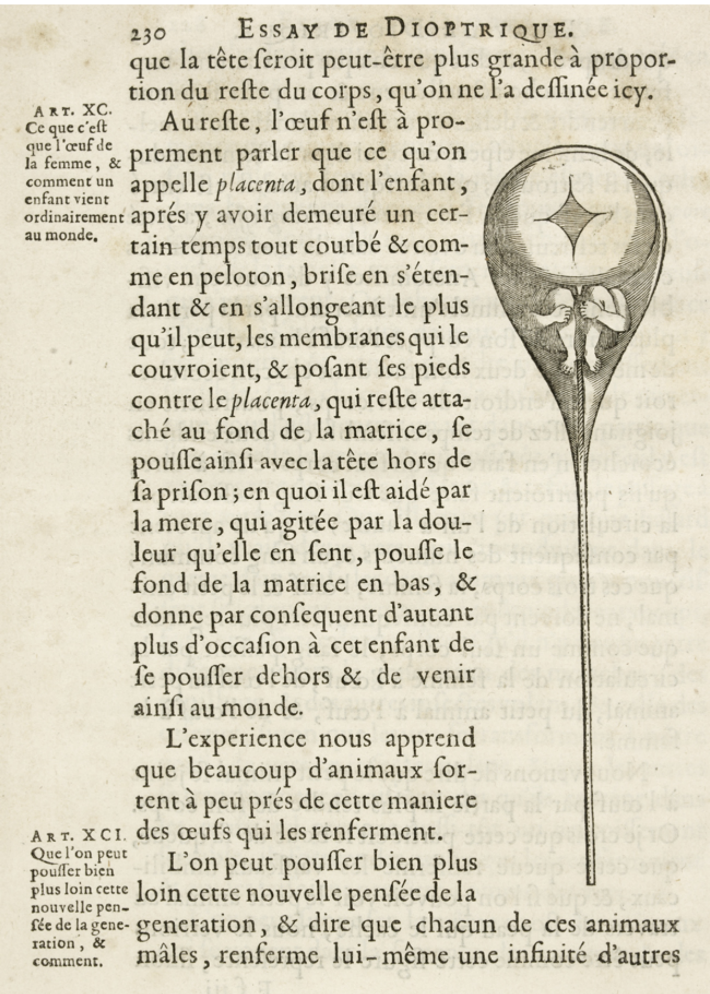

230 ESSAY DE DIOPTRIQUE.

que la tête ſeroit peut-être plus grande à proportion du reſte du corps, qu'on ne l'a deſſinée icy.

ART. XC. Ce que c'eſt que l'œuf de la femme, & comment un enfant vient ordinairement au monde.

Au reſte, l'œuf n'eſt à proprement parler que ce qu'on appelle *placenta*, dont l'enfant, aprés y avoir demeuré un certain temps tout courbé & comme en peloton, briſe en s'étendant & en s'allongeant le plus qu'il peut, les membranes qui le couvroient, & poſant ſes pieds contre le *placenta*, qui reſte attaché au fond de la matrice, ſe pouſſe ainſi avec la tête hors de ſa priſon; en quoi il eſt aidé par la mere, qui agitée par la douleur qu'elle en ſent, pouſſe le fond de la matrice en bas, & donne par conſequent d'autant plus d'occaſion à cet enfant de ſe pouſſer dehors & de venir ainſi au monde.

L'experience nous apprend que beaucoup d'animaux ſortent à peu prés de cette maniere des œufs qui les renferment.

ART. XCI. Que l'on peut pouſſer bien plus loin cette nouvelle penſée de la generation, & comment.

L'on peut pouſſer bien plus loin cette nouvelle penſée de la generation, & dire que chacun de ces animaux mâles, renferme lui-même une infinité d'autres

Figure 1.1: **Nicolaas Hartsoeker, "le petit infant"**, in *Essay de dioptrique*, 1694. This famous woodcut shows of a sperm cell, and the pre-formed human that it supposedly contains.

1.2 A matter of scales

To give a better idea of the problem, here is a summary of the scale of different components of life (table 1.1). For example, the typical size of a bacterial protein is about 5 nm [2], which is about one hundredth of the size of the bacterium itself. On top of that, enzymes have no long distance sight and no memory, so they cannot build structures larger than themselves by refering to a determined construction plan. A major challenge in building the shape of organisms is thus to transmit information from one scale to another.

Table 1.1: Orders of magnitude of the size of different components in life.

Size	Object
0.1 nm	Distance between two atoms in the main chain of a protein
1 nm	Length of one disaccharide unit in *E. coli*'s cell wall [3]
10 nm	Order of magnitude of the diameter of an enzyme [4]
100 nm	Size of the λ-phage (multi-protein assembly)
1 000 nm	Diameter of an *E. coli* cell
10 000 nm	Diameter of a human red blood cell [2]
100 000 nm	Diameter of a human oocyte [2]

Many processes can be responsible for generating the shape of an organism, and most of them are not really well understood. Some simple morphogenetic principles are commonly found in nature. Here are a few well-known examples of them.

While the size of a single protein is limited, it is possible for multiple proteins to assemble together and form larger complexes. The eukyarotic cytoskeleton is a prominent example of this. Among others, actin and tubulin form filaments of different sizes that are responsible for cell shape, motility and intracellular transport [5].

Fractal structures are extremely common across life (figure 1.2). They can typically extend over multiple scales, as they are self-similar: the layout of the entire system mirrors the layout of individual parts [6, 7]. The most obvious self-similar pattern is perhaps phyllotactic spirals, which are found in many plants [8] (figure 1.2) and allow for efficient packing of leaves using only very simple instructions. Fractal shapes have the advantage of maximizing surface contact while minimizing transport distances [7]. They can be found in coral growth, in the organization of blood vessels of mammals, in neural networks [9] and also in the shape of some bacterial colonies [10].

The synthesis of curved surfaces is also a common way for organisms to generate large scale organization, as the construction of materials with a forced intrinsic curvature, positive or negative, can generate complex shapes (figure 1.3), a phenomenon that is common in corals and algae, and is a well-known technique in crochet knitting. This phenomenon was also suggested to play a role in the blastulation and gastrulation of metazoan embryos [11, 12] and in the morphogenesis of some eukaryotic cells [13].

Above the cellular level, the morphogenesis of organisms often involves gene regulatory networks combined with the diffusion of morphogenes. Due to the limits of

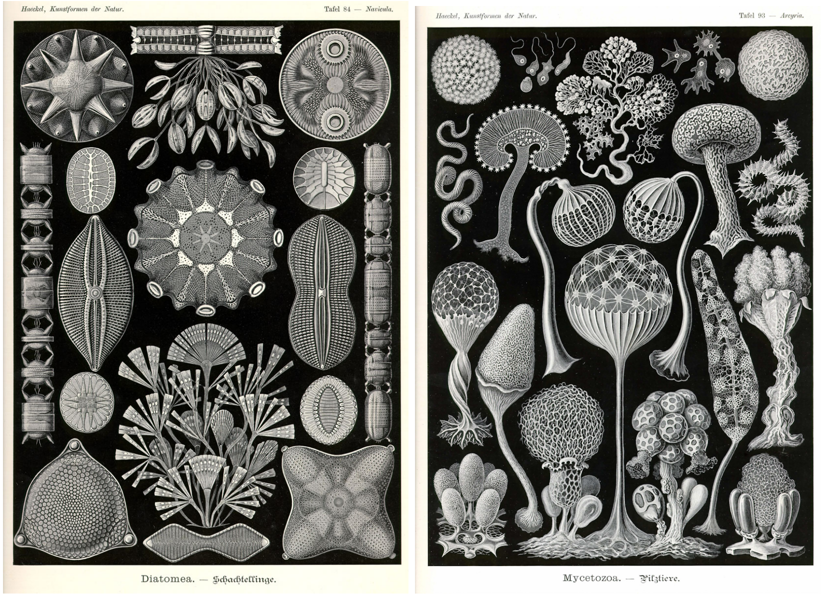

Figure 1.2: **Ernst Haeckel, “Diatomea” and “Mycetozoa”**, in *Kunstformen der Natur*, 1904. Notice the potential fractal organization, reaction-diffusion patterns and phyllotactic spirals.

Figure 1.3: **A negative-curvature cactus, belonging to the author’s mother**. Mathematically, it is not possible to tile an Euclidian surface such that the average number of neighbors per tile is larger than six [11]. I speculate that, in this cactus, because each spine bundle tends to have more than six equally-spaced neighbors, a negatively-curved surface is created, resulting in large folds.

protein size, long distances cannot be directly encoded in genetic information. However, DNA sequences can encode for products with specific diffusion speeds and reaction rates, which in turn allow to describe structures much bigger than the size of the protein themselves [14].

This has been studied in depth for the development of drosophila embryo [15], where the diffusion of morphogenes (e.g. bicoid and hunchback) serves as a basis for the development of the anterior-posterior axis. Positive feedback in the expression of a diffusing morphogene can be used for symmetry-breaking and axial patterning [16]. The differential expression of cell-cell adhesion molecules can reorganize the cells spatially, a property that has been used to generate artificial multi-cellular structures [17]. Turing patterns are another famous example of reaction-diffusion process, where two morphogenes with different diffusion constants generate complex motifs (figure 1.2). This is found, among many others, in the stripes of the zebra fish [18, 19]. Amusingly, some bacterial proteins are also able to generate dynamic patterns. This was observed by transfering proteins from *E. coli*'s Min system on a supported lipid bilayer [20, 21], although the origin of these patterns is still controversial [22]. The scale of such patterns is much larger than the size of the cells of *E. coli*. Inside living cells, the MinDE proteins form a dynamical system that oscillates from pole to pole and acts as a sensor for cell geometry [23]. The resulting gradient allows to find the middle of the cell and determines the position of the FtsZ ring to initiate cell division. They may also influence the localization of many other membrane proteins in *E. coli* [24].

1.3 Understanding bacterial morphogenesis

The shape of a bacterial cell

Bacteria are relatively simple organisms, as they are made of only one cell without any organelle. In particular, model organisms like *Escherichia coli* or *Bacillus subtilis* have been studied extensively, a large part of their genomes is annotated, and they are arguably the organisms that scientists know the best. Yet, the origin of their shape is still poorly understood.

Bacteria can have a wide diversity of shapes, reflecting their mechanism of growth and division. The most well-known bacterial morphologies are bacilliform (rods) and cocci (spheres). Not only are they widespread in nature, they also tend to be frequent among pathogens, making them more likely to be studied [25]. Interestingly, rod-shaped bacteria are not monophyletic. They can be found in very diverse taxa, that usually contain many other shapes (figure 1.4), suggesting that it appeared and disappeared multiple times throughout evolution [26, 25]. Typically, *E. coli* and *B. subtilis* would be hard to distinguish on an electron micrograph, yet belong to completely different clades in the phylogeny of bacteria.

Another sign of convergent evolution is that taxa with the same rod-like shape can use very different modes of construction (lateral elongation, polar elongation or budding) [27]. Together, this highlights how having a rod shape can provide an evolutionary advantage. The exact reasons why the rod shape is beneficial are not clear [28], especially since one single shape rarely dominates a given environment [29]. Among the factors that could put selective pressure on bacterial shape, there is the rate of nutrient uptake, mechanical resistance, gradient sensing, equal partition during division and the ability for dispersing or sticking to a niche. Cell morphology can also adapt to the conditions, for example some pathogenic strains of *E. coli* can grow as filaments to escape phagocytosis [30]. Some bacteria (like *E. coli* but not *B. subtilis*) also have different diameters depending on their growth rate [31, 32].

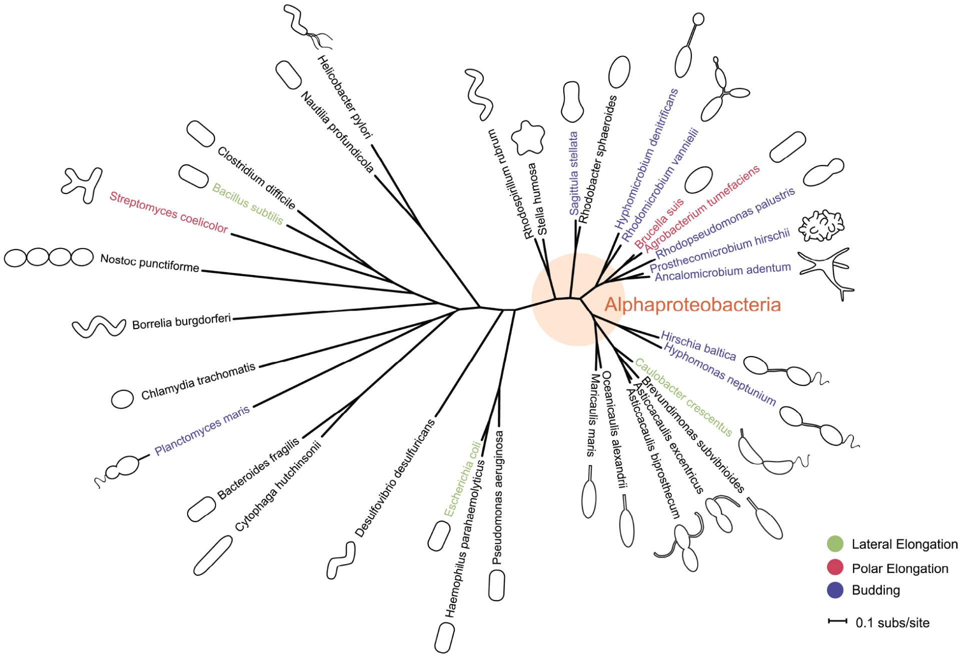

Figure 1.4: Phylogenetic tree of diverse bacteria and their morphology. Reprinted with permission from [26].

The cell wall

Within one species's population, the shape of individual cells is remarkably robust, revealing a tight control of shape determination [28]. To understand the shape of bacteria, one must understand the structure of the peptidoglycan cell wall. This large molecule forms a cage around the cell and is responsible for its shape, mechanical resistance and elasticity. When isolated, the peptidoglycan sacculus retains its shape [33], as can be seen in figure 1.5. This makes it one of the largest molecules in nature that have a defined spatial structure on its own.

In monoderm (gram-positive) bacteria, the envelope is made of one lipidic membrane surrounded by a thick layer of peptidoglycan, while in diderm (gram-negative) bacteria, there is one thin layer of peptidoglycan that stands between an inner membrane and an outer membrane. In the later case, peptidoglycan is covalently attached to the outer membrane by Braun's lipoprotein [35].

The chemical composition of peptidoglycan is the same for monoderm and diderm bacteria. Large glycan strands strands are arranged perpendicularly to the cell axis [36]. At the chemical level, they consist in the repetition of two monosaccharide units, N-acetyl-glucosamine and N-acetyl-muraminic acid. These strands are covered with peptide stems that can be cross-linked together, to form a 2D (diderm) or 3D (monoderm) meshwork. As peptide crosslinks are more flexible than glycan strands, rod cells exhibit anisotropic elasticity and stretch more easily in the direction of their long axis.

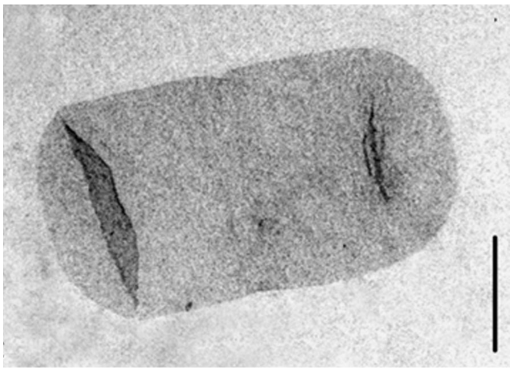

Figure 1.5: Purified sacculus from *E. coli* observed under a transmission electron microscope, retaining the bacteria's rod shape.
Scale bar: 0.5 µm. Reprinted with permission from [34].

A bacterial cytoskeleton?

Analogous to the cytoskeleton that determines eukyarotic cell's shape, the hypothesis that bacteria have a rigid cytoskeleton formed by a multi-protein assembly received a lot of attention. A homolog of tubulin, FtsZ, was indeed discovered in *E. coli* in the 1990s [37, 38], followed by a homolog of actin called MreB [39]. At the time, MreB was thought to form a spiral structure spanning the entire cell, and effectively serve as a bacterial cytoskeleton [40]. Figure 1.6 shows a model from 2001 about how MreB could possibly be responsible for bacterial rod shape.

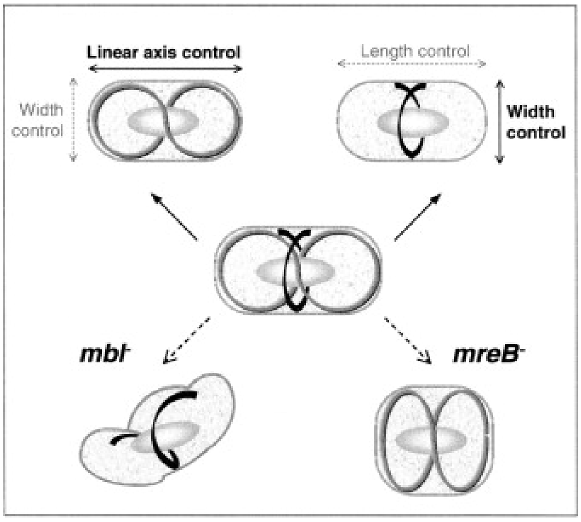

Figure 1.6: Early model of actin-like polymers forming a skeleton inside *B. subtilis* cells. Reprinted with permission from [40].

Unfortunately, more than ten years later, it turned out that the long helical structure was in fact an artefact due to the fusion of a yellow fluorescent protein to MreB.

In fact cytoskeleton-like structure disappeared when looking at MreB by electron cryotomography or at an internal mCherry fusion [41]. Rather than forming cell-spanning helices, MreB forms a large number of filaments whose length averages about 300 nm [42, 43, 44], meaning that they are not long enough to form a spiral scaffold holding the cell together. In addition, these patches are very dynamic and their number, length and orientation varies with conditions. Therefore, they are unlikely to serve as a cytoskeleton that would directly determine cell shape.

Local coordination of cell wall synthesis

Simulations have found that a local coordination of peptidoglycan insertion can be sufficient to maintain rod-shape without a cell-wide skeleton [45]. Indeed, recent experiments suggest a feedback between strain on the envelope and cell wall insertion [46, 47]. In some models, filaments of MreB are thought to sense the curvature of the peptidoglycan and drive insertion accordingly. For example, it was suggested that MreB filaments tend to localize in regions of negative curvature [48]. If true, this would result in more insertion in the negatively-curved regions, thus cell straightening. However, in a curved cell, the circumferential rotation of MreB [49, 50] along the curved envelope would also focalize filaments in the negative-curvature regions, so it is not clear if this is an active process . More recently, mechanical strain on MreB filaments in reaction to curvature has been proposed to determine their trajectories [51, 52], even if it might not be the only factor.

Moreover, rod-like bacteria usually possess multiple paralogs of the essential components of cell-wall synthesis, one being used for cylindrical cell elongation, and one for spherical pole formation [53, 26]. For example, in *E. coli*, PBP2, RodA and PBP1A fill roughly the same role in elongation as PBP3, FtsW and PBP1B do in division, respectively. This suggests that the specific structure of polymerization enzymes determines the local curvature of the peptidoglycan they construct.

1.4 Investigating cell wall synthesis as a dynamical system

As most of the genes involved in peptidoglycan synthesis are essential genes, it is not possible to simply delete them and study the behaviour of the knock-out organism. It is however possible to perturb the concentration of components *in vivo* and observe how the modified organisms grow, if their morphology has changed, and if they have different physical or mechanical properties.

Furthermore, the components involved in bacterial growth are all interlinked, interacting dynamically and adapting their activity to growth conditions and to the current state of the cell. Thus, by changing the amount of one part, we can look at how the other parts respond and find quantitative relationships between the different machineries.

When this work started, the bacterial immune system CRISPR had just been repurposed for all kinds of biotechnological applications, including the control of gene expression [54]. At the time, such a method was limited to proofs of concept and had not been applied to actual scientific questions. Therefore, I set to use CRISPR-based repression systems to explore bacterial morphogenesis, with the hope of improving the characterization of CRISPR systems in the way, finding their advantages, and their limitations.

Chapter 2 will cover the progress that has been made in recent years in the development of CRISPR-based tools to control transcription. It is meant as a review of the different biotechnological applications of CRISPR knock-down and the mechanistic knowledge that could be gained from them. Chapter 3 is a published article about the use of mismatched CRISPR guides to change the level of genes by fractional amounts. This work studied the outcome of collisions between RNA polymerases and dCas9 on a strand of DNA, and uncovered a new parameter, the passage probability of the polymerase, that has important consequences for the strength of the repression. In chapter 4, I present a design for a high-throughput experiment to understand how the sequence of a guide RNA influences the polymerase's passage probability. The measurement has not been done yet, but I will discuss the theoretical considerations that drove the library design.

In chapter 5, I put the CRISPR knock-down technology into practice and systematically modulate the concentration of the core components of the cell wall synthesis machinery. I find that, even for enzymes with the same biochemical activity, a perturbation in concentration can elicit completely different responses in cell morphology. As our method allows to observe strains with essential enzymes repressed close to the lethal level while they are still growing steadily, I perform biophysical and biochemical measurements to better understand the function of these enzymes. This work highlights fundamental differences between the Rod complex and class A PBPs, and suggests that the later act on a smaller scale, repairing the cell wall and maintaining its integrity. Chapter 6 recounts how an unexpected side effect of CRISPR knock-down affected the study of cell wall synthesis. I discuss how the so-called Bad Seed Effect led to false conclusions, and how we could overcome it.

In chapter 7, I focus on another aspect of class A PBPs' function, which is their subcellular localization. I find that these enzymes have specific patterns of localization along the cell, and discover multiple factors that contribute to these patterns. In chapter 8, I investigate the effect of D-aminoacids on the cells, as they seem to interact with class A PBPs, though their biological significance is unknown. We perform a series of genome-wide CRISPR screens to find which cellular processes are related to it, and validate them. Finally, in chapter 9, I present two small side projects, both related to CRISPR knock-down, that gave promising and interesting results, but that I could not turn into complete stories due to the lack of time.

Chapter 2

Progress and mysteries in CRISPR control of bacterial transcription

2.1 Introduction

The ability to control gene expression levels in live bacteria is attractive for many reasons. First, modifying the concentration of a protein or enzyme is a classical way of understanding gene function. This is especially relevant in the case of essential genes were a simple knock-out is impossible. By comparing the phenotypes of cells at different levels of a gene of interest, one can gain fundamental insight on its function, and on the importance of this function for the organism's fitness. Controlling gene expression is also a way to discover regulatory circuits, by applying a perturbation and measuring how the expression of other genes adapts as a response. Furthermore, recent research in systems biology has aimed to understand the biological significance of gene expression levels in a broader context. Experimenting with gene expression levels has helped understand the evolutionary dynamics of gene regulation [55, 56], and the importance of stochastic processes in protein expression [57, 58]. Finally, the fine-tuning of gene expression level has great potential for the engineering of organisms with the aim of making them more efficient for industrial metabolite production or to create artificial regulatory circuits to be used in bio-sensors and diagnostic tools [59, 60].

Thus, there is a great interest for biotechnological methods that would allow to change gene expression in a programmable way, in the sense that the expression of any protein of interest can be set to arbitrary levels, according to some user-defined input in the form of a DNA sequence. However, the development of programmable biological devices has remained limited by a longstanding barrier: the complexity of macromolecule folding and their interactions makes it very difficult to design sequences *de novo* such that they have the desired function *in vivo*. For this reason, biotechnological design has typically been limited to the recycling of components from nature, or the artificial generation of many random devices followed by selection. In particular, inducible promoters are established as the standard tool for the control of gene expression in bacteria, allowing to link the expression level of a gene to the concentration of a chemical in the medium. While this method is extremely useful for a range of applications, the recent emergence of programmable methods has brought up new possibilities, especially in conjunction with high-throughput sequencing and DNA-synthesis technologies. Such technologies offer many advantages in principle: as they are generative, it is easy to create large scale libraries, or to make multiple orthogonal systems to be used at once in the same cell. As they are genetically-encoded, they can themselves act as barcodes, allowing for identification by sequencing. The field of eukaryotic biology was first to be revolutionized by programmable control of gene expression, with the development of RNA interference (RNAi) during the 1990s [61]. It took a few more years before similar methods were discovered for bacteria: the first tools based on antisense RNA (asRNA) were developped in the 2000s [62, 63, 64], before the rise of CRISPR in the 2010s [65, 54, 66].

In both cases, the target of repression is specified by cloning a part of the gene sequence next to a short scaffold sequence which may serve as a recognition site for helper proteins. Antisense RNAs act by forming a duplex with cognate messenger RNA and recruiting host-specific proteins, such as Hfq in *E. coli*, which leads to the degradation of the messenger [67]. The strength of asRNA knock-down is tunable by changing the binding energy between the asRNA and the target mRNA [68, 69] and it can be used on multiple targets in parallel [70]. Unfortunately, some technical constraints have limited the use of asRNAs for engineering gene expression. First, their efficiency strongly depends on the concentration of the antisense RNA, making it necessary to express it in excess compared to the target mRNA [67]. The scaffold sequence is also specific to each species, and the presence of endogenous nucleases may greatly impair the applicability of the method, in particular in *E. coli*, a problem that can be alleviated by using paired termini [64].

A few years ago, the discovery of the CRISPR bacterial immune system brought an alternative repression method to the spotlights.

2.2 Turning the CRISPR adaptative immune system into artificial transcription factors

By analogy with RNAi, gene knockdown using CRISPR effectors has been dubbed CRISPRi. However, unlike RNAi, which acts on translation, CRISPRi typically works by stopping transcription. CRISPR systems are an extremely diverse ensemble of adaptative immune systems found in bacteria and archea, that can be grouped in two classes, each comprising many types and subtypes (reviewed in Koonin et al. [71]) with very different mechanisms. To grant protection against bacteriophage infection, CRISPR systems work in two phases. The first one, called *adaptation*, is responsible for sampling short DNA sequences from the genomes of phages, and storing them in the form of a series of fixed-length sequences called the CRISPR array (for *Clustered Regularly Interspaced Short Palindromic Repeats*). The second phase is called *interference* and uses the collection of stored phage sequences to recognize their invading DNA and destroy it.

The machinery involved in the interference step can be repurposed to artificially control transcription. In nature, the CRISPR array is first transcribed and processed into individual guide RNAs, which are then associated with one or several enzymes (the CRISPR effectors) to form a nucleoprotein with nuclease activity. Upon phage infection, this nuclease will recognize the invading genome through base pairing and introduce a double-strand break to stop the infection. The nature of CRISPR effectors can be very different depending on the class and type of CRISPR system. For some types, the effector is one single enzyme, making them very popular for biotechnology. This is the case for the Type II which uses the famous Cas9 protein, as well as the Type V systems, with their effector Cas12a (formerly Cpf1) which have recently gained a lot of attention. In other cases, the effector consists in a large multi-protein complex, like the Cascade complex of Type I systems. By disabling the nuclease activity of the CRISPR effectors, it is possible to create an artificial DNA-binding protein, that can then be sent to any DNA sequence by putting arbitrary addresses in the CRISPR array.

To reprogram a CRISPR system, one can simply replace the native sequences in the CRISPR array by the desired target sequences and rely on natural processing and assembly of the nucleoprotein complex. Type II systems rely on a ternary complex comprising Cas9, the processed guide RNA and a linker called the tracrRNA. As an alternative, it is possible to use a pre-processed construct called single-guide RNA (sgRNA) [72]. In type V systems, there is no tracrRNA and the effector Cas12a is able to process the arrays by itself, so there is no major advantage in a single-guide design.

Not any position can be targeted by CRISPR effectors. The target sequence must be flanked by a DNA motif called the PAM[1]. The sequence of the PAM is different depending on which ortholog of CRISPR is being used, but is typically between 3 and 8 nucleotides long, meaning that there are usually many discrete possible targeting sites throughout a given sequence. Some CRISPR effectors have strict PAM requirements while others recognize a more variable range of motifs. For example, the PAM for the widely popular Cas9 from *Streptococcus pyogenes* (SpCas9) is `NGG` in 3' of the target [65], while *Eubacterium eligens*'s Cas12a requires `TTTV` in 5' of the target [73]. The length of the PAM determines the frequency of possible targets: on average, SpCas9 has one target every 8 bp in *E. coli*'s genome if both DNA strands are considered. This of course depends on the characteristics of the target genome: as SpCas9's PAM is `NGG`, it is not as common in genomes with a low GC-content. After binding to the DNA, the CRISPR effector starts to unwrap the DNA starting from the side of the PAM [74]. As the DNA unwinds, the guide RNA progressively forms an hybrid with the target DNA [75, 76]. This structure is called the R-loop. When the entire guide is annealed, a conformation shift occurs and a double-strand break is introduced in the DNA.

To simply block gene expression without cutting the target DNA, the nuclease activity of the CRISPR effectors must be eliminated. For the types II and V, this is done by mutating the catalytic residues [65, 66]. The resulting enzymes are marked with the letter "d" (for "dead"), for example the inactive variant of Cas9 is called dCas9. For type I, where the CRISPR effector is a multi-protein complex, the deletion of one of the subunits is also possible to abolish nuclease activity [77].

Owing to the remarkable effectiveness of CRISPR systems, many applications were quickly developed even with a limited knowledge of its exact mechanism. As a result, many rules of thumb were discovered during the testing and optimization of particular applications and research is still on going to develop an unified, predictive biophysical model.

---

[1] PAM stands for *Protospacer Adjacent Motif*. This name goes back to the time where the function of CRISPR systems was not well understood. Protospacer designates the part of phage DNA that will eventually be incorporated into the CRISPR array as a *spacer* during CRISPR adaptation.

2.3 Molecular and systemic mechanism

A roadblock on the way of the RNA-polymerase

To repress a gene, multiple choices of target are possible. If the effector (e.g. the dCas9/sgRNA complex) binds to the promoter region of the target, it lowers the number of mRNA transcripts by blocking the initiation of transcription. If the target is located within the coding sequence of the target gene, it interrupts elongation by standing in the way of the RNA-polymerase (RNAP) [66, 78].

When the target is in the promoter sequence, any DNA strand can be targeted and the repression will be equally strong. This has been observed for all types of CRISPR used so far: Type II [54, 79], Type V [73, 80] or Type I [77]. On the contrary, when the target is downstream of the promoter, within the coding sequence, target orientation has a crucial importance and the best orientation varies depending on the type of CRISPR system. For dCas9 (type II), repression is effective only if the guide RNA pairs with the *non-template* strand (i.e. when the guide RNA is homologous to the template strand, figure 2.1, top). If dCas9 is in the other orientation, the repressive effect virtually disappears [79]. Interestingly, an opposite behaviour has been observed for dCas12a (type V), which produces a stronger repression when it binds to the *template* strain [73] (figure 2.1, middle). For Type-I CRISPR of *E. coli*, the guide RNA must bind to the non-template strain to produce a strong repression [77] (figure 2.1, bottom). Together, these indicate that no simple rule determines which orientation is most effective for a given type of CRISPR system, be it PAM position, the direction of R-loop extension or the nature of the targeted strand. The exact mechanism of the collision thus remains to be elucidated on a more structural level, especially for effectors other than *S. pyogenes*'s dCas9. Importantly, for dCas9, the ability to stop the RNAP strongly depends on temperature, higher temperatures leading to weaker repression [81, 82]. It is not known if other effectors (such a dCas12a) are affected in the same way.

Consequences of the collision

Early experiments on the effect of target position within a gene suggested that targets farther away from the initiation codon tend to be less efficient for target repression [66], with no conclusive molecular explanation. More recent studies have since contradicted this phenomenon [79, 83], showing that on average the position of the target does not systematically affect the repression strength, as long as the target is far enough from the promoter to avoid interactions with the initiation step.

When elongation by the RNAP is interrupted, an incomplete mRNA is generated. If the target is inside the coding sequence of a protein, the incomplete transcript may have a ribosome binding site but no stop codon. In that case, it will likely be subject to degradation to avoid ribosome stalling [84], however the exact fate of the incomplete mRNA is hard to predict. Sequencing of the incomplete transcripts suggested that, after encountering dCas9, the RNAP may remain in place for some time, giving birth to trains of stalled polymerases [85]. There is also evidence that, depending on the interaction strength between the dCas9/sgRNA complex and the target, the RNAP can actively displace dCas9 and continue elongation to produce a full mRNA transcript [82].

Another crucial aspect of transcription interruption in bacteria is that genes are often co-transcribed in operons. As a result, interfering with one gene will likely have

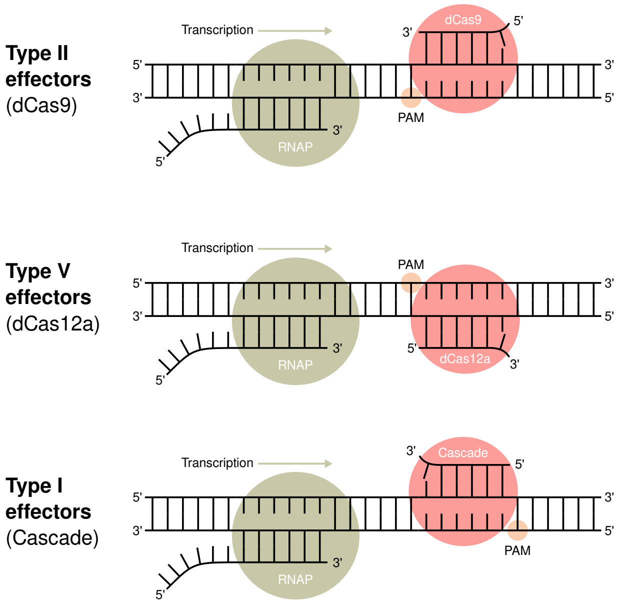

Figure 2.1: **Targeting the right strand for efficient repression.** The configuration depicted here is the one that leads to the strongest repression. The R-loop typically forms next to the PAM, then extends along the CRISPR guide. This is represented here by an imperfect annealing on the PAM-distal side.

effects on the other genes from the same mRNA molecule, referred to as polar effects[2]. Repression by CRISPR with a target inside an operon has a clear effect on all downstream genes, which are also repressed [87], a property that has been exploited to reveal the presence of unknown cryptic promoters in the middle of operons [87].

There is also some evidence that genes upstream of the target in an operon can be affected [78], especially when the target is within the first 50 bp of the gene [88]. This is probably due to changes in mRNA stability, however the exact process is not fully understood and might be specific to each operon due to different mRNA regulation motifs [89]. Possibly for similar reasons, a target within 100 bp downstream of the stop codon may also reduce gene repression to some extent [79].

Polar effects may be troublesome for singling out the effect of one gene, they may also be an advantage as operons usually consist of genes of related functions, from the same metabolic pathway or machinery. As a result, polar effects allow to reduce the number of targets needed in screening libraries.

Other factors may interfere with dCas9 binding to its target. One potentially important contextual factor is transcription on the opposite DNA strand in the case of two convergent promoters [90]. RNAP transcribing the “bottom” strand will eject dCas9 from the DNA with a very high probability, possibly alleviating the repression in the “top” direction. DNA supercoiling has also been shown to affect dCas9’s binding, as it increases the force required to unwind the DNA for target recognition. This may be important when using multiple binding sites on the same target, hoping to increase

---

[2] It should also be noted that antisense RNA, in spite of acting at the translation step, are also subject to polar effects since they trigger RNA degration [64, 86], though this effect is only partial.

the repression strength: if the targets are too close from each other, they might exhibit anti-cooperative behaviour [91].

Mismatched guides and off-targets

Large data sets have been produced to understand the effect of mismatches between the guide and the target. These efforts have currently focused on DNA cleavage by Cas9, for which many sequences have been compared using a repurposed sequencing flow cell [92] or the tx/tl *in vitro* translation system [93]. In most cases, the seed sequence (first 5 bp next to the PAM) is of essential importance for stable binding to the target. This is however not an universal rule, as mismatches in the seed do not necessarily abolish repression when the target is in a promoter [94].

The other end of the guide, the PAM-distal side, is typically important for DNA cleavage, but not necessary for strong binding, and guides with up to 9 mismatches on that side can still have a significant repressive effect [54]. For both dCas9 and dCas12a, the complementarity of the PAM-distal region influences the dissociation rate, to the point that it was called the reversibility-defining region [92]. This must be taken into account during guide design, in order to avoid off-targets in essential genes that could have a major impact on growth.

Kinetic models have been used to understand the behaviour of CRISPR effectors in the presence of a mismatched target. In these models, the system is broken up into a finite number of states, with kinetic parameters associated with the different transitions [95, 96]. As the R-loop extends from the PAM-proximal to the PAM-distal end of the guide, mismatches between the guide and the target can be seen as high potential barriers that can be overcome, in agreement with the observation that when the R-loop has extended past a mismatch, it can continue to extend normally [97]. Such models make interesting predictions: for example, they have been used to explain the somewhat paradoxical result that Cas9 variants with more relaxed PAM recognition tend to have less off-target cutting sites, despite having a higher number of potential targets [98, 95]. Interestingly, owing to the long-lasting binding of Cas9 to the target, the unbinding rate is usually much lower than the catalytic rate [95]. The consequence is that, for DNA cleavage, the kinetic equilibrium (where unbinding happens as fast as binding) will never be reached in most cases. This is a major difference with repression by deactivated nucleases, where the system may eventually reach equilibrium, and is an important reason why repression efficiency cannot be extrapolated from cutting efficiency.

Temporal dynamics and the search for target

Many points of the mechanism of effector assembly and association to the guide RNA remain to be elucidated. It is likely that the assembly of Cas9 and the guide RNA (crRNA or sgRNA) is quite stable and the two pieces stay together after initial association, as free Cas9 has a quite flexible structure and is stabilized by the crRNA [99].

The process by which the CRISPR effectors find their target has also received a lot of focus. Most known transcriptional regulators, such as those involved in inducible promoters, recognize their binding motif from the side, without unwrapping the two strands of the DNA. They can thus slide along the DNA groove until the operator is found. For CRISPR systems, however, this is not possible as target recognition involves complementary Watson-Crick base pairing and double-stranded DNA has to be open. Experiments with DNA curtains and fluorescently-labelled effectors allow to monitor the target search process *in vitro*. Such data exists for type II (Cas9) and type V (Cas12a). For both, there is a first step of 3D-diffusion until a DNA molecule is encountered [100]. This is followed by 1D-diffusion along DNA [101] though the contact with DNA is only intermittent. For Cas9, the 1D-diffusion is limited to very short distances (along 20 bp) but allows to jump from one PAM to another. For Cas12a, however, the 1D-diffusion step is dominant [102], and a molecule of Cas12a can appear to diffuse along the DNA molecule for extended periods of time. Another core difference between Cas9 and Cas12a regarding target search is that Cas9 needs only a PAM to bind to the DNA, even without any matching sequence. Cas12a will typically not stay associated with a PAM if the sequence next to it has no complementarity with the guide. In fact, Cas9 transiently associates with non-matching sites, with a residence time that depends on complementarity [99]. As a result, it spends a few milliseconds on each potential binding site, and a single dCas9 molecule may take several hours to find its target [103]. This search time has been evaluated to about 6 hours for *E. coli*'s 4 Mbp genome. Thus a large number of Cas9 complexes might be required for quick response, which is of particular importance for anti-phage defense. The importance of this for gene knock-down is still unclear.

The dissociation of dCas9 from the target is also very slow [100], in the order of a few hours *in vitro*. Because of that, the amount of effector that is required for gene silencing is very small. In fact, one single complex per target locus might be sufficient to shut down expression until it gets kicked out by the RNAP or the replication fork. After stopping the expression of dCas9, it takes up to five hours to reach the original expression level [66, 104]. This process can be made faster by using antisense RNA to trigger guide RNA degradation [105].

2.4 Improving CRISPR control of transcription

While the repurposing of natural CRISPR systems quickly lead to impressive results, a lot of effort has been undertaken to extend their capabilities. Here we discuss recent advances in improving the repression strength, controlling multiple targets at the same time and extending the application of CRISPR knock-down to a broader range of species, including some organisms that are not standard laboratory models. We also review the efforts that have been made to detect the potential undesirable effects of CRISPR systems, and strategies to tamper with them.

Tunable gene repression and activation

To obtained partial repression of the gene of interest, multiple approaches have been undertaken. The most straightforward one is to express the CRISPR system from an inducible promoter such at P_{bad} in *E. coli* [104, 106], or P_{xyl} in *B. subtillis* [78]. In that case, the repression strength is controlled by using variable amounts of a chemical in the medium, using a single strain. Changing the amount of sgRNA, rather than of dCas9, may provide better control [107]. Alternatively, by expressing a mismatched guide RNA and a constant amount of effector, it is possible to repress genes by a well-defined fraction [82]. While the later strategy requires several plasmids for different repression factors, it is easier to multiplex and is less noisy.

Inducible promoters, that are often used to turn CRISPR knock-down on or off, usually produce a base rate of leaky expression even when they are not induced. As previously discussed, due the long residence time of CRISPR effectors on the DNA, a small number of repressor complexes are enough to silence a target. Thus, even tight promoters can produce significant repression of the target in the absence of inducer [78, 104, 80]. One way to improve the dynamic range is to use a genetically recoded organism, with a non-natural aminoacid in dCas9. In this case, the leaky repression is strongly alleviated unless the non-natural aminoacid is also present [108]. While effective, this method is currently limited to one heavily-modified strain of *E. coli* and cannot be easily adapted to other organisms. Using anti-sense RNA targeted at the CRISPR guide itself, it is possible to antagonize repression, probably by actively triggering degradation of the guide RNA [109]. This provides another layer of regulation to construct genetic circuits, and a way to quickly recover gene expression once the repression is established.

Finally, CRISPR-based programmable transcription factors are not restricted to gene repression. By linking dCas9 to a transcription activator, it is also possible to increase the expression level of a target. Initial studies used the σ sub-unit from the RNA polymerase to induce expression [54], but subsequent screening found much more potent activators, in particular SoxS [110], an activator normally involved in oxydative stress response. When SoxS is tethered to dCas9 and the complex is targeted upstream of a promoter, expression of the reporter can be increased by more than 10-fold, making it possible to look at over-expression phenotypes for many genes in an easy way. Gene activation is also possible in *B. subtilis* using a similar approach [111]. A potential drawback for this method is that it requires a PAM at the right distance from the promoter, as the range of target positions that are effective for activation is very narrow, highlighting the importance of developing CRISPR effectors variant with different PAM specificities.

Simultaneous control of multiple targets

Natural CRISPR arrays often contain several dozens, sometimes hundreds, of guides [112]. Accordingly, is it possible to express multiple guides with a deactivated effector to repress multiple target at the same time. The upper limit on the number of guides used simultaneously for repression is unknown, but up to 8 sgRNAs have been used at the same time without any loss in repression strength [78]. Multiplex gene repression has been useful to find pairs of synthetic lethal gene and measure epistatic interactions [78, 113], as well as for metabolic engineering. Moreover, activation and repression can be used in the same cell by using a sgRNA-linked aptamer to recruit the activation tag only on certain targets [110].

Co-expressing sgRNAs can be quite cumbersome, as each of them requires its own promoter and transcription terminator. CRISPR arrays, similar to what is found in nature, might be more practical for the expression of many guides. Owing to the minimal processing of the array, dCas12a is particularly attractive for this purpose [114]. Due to their very repetitive nature, it is challenging to produce long CRISPR arrays with multiple spacers using standard DNA synthesis. However, by splitting the array into multiple parts to separate the repeats, streamlined protocols to assemble large CRISPR arrays have been designed, either using iterative [115, 77] or single-step assembly methods [107]. As the pool of effectors is shared between all CRISPR guides, having more guides in one array makes each individual complex less abundant, which can lead to reduced efficiency when targeting the promoter [77]. The number of complexes carrying each guide may also be different depending on the guide's context and position within the array. However, if the target is in the coding region and if the concentration of dCas9 is sufficient to saturate the binding sites, the strength of repression should not be affected [82].

From one bacterium to all others

One reason for the popularity of CRISPR systems is the fact that they are remarkably portable. Within just a few years after their discovery, CRISPR-based technologies were successfully used in all kingdoms of life [116, 117, 118, 119, 120]. Systems for gene knock-down are readily available for many bacteria, including species for which the available genetic tools are limited [121], bacteria used in industrial context [122, 123] or clinical pathogenic strains [124]. By using easily transferable, modular plasmid systems relying on bacterial conjugation, it is possible to perform genetic screens on non-model bacteria, including many human pathogens [85]. Furthermore, a thermostable variant of dCas9 was characterized for use in thermophilic organisms [125].

As about 45% of bacterial species possess a native CRISPR immune system [112], it is also possible to use it for repression. This has been done with *E. coli*'s endogenous Type I CRISPR system, where a simple deletion of the Cas3 protein, which carries the nuclease activity, allowed to create a programmable repressor [77].

Addressing side effects

When expressed at an excessive level, dCas9 itself can have some toxic effects on bacteria [126]. Morphological defects have been reported upon over-expression [127]. But the main source of side effects when using CRISPR knock-down is off-target binding. Even if a good complementarity between the guide and the target is necessary for strong repression, only a few matching bases in the PAM-proximal region may be enough to produce a small repressive effect [79]. If this effect happens on an essential gene, a severe growth defect may ensue. For some applications, off-target binding can be greatly reduced by replacing the PAM-binding domain of dCas9 with a binding domain from the PhlF repressor [128]. Consequently, dCas9 can only be targeted at regions containing the PhlF operator sequence, which restricts the application of this system to synthetic biology.

Another unresolved problem is the "bad seed effect" (BSE) [79]. Among all the possible seed sequences (the last five nucleotides in 3' of a guide), a few of them systematically cause a strong fitness defect when used with *S. pyogenes*'s dCas9. For instance, when a guide finishing in ACCCA is expressed in K-12 *E. coli*, it causes a near-complete death of the population. About 130 seed sequences (out of 1024 possible) cause this kind of sickness. A list of the ten most toxic ones is provided in table 2.1. The origin of this effect is still unknown. It does not appear to be due to off-target binding to a particularly critical locus, but may involve multiple simultaneous binding events, or binding to substrates other than genomic DNA [79]. This effect is very pervasive and can go unnoticed: for example, we could find evidence for BSE in data previously published by others [83] (figure 2.2), showing that it could be an unsuspected source of noise. To date, the best solution to avoid the BSE is simply to avoid bad seeds when designing a CRISPR guide. However, it was also shown that the BSE depends on dCas9's concentration, and that it can be almost erased by using a carefully-chosen expression cassette [79], while still retaining a strong repression capacity. We hope that future work will elucidate the origin of the BSE.

Seed sequence	Mean $\log_2$(fold-change)	
	High dCas9	Low dCas9
AGGAA	-6.50	-2.98
TGACT	-5.90	-1.34
ACCCA	-5.87	-2.46
AAAGG	-5.63	-1.68
GAGGC	-5.41	-1.91
CGGAA	-5.40	-1.51
ATATG	-5.37	-1.08
AACTA	-5.10	-0.88
TGGAA	-5.07	-1.26
CACTC	-5.01	-1.76

Table 2.1: **The 10 seed sequences that have the highest toxic effect on *E. coli***, according to Cui et al. [79]. Using an optimized strain with low dCas9 expression allows to greatly reduce the bad seed effect, but not completely abolish it. CRISPR guides with these seed sequences should be avoided if possible.

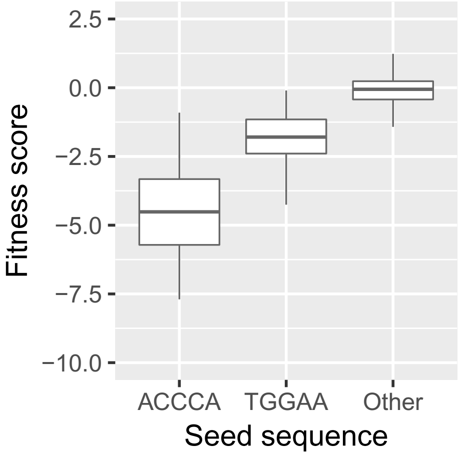

Figure 2.2: **Unnoticed "bad seed" effect in Wang et al.'s CRISPR screen** Using only CRISPR guides that target non-essential genes, we calculated the average fitness score ($\log_2$ of fold-change) of guides depending on their seed sequence. The sequences ACCCA and TGGAA are the two most toxic "bad seeds" discovered in Cui et al. [79]. In Wang et al. [83], guides carrying these two seeds produce a large fitness defect regardless of the gene they target.

2.5 Current applications

Genome-wide CRISPR screens

For a few model organisms, large collections of knock-out strains have been developped and used successfully. This includes the Keio collection for *E. coli* [129] and two barcoded deletion libraries in *B. subtilis* [130]. While these work-intensive construction projects are extremely valuable for the people working on these two models bacteria, they are impossible to transfer to new strains or species and, most importantly, they are limited to non-essential genes.

Early screens for essential genes were conducted using antisense RNA [63, 62, 86] though they were limited by the DNA synthesis and sequencing capabilities of the time. More recently, the random insertion of transposons in the genome has been leveraged to find essential genes in bacteria, a technique called Tn-Seq [131, 132]. As the insertion is random and not necessarily homogeneous across all the chromosome, deep sequencing is required to cover the entire genome. Long genes are more likely to be disrupted, while short sequences like non-coding RNAs are unlikely to be targeted, making it difficult to reach the desired precision on fitness measurement.

As an alternative, the fact that CRISPR knock-down and activation can control the expression of chromosomal genes remotely, even from a plasmid, makes it a promising tool for genome-wide screens. To create a CRISPR guide, one just needs to insert a short sequence (20 bp in the case of SpdCas9) in a well-defined locus. Thus, the construction procedure can be standardized and streamlined so that a large number of guides can be assembled in parallel, allowing to make customized screening libraries using on-chip oligonucleotide synthesis. Several cloning methods, using homologous assembly [115], golden-gate assembly [79, 133] or direct oligo integration coupled with a negative selection [104], have made it possible to assemble CRISPR guides in a single-step. Moreover, strains repressed by a CRISPR effector can easily be genotyped by simply sequencing the CRISPR guide, eliminating the need for a barcode or for a complex amplification protocol to locate an inserted sequence in the genome like in Tn-Seq.

Multiple CRISPR screens have already been used to find essential genes in various conditions [83, 87, 134, 135]. The applications of these data include discovery of drug targets, searching for synthetic lethal pairs, or genome minimization. Partial repression can also be useful to find phenotypes for essential genes [78]. CRISPR screens are also more versatile than TnSeq, as one can target only a subset of genes of interest, for example by targeting only genes implicated in a function of interest, or taking advantage of closely-related paralogs which are likely to be functionally identical [83]. If CRISPR guides are expressed from a plasmid, the same library can easily be re-used on many strains and in many conditions, making the method more cost-effective in the long run.

Measuring fitness through competition assays is perhaps the most evident output for a genome-wide CRISPR screening, but it is not the only one. For example, by performing a complete phage replication cycle in a population repressed by such a screening library, it was possible to identify host factors necessary for the production of infectious phage particles [87]. A CRISPR library has been combined with high-content microscopy to find the effect on growth, morphology, and identify the function of unknown genes in the pathogen *S. pneumoniae* [134]. In another study, comparing growth of a CRISPR strain library in the presence of a variety of chemicals allowed to reconstruct genetic networks and identify the target of antibiotics [78]. These last two approaches required isolated cultures of the different library members, greatly limiting the throughput of the screen. Recently, a method was developed to identify the genotype of CRISPR-repressed strains *in-situ* during a pooled assay, using fluorescence measurements [136]. While this proof of concept was only using a small number of strains, this principle could be scaled up to analyse large-scale libraries by high-content microscopy.

Synthetic biology and metabolic engineering

The programmability of CRISPR has made it popular among synthetic biologists. By expressing multiple guides at the same time, targeting them at each other, it is possible to construct predictable genetic circuits. As these circuits can interface with native chromosomal genes, it makes it easy to build artificial regulatory networks that control the bacteria's natural functions [126]. Such genetic circuits have been used to improve the yield of protein expression, by creating a feedback between metabolic burden and transcription [137], so that protein expression is regulated to an optimal level. The emergence of high-throughput transcriptomics and proteomics methods [138] makes it possible to measure how organisms respond to perturbations at the genome-scale, making the method very promising for deciphering regulatory motifs.

Aside from gene repression or activation, dCas9 has been programmed to interfere with various processes in the cell. This includes modifying the spatial structure of *E. coli*'s chromosome to create artificial DNA loops [139], blocking the initiation of replication to take control on cell cycle [81], and triggering cell filamentation in a reversible manner [140].

Another successful domain of application of CRISPR knock-down is metabolic engineering. CRISPR-based methods allow to quickly identify competing pathways and optimize metabolic fluxes [141] for the production of a compound of interest. CRISPRi has been set-up in multiple industrially-relevant organisms, such as *Lactococcus lactis* [122], *Clostridium beijerinckii* [88] or *Corynebacterium glutamicum* [123]. A review of other industrial strains were CRISPRi has been used can be found in [142], along with strategies used to improve production yield. Guides targeted at genes involved in rod-shape maintenance were used to diversify the morphology of cells and optimize production of a biodegradable plastic [143]. Finally, by inhibition of cell growth, one can optimize the balance between the production of biomass and the synthesis of metabolites [144].

2.6 Conclusion

Compared to the usual speed of biotechnological development, CRISPR systems were repurposed as tools in a particularly short time after their discovery. Owing to the multiplicity of their components, many degrees of freedom, like the sequence of the guide RNA scaffold or the stoichiometry of different parts were not fully explored. After a few years, we now know better the importance of each part, and begin to have a clear overview of how CRISPR interference happens, including the assembly of dCas9 complex, the search for target, the extension of the R-loop and the outcome of collisions with RNA polymerase. While many questions remain open, the control of transcription by CRISPR is becoming a mature technology, that can now be used for more ambitious large-scale projects.

Modern biology is in need for precise and quantitative results, as opposed to qualitative differences that simply pass the test for significance. Hence, it is crucial to identify all potential artifacts and false-positive that are likely to arise when using CRISPR systems. Off-target binding, time- and concentration-dependence, and the bad seed effect are all important challenges that need to be understood better to take full advantage of CRISPR's capabilities.

Chapter 3

Tuning dCas9's ability to block transcription enables robust, noiseless knockdown of bacterial genes

This part of the project was an initial characterization of CRISPR knock-down. Using a toy bacteria with multiple fluorescent reporters, the goal was to have an idea of the timescale, strength and reproducibility of the repression.

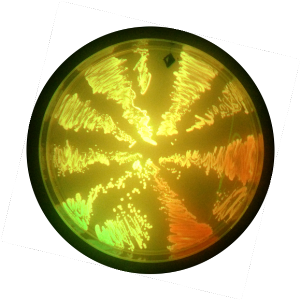

Figure 3.1: Rainbow plate obtained by setting RFP and GFP to various levels using CRISPR knock-down.

In particular, as we expected to use this method for single-cell studies, we wanted to know how repression is distributed across the population. This was the beginning of a long study on CRISPR knock-down that ended up revealing an unsuspected mechanism.

The next pages were published as:

Antoine Vigouroux, Enno Oldewurtel, Lun Cui, David Bikard, and Sven van Teeffelen, Tuning dCas9's ability to block transcription enables ro- bust, noiseless knockdown of bacterial genes. *Molecular Systems Biology*, 14(3):e7899, March 2018, ISSN-1744-4292. `doi:10.15252/msb.20177899.`

Article

SOURCE DATA
TRANSPARENT PROCESS
OPEN ACCESS

molecular systems biology

Tuning dCas9's ability to block transcription enables robust, noiseless knockdown of bacterial genes

Antoine Vigouroux[1,2], Enno Oldewurtel[2], Lun Cui[1], David Bikard[1,*] & Sven van Teeffelen[2,**]

Abstract

Over the past few years, tools that make use of the Cas9 nuclease have led to many breakthroughs, including in the control of gene expression. The catalytically dead variant of Cas9 known as dCas9 can be guided by small RNAs to block transcription of target genes, in a strategy also known as CRISPRi. Here, we reveal that the level of complementarity between the guide RNA and the target controls the rate at which RNA polymerase "kicks out" dCas9 from the target and completes transcription. We use this mechanism to precisely and robustly reduce gene expression by defined relative amounts. Alternatively, tuning repression by changing dCas9 concentration is noisy and promoter-strength dependent. We demonstrate broad applicability of this method to the study of genetic regulation and cellular physiology. First, we characterize feedback strength of a model auto-repressor. Second, we study the impact of amount variations of cell-wall synthesizing enzymes on cell morphology. Finally, we multiplex the system to obtain any combination of fractional repression of two genes.

Keywords CRISPR-dCas9; CRISPRi; gene-expression noise; peptidoglycan cell wall; single-cell

Subject Categories Quantitative Biology & Dynamical Systems; Synthetic Biology & Biotechnology; Transcription

DOI 10.15252/msb.20177899 | Received 4 August 2017 | Revised 8 February 2018 | Accepted 14 February 2018

Mol Syst Biol. (2018) 14: e7899

Introduction

A powerful way to investigate genes and their regulation in bacteria is to vary their expression levels and investigate the response of the cell. To that end, genes are typically placed under inducible promoters. While easy to implement, this approach has multiple disadvantages: First, native expression can lie outside the dynamic range of the inducible promoter. Second, inducible promoters typically increase expression noise in comparison with native promoters (Elowitz *et al*, 2002). And third, only few orthogonal inducible systems exist, thus making multiplexing difficult. Recently, different strategies have been devised to knock down gene expression by relative amounts from their native levels: Specifically, antisense transcription can reduce gene expression in a defined manner (Brophy & Voigt, 2016). While this approach works well for moderate promoter strength, it becomes less efficient the stronger the promoter. As an alternative strategy, genes can be knocked down from their native locus to varying degrees using CRISPR technology (Bikard *et al*, 2013; Qi *et al*, 2013). The catalytic mutant form of the RNA-guided Cas9 nuclease from *Streptococcus pyogenes* (dCas9) can be easily programmed to bind any position of interest on the chromosome, with the requirement of an "NGG" protospacer adjacent motif (PAM). dCas9 is unable to cleave target DNA, but still binds DNA strongly. If the target is chosen downstream of the promoter, dCas9 serves as a roadblock that blocks transcription elongation. Here, we characterize this system at the single-cell level, with interesting implications for the native CRISPR immune system. We then develop a strategy to use this system for precise and noise-preserving relative gene repression that is independent of promoter strength.

Target search of Cas9 begins by probing DNA for the presence of a PAM motif followed by DNA melting and complementarity-dependent RNA strand invasion (Sternberg *et al*, 2014; Szczelkun *et al*, 2014). While complementarity in the PAM-proximal region known as the seed sequence is important for binding, several mismatches in the PAM-distal region can be tolerated as demonstrated by DNA binding assays (Kuscu *et al*, 2014; Wu *et al*, 2014) and by monitoring target-gene repression in *Eschericha coli* (Bikard *et al*, 2013). The degree of gene repression can then be controlled quantitatively in two different ways: first, by changing the level of dCas9 expression from an inducible promoter, which impacts the probability of dCas9 binding to target DNA. This has recently been demonstrated in *Bacillus subtilis* where dCas9 was placed under the control of a xylose-inducible promoter (Peters *et al*, 2016), as well as in an *E. coli* strain modified to enable tunable control of expression from a P_{BAD} promoter (Li *et al*, 2016); second, by introducing mismatches between the guide RNA and the target DNA, as demonstrated in *E. coli* (Bikard *et al*, 2013). While a perfectly matched guide RNA leads

---

1 Synthetic Biology Laboratory, Institut Pasteur, Paris, France
2 Microbial Morphogenesis and Growth Laboratory, Institut Pasteur, Paris, France
*Corresponding author. Tel: +33 1 45 61 39 24; E-mail: david.bikard@pasteur.fr
**Corresponding author. Tel: +33 1 45 68 80 16; E-mail: sven.van-teeffelen@pasteur.fr

to very strong repression, decreasing complementarity in the PAM-distal region progressively reduces the repression strength (Bikard *et al*, 2013).

Here, we compare these two repression strategies by characterizing the properties of dCas9-mediated repression at the single-cell level. This enables us to propose a novel physical model of dCas9-mediated repression. It was previously assumed that decreased levels of guide RNA complementarity would decrease repression strength by virtue of reduced occupancy of the target by dCas9 (Farasat & Salis, 2016). Here, we demonstrate a different mechanism: If the target is inside an open reading frame (ORF), complementarity determines the probability that RNA polymerase (RNAP) kicks out dCas9 during the transcription attempt, while the rate of spontaneous dCas9 unbinding is negligibly small. If dCas9 levels are high enough to saturate the target, this mechanism alone determines repression strength. This leads to desirable properties: first, relative repression strength is independent of native expression levels. Second, repression does not add any extrinsic noise to gene expression. On the contrary, tuning gene expression by changing the level of dCas9 expression is inherently noisy and depends on the promoter strength of the target.

We demonstrate the use of complementarity-based CRISPR knockdown in combination with fluorescent-protein reporters inserted upstream of a gene of interest to precisely and robustly control its expression. The use of reporter gene fusions rather than direct targeting of the gene of interest yields a predictable repression fold as characterized in this study and provides an easy way to monitor expression levels in single cells. We demonstrate the versatility of our approach using two examples: first, the accurate control of the rate at which the RNAP kicks out dCas9 enables us to quantify the degree of feedback in a model auto-repressor by measuring how much actual gene expression differs from the controlled rate. Second, we take advantage of the ability to obtain a precise degree of repression during steady-state growth to investigate the impact of expression level of an operon coding for two essential cell-wall synthesis enzymes of the “rod” complex, PBP2 and RodA. Finally, we demonstrate that this system can be easily and robustly multiplexed to obtain any combination of the fractional repression of two genes.

Results

Varying levels of guide RNA-target complementarity enables controlling gene expression without addition of noise

To quantify how CRISPR-dCas9 modulates gene expression at the single-cell level, we integrated expression cassettes for two constitutively expressed reporters, *sfgfp* coding for the superfolder green fluorescent protein (GFP) and *mCherry* coding for a red fluorescent protein (RFP) at two different chromosomal loci of *E. coli* strain MG1655. To repress either of these genes using CRISPR knockdown, we integrated the *dcas9* gene from *S. pyogenes* under a P_{tet} promoter, inducible by the addition of anhydrotetracycline (aTc) (Qi *et al*, 2013). We then guided the dCas9 protein to target the coding strand of GFP- and RFP-coding ORFs using a constitutively expressed CRISPR array coding for the guide RNAs and the necessary tracrRNA, which form a complex together with dCas9 (Hsu *et al*, 2014). Inducing dCas9 expression in this setup did not have an impact on growth (Appendix Fig S1). We also measured the stability of the target-gene repression over time and saw repression over 5 days of culture. Once we stopped dCas9 induction all 40 clones tested recovered the target-gene expression. This genetic system is thus very stable, and dCas9 expression did not show any toxicity.

In this system, repression strength can be tuned in two different ways: either by modulating dCas9 expression level using different aTc concentrations or by modulating spacer complementarity to the target gene using different numbers of mismatches at the 5′ side of the spacer. We employed these two different strategies to repress GFP by different amounts and measured GFP concentration at the single-cell level by high-throughput microscopy (Fig 1A and B). As expected, average GFP levels decreased with increasing aTc concentration or increasing spacer complementarity. However, the distributions of single-cell GFP concentrations differed significantly between the two different modes of repression modulation (Fig 1C and D). Specifically, using a perfectly matched guide RNA and varying aTc concentrations led to large cell-to-cell fluctuations in the intermediate induction regime, where fluctuations of dCas9 levels strongly affect gene expression (Fig 1D and Appendix Fig S2). When dCas9 was not induced, fluctuations of the non-repressed constitutive promoter were recovered. For strong dCas9 expression, fluctuations were presumably reduced as the target site was saturated with dCas9 as elaborated below. On the contrary, inducing dCas9 at a constant high level with 100 ng/ml of aTc and varying the degree of guide RNA complementarity maintained the noise (standard deviation over the mean) of single-cell GFP concentration almost constant (Fig 1C and Appendix Fig S2). The plateau value of the expression noise of about 0.3 (corresponding to cell-to-cell variations of 30%) is similar to measurements made by others for constitutive genes in wild-type *E. coli* (Taniguchi *et al*, 2010). Complementarity-based gene repression is qualitatively different from gene repression using transcriptional repressors. For example, the Lac repressor can increase the extrinsic part of the noise of its targets by about fivefold as compared to the unrepressed case (see Appendix Fig S3), in agreement with previous measurements (Elowitz *et al*, 2002). Accordingly, a similar increase of noise is observed if repression is modulated by inducer concentration. The alternative system proposed here thus enables to tune expression levels with high precision in single cells.

RNAP can transcribe dCas9-bound targets in a complementarity-dependent manner

The lack of additional noise in gene expression at high dCas9 concentrations for different numbers of mismatches suggested to us that repression might be independent of fluctuations in dCas9 concentration. To test this hypothesis, we reduced the fraction of active dCas9 complexes roughly by a factor of two by introducing a decoy guide RNA (Fig 2A). We then measured population-averaged gene expression by flow cytometry. Indeed, we found the level of gene repression to be constant in the presence or absence of the decoy for both high and low degrees of complementarity (Fig 2B), confirming the hypothesis that the target is saturated by dCas9 for degrees of complementarity between 20

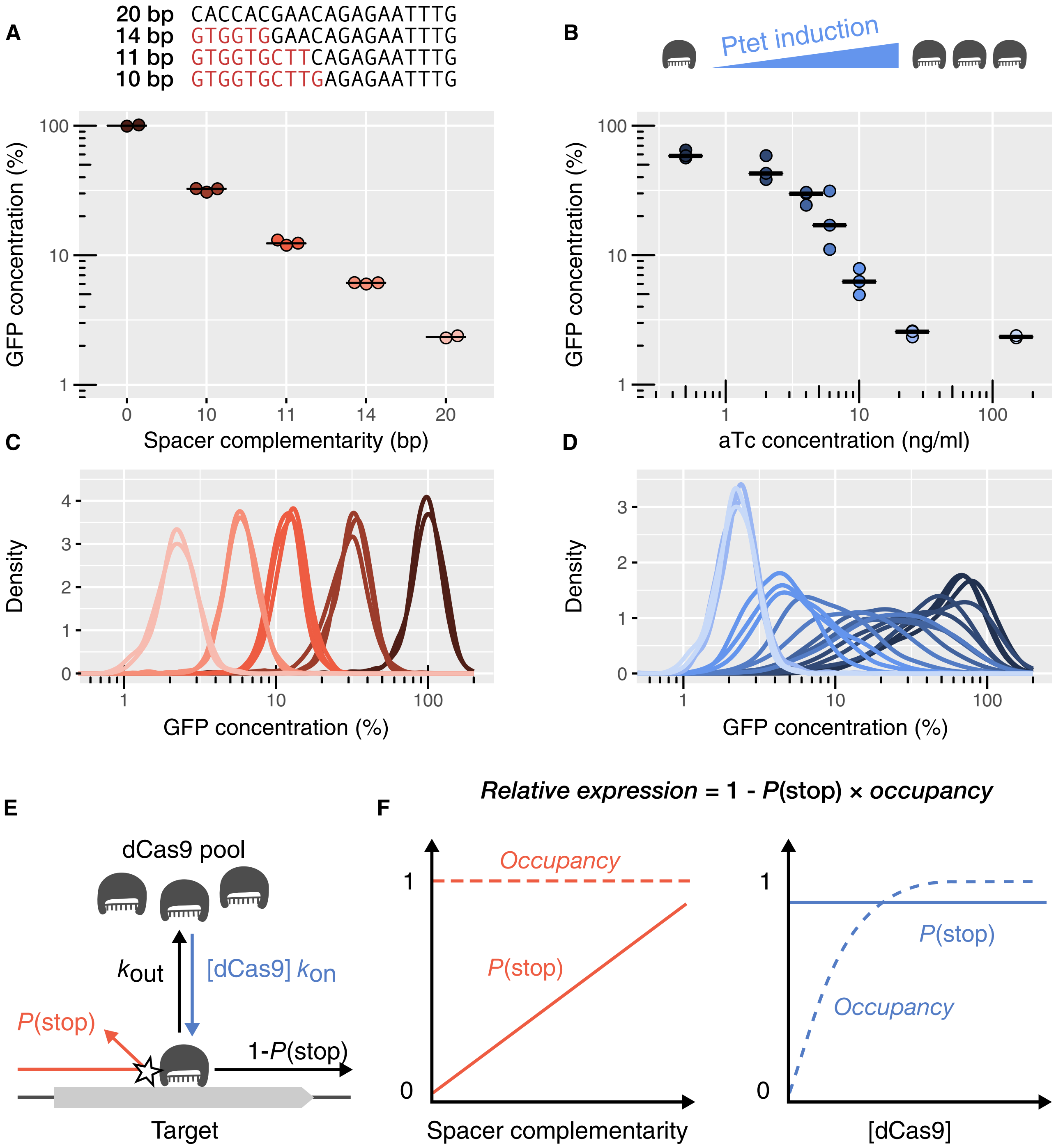

Figure 1. In saturating conditions, CRISPR knockdown can modulate gene expression over a large dynamic range without generating noise.

A, B Average cellular GFP concentration obtained (A) by changing guide RNA-target complementarity at a constant high dCas9 concentration or (B) by varying dCas9 levels with increasing concentration of the aTc inducer. Relative GFP concentrations are obtained by high-throughput microscopy and given relatively to the non-targeting spacer at high dCas9 expression. Individual points represent independent replicates. Horizontal bars represent the median of three replicates.

C, D Distribution of GFP concentrations for each experiment in panels (A and B). Curves of the same color represent replicates of the same condition.

E Mechanistic model of dCas9-mediated repression. The expression level of a dCas9-targeted gene is reduced by the product of two probabilities: the probability *P*(stop) of dCas9 blocking RNAP upon collision if occupying the target, and the probability of dCas9 occupying the target (termed occupancy). The occupancy is determined by binding constant k_{on}, dCas9 concentration [dCas9], and dCas9 unbinding rate k_{out}. The unbinding rate k_{out}, in turn, is the sum of transcription-independent unbinding rate and kick-out rate due to collision with the RNAP (see Materials and Methods for details).

F The two panels schematically illustrate the behavior of the probability of dCas9 blocking RNAP *P*(stop) and dCas9 occupancy if repression strength is controlled by guide RNA complementarity (left) or dCas9 concentration (right), respectively.

Source data are available online for this figure.

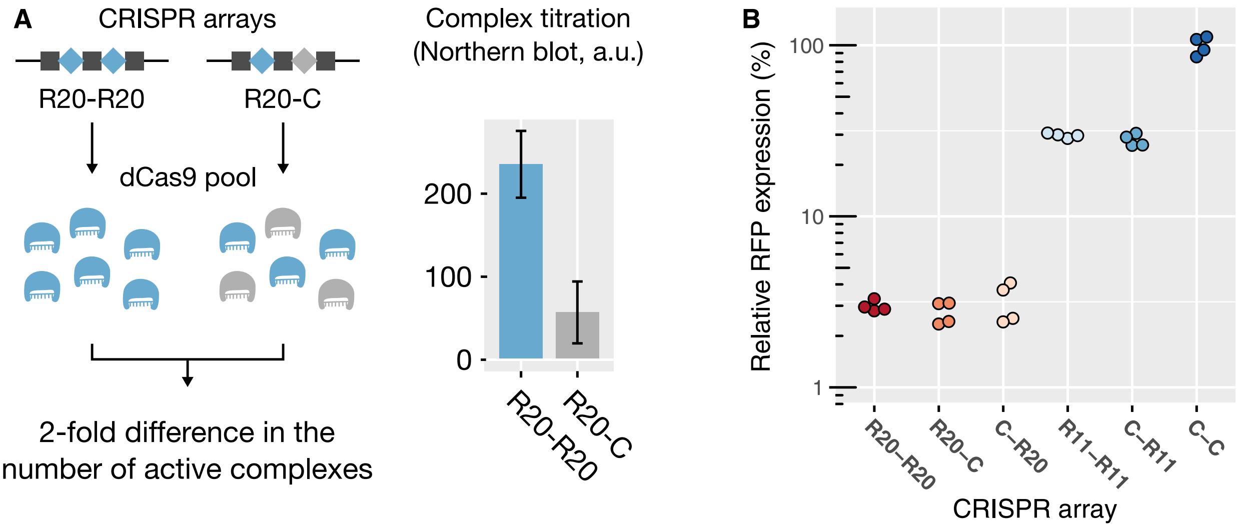

Figure 2. In saturating conditions, CRISPR knockdown by mismatched guide RNAs does not depend on the concentration of active dCas9 complexes.

A Left: Schematic of the assay used to investigate dependence on dCas9 complex concentration. R20 is a spacer targeting RFP with a perfect match. R11 targets RFP with 11 bp of complementarity. C is a non-targeting spacer. Introducing the spacer C in the CRISPR array acts as a decoy and halves the concentration of active dCas9 complex. Right: Northern blot measurement of the concentration of the processed guide RNA R20, reflecting the amount of complexes carrying R20 at the moment of the measurement. Error bars represent standard deviations of three biological replicates. a.u.: arbitrary units.

B Flow cytometry measurement of relative RFP expression levels, with each point representing one biological replicate. The values are normalized with respect to the non-targeting CRISPR array (C-C). Expression did not differ in the presence of the decoy (C-R20 vs. R20-R20, *P*-value: 0.68), nor when the order of the array was reversed (C-R20 vs. R20-C, *P*-value: 0.21), even with only 11 bp of complementarity (C-R11 vs. R11-R11, *P*-value: 0.53). *P*-values come from a two-sided Student's *t*-test applied to the natural logarithms of the mean expression (significance threshold: 0.017 after Bonferroni correction).

Source data are available online for this figure.

and 11 bp. This remained true even with three decoy spacers in a CRISPR array, regardless of the position of the active spacer in the array (Appendix Fig S4). The effectiveness of the decoy strategy was confirmed by gradually lowering the concentration of aTc until we observed the transition from strong repression to no repression. As expected, the transition happened at higher aTc concentrations with three decoys than with one (Appendix Fig S4B), confirming that decoys reduce the concentration of active complex. In both cases, at high induction, the residual expression reached a plateau value around 3%, corresponding to the concentration-independent regime. We note that these and the following measurements of population averages are performed by flow cytometry and are thus generally noisier than the results obtained by high-throughput microscopy presented in Fig 1.

Previously, it was thought that the repression strength due to dCas9 is solely determined by the occupancy of target DNA, that is, by the rates of target binding and spontaneous unbinding. According to this simple view, low and intermediate levels of target repression should inherently depend on dCas9 concentration, as higher dCas9 concentrations lead to higher equilibrium binding rates and thus higher occupancy, if the target is not fully occupied. This view is in clear contradiction to the observed independence of repression on dCas9 concentration for low and intermediate levels of repression (Fig 2B). On the contrary, independence of dCas9 concentration suggests that the target is saturated by dCas9, that is, that dCas9 is bound to the target at almost all times, and that a different mechanism must be responsible for different degrees of repression strength.

To reconcile the robustness of repression strength with respect to dCas9 concentration, we hypothesize that residual expression of the target gene might be possible even if dCas9 is saturating the target. We suggest that upon collision of RNAP with dCas9, dCas9 blocks the RNAP with a probability $P(\text{stop}) \leq 1$ that depends on guide RNA-target complementarity (Fig 1E). If $P(\text{stop}) = 1$, the system efficiently blocks RNAP every time RNAP and dCas9 collide. At the opposite extreme, if $P(\text{stop}) = 0$, dCas9 never blocks RNAP (Fig 1F). According to this mechanism, the expression level of a dCas9-targeted gene is given by

$$\gamma = \gamma_0[1 - P(\text{stop})P(\text{bound})].$$

Here, γ_0 is the native transcription rate and $P(\text{bound})$ is the probability that dCas9 is occupying the target.

The probability $P(\text{stop})$ only depends on guide RNA-target complementarity. Therefore, repression is independent of dCas9 concentration, if the occupancy is very close to 1, that is, if the target is saturated. In these conditions, cell-to-cell fluctuations of dCas9 concentration also no longer affect the repression of the target, thus explaining the low and constant noise obtained for different degrees of repression (Fig 1C and Appendix Fig S2).

Interestingly, when the same target is moved from the ORF to the promoter region, repression is increased and depends on concentration of active dCas9 complex (Appendix Fig S5). This finding suggests that RNAP can pass the occupied target site inside the ORF thanks to its processive polymerase activity, but that the RNAP cannot bind at the occupied target site inside the promoter region, where it relies on diffusion.

If dCas9 is saturating the target, relative repression is independent of target-gene promoter strength

To use CRISPR knockdown on genes with different native expression levels, it is important to know whether the transcription rate of the target has an influence on the relative repression. According to our model definition, the probability *P*(stop) that dCas9 blocks RNAP does not depend on promoter strength. Repression strength should thus not be measurably affected for promoters of different strengths, if dCas9 is saturating the target, that is if *P*(bound) is very close to 1. To verify this prediction, we put *sfgfp* under the control of two promoters of different strengths (P_{127} and P_{PhlF}) and blocked expression using four different guide RNAs with an increasing number of mismatches. While the strain with P_{PhlF} expressed about three times more GFP than the strain with P_{127} (Fig 3A), the repression fold with regard to the promoter's initial expression level was identical in each case (Fig 3B). We found the same behavior when we compared P_{127} with the 12 times weaker P_{Lac} promoter with 1 mM IPTG (Appendix Fig S6). These observations confirm that repression by mismatched guide RNAs in saturating conditions is independent of promoter strength.

If dCas9 is not saturating the target, relative repression depends on promoter strength, supporting a "kick-out" model of dCas9 ejection by RNAP

As transcription can be successful if dCas9 is saturating the target, we wondered whether dCas9 would be ejected from the target by RNAP during successful transcription events. While physical displacements would not affect repression in saturating conditions, they could measurably reduce the occupancy of the target *P*(bound) if dCas9 does not saturate the target, for example, if repression is controlled by dCas9 concentration. According to our kick-out model of dCas9 ejection by RNAP, the occupancy is given by

$$P(\text{bound}) = \frac{k_{on}[\text{dCas9}]}{k_{on}[\text{dCas9}] + k_{out}}.$$

Here, k_{on}[dCas9] is the rate of binding and k_{out} is the combined rate of RNAP-induced ejections, spontaneous unbinding and possibly replication-fork-based displacements (Jones *et al*, 2017; see Materials and Methods for details). A stronger promoter would increase the unbinding rate k_{out} and therefore reduce the occupancy *P*(bound), which, in turn, would reduce the repression fold. Indeed, we observed a weaker repression of the stronger P_{Phlf} promoter compared to P_{127} at low dCas9 concentrations. This observation quantitatively agrees with our kick-out model for full and intermediate (14 bp) levels of complementarity, respectively (Fig 3C and Appendix Fig S7A). For these levels of complementarity, our model also predicts that unbinding is dominated by kick-out events, while spontaneous unbinding is rare (Materials and Methods; Appendix Fig S7B).

For full complementarity, our model is compatible with the hypothesis that dCas9 never leaves the target spontaneously but gets kicked out either by the RNAP or during DNA replication. This prediction is consistent with the long half-life of dCas9 binding recently reported *in vivo* (Jones *et al*, 2017) and previously reported *in vitro* (Sternberg *et al*, 2014).

The kick-out model is expected to be valid for levels of complementarity lower than 14 bp, as the rate of successful transcription is increased (Fig 1A) while the target remains saturated down to 11 bp at high dCas9 concentrations (Fig 2B). However, spontaneous

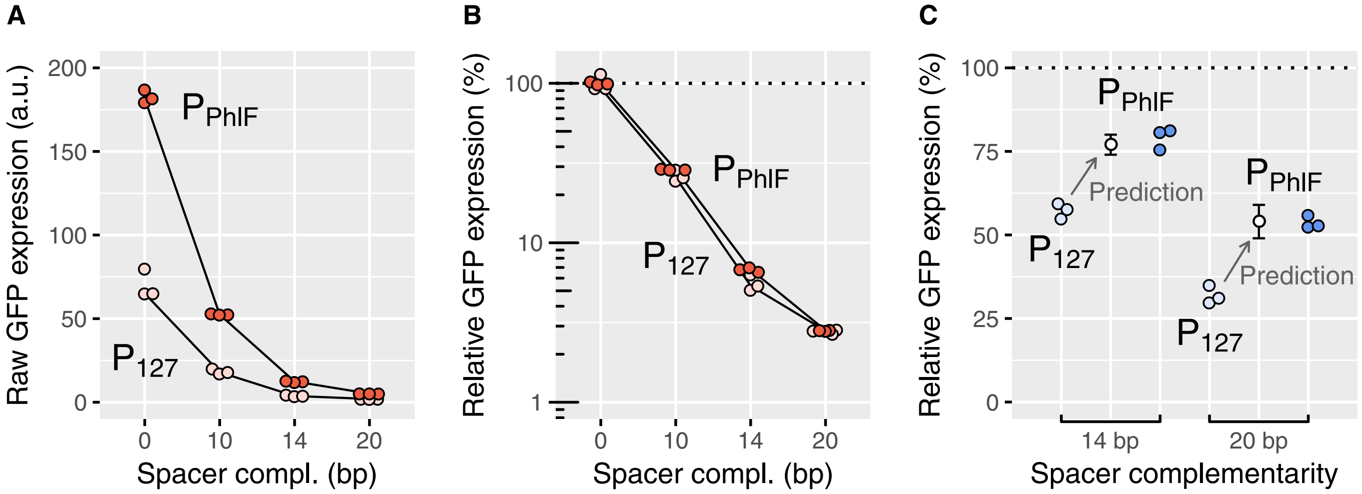

Figure 3. Relative repression by dCas9 is independent of promoter strength only in saturating conditions.

Relative GFP expression measured by flow cytometry for two promoters of different strengths (P_{127} and P_{Phlf}) and repressed using the same set of spacers for saturating (A, B) and non-saturating (C) dCas9 concentrations.

A, B Raw GFP expression (A) and relative GFP expression with respect to a non-targeting spacer (B) for a saturating dCas9 concentration. While P_{PhlF} is about three times stronger than P_{127}, the relative expression levels after repression are similar for both promoters.

C Experimental and predicted relative GFP expression for a non-saturating dCas9 concentration (using a 40 times lower concentration of aTc). Repression is weaker for the stronger P_{Phlf} promoter for up to six mismatches on the guide RNA, in quantitative agreement with the kick-out model (see Appendix). Error bars: standard error of the mean of the computational prediction.

Source data are available online for this figure.

unbinding is expected to become equally or more important than collision-based ejections below some level of complementarity below 14 bp. Yet, at high dCas9 concentrations used for all applications below, the combined rates of unbinding and ejections are still much lower than the rate of rebinding (see previous paragraph).

Finally, we note that our observation of promoter-strength dependence is compatible with any mechanism, for which the ejection rate is proportional to transcription rate, that is, it is in principle possible that a fraction of successful transcription events leaves dCas9 bound to the coding strand while the RNAP reads the template strand (see Materials and Methods for details).

dCas9 ejection probability increases with temperature

It was recently reported (Wiktor *et al*, 2016) that dCas9 is no longer active at 42°C, suggesting that repression strength might decrease with increasing temperature. This observation also bears the possibility that our system becomes less robust with respect to dCas9-copy number fluctuations and promoter strength with increasing temperature, if the condition of target saturation was not fulfilled. To quantify the temperature dependence of repression and test for robustness, we measured the repression of RFP by guide RNAs with 11 bp or 20 bp of complementarity at temperatures ranging from 30 to 42°C. The repression strength decayed continuously with increasing temperature (Fig 4), displaying a sharp decrease of repression between 37 and 42°C. Regardless of the temperature, repression strength was not affected by dCas9 complex concentration (Appendix Fig S8). From our model, we can thus conclude that increasing temperature does not affect dCas9 occupancy but increases the probability of dCas9 being kicked out by the RNAP. This also indicates that our system should work independently of promoter strength at all temperatures tested.

CRISPR knockdown in combination with fluorescent-protein insertions can be used to repress and monitor genes in their native contexts

Precision, robustness, and large dynamic range make complementarity-based CRISPR knockdown a versatile repression strategy. To repress genes of interest in their native context, we propose to insert *sfgfp* or *mCherry* reporters as transcriptional or translational fusions upstream of the gene. We provide here a convenient CRISPR-based method to perform these insertions inspired by a previous allelic exchange strategy (Pósfai *et al*, 1999) (see Appendix Text and Appendix Fig S9). A library of CRISPR plasmids can then be introduced to repress the fusions to the desired levels by targeting the *sfgfp* or *mCherry* coding sequences. The method thus allows taking advantage of the measured repression levels for constitutive promoters established above. Furthermore, gene expression can be measured at the single-cell level, revealing cell-to-cell variations. The library of CRISPR plasmids used here can be obtained through addgene (https://www.addgene.org/depositor-collections/bikard-crispr-repression/).

In the following, we demonstrate that this system has broad applicability for the study of genetic regulation and cellular physiology: first, we study the regulation of a model transcriptional feedback circuit, and second, we quantify the effect of fractional protein repression on cell morphology during steady-state growth.

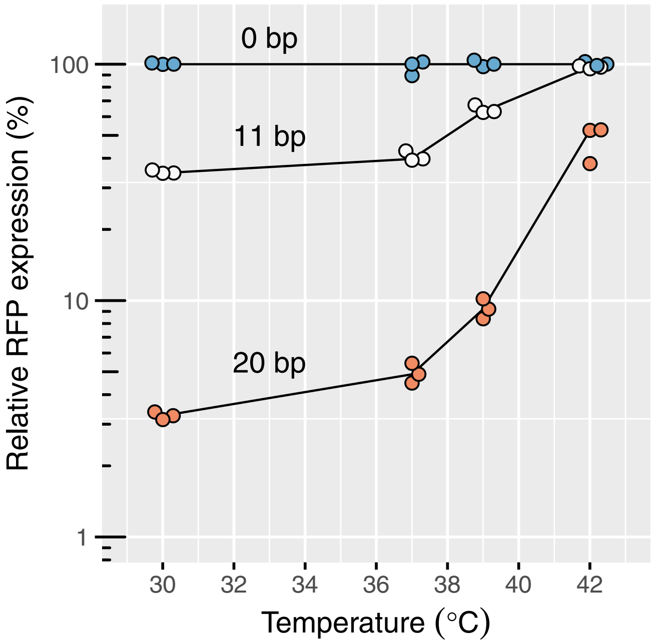

Figure 4. The efficiency of CRISPR knockdown is affected by high temperatures.

Relative RFP expression measured by flow cytometry upon repression with different levels of complementarity and at different temperatures. The values are normalized with respect to the non-targeting spacer at each temperature.

Source data are available online for this figure.

CRISPR knockdown can be used to uncover and characterize genetic feedback

To demonstrate the versatility of our system for the study of genetic circuits, we chose the previously described PhlF autorepressor from *Pseudomonas fluorescens* (Abbas *et al*, 2002) as a model system: We constructed a synthetic operon consisting in the P_{PhlF} promoter followed by the *sfgfp* and *phlF* genes in a single operon (Fig 5A). The PhlF repressor binds to the P_{PhlF} promoter and decreases transcription initiation, thus creating an artificial negative feedback loop. The strength of this feedback can be externally reduced by adding the chemical inducer 2,4-diacetyl-phloroglucinol (DAPG) that blocks binding of PhlF to the promoter. Accordingly, higher DAPG concentrations lead to higher steady-state concentrations of PhlF and GFP (Appendix Fig S10). To determine whether PhlF binds to the operator cooperatively, we aimed to quantify the feedback strength as a function of promoter strength for different DAPG concentrations. To mimic different promoter strengths, we targeted the *sfgfp* ORF using spacers with variable degrees of complementarity (Fig 5). CRISPR knockdown of GFP should lead to an increased transcription-initiation rate of the promoter. As a consequence, the fold change of expression during CRISPR knockdown should be lower in the case of feedback than without feedback. The quantitative difference between the two situations can then be used to quantify the feedback strength.

As anticipated, expression of GFP decreased with increasing complementarity and the relative reduction of expression was less pronounced with feedback than without feedback (Fig 5B). We then fit the expression data to a mathematical model of gene repression (Fig 5B, Appendix Fig S11 and Appendix Text) to calculate for each DAPG concentration the binding constant of the repressor K and a Hill coefficient n, which describe the dependence of repression on promoter strength. We observe that a Hill coefficient of $n = 2$ describes our data for low DAPG concentrations (0 and 5 μM), while a Hill coefficient of $n = 1$ was required to describe our observations at 50 μM. PhlF proteins dimerize *in vitro* and are thought to bind the operator as a dimer (Abbas *et al*, 2002). To reconcile our observation, we speculated that PhlF might be predominantly found as monomers at high DAPG concentrations and as dimers at low DAPG concentrations (see the Appendix Text for details). However, the detailed mechanism underlying the sharp transition in Hill coefficients remains to be studied by independent experiments.

The detailed insights obtained here demonstrate the usefulness of precisely controlling the rate at which the RNAP is blocked by dCas9, while monitoring residual expression with a fluorescent reporter. The same method can be applied to other and more complex problems of gene regulation, for example, by monitoring the response of one gene to the precisely tuned levels of another gene repressed by CRISPR knockdown.

CRISPR knockdown reveals how cells adapt their shapes to low levels of an essential cell-wall synthesis operon

We then used our approach to explore the morphological response of cells to different expression levels of two essential proteins for peptidoglycan cell-wall synthesis encoded by the *mrdAB* operon. PBP2 (encoded by *mrdA*) and RodA (encoded by *mrdB*) are inner membrane proteins with, respectively, transglycosylase (Meeske *et al*, 2016) and transpeptidase activity (Sauvage *et al*, 2008). The two highly conserved enzymes are part of the multi-enzyme “rod” complex, which is essential for cell-wall synthesis during cell elongation (Cho *et al*, 2016).

Previous depletion experiments suggest that PBP2 expression is buffered against large fluctuations in enzyme number, as cells grow for multiple generations before showing a reduction of growth rate (Lee *et al*, 2014). The drawback of depletion experiments is that they do not allow studying the effect of protein abundance in the steady state. To quantify the relation between PBP2 levels and morphological response during steady-state growth, we constructed a translational protein fusion by seamlessly integrating *mCherry* in front of the *mrdA* ORF in the native chromosomal *mrdAB* locus (Fig 6A). The mCherry-PBP2 fusion is fully functional, similarly to a fusion constructed previously (Lee *et al*, 2014). We then introduced a chromosomal P$_{tet}$-*dCas9* cassette and different pCRRNA plasmids programmed to target *mCherry* with 0, 11, 18 or 20 bp of complementarity in order to obtain a range of transcription rates for the operon. These strains were induced for dCas9 expression and grown until protein levels and cell dimensions reached steady state (Appendix Fig S12). Single-cell measurements were then performed by phase-contrast and epi-fluorescence microscopy.

Lowering expression of the *mrdAB* operon led to increasing cell width, with a sharp rise of cell width below ~20% of the native expression level (Fig 6B and C, and Appendix Fig S13A), while cell length was largely unaffected except for the highest repression strength (Appendix Figs S13B and S14), consistently with PBP2 and RodA being essential for building the cylindrical part of the cell wall but not the cell septum. We then wondered whether enzyme levels in individual cells were responsible for cell-to-cell variations in cell

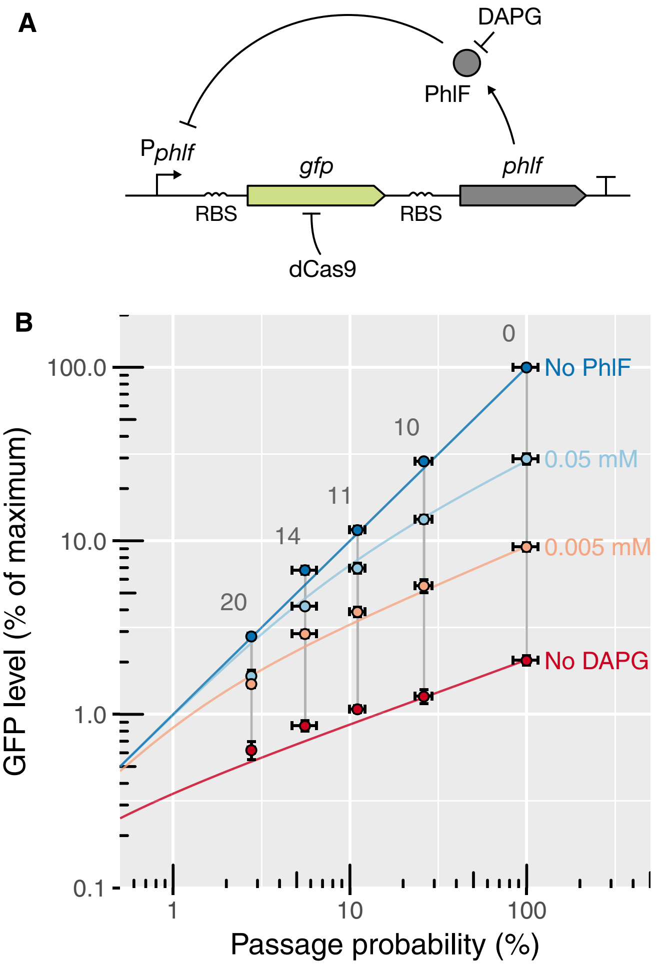

Figure 5. CRISPR knockdown can be used to quantitatively characterize feedback loops.

A Schematic of the synthetic feedback loop constructed for this experiment. The strength of the feedback can be modulated by addition of DAPG, an inhibitor of PhlF. RBS: ribosome binding site. T: transcription terminator.

B Flow cytometry measurements and fits to a theoretical model of relative GFP expression levels, where GFP is expressed from the artificial feedback loop presented in panel (A). GFP expression is normalized by the maximal level of GFP expressed constitutively from the P$_{PhlF}$ promoter alone (indicated as “No PhlF”). The GFP is repressed using four different guide RNAs with, respectively, 10, 11, 14, and 20 bp of complementarity. The passage probability 1 – P(stop) associated with each of these guide RNAs was measured in parallel on a strain expressing GFP constitutively from the P$_{127}$ promoter. Adding different amounts of DAPG to the medium reduces the strength of the feedback, causing the steady-state level to increase and repression to become more efficient. The colored lines represent the GFP expression as predicted by a mathematical model that was fitted to the data (see Appendix). For each DAPG concentration, a binding constant characterizing the strength of the feedback and a Hill coefficient were determined. Error bars: 95% confidence interval of the mean based on three biological replicates.

Source data are available online for this figure.

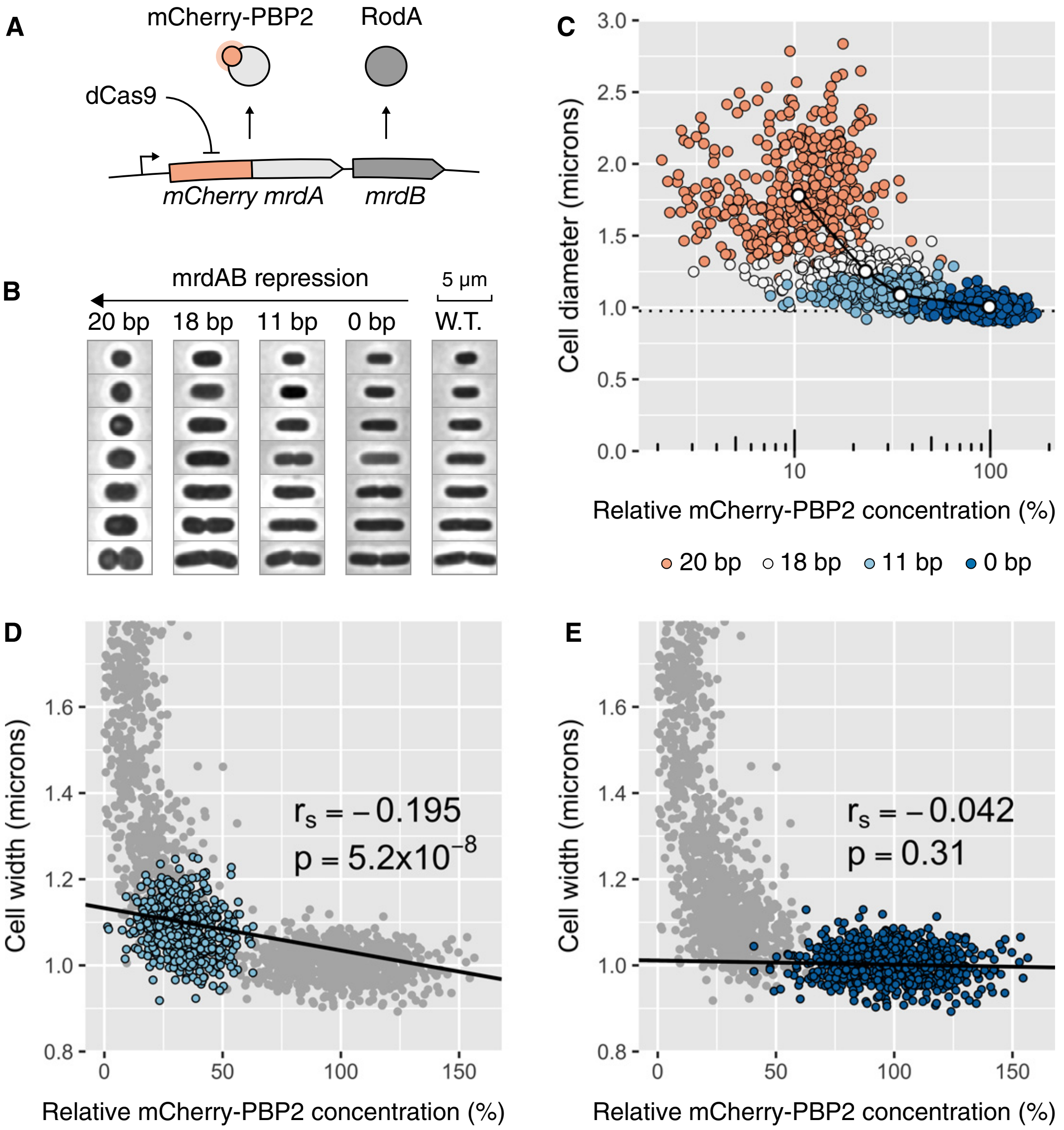

Figure 6. CRISPR knockdown of the *mrdAB* operon increases cell width at high repression strengths.

A Schematic of the modified chromosomal locus of the *mrdAB* operon in strain AV08.

B Cell shapes observed by phase-contrast microscopy for cells grown in M63 minimal medium. Different repression levels of the *mrdAB* operon are compared to wild-type *Eschericha coli*. Cells with different cell lengths were picked at random and images were rotated numerically.

C Cell width as a function of the mCherry-PBP2 concentration measured by fluorescence microscopy. Each point represents a cell, and colors represent different levels of spacer complementarity. The connected white dots represent the population averages (mean of three biological replicates). The dotted line represents the average cell width for wild-type *E. coli* (mean of three replicates). The values are normalized with respect to the non-targeting spacer.

D, E Linear regression between mCherry-PBP2 concentration level and cell width, for the strains repressed with 11 bp (panel D) and 0 bp (no repression, panel E). r_S is the Spearman correlation coefficient (median of three biological replicates). The negative value indicates that cells with a lower level of PBP2/RodA tend to be wider. The *P*-values (two-sided *F*-test) measure the certainty that the slope is different from 0.

Source data are available online for this figure.

diameter at low or intermediate expression levels, where the average cell diameter was affected by *mrdAB* repression. Indeed, we found cell-to-cell fluctuations in the intracellular density of mCherry-PBP2 to be negatively correlated with cell diameter for intermediate *mrdAB* repression (at 11-bp guide RNA/target complementarity; Fig 6D). Such a correlation was not observed when the operon was not repressed (Fig 6E), indicating that the cells buffer natural fluctuations of *mrdAB* and thus avoid fluctuations of cell morphology, as previously suggested (Lee *et al*, 2014). By gradually lowering the levels of PBP2 and RodA, we were able to take the cells out of the buffering regime at about 30% of native expression. Together, these experiments demonstrate that cells buffer stochastic gene expression of an essential operon against fluctuations of about threefold and that cells cope with even stronger fluctuations by adjusting their surface-to-volume ratio. However, once expression levels are reduced by more than fivefold, cells show severe growth defects.

CRISPR knockdown can be used to modulate the expression of two genes

With our method, the fractional repression level of any target gene is controlled genetically rather than chemically by the concentration of an inducer. It can thus be used to modify expression of multiple genes independently. To assess this potential, we built a library of CRISPR arrays containing two spacers, one targeting *sfgfp* and the other *mCherry*. We selected five spacers with varying levels of complementarity to each of the target, spanning a large range of expression, from 2 to 100% of the initial level. We combined these spacers to form 20 CRISPR arrays that cover the entire space of expression and used them to control the concentrations of GFP and RFP expressed from the chromosome (Fig 7A). As expected, the repression of one gene is independent of the repression of the other (Fig 7B). Strong correlations between GFP and RFP in single cells targeted with the same combinations of guide RNAs are due to common sources of extrinsic noise (Elowitz *et al*, 2002). We anticipate this to be a useful tool to study interactions of genes and specifically the effect of stoichiometry in genetic networks.

Discussion

Here, we demonstrate that tuning gene expression through complementarity between guide RNA and target works robustly at the single-cell level, with two specific advantages over previous methods: First, relative repression strength is independent of native expression levels, making the system applicable to study genes of vastly different promoter strengths. Second, the system preserves endogenous expression noise of the repressed gene. This allows studying the impact of gene repression on cellular physiology without generating stochastic cell-to-cell variability, which is known to have important downstream consequences for processes such as cell differentiation or the emergence of spatial structure in populations (Çağatay *et al*, 2009; Waite *et al*, 2016).

The ability to control gene expression level through guide RNA complementarity rather than the concentration of an inducer has other advantages: For example, it enables differential control of different cells within the same culture. This could prove useful in pooled screens or competition assays. Furthermore, the strategy can be multiplexed to enable the simultaneous control of multiple genes independently without requiring multiple chemical inducers. We demonstrated this ability with two targets (GFP and RFP; Fig 7), which can be inserted in front of genes of interest. The strategy can easily be extended to include more than two fluorescent reporters as targets, as demonstrated in Appendix Fig S4.

Alternatively to using fluorescent-protein fusions it is also possible to guide dCas9 directly to the gene of interest, but this comes with the disadvantage of uncertainty about the exact repression strength due to two reasons: first, the rate at which dCas9 blocks the RNAP is dependent on the specific target sequence. In the future, it might thus be desirable to develop computational means to predict target repression based on sequence alone (Boyle *et al*, 2017). Second, any feedback controlling the expression of the target could lead to altered transcription-initiation rates (Fig 5). Therefore, using fluorescent-protein fusions has the advantage to report the exact expression level.

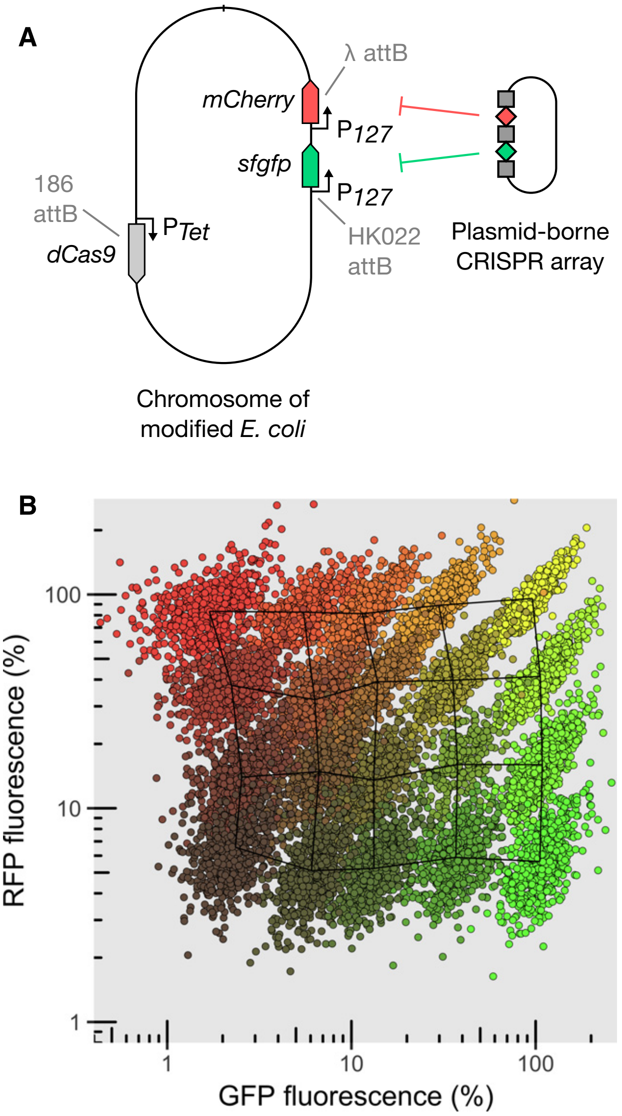

Figure 7. CRISPR knockdown can be multiplexed to modulate expression of two genes without cross-talk.

A Schematic of the strain expressing two reporters and P_{Tet}-*dCas9* integrated in the chromosome at phage attachment sites. The levels of the two reporters can be controlled using a plasmid-borne CRISPR array coding for guide RNAs (diamonds) interspaced with CRISPR repeat motifs (squares), and also carrying the tracrRNA sequence (not shown).

B Relative GFP and RFP concentration given relatively to the non-targeting spacer measured by high-throughput microscopy for a collection of 20 CRISPR plasmids. Each point represents a single cell, and each color represents the population obtained with one CRISPR plasmid. The overlaid meshwork connects the median values of the different populations.

Source data are available online for this figure.

The properties of dCas9 repression described in this study originate from the mechanism of dCas9 binding to DNA inside ORFs. We show that at high concentrations, dCas9 is saturating the target site even when using guide RNAs with large numbers of mismatches, where repression of the target gene is weak. We explain these observations by a "kick-out" model of repression, according to which RNAP kicks out dCas9 with a probability that can be tuned by spacer complementarity. The exact passage probability depends on the crRNA sequence. Here we provide a collection of guide RNAs against *mcherry* and *sfgfp* with known passage probabilities. Further work and larger datasets of diverse sequences will help to design new guides with predictable repression strength on arbitrary targets. The model predicts that repression is promoter-strength dependent in non-saturating conditions, in quantitative agreement with experiments (Fig 3C).

For full complementarity, our model is compatible with the hypothesis that dCas9 never leaves the target spontaneously but gets kicked out either by the RNAP or during DNA replication, consistent with the long half-life of dCas9 binding recently observed by single-molecule tracking and by restriction-protection assays (Jones *et al*, 2017) and previously also observed *in vitro* (Sternberg *et al*, 2014). A recent high-throughput study of dCas9 off-target binding and unbinding suggests that mutations in the PAM-distal region control the unbinding kinetics of dCas9 (Boyle *et al*, 2017). Since unbinding is dominated by RNAP-dCas9 collisions for the promoters tested here and as rebinding to the target is fast at high dCas9 concentrations, spontaneous unbinding plays no significant role for gene repression in our model system. However, if dCas9 targets the promoter rather than the coding region, spontaneous unbinding or replication-fork-based displacements might be the only modes allowing residual gene expression. This view is supported by the higher repression strength observed when targeting the promoter region (Bikard *et al*, 2013; Qi *et al*, 2013) and by the dependence on concentration (Appendix Fig S5).

Our results also suggest that dCas9 ejection does not lead to bursts of transcription, but that instead dCas9 returns to the target site after ejection in a time that is small with respect to the typical time interval between transcription initiations. It is still conceivable that such bursts may occur for transcription rates higher than the strongest promoter we used.

The results presented here argue for the use of high levels of dCas9 when performing CRISPRi assays in order to ensure that the target position is saturated. It is however important to highlight that the overexpression of dCas9 has been reported to be toxic for *E. coli* (Nielsen & Voigt, 2014). It is therefore preferable not to overexpress dCas9 far above the saturation point.

Our strategy enables to precisely control gene expression without introducing cell-to-cell variability, and should be useful for any quantitative measurements that depend on the expression level of a gene. By taking advantage of the ability to precisely control the rate at which dCas9 blocks the RNAP we could characterize a synthetic feedback loop, revealing unexpected properties of Phlf repression activity. In a second example, we took advantage of the ability to fine-tune expression levels at the steady state to quantitatively measure cell shape as a function of the levels of PBP2 and RodA. The level of precision achieved here would be hard to establish with conventional methods. Accordingly, this is the first study to establish a quantitative relationship between the abundance of cell-wall synthesizing proteins and cell morphology at the population and single-cell levels. We anticipate that our method will be useful to study many other systems and in particular genetic circuits that include high levels of noise, such as stochastic switches, or other noise-dependent processes, where preservation of a well-defined level of expression noise is desirable.

Materials and Methods

Kick-out model of CRISPR knockdown

As already described in the main text, dCas9 is thought to bind to target DNA where it provides a roadblock for RNAP, thus blocking transcription. According to this mechanism, the expression level γ of a dCas9-targeted gene is given by

$$\gamma = \gamma_0[1 - P(\text{stop})P(\text{bound})]. \tag{1}$$

Here, γ_0 is the native transcription rate, P(stop) is the probability of dCas9 blocking RNAP if dCas9 is occupying the target, and P(bound) is the probability that dCas9 is occupying the target (henceforth also termed occupancy).

While the probability P(stop) only depends on guide RNA-target complementarity, the occupancy P(bound) generally depends on complementarity, dCas9 concentration, and possibly on transcription-initiation rate (see the following paragraph). Therefore, repression is independent of dCas9 concentration only if the occupancy is very close to one ($1 - P(\text{bound}) \ll 1$), that is, if the target is saturated.

According to straight-forward reaction kinetics, the occupancy is given by

$$P(\text{bound}) = \frac{k_{\text{on}}[\text{dCas9}]}{k_{\text{on}}[\text{dCas9}] + k_{\text{out}}}, \tag{2}$$

where k_{out} is the rate of dCas9 leaving the target. dCas9 can in principle leave the target by two different mechanisms, by transcription-independent unbinding (with rate k_{off} if bound to the target), or by being kicked out from the target during all or part of the successful RNAP passage events, that is, during collisions where transcription continues. Alternatively, dCas9 could stay bound during all successful passage events. According to the two different models, k_{out} is given by

$$k_{\text{out}} = \delta[1 - P(\text{stop})]\gamma_0 + k_{\text{off}}, \tag{3}$$

where we introduced an ejection frequency δ. If $\delta = 1$, all successful passage events lead to dCas9 ejection. On the contrary, $\delta = 0$ corresponds to the scenario, where dCas9 stays bound during successful passage events. If the kick-out model was correct ($\delta > 0$), higher transcription-initiation rates γ_0 should thus lead to lower target occupancy. If the spontaneous unbinding model was correct ($\delta = 0$), occupancy should be independent of γ_0.

To identify the correct collision mechanism, we measured repression of *msfgfp* placed under two promoters with different promoter strengths at an intermediate level of dCas9 concentration, where the target is not saturated by dCas9 and where changes of occupancy due to promoter strength should be clearly visible. We found that the relative GFP expression (normalized with respect to the unrepressed case) of a promoter with 2.6-fold higher promoter strength is increased by 1.7-fold as compared to the weaker promoter for full complementarity between guide RNA and target (Fig 3C). Thus, repression shows a strong dependence on promoter strength. This observation suggests that dCas9 is kicked out of the target site during all or part of the successful passage events. Plugging equation (2) into equation (1) and using equation (3) for k_{out}, the kick-out model of dCas9-based gene repression thus predicts a normalized transcription rate

$$\gamma^* = \frac{1 - P(\mathrm{stop})k_{\mathrm{on}}[\mathrm{dCas9}]}{k_{\mathrm{on}}[\mathrm{dCas9}] + \delta[1 - P(\mathrm{stop})]\gamma_0 + k_{\mathrm{off}}}, \tag{4}$$

where we defined $\gamma^* = \gamma/\gamma_0$. Equation (4) is the central result of our model.

Quantitative comparison with the experiment

Here, we compare model prediction and experimental expression rates for two different promoters in saturating and non-saturating conditions (Fig 3B and C, respectively). We first consider the case of full complementarity between guide RNA and target. For a quantitative comparison, we eliminate one of the three experimentally unknown parameters, the dCas9 rebinding rate $k_{\mathrm{on}}[\mathrm{dCas9}]$, by introducing the following dimensionless quantities: $\lambda = \delta\gamma_0/(k_{\mathrm{on}}[\mathrm{dCas9}])$ is the ratio of the rate of induced dCas9 displacements over the rate of dCas9 rebinding, $\alpha = k_{\mathrm{off}}/(k_{\mathrm{on}}[\mathrm{dCas9}])$ is the ratio of transcription-independent unbinding rate over rebinding rate, and $r = 1 - P(\mathrm{stop})$ is the probability of successful transcription in the presence of target-bound dCas9. The latter probability is known to be $r = 0.026 \pm 0.003$ for full complementarity between guide RNA and target from independent experiments in saturating conditions (Fig 3B). Equation (4) can then be written as

$$\gamma^* = \frac{r + \lambda r + \alpha}{1 + \lambda r + \alpha} \tag{5}$$

leaving two unknown parameters, λ and α.

The lifetime of dCas9-DNA complexes is greater than 45 min *in vitro* (Sternberg *et al*, 2014), suggesting that the unbinding rate k_{off} is low *in vivo*. We thus hypothesized that the dimensionless transcription-independent unbinding rate might be negligibly small, that is, $\alpha \ll 1 + \lambda r$, which would allow us to simplify

$$\gamma^* \approx \frac{r + \lambda r}{1 + \lambda r},\ \text{if } \alpha \ll 1 + \lambda r \tag{6}$$

thus leaving only one unknown parameter λ.

To test this hypothesis, we compare the predicted expression level (equation 5) for zero and finite values of α to our experimentally obtained data of GFP expression from the two promoters $\mathrm{P_{PhlF}}$ and $\mathrm{P_{127}}$ (Fig 3C). In Appendix Fig S7A, the predicted expression γ^* is plotted as a function of λr for two values of α ($\alpha = 0$, $\alpha = 0.3$).

To obtain the prediction of GFP expression, we used the measurements of $\mathrm{P_{127}}$-GFP as a reference to infer the normalized kick-out rate $\lambda(\mathrm{P_{127}})r$ corresponding to the experimental GFP expression levels of $\gamma^*_{\mathrm{ex}}(\mathrm{P_{127}}) = 0.32 \pm 0.04$ (Fig 2C),

$$\lambda(\mathrm{P_{127}})r = \frac{(1 + \alpha)\gamma^*_{\mathrm{ex}}(\mathrm{P_{127}}) - r - \alpha}{1 - \gamma^*_{\mathrm{ex}}(\mathrm{P_{127}})} \tag{7}$$

also indicated by the gray vertical lines in Appendix Fig S5A for the two values of $\alpha = 0$ and $\alpha = 0.3$. Then, we asked for the predicted relative expression level of the repressed $\mathrm{P_{PhlF}}$-GFP, given prior knowledge that the $\mathrm{P_{PhlF}}$ promoter is (2.6 ± 0.2)-times stronger than $\mathrm{P_{127}}$ (Fig 3A) and therefore $\lambda(\mathrm{P_{PhlF}}) = (2.6 \pm 0.2)\lambda(\mathrm{P_{127}})$. The predicted expression level of the $\mathrm{P_{PhlF}}$ promoter is thus

$$\gamma^*(\mathrm{P_{PhlF}}) = \frac{r + \lambda(\mathrm{P_{PhlF}})r + \alpha}{1 + \lambda(\mathrm{P_{PhlF}})r + \alpha}. \tag{8}$$

According to our hypothesis of $\alpha = 0$, we obtain $\gamma^*(\mathrm{P_{Phlf}}) = 0.54 \pm 0.05$. This value is in great quantitative agreement with the measured expression level of $\gamma^*_{\mathrm{ex}}(\mathrm{P_{PhlF}}) = 0.54 \pm 0.02$. On the contrary, values of $\alpha > 0.14$ lead to predicted expression levels significantly lower than the experimental value (Appendix Fig S7B). Together, these results confirm that the kick-out model quantitatively describes the mechanism of dCas9 repression and suggest that the transcription-independent unbinding rate for guide RNAs of full complementarity to their targets is indeed much lower than the rebinding rate ($k_{\mathrm{off}} \ll k_{\mathrm{on}}[\mathrm{dCas9}]$).

We then wondered whether the transcription-independent unbinding rate α would increase for reduced degrees of complementarity. To that end, we performed the same analysis as above on experimental data for GFP expression from the two promoters at non-saturating levels of dCas9 but now for guide RNA that carries six mismatches (corresponding to a increased passage probability of $r = 0.056 \pm 0.001$). As in the case of full complementarity, we found an excellent agreement between the experimental and predicted GFP expression levels ($\gamma^*_{\mathrm{ex}}(\mathrm{P_{PhlF}}) = 0.79 \pm 0.04$ vs. $\gamma^*(\mathrm{P_{PhlF}}) = 0.77 \pm 0.03$) for a transcription-independent unbinding rate of $\alpha = 0$ while predicted expression values for $\alpha > 0.35$ are significantly lower than the measured expression level. We also carried out experiments with a guide RNA of 10 mismatches. However, the experimental data showed uncertainties too large to make conclusions about the level of α. We thus conclude that the dCas9-target complex is stable even for reduced degrees of complementarity of down to 14 bp and maybe less.

A lower limit for the lifetime of the dCas9-DNA complex

To obtain a quantitative estimate of the rate k_{off} in the case of full complementarity, we took advantage of the relationship

$$k_{\mathrm{off}} \lesssim 0.14 k_{\mathrm{on}}[\mathrm{dCas9}] = \frac{0.14\delta\gamma_0}{\lambda} \approx 8 \times 10^{-3}\delta\gamma_0,$$

where we used $\lambda r(\mathrm{P_{127}}) \approx 0.43$ and $r \approx 0.026$. $\mathrm{P_{127}}$ is based on the consensus promoter sequence and thus not expected to be stronger than well-studied model promoters in *E. coli*, which display transcription rates of not more than about 20 min^{-1} (Kennell & Riezman, 1977; So *et al*, 2011). This suggests that the unbinding rate of dCas9 in the absence of RNAP-based collisions is smaller than 1/6 min^{-1}. This is based on the conservative assumption that all successful transcription events lead to a displacement of dCas9 from the target, that is, δ = 1. For the reduced complementarity of 6 mismatches we obtain a lower limit of $1/2.4\ \text{min}^{-1}$.

The average number of chromosomal loci per cell coding for *msfgfp* is about 2, given a doubling time of about $t_d \approx 30$ min in our growth conditions, an average DNA replication time of about $t_C \approx 60$ min at 30°C (Breier *et al*, 2005), and assuming a D-period of $t_D = 20$ min. The gene copy number per cell is then given by $n(\Phi) = 2^{t_C(1-|\Phi|)} + t_D \approx 2$, where $\Phi = 0.66$ is the relative distance of the gene locus from the origin of replication, if distance is normalized with respect to the distance between origin and terminus. Thus, the lifetime of a single dCas9-DNA complex (n/k_{off}) is greater than about 12 min (full complementarity) or 5 min (6 mismatches). Notably, these timescales should be regarded as lower bounds, while the actual lifetimes might be significantly larger. This estimate is thus in agreement with recent single-molecule tracking and restriction-protection assays (Jones *et al*, 2017), which demonstrate that the lifetime of the dCas9-DNA complex is equal to the cellular doubling time in the case of full complementarity. It is also in agreement with *in vitro* data, which suggest that the lifetime is greater than 45 min (Sternberg *et al*, 2014). Given that the lower limit of the *in vivo* lifetime is of the same order of magnitude as the cell doubling time of 30 min, it is conceivable that dCas9 virtually never leaves the target site by equilibrium unbinding but instead is kicked out during DNA replication events by the DNA replication machinery, as also strongly supported by (Jones *et al*, 2017).

Genome modifications

All the strains used for measurements derive from *E. coli* MG1655. Appendix Table S1 details the construction of the strains used in this study.

For integration of cassettes at phage attachment sites, we used the “clonetegration” method (St-Pierre *et al*, 2013). Integrated backbones were excised by expressing a flippase from pE-FLP. Plasmid pLC97 can be used to easily integrate P_{tet}-*dCas9* at the lambda attB site.

For scarless integration of *mCherry-mrdA* in the native *mrdAB* operon, we used the pCas/pTarget system (Jiang *et al*, 2015). The PAmCherry-PBP2 protein fusion present in strain TKL130 (Subach *et al*, 2009; Lee *et al*, 2014) was replaced by a translational fusion with *mCherry* extracted from plasmid pFB262 (Bendezú *et al*, 2009). To this end, the pAV06 variant of pTarget was constructed and genome editing was performed as described in reference (Jiang *et al*, 2015). The deletion of the *lacY* gene in AV76 was done by P1 transduction using the strain JW0334 from the Keio collection (Baba *et al*, 2006) as a donor.

We also propose a novel CRISPR-Cas9 allelic exchange strategy for the scarless integration of *mCherry* or *sfgfp* in front of genes of interest. This strategy is detailed in the Appendix Fig S9.

The sequences of the *sfgfp* and *mCherry* genes used in this study can be found on the GenBank database with accession codes KT192141.2 and JX155246.1, respectively.

Plasmid design and construction

The CRISPR targets were chosen next to the beginning of the ORF, but at least 50 bp away from the initiation codon, in order to preclude unwanted interactions with the native regulation of transcription. None of the spacers used in this study have any off-target position with more than 8 bp of complementarity in the PAM-proximal region. Spacers were cloned into the CRISPR array of plasmid pCRRNA using Golden-Gate assembly as previously described (Bikard *et al*, 2014; Cui & Bikard, 2016). The oligonucleotide sequences are available in Appendix Table S4.

The other plasmids from this study were constructed by Gibson assembly (Gibson *et al*, 2009). The fragments are described in Appendix Table S2 and the primer sequences in Appendix Table S3. DNA constructions were electroporated in *E. coli* strain DH5α or Pi1 for *pir*-dependent origins of replication (Shafferman & Helinski, 1983).

Media and reagents

For all flow cytometry measurements, the cells were grown in Luria-Bertani (LB) broth. As a minimal medium for the *mrdAB* measurements, we used M63 medium supplemented with 2 g/l of glucose, 10 mg/l of thiamine, 10 mM of $MgSO_4$, and 1 g/l of casaminoacids. When needed, we used various antibiotics (25 μg/ml chloramphenicol, 100 μg/ml carbenicillin, 50 μg/ml kanamycin, 100 μg/ml spectinomycin). Di-acetyl-phloroglucinol (DAPG), anhydrotetracycline (aTc), and isopropyl β-D-1-thiogalactopyranoside (IPTG) were used, respectively, for induction of P_{PhlF}, P_{Tet}, and P_{Lac} promoters. All oligonucleotides were obtained from Eurofins Genomics.

Preparation of steady-state exponential cultures

Unless stated otherwise, all cultures were grown at 30°C. Strains were first re-streaked from a freezer stock. Independent single colonies were picked for each replicate. Cells were then grown overnight in 96-deep-well plates using a tabletop shaker in 1 ml of medium with 100 ng/ml of aTc and 50 μg/ml of kanamycin (Eppendorf). The day of the measurement, cultures were back-diluted 250 times in fresh medium with aTc and kanamycin, and grown for 1 h 45 min into exponential phase. We then fixed the cells with 4% formaldehyde (30 min on ice) and washed with phosphate-buffered saline (PBS).

Growth rate measurements

To determine the doubling times of *E. coli* with various induction levels of dCas9, we prepared the cells into steady-state exponential growth then diluted the cultures 1/250 in a flat-bottomed 96-microwell plate (Greiner) and recorded optical density along growth using a microplate reader (Tecan). We fitted an exponential function to the data points corresponding to the exponential phase in order to calculate the doubling time.

Flow cytometry

Fluorescence of single cells was recorded using a Miltenyi MACSquant flux cytometer. 10,000 events were recorded per replicate. In all cases, the AV01 strain (with no reporters) carrying a non-targeting pCRRNA plasmid was used to measure the auto-fluorescence background. We calculated the mean fluorescence signal of each population and subtracted the mean auto-fluorescence signal.

To test whether differences in expression were significant, we performed Student's *t*-test on the natural logarithms of the average fluorescence (Beal *et al*, 2016).

High-throughput microscopy (imaging cytometry)

An Amnis ImageStreamX (EMD Millipore) imaging cytometer was used to image the cells in high-throughput in brightfield, GFP, and RFP channels. Images were analyzed using the IDEAS® (EMD Millipore) software suite. For each condition, at least 10,000 events were recorded per replicate. Cells that were out of focus or tilted were identified by calculating the average gradient of a pixel normalized for variations in intensity levels (*Gradient RMS* feature in IDEAS®). Additionally, we used the Feature Finder script of IDEAS® to remove contaminating particles, images with multiple cells and beads. After filtering, at least 2,000 images remained per sample. The fluorescence channels were not used for filtering. A color compensation matrix was calculated to account for spectral overlap of GFP and RFP emission spectra, so cultures of AV02 (GFP only) and AV04 (RFP only) would each have a null signal on the converse channel. As a proxy for the reporter's intracellular concentration, we used the average image intensity inside the area corresponding to each cell. The cell area was determined by using a threshold on the bright field images. Single points located more than three standard deviations away from the population average were discarded as outliers, as they can disrupt the noise computations. The average fluorescence μ of each sample was calculated by taking the mean of the single-cell fluorescence. The noise was defined as σ/μ, with $\sigma = \sqrt{\sigma_{\text{sample}} - \sigma_{\text{blank}}}$ where σ_{sample} is the standard deviation of the intracellular average intensity of the sample, and σ_{blank} is the standard deviation of a sample with no fluorescent reporter (noise from auto-fluorescence).

Fluorescence and phase-contrast microscopy

Fixed cells were transferred to PBS microscopy pads with 1.5% UltraPure Agarose (Invitrogen) and imaged using an inverted microscope (TI-E, Nikon Inc.) equipped with a 100× phase-contrast objective (CFI PlanApo LambdaDM100× 1.4NA, Nikon Inc.), a solid-state light source (Spectra X, Lumencor Inc.), a multiband dichroic (69002bs, Chroma Technology Corp.). mCherry fluorescence was measured using excitation (560/32) and emission (632/60) filters. Images were acquired using a sCMOS camera (Orca Flash 4.0, Hamamatsu) with an effective pixel size of 65 nm.

MATLAB code adapted from the Morphometrics package (Ursell *et al*, 2017) was used to find cell contours from phase-contrast images. Background intensity, uneven illumination, and cell auto-fluorescence were accounted for in the analysis. For the analysis of fluorescence signal, we corrected the raw mCherry values for uneven illumination, background intensity, and cell auto-fluorescence. Intracellular protein concentration was obtained as the mean pixel intensity inside the cell area. Total regression was used to find the major axis of the cell. Cell width was defined as the average distance between the cell contour and this axis, excluding the poles.

Measurements of cell morphology during steady-state exponential growth (Appendix Fig S12) were performed after overnight induction of dCas9, followed by 1/250 dilution of the culture in fresh M63 medium with aTc and while the culture was kept in exponential growth phase at an optical density below 0.1. Samples were taken from the culture, fixed, and imaged after 2 and 4 h.

Northern blot

Total RNA was extracted from cultures in early stationary phase using TRIzol. Electrophoresis on Novex® TBE-Urea Gels (10% polyacrylamide gels containing 7 M urea, Invitrogen) was used to separate RNAs. The gels were blotted onto Nylon membranes (Invitrogen), which were subsequently cross-linked with 1-ethyl-3-(3-dimethylaminopropyl) carbodiimide (EDC, Thermo Scientific) buffer (Pall & Hamilton, 2008). The probes were labeled as follows: 100 pmol of oligonucleotide was heat denatured, labeled, and phosphorylated by mixing 40 μCi of ^{32}P-γ-ATP (PerkinElmer) and T4 PNK (NEB) reagents. A labeled probe specific to the guide RNA R20 (5′ GCATAGCTCTAAAACTCCGTATGAAGGCACCCAGA 3′) was column purified (Macherey-Nagel PCR cleanup kit) and used for overnight hybridization. The intensity of the shortest band, corresponding to the fully processed guide RNA, was quantified using the Fiji software package.

Expanded View for this article is available online.

Acknowledgements

We thank T. K. Lee and K.C. Huang for providing strain TKL130, F. Bendezù for providing plasmid pFB262, H. Cho and T. Bernhardt for providing plasmid pHC942, and D. Mazel for providing plasmid pSW23t. We thank J. Fernández-Rodríguez for providing the P_{PhlF}-*sfgfp-phlF* DNA fragment. We thank E. Brambilla and E. Oldewurtel for support in microscopy, as well as A. Soler and M. Hasan for support regarding flux cytometry and imaging cytometry. We acknowledge the Technology Core of the Center for Translational Science (CRT) at Institut Pasteur for support in conducting this study. This work was supported by the European Research Council (ERC) under the Europe Union's Horizon 2020 research and innovation program [Grant Agreement No. (677823) to DB and No. (679980) to SvT]; the French Government's Investissement d'Avenir program Laboratoire d'Excellence "Integrative Biology of Emerging Infectious Diseases" (ANR-10-LABX-62-IBEID) to SvT, DB, and AV; the Marie de Paris "Emergence(s)" program and the Volkswagen Foundation to SvT; and the Pasteur-Weizmann consortium to DB.

Author contributions

DB, SvT, and AV designed the study. AV constructed the strains and plasmids and performed all measurements and data analysis. SvT developed the mathematical models. LC took part in strain construction, and EO performed the compensation of uneven illumination for the measurement of mCherry-PBP2 by microscopy. AV, DB, and SvT wrote the manuscript.

Conflict of interest

The authors declare that they have no conflict of interest.

References

Abbas A, Morrissey JP, Marquez PC, Sheehan MM, Delany IR, O'Gara F (2002) Characterization of interactions between the transcriptional repressor PhlF and Its binding site at the phlA promoter in *Pseudomonas fluorescens* F113. *J Bacteriol* 184: 3008 – 3016

Baba T, Ara T, Hasegawa M, Takai Y, Okumura Y, Baba M, Datsenko KA, Tomita M, Wanner BL, Mori H (2006) Construction of *Escherichia coli* K-12 in-frame, single-gene knockout mutants: the Keio collection. *Mol Syst Biol* 2: 2006.0008

Beal J, Haddock-Angelli T, Gershater M, de Mora K, Lizarazo M, Hollenhorst J, Rettberg R, iGEM Interlab Study Contributors (2016) Reproducibility of fluorescent expression from engineered biological constructs in *E. coli*. *PLoS One* 11: e0150182

Bendezú FO, Hale CA, Bernhardt TG, de Boer PAJ (2009) RodZ (YfgA) is required for proper assembly of the MreB actin cytoskeleton and cell shape in *E. coli*. *EMBO J* 28: 193 – 204

Bikard D, Jiang W, Samai P, Hochschild A, Zhang F, Marraffini LA (2013) Programmable repression and activation of bacterial gene expression using an engineered CRISPR-Cas system. *Nucleic Acids Res* 41: 7429 – 7437

Bikard D, Euler CW, Jiang W, Nussenzweig PM, Goldberg GW, Duportet X, Fischetti VA, Marraffini LA (2014) Exploiting CRISPR-Cas nucleases to produce sequence-specific antimicrobials. *Nat Biotechnol* 32: 1146 – 1150

Boyle EA, Andreasson JOL, Chircus LM, Sternberg SH, Wu MJ, Guegler CK, Doudna JA, Greenleaf WJ (2017) High-throughput biochemical profiling reveals sequence determinants of dCas9 off-target binding and unbinding. *Proc Natl Acad Sci USA* 114: 5461 – 5466

Breier AM, Weier H-UG, Cozzarelli NR (2005) Independence of replisomes in *Escherichia coli* chromosomal replication. *Proc Natl Acad Sci USA* 102: 3942 – 3947

Brophy JA, Voigt CA (2016) Antisense transcription as a tool to tune gene expression. *Mol Syst Biol* 12: 854

Çağatay T, Turcotte M, Elowitz MB, Garcia-Ojalvo J, Süel GM (2009) Architecture-dependent noise discriminates functionally analogous differentiation circuits. *Cell* 139: 512 – 522

Cho H, Wivagg CN, Kapoor M, Barry Z, Rohs PDA, Suh H, Marto JA, Garner EC, Bernhardt TG (2016) Bacterial cell wall biogenesis is mediated by SEDS and PBP polymerase families functioning semi-autonomously. *Nat Microbiol* 1: 16172

Cui L, Bikard D (2016) Consequences of Cas9 cleavage in the chromosome of *Escherichia coli*. *Nucleic Acids Res* 44: 4243 – 4251

Elowitz MB, Levine AJ, Siggia ED, Swain PS (2002) Stochastic gene expression in a single cell. *Science* 297: 1183 – 1186

Farasat I, Salis HM (2016) A biophysical model of CRISPR/Cas9 activity for rational design of genome editing and gene regulation. *PLoS Comput Biol* 12: e1004724

Gibson DG, Young L, Chuang RY, Venter JC, Hutchison CA III, Smith HO (2009) Enzymatic assembly of DNA molecules up to several hundred kilobases. *Nat Methods* 6: 343 – 345

Hsu PD, Lander ES, Zhang F (2014) Development and applications of CRISPR-Cas9 for genome engineering. *Cell* 157: 1262 – 1278

Jiang Y, Chen B, Duan C, Sun B, Yang J, Yang S (2015) Multigene editing in the *Escherichia coli* genome via the CRISPR-Cas9 system. *Appl Environ Microbiol* 81: 2506 – 2514

Jones DL, Leroy P, Unoson C, Fange D, Ćurić V, Lawson MJ, Elf J (2017) Kinetics of dCas9 target search in *Escherichia coli*. *Science* 357: 1420 – 1424

Kennell D, Riezman H (1977) Transcription and translation initiation frequencies of the *Escherichia coli* lac operon. *J Mol Biol* 114: 1 – 21

Kuscu C, Arslan S, Singh R, Thorpe J, Adli M (2014) Genome-wide analysis reveals characteristics of off-target sites bound by the Cas9 endonuclease. *Nat Biotechnol* 32: 677 – 683

Lee TK, Tropini C, Hsin J, Desmarais SM, Ursell TS, Gong E, Gitai Z, Monds RD, Huang KC (2014) A dynamically assembled cell wall synthesis machinery buffers cell growth. *Proc Natl Acad Sci USA* 111: 4554 – 4559

Li X, Jun Y, Erickstad MJ, Brown SD, Parks A, Court DL, Jun S (2016) tCRISPRi: tunable and reversible, one-step control of gene expression. *Sci Rep* 6: 39076

Meeske AJ, Riley EP, Robins WP, Uehara T, Mekalanos JJ, Kahne D, Walker S, Kruse AC, Bernhardt TG, Rudner DZ (2016) SEDS proteins are a widespread family of bacterial cell wall polymerases. *Nature* 537: 634 – 638

Nielsen AA, Voigt CA (2014) Multi-input CRISPR/Cas genetic circuits that interface host regulatory networks. *Mol Syst Biol* 10: 763

Pall GS, Hamilton AJ (2008) Improved northern blot method for enhanced detection of small RNA. *Nat Protoc* 3: 1077 – 1084

Peters JM, Colavin A, Shi H, Czarny TL, Larson MH, Wong S, Hawkins JS, Lu CHS, Koo B-M, Marta E, Shiver AL, Whitehead EH, Weissman JS, Brown ED, Qi LS, Huang KC, Gross CA (2016) A comprehensive, CRISPR-based functional analysis of essential genes in bacteria. *Cell* 165: 1493 – 1506

Pósfai G, Kolisnychenko V, Bereczki Z, Blattner FR (1999) Markerless gene replacement in *Escherichia coli* stimulated by a double-strand break in the chromosome. *Nucleic Acids Res* 27: 4409 – 4415

Qi LS, Larson MH, Gilbert LA, Doudna JA, Weissman JS, Arkin AP, Lim WA (2013) Repurposing CRISPR as an RNA-guided platform for sequence-specific control of gene expression. *Cell* 152: 1173 – 1183

Sauvage E, Kerff F, Terrak M, Ayala JA, Charlier P (2008) The penicillin-binding proteins: structure and role in peptidoglycan biosynthesis. *FEMS Microbiol Rev* 32: 234 – 258

Shafferman A, Helinski DR (1983) Structural properties of the beta origin of replication of plasmid R6K. *J Biol Chem* 258: 4083 – 4090

So L-H, Ghosh A, Zong C, Sepúlveda LA, Segev R, Golding I (2011) General properties of transcriptional time series in *Escherichia coli*. *Nat Genet* 43: 554 – 560

Sternberg SH, Redding S, Jinek M, Greene EC, Doudna JA (2014) DNA interrogation by the CRISPR RNA-guided endonuclease Cas9. *Nature* 507: 62 – 67

St-Pierre F, Cui L, Priest DG, Endy D, Dodd IB, Shearwin KE (2013) One-step cloning and chromosomal integration of DNA. *ACS Synth Biol* 2: 537 – 541

Subach FV, Patterson GH, Manley S, Gillette JM, Lippincott-Schwartz J, Verkhusha VV (2009) Photoactivatable mCherry for high-resolution two-color fluorescence microscopy. *Nat Methods* 6: 153 – 159

Szczelkun MD, Tikhomirova MS, Sinkunas T, Gasiunas G, Karvelis T, Pschera P, Siksnys V, Seidel R (2014) Direct observation of R-loop formation by single RNA-guided Cas9 and Cascade effector complexes. *Proc Natl Acad Sci USA* 111: 9798 – 9803

Taniguchi Y, Choi PJ, Li G-W, Chen H, Babu M, Hearn J, Emili A, Xie XS (2010) Quantifying *E. coli* proteome and transcriptome with single-molecule sensitivity in single cells. *Science* 329: 533 – 538

Ursell T, Lee TK, Shiomi D, Shi H, Tropini C, Monds RD, Colavin A, Billings G, Bhaya-Grossman I, Broxton M, Huang BE, Niki H, Huang KC (2017) Rapid, precise quantification of bacterial cellular dimensions across a genomic-scale knockout library. *BMC Biol* 15: 17

Waite AJ, Frankel NW, Dufour YS, Johnston JF, Long J, Emonet T (2016) Non-genetic diversity modulates population performance. *Mol Syst Biol* 12: 895

Wiktor J, Lesterlin C, Sherratt DJ, Dekker C (2016) CRISPR-mediated control of the bacterial initiation of replication. *Nucleic Acids Res* 44: 3801 – 3810

Wu X, Scott DA, Kriz AJ, Chiu AC, Hsu PD, Dadon DB, Cheng AW, Trevino AE, Konermann S, Chen S, Jaenisch R, Zhang F, Sharp PA (2014) Genome-wide binding of the CRISPR endonuclease Cas9 in mammalian cells. *Nat Biotechnol* 32: 670 – 676

Appendix to the manuscript:

Tuning dCas9's ability to block transcription enables robust, noiseless knockdown of bacterial genes

Antoine Vigouroux, Enno Oldewurtel, Lun Cui, David Bikard and Sven van Teeffelen

Table of contents

1 A novel method of allelic exchange using CRISPR/Cas9

To make scar-less genome modifications easier, we developed a new method which relies on the integration of a non-replicating plasmid through homologous recombination followed by backbone removal promoted by Cas9 cleavage in the antibiotic resistance gene (Appendix Fig S9). This method was inspired from a similar strategy that makes use of the I-SceI nuclease instead of Cas9 (Posfai *et al.*, 1999).

The chromosomal modifications are carried out using a plasmid typically made by assembling together four PCR fragments: 1) a chloramphenicol-resistant backbone with the R6K conditional origin of replication (such as pSW23t), 2) a homology region of about 1 kbp matching the sequence before the desired site of insertion, 3) a reporter sequence, possibly using a linker for protein fusions, or a stop codon and a ribosome binding site for mRNA fusions, 4) a second homology region of 1 kbp matching the sequence after the site of insertion, i.e. the beginning of the gene of interest.

This plasmid is electroporated in the recipient strain. Cells that have integrated the plasmid by homologous recombination (HR) are selected by plating on chloramphenicol. Either one or the other homology arm will be used for HR. The two insertion orders can be told apart by colony PCR with one primer in the backbone and one primer on the chromosome. We then pick a colony from each insertion order, dilute them in 500 ul of LB and grow them during 1h30, after which cells are centrifuged and recovered in 100 ul of TSS (Transformation and Storage Solution) (Chung, Niemela and Miller, 1989).The cells are then transformed with plasmid pAV10, expressing Cas9 under the control of a DAPG-inducible promoter and a sgRNA targeting the *cat* gene of the suicide vector, followed by plating on LB agar with kanamycin and DAPG at 30°C. Cleavage by Cas9 in the chromosome triggers the resolution of the co-integrate in two possible ways: recombination can either restore the wild-type locus, or lead to the desired seamless modification. Several colonies from each insertion order are re-streaked on LB agar without kanamycin and grown at 42°C to eliminate thermo-sensitive pAV10 and obtain clonal populations. Excising the backbone from both insertion orders greatly increases the chances of finding a good clone, as for each order the recombination might be biased towards a particular outcome. We recommend to re-streak a minimum of 2 colonies for each order. Finally, we screen for edited clones by colony PCR with one primer on each side of the insert.

As a demonstration for this method, we created plasmid pAV25, allowing integration of a PAmCherry-PBP2 fusion in the native locus using a variant of the *PAmCherry* gene that can be targeted by our collection of guide RNAs. Without changing the amino-acid sequence of PAmCherry, the nucleotide sequence of the ORF was silently modified so the *mCherry*-targeted guide RNAs would also be effective on the photo-activatable version. Thus we produce a strain where the concentration of PBP2 and RodA can be controlled like in Figure 6, but whose mCherry can be activated by light for single-molecule tracking.

2 Autorepressor model

In this section we present two simplified models of the PhlF-autorepressor. In both cases, PhlF expression is represented by the straight-forward reaction kinetics

$$\dot{R} = f(R,c)\beta\alpha - \lambda R\,, \tag{2.1}$$

where R is the PhlF concentration (including proteins bound in dimers or other multimers), α is the rate of the protein production in the absence of any feedback or CRISPR knockdown, β is the passage probability due to dCas9, λ is the protein dilution rate, and $f(R,c)$ characterises the feedback strength as a function of protein concentration R and DAPG concentration c. During steady-state conditions PhlF expression is thus determined by the self-consistent equation

$$f(r,c)\beta - r = 0\,. \tag{2.2}$$

Here, $r = R/(\alpha/\lambda)$ is the PhlF concentration normalised with respect to the PhlF concentration in the absence of feedback or CRISPR-knockdown.

2.1 Repression modelled by Hill-function

In the first model (model a), auto-repression through PhlF proteins is represented by a Hill function

$$f(r,c) = 1/\left[1 + (r/k(c))^n\right]\,. \tag{2.3}$$

Here, cooperativity of two or more PhlF proteins in dimers or multimers is subsumed in the Hill exponent n and any DAPG-dependent reduction of repression is modelled by an effective binding constant $k(c)$. Here, we assume that DAPG binding and unbinding to PhlF proteins is much more rapid than the dynamics of PhlF expression and dilution.

Together, Eqs. (2.2, 2.3) lead to a self-consistent equation for r:

$$r\left[1 + (r/k(c))^n\right] - \beta = 0\,. \tag{2.4}$$

In Appendix Figures S11A and S11B this model is fit to the experimental data of GFP expression assuming two different values of $n = 1, 2$. The model with $n = 2$ fits the data well for 0 and 5 uM DAPG, but not for 50 uM. On the contrary, the model with $n = 1$ fits the data well for 50 uM, but not for 0 and 5 uM.

2.2 Repression modelled by dimer formation

Since PhlF is known to dimerise *in vitro* (Abbas *et al.*, 2002) and thought to bind the operator site as dimer we hypothesised that the different Hill coefficients observed could come about because PhlF proteins are predominantly found as monomers at low DAPG concentrations, thus rendering dimer concentration proportional to r^2, while they are mostly found as dimers at high DAPG concentration, thus rendering dimer concentration proportional to r. We thus formulated a simple model (model b) of dimer-based repression

$$f(r,c) = 1/\left[1 + d/K(c)\right] , \tag{2.5}$$

where d is the concentration of all PhlF dimers, normalised with respect to the maximum number of PhlF proteins (α/λ), and $K(c)$ is the DAPG-dependent effective binding constant of dimers, considering that only a sub-fraction of dimers can efficiently bind the operator. During steady-state conditions the concentration of dimers is determined by

$$\dot{d} = k_{\mathrm{on}}(r - 2d)^2 - k_{\mathrm{off}}d = 0 , \tag{2.6}$$

where k_{on} and k_{off} are binding and unbinding constants. Introducing the parameter $a = k_{\mathrm{off}}/k_{\mathrm{on}}$, we can solve Eq. (2.6) for d:

$$d = \frac{1}{8}\left(a + 4r - \sqrt{a^2 + 8ar}\right) . \tag{2.7}$$

For low PhlF concentrations ($r \ll a$), dimer concentration is approximately given by $d \approx r^2/a$, which is equivalent to model a with a Hill coefficient of $n = 2$. For values $r \gg a$, dimer formation is approximately given by $d \approx r/2$, which corresponds to a Hill coefficient of $n = 1$. We thus wondered whether the transition in Hill coefficients observed for different DAPG concentrations could come about by a concomitant change of PhlF concentration alone, i.e., if the dimerisation binding constant a remains independent of DAPG concentration. We thus fit the model Eqs. (2.6, 2.7) to the experimental data, using a single binding constant a for all DAPG concentrations but different values of $K(c)$, which reflect different fractions of dimers being capable of binding the operator site.

Empirically, we found for a value of $a = 0.15$ that the increasing PhlF concentration upon increasing DAPG concentration can partially explain the transition in Hill coefficient (Appendix the S11C), while lower or higher values of a provide better fits for the regimes of low or high DAPG concentrations, respectively, but not for both regimes. However, it appears that the transition is more sudden in the experimental data than in the fit. The discrepancy between model and experimental data can be alleviated by rendering the dimerisation constant a DAPG-dependent, with a higher value of $a \approx 2$ for low DAPG concentrations (0 uM and 5 uM) and a low value of $a \approx 0.01$ for high DAPG concentrations (50 uM) (Appendix Fig S11D).

The molecular mechanism underlying the DAPG-dependent binding constant is not understood yet. One potential scenario (possibly among others) is the following: DAPG could effectively stabilise the fraction of dimers that are capable to repress the promoter. A stabilisation of operator-binding dimers through DAPG would be surprising, as DAPG is thought to inhibit operator binding. However, it is conceivable that 'UB'-dimers, where one of the two protomers is DAPG-bound (B) while the other is unbound (U), still bind to the operator, possibly with reduced affinity or increased unbinding rate. These dimers could be stabilised at high DAPG concentrations due to direct or indirect effects of DAPG binding on dimer formation. One possible explanations is the following: If dimers of both protomers DAPG-bound ('BB'-dimers) were energetically unfavourable to form, the pool of DAPG-bound monomers would be high at high DAPG levels. This pool would then effectively facilitate dimerisation of 'UB'-dimers. We note that this hypothesis remains highly speculative and other mechanisms might be responsible for the transition in Hill coefficients observed.

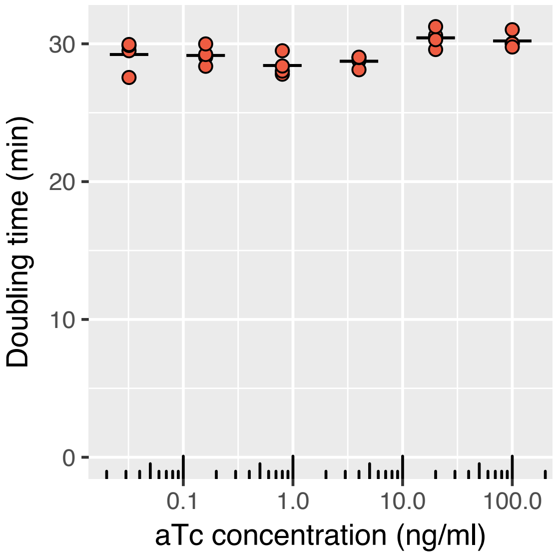

Appendix Figure S1 – Expression of dCas9 from P_{tet} with up to 100 ng/ml of aTc does not produce growth defects. Here the doubling time is measured on the strain AV03 with a non-targeting CRISPR array, in LB at 30°C.

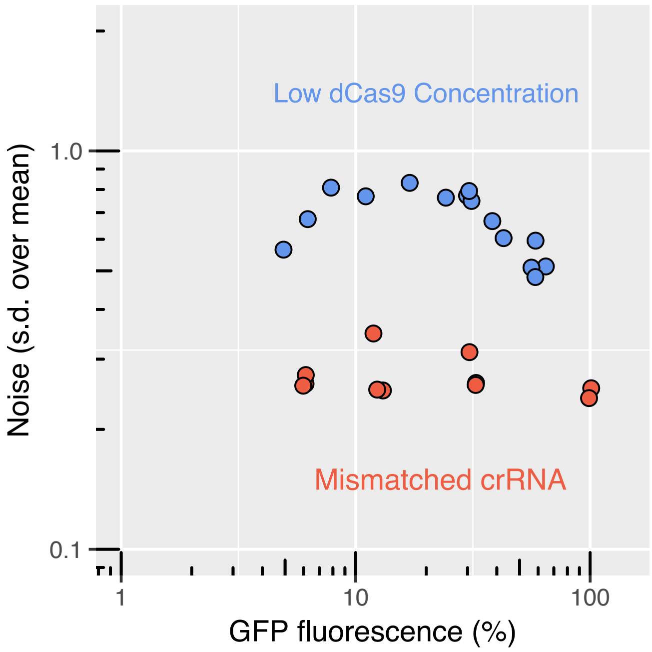

Appendix Figure S2 – GFP is expressed from P_{127} promoter and repressed using dCas9. For a given expression level, the noise is ~3 times lower if expression is tuned by guide RNA complementarity than if expression is tuned by changing dCas9 induction level. The points corresponding to maximal repression (spacer without mismatch at the highest induction level of dCas9) are omitted, as their exact noise could not be quantified accurately using our setup (high-throughput microscopy). Fluorescence values are population means, as a percentage of the fluorescence of P_{127}-*sfGFP* in a strain with no repression. S.d.: standard deviation.

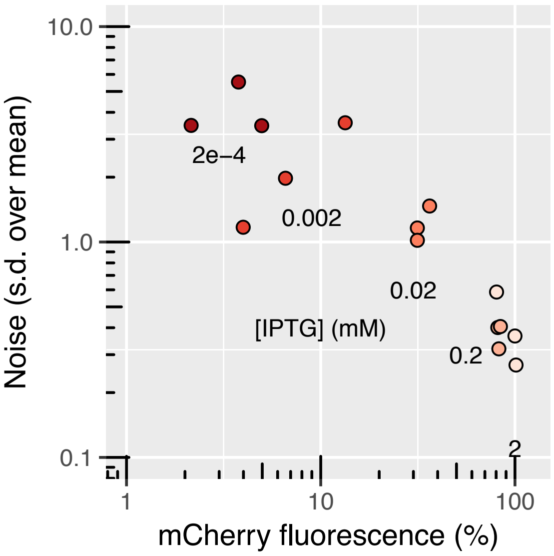

Appendix Figure S3 – Noise in mCherry concentration as a function of expression level from a P_{Lac}-inducible promoter.

mCherry is expressed from P_{Lac} in a Δ*lacY* background and its concentration is changed using different concentrations of IPTG. Fluorescence values are population averages, as a percentage of the fluorescence of P_{Lac}-*mCherry* in a strain with no repression and 2 mM of IPTG. This measurement was done by fluorescence microscopy using agarose pads, as expression from P_{Lac} is much lower than expression from P_{127}.

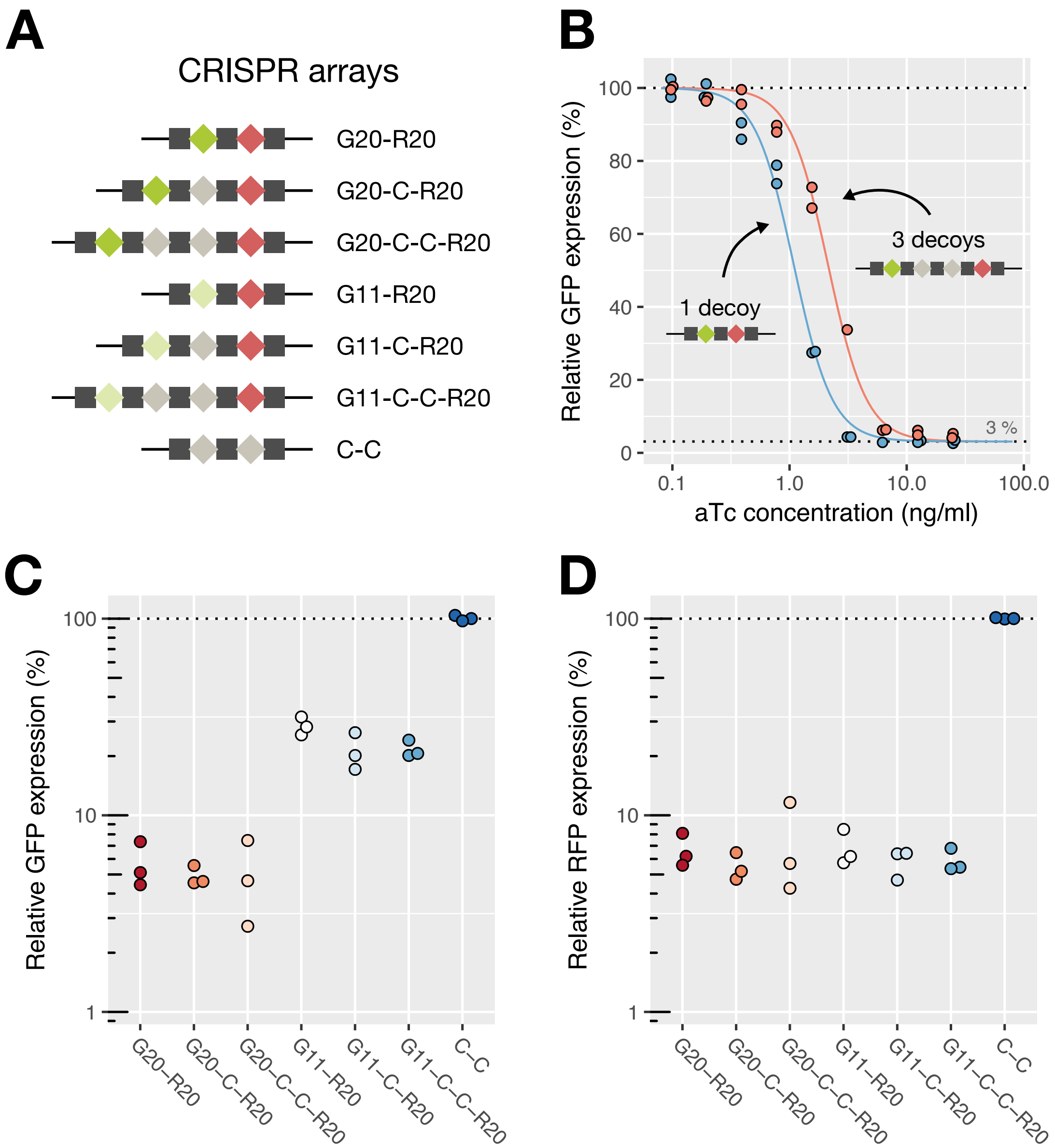

Appendix Figure S4 – At least 4 mismatched guide RNAs can be expressed at the same time while saturating the target.

A: Schematics of the CRISPR arrays used in this experiment. G20 targets the *sfGFP* ORF with full complementarity (20bp), G11 targets it with 11bp of complementarity (9 mismatches), R20 targets the *mCherry* ORF with full complementarity. The C guides have no target in *E. coli*'s chromosome.

B: Flow cytometry measurement of GFP fluorescence when dCas9 is induced with different amounts of aTc. For a low enough aTc concentration, we leave the saturation regime and enter the concentration-dependent regime. Adding other spacers (decoys) to the CRISPR array decreases the concentration of active complex. Therefore, the concentration of aTc required to reach the saturation regime is higher with 3 decoys than with 1 decoy.

C: With 100 ng/ml of aTc, at least 4 different spacers can be added to the array without leaving the saturation regime. This is true even with a mismatched crRNA (G11).

D: The last guide RNA of the CRISPR array (R20) with four spacers is still expressed highly enough to reach saturation of the target and repress mCherry strongly.

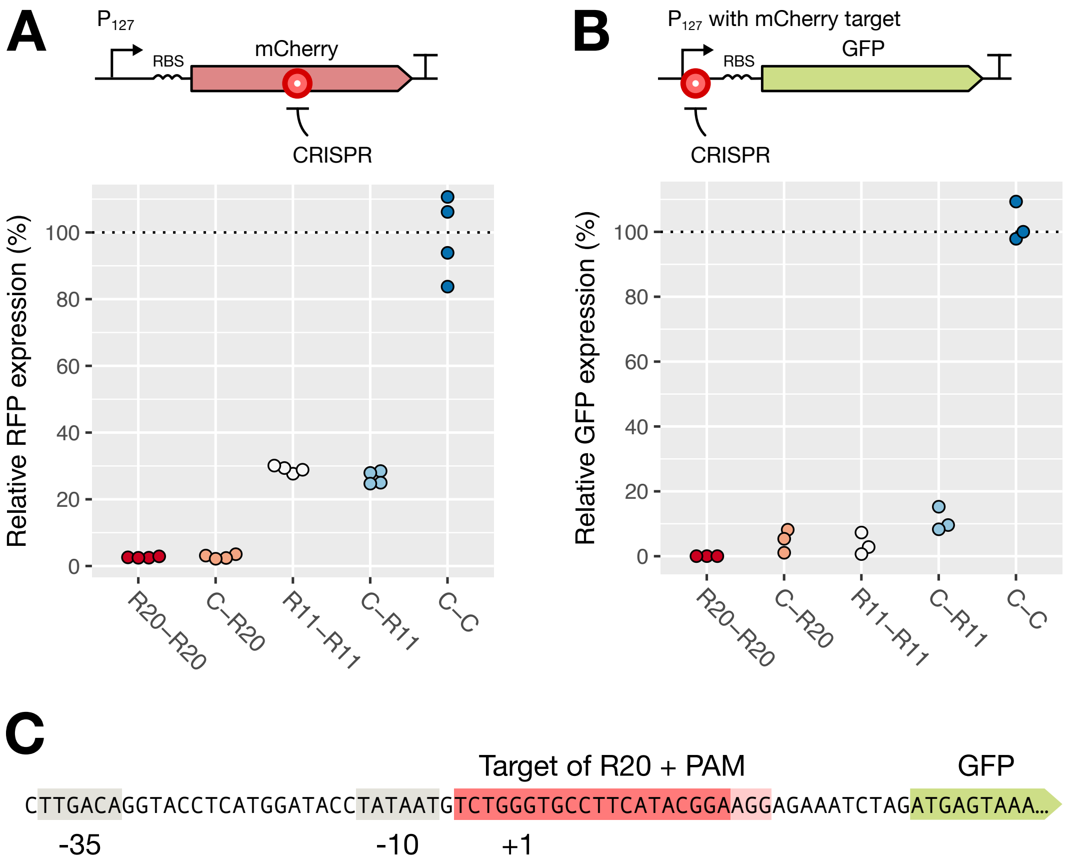

Appendix Figure S5 – Targeting the same sequence inside the ORF or inside the promoter region shows qualitatively different behavior.
Comparison between two strains with the same target either inside the *mCherry* ORF (A; reproduced from Figure 2B) or inside the promoter sequence to *gfp* (B). In the new strain (sequence indicated in C), the P_{127} promoter was modified to include the target sequence (red) otherwise found inside the mCherry ORF. This way, the R20-R20, C-R20, R11-R11 and C-R11 CRISPR arrays used previously (panel a) can bind to the promoter region in this strain, but not to the *gfp* ORF. As dCas9 now blocks transcription initiation rather than elongation, it cannot be kicked out by the RNAP. Accordingly, repression is stronger for low levels of complementarity but dependent on dCas9-complex concentration.

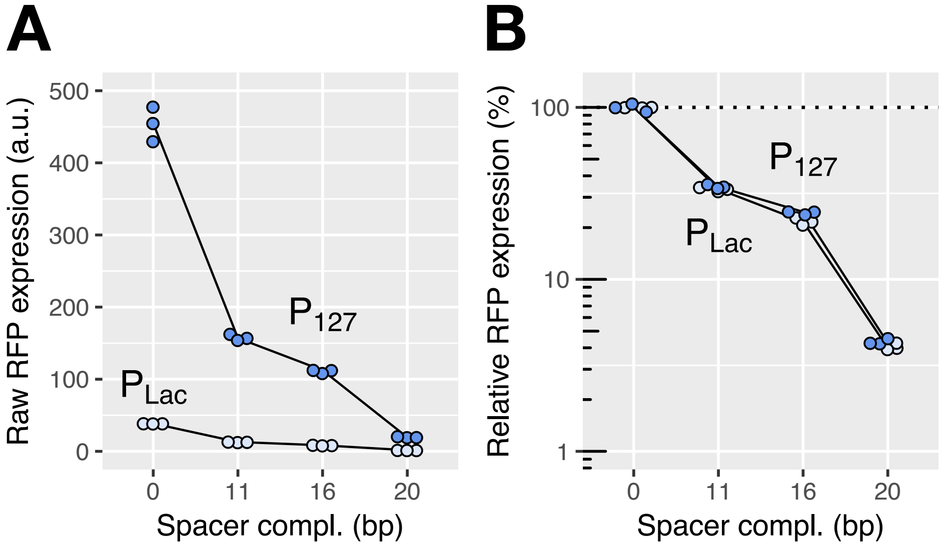

Appendix Figure S6 – Repression by dCas9 is independent of promoter strength over a wide range of transcription rates.

A: Raw RFP expression measured by flow cytometry for P_{127} (also used in Fig 3) and P_{Lac} in the presence of 1 mM of IPTG and repressed using 4 different guide RNAs in saturating conditions. In these conditions, the native expression from P_{Lac} is about 12 times weaker than P_{127}.

B: Relative GFP expression normalized with respect to the non-targeting spacer. The relative expression levels are similar for both promoters. Together with Fig 3, this shows that the independence on transcription rate applies also at a low expression level.

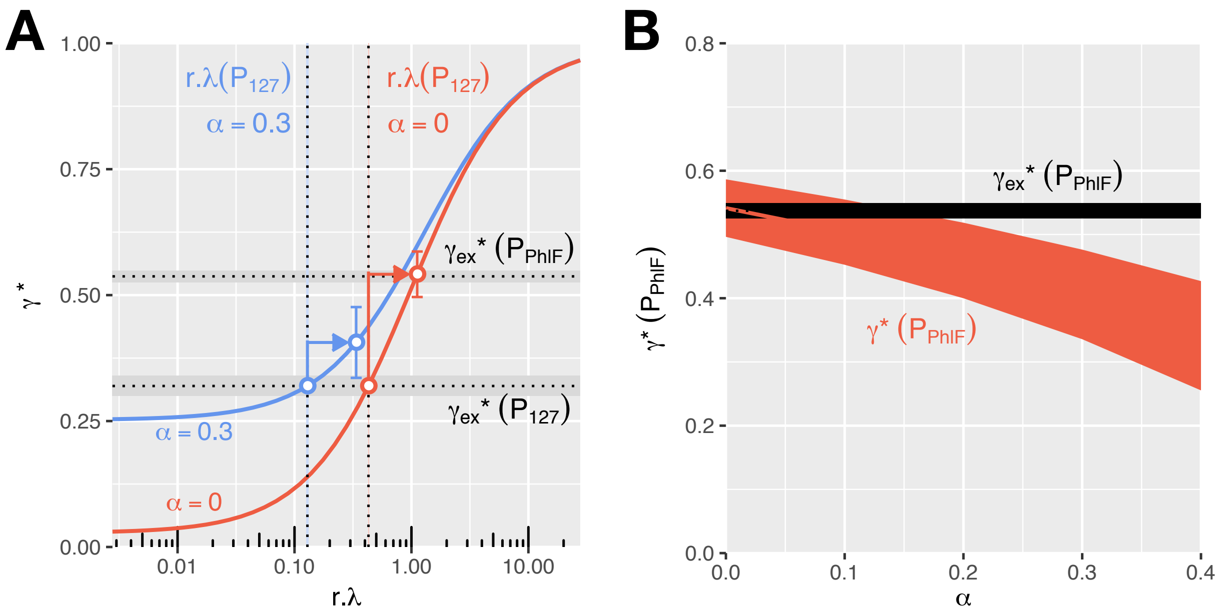

Appendix Figure S7 – Predictions from the kick-out model of CRISPR knockdown: The effect of promoter strength and dCas9 transcription-independent unbinding on gene repression at low and intermediate dCas9 concentrations in the case of full complementarity.

A: The relative GFP expression γ^* is plotted as a function of the kick-out rate $r\lambda$, where λ is the ratio of the rate of transcription-induced dCas9 displacements (given by the product of transcription initiation rate γ_0 and the ejection frequency δ) over the rate of dCas9 rebinding ([dCas9]k_{on}), and r = 1-P(stop) is the probability of dCas9 leaving the target upon collision with the RNAP (see Appendix text for details). The red and blue curves are generated based on the kick-out model and correspond to zero (red) and finite (blue) rates of transcription-independent dCas9 unbinding. Here, α is the transcription-independent unbinding rate normalized by the rebinding rate. The relative expression of the P_{127} promoter $\gamma_{ex}^*(P_{127})$ (the lower of the two horizontal lines, see also Figure 3C) is used as a reference to infer the unknown kick-out rate $r\lambda$ (P_{127}) as the intersection point of the two lines (indicated as the lower blue and red open circles). Predicted values for GFP expression from the P_{PhlF}-promoter are indicated by open circles with error bars corresponding to 95% confidence intervals. The experimental GFP expression from the P_{PhlF}-promoter $\gamma_{ex}^*(P_{PhlF})$ (the higher of the two horizontal lines) is predicted correctly by the model if the transcription-independent unbinding rate is assumed to be $\alpha = 0$, but not if $\alpha = 0.3$.

B: Predicted and measured relative expression of P_{PhlF}-*gfp* as a function of α. Only the values of α lower than 0.14 show agreement between prediction and measurement, indicating that transcription-independent unbinding of dCas9 occurs at a rate much smaller than the rate of dCas9 rebinding and smaller than the rate of dCas9 being kicked out by the RNAP.

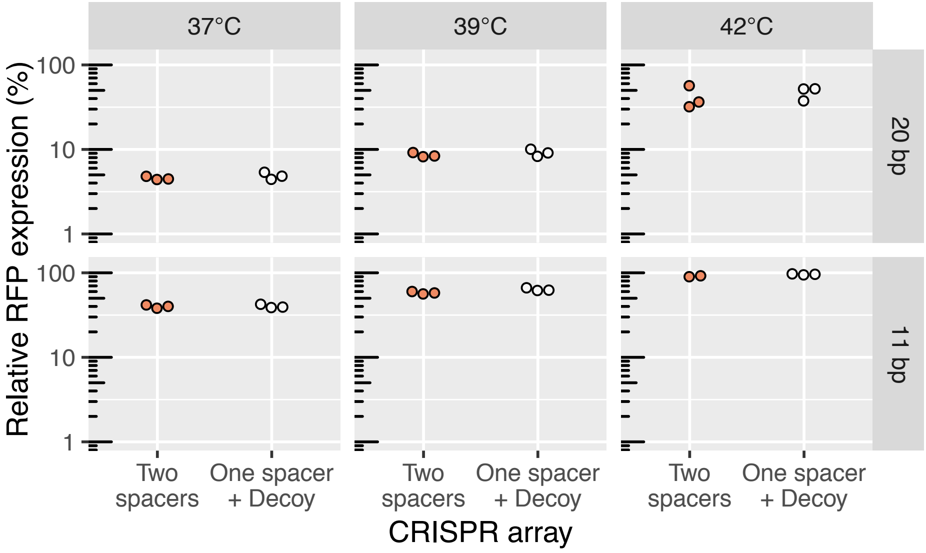

Appendix Figure S8 – Relative RFP expression for different temperatures with either 20 or 11 bp of complementarity, in the presence or absence of a decoy guide RNA.

RFP expression levels are first normalized with respect to a constitutively expressed GFP reporter. RFP/GFP ratios are then normalized with respect to the non-targeting CRISPR array. Doubling of dCas9 concentration does not affect the repression strength at any temperature even with partial complementarity.

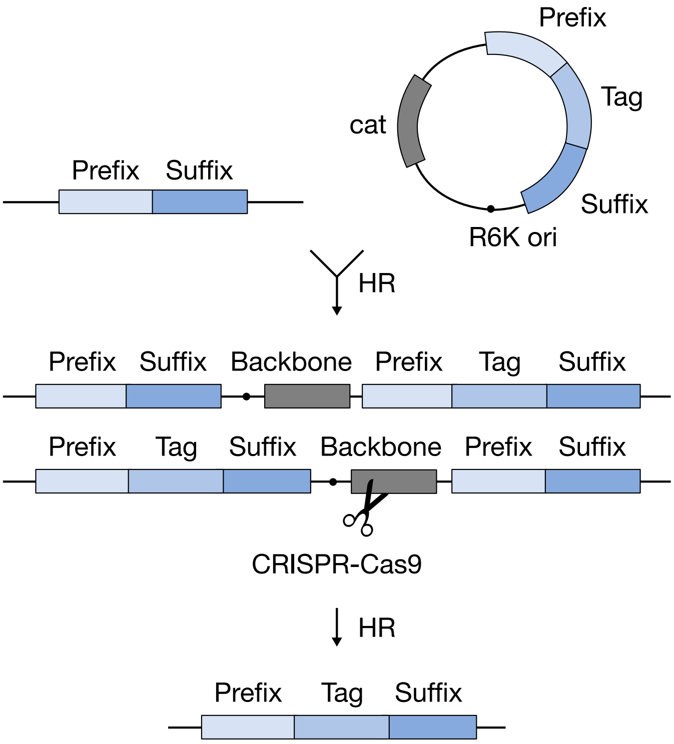

Appendix Figure S9 – Overview of the allelic exchange procedure to integrate a reporter in front of a target gene, using CRISPR/Cas9-triggered excision.
HR: Homologous recombination. Ori: Origin of replication. *cat*: chloramphenicol acetyl-transferase. This procedure is described in details in Appendix text, section 1.

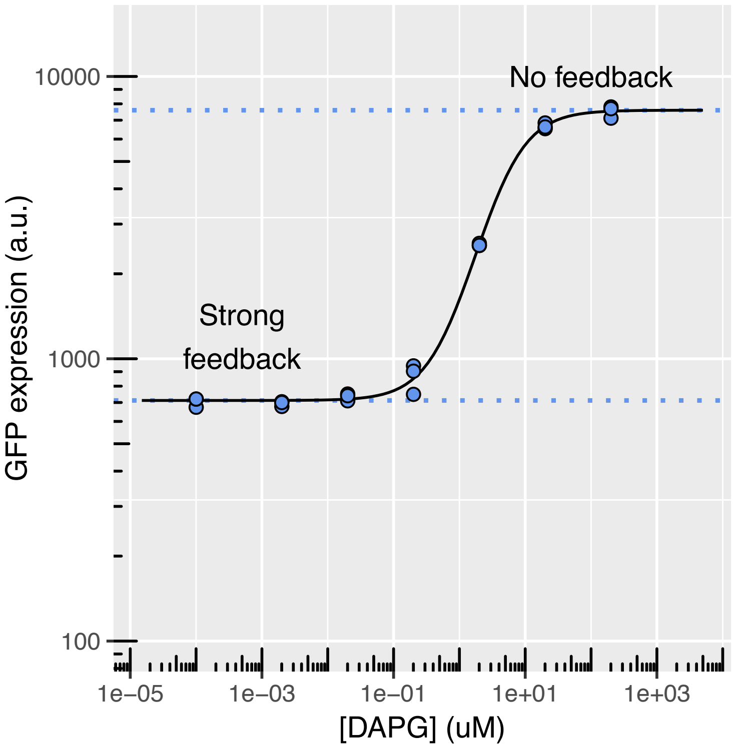

Appendix Figure S10 – Steady-state GFP expression levels with GFP expressed from the feedback loop as a function of the concentration of DAPG, modulating the strength of the feedback. Each point represents one biological replicate. The black line is a fit of the data using a Hill function. The Hill coefficient was calculated to be 1.25±0.07.

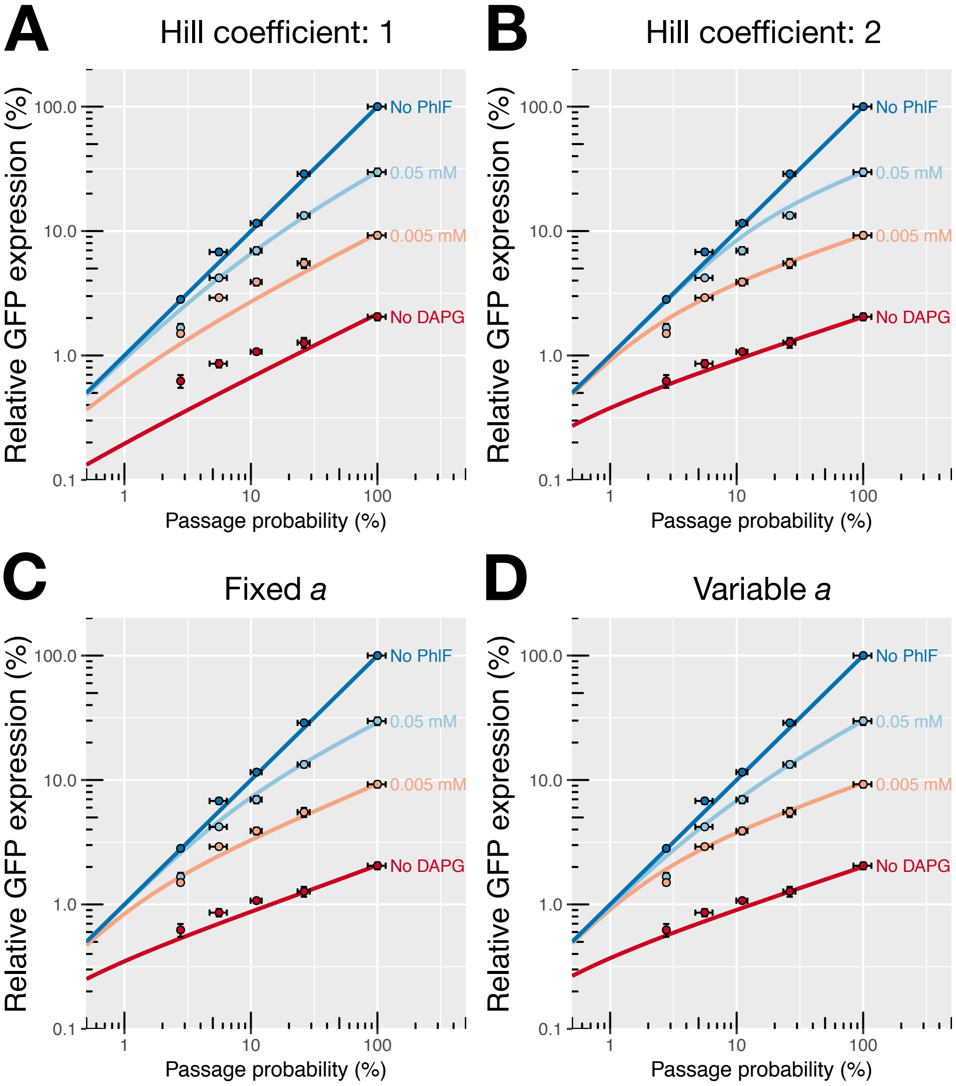

Appendix Figure S11 - Different mathematical models for the PhlF auto-repressor. Points represent relative GFP expression levels as shown in Figure 4. Solid lines represent the values predicted by the different models. a: The transcriptional response of P_{PhlF} is modeled as a Hill function with Hill coefficient *n* = 1 (A) or *n* = 2 (B) (model a). b: Biophysical model accounting for PhlF binding to DAPG and its dimerization with either fixed (C) or variable (D) dimerization binding constant *a* (model B). See Appendix text for more details.

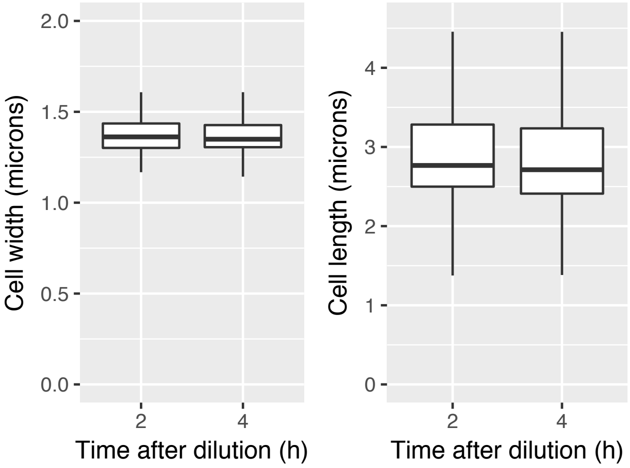

Appendix Figure S12 – **Upon partial depletion of PBP2 and RodA by CRISPR knockdown, the cells maintain their altered morphology stably over time.** The *mCherry-mrdA* fusion gene was repressed using a guide RNA with 18 bp of complementarity (lowering *mrdAB* to 20% of the native level) then the culture was maintained in exponential phase. At two time points (after 2h and after 4h) a sample of the culture was fixed and imaged by microscopy.

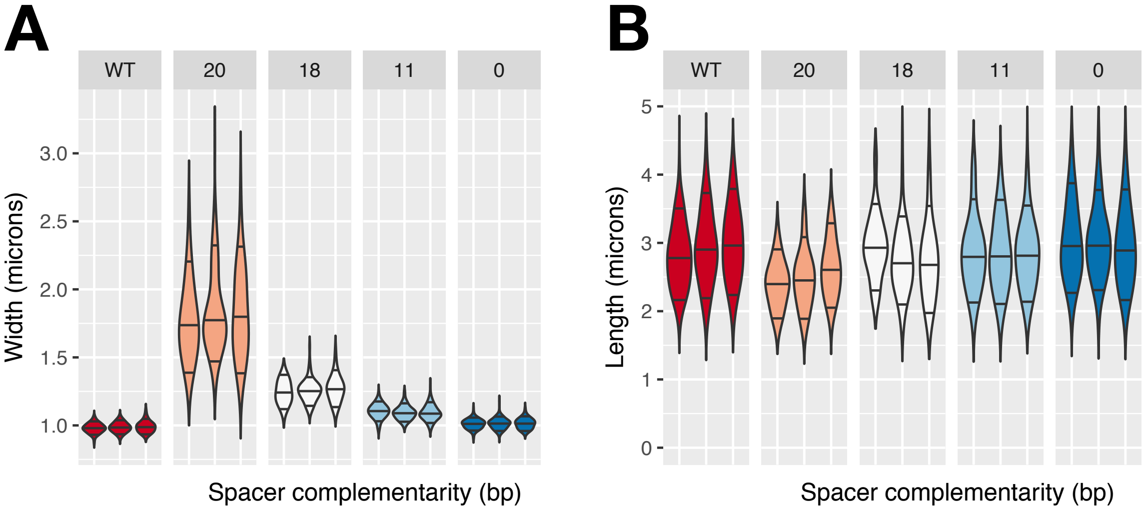

Appendix Figure S13. Distribution of cell diameter (A) and cell length (B) for different levels of *mrdAB* repression. Horizontal lines indicate, from top to bottom, the 90th percentile, the median and the 10th percentile. WT: wild-type.

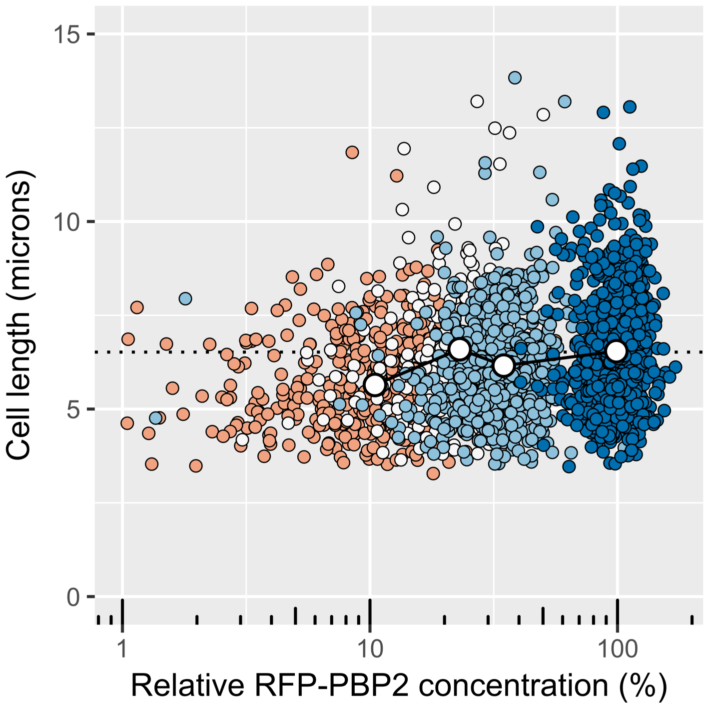

Appendix Figure S14. Cell length as a function of the cellular concentration of RFP-PBP2. Each color represents the population obtained with one CRISPR plasmid. The connected white dots represent the population averages (mean of 3 biological replicates). The dotted line represents the mean cell length for wild-type *E. coli* (mean of 3 replicates).

Table S1: New strains used in this study and the successive plasmid transformations used to make them from their parental strain. All strains derive from MG1655 *E. coli*, except AV08 that derives from TKL130 (Lee *et al*, 2014).

Name	Genotype	Construction
AV01	186::P_{tet}-*dcas9*	pAV03 → pE-FLP
AV02	186::P_{tet}-*dcas9*, HK022::P_{127}-*sfgfp*	pAV03 → pE-FLP → pAV01 → pE-FLP
AV03	186::P_{tet}-*dcas9*, HK022::P_{127}-*sfgfp*, λ::P_{127}-*mcherry*	pAV03 → pE-FLP → pAV01 → pE-FLP → pAV02 → pE-FLP
AV04	186::P_{tet}-*dcas9*, λ::P_{127}-*mcherry*	pAV03 → pE-FLP → pAV02 → pE-FLP
AV06	186::P_{tet}-*dcas9*, HK022::P_{127}-*sfgfp*, λ::P_{lac}-*mcherry*	pAV03 → pE-FLP → pAV01 → pE-FLP → pAV04 → pE-FLP
AV08	*mrdA*::*mcherry-mrdA*, λ::P_{tet}-*dcas9*	pCas → pAV07 → pLC97 → pE-FLP
AV14	186::P_{tet}-*dcas9,* λ::P_{phlf}-*sfgfp-phlF*	pAV03 → pE-FLP → pAV14 → pE-FLP
AV27	186::P_{tet}-*dcas9, mrdA*::*pamcherry-mrdA* (repressible variant)	pAV03 → pE-FLP → pAV25 → pAV10
AV75	186::P_{tet}-*dcas9*, HK022::P_{127}-*sfgfp*, λ ::P_{lac}-*mcherry*, Δ *lacY*	pAV03 → pE-FLP → pAV01 → pE-FLP → pAV04 → pE-FLP → P1 from JW0334 (Baba *et al*, 2006) → pE-FLP
AV76	186::P_{tet}-*dcas9*, HK022::P_{127}(R20 target)-*sfgfp*	pAV03 → pE-FLP → pAV81 → pE-FLP

Table S2: Plasmids constructed or used for this study and the corresponding assembly fragments (either PCR products or digested plasmids). In brackets: Addgene IDs.

Name	Description	PCR primers or restriction enzyme		Template	Reference
pAV01	P_{127}-*sfgfp* integration in HK022 site	V1	V2	pDB127	(Bikard *et al*, 2013)
		V3	V4	pHC942	(Cho *et al*, 2016)
		EcoR1	Pst1	pIT5-KH (45983)	(St-Pierre *et al*, 2013)
pAV02	P_{127}-*mcherry* integration in λ site	V1	V40	pDB127	(Bikard *et al*, 2013)
		V38	V39	pFB262	(Bendezú *et al*, 2009)
		EcoR1	Pst1	pIT5-KL (45984)	(St-Pierre *et al*, 2013)
pAV03	P_{tet}-*dcas9* integration in 186 site	LC100	LC283	pDB275	(Depardieu *et al*, 2016)
		LC284	LC285	pdCas9-bacteria	(Qi *et al*, 2013)
		EcoR1	Pst1	pIT5-KO (45985)	(St-Pierre *et al*, 2013)
pLC97*	P_{tet}-*dcas9* integration in λ site	LC100	LC283	pDB275	(Depardieu *et al*, 2016)
		LC284	LC285	pdCas9-bacteria	(Qi *et al*, 2013)
		EcoR1	Pst1	pIT5-KL (45984)	(St-Pierre *et al*, 2013)
pAV04	P_{lac}-*mcherry* integration in λ site	V75	V76	MG1655	
		V77	V78	pFB262	(Bendezú *et al*, 2009)
		EcoR1	Pst1	pIT5-KL (45984)	(St-Pierre *et al*, 2013)
pAV06	Replaces *pamcherry-mrdA* with *mcherry-mrdA*	V67	V68	TKL130	(Lee *et al*, 2014)
		V69	V70	pFB262	(Bendezú *et al*, 2009)
		V71	V72	TKL130	(Lee *et al*, 2014)
		V73	V93	pTargetF	(Jiang *et al*, 2015)
		V66	V92	pTargetF	(Jiang *et al*, 2015)
pAV10	P_{PhlF}-*Cas9*-gRNA			pJF1	Gift from Eligo Bioscience
pAV14	P_{Phlf}-*sfgfp-phlF* integration in λ site	V140	V143	P_{PhlF}-*sfgfp-phlF* (synthesis)	(Stanton *et al*, 2014)
		EcoR1	Pst1	pIT5-KL (45984)	(St-Pierre *et al*, 2013)
pAV25	Integrates *pamcherry-mrdA* in the native locus	V170	V171	pSW23t	(Demarre *et al*, 2005)
		V180	V188	TKL130	(Lee *et al*, 2014)
		V185	V189	TKL130	(Lee *et al*, 2014)
pAV81	P_{127}(R20 target)-*sfgfp* integration in HK022 site.	V1	V351	AV02	(This study)
		V4	V350	AV02	(This study)
		EcoR1	Pst1	pIT5-KH (45983)	(St-Pierre *et al*, 2013)
pCas	Cas9, λ-red				(Jiang *et al*, 2015)
pE-FLP	Flippase				(St-Pierre *et al*, 2013)
pCRRNA-cos	CRISPR array cloning vector				(Cui & Bikard, 2016)

*pLC97 is available on Addgene at https://www.addgene.org/depositor-collections/bikard-crispr-repression/

Table S3. PCR primers used in this study.

Name	Sequence (5’ to 3’)
V1	CGCCATAAACTGCCAGGAATTGGGGATCGGCCTATGAACTGTCGACTCGAGG
V2	TTCTTCACCTTTACTCATCTAGATTTCTCCTCTTTAAAGG
V3	GGAGAAATCTAGATGAGTAAAGGTGAAGAACTGTTCACC
V4	TTAGGCGCCATGCATCTCGAGGCATGCCTGCATTATTTGTAGAGTTCATCCATGCCGTGC
V38	GGAGAAATCTAGATGGTTTCCAAGGGCGAGGAGGAT
V39	TTAGGCGCCATGCATCTCGAGGCATGCCTGCATTATTTGTACAGCTCATCCATGCC
V40	ATCCTCCTCGCCCTTGGAAACCATCTAGATTTCTCCTCTTTAAAGGAATTCC
V66	GCTGGACGTACCCGTACAGATGACAAAAAAAGCACCGACTC
V67	GAGTCGGTGCTTTTTTTGTCATCTGTACGGGTACGTCCAGC
V69	AGTAGAAAACGCAGCGGATGGTTTCCAAGGGCGAGG
V71	GCATGGATGAGCTGTACAAAACCGGTTCCGGAGGGCATG
V73	GCGGCAACGCATGATATCGGGAATTCTCTAGAGTCGACCTGCAGAAG
V75	CTGCCAGGAATTGGGGATCGGAATTCGCAACGCAATTAATGTGAG
V76	TCCTCGCCCTTGGAAACCATAGCTGTTTCCTGTGTGAAATTG
V77	ATTTCACACAGGAAACAGCTATGGTTTCCAAGGGCGAGG
V78	CATCTCGAGGCATGCCTGCATTATTTGTACAGCTCATCCATGCC
V101	TGGTGGCTGGCACAAGTGCCCTCCAGCTTTTGTTCCCTTTAGTGAGGGTTAATTGC
V102	TGACAACAAGCATTACCGCGGCTGCAGGAATTCGATATCAAGCT
V103	TGATATCGAATTCCTGCAGCCGCGGTAATGCTTGTTGTCAG
V108	AAAGGGAACAAAAGCTGGAGGGCACTTGTGCCAGCCAC
V109	AAGGTAAAAGATCTCTCCGGCTCCAGCTTTTGTTCCCTTTAGT
V110	CCATCCGTGGCGGCTCTTCGGGCTGCAGGAATTCGATATCAAGC
V111	GATATCGAATTCCTGCAGCCCGAAGAGCCGCCACGGAT
V116	AAAGGGAACAAAAGCTGGAGCCGGAGAGATCTTTTACCTTATCGC
V140	CGCCATAAACTGCCAGGAATTGGGGATCGGATCTGATTCGTTACCAATTGACATGATACG
V143	TTAGGCGCCATGCATCTCGAGGCATGCCTGCATAGTTAACGCTGTGTACCCGGACA
V170	CTCCAGCTTTTGTTCCCTTTAG
V171	GGCTGCAGGAATTCGATATCAAG
V180	TCGATAAGCTTGATATCGAATTCCTGCAGCCgccgtgccatcggggtc
V185	AACCCTCACTAAAGGGAACAAAAGCTGGAGcagtcacgataacgtttttccg
V188	CAGTTTGGCGGTCTGGGTGCCTTCATACGGACGGCCCTCGCCTTCACCTTCG
V189	GCCGTCCGTATGAAGGCACCCAGACCGCCAAACTGAAGGTGACGAAGGGTGGTC
V350	TCTGGGTGCCTTCATACGGAAGGAGAAATCTAGATGAGTAAAGGTG
V351	TCCTTCCGTATGAAGGCACCCAGACATTATAGGTATCCATGAGGTACCTG
LC100	GCAGGACGCCCGCCATAAACTGCCAGGAATTGGGGATCGGTTAAGACCCACTTTCACATTTAAG
LC283	TCCATTTTTGCCTCCTAACTAGGTCATTTGATATGCCTCC
LC284	CCTAGTTAGGAGGCAAAAATGGATAAGAAATACTCAATAGGC
LC285	AGTTTAGGTTAGGCGCCATGCATCTCGAGGCATGCCTGCAATGCCTGGAGATCCTTACTC

Table S4. Oligonucleotides pairs ligated in vectors to construct the CRISPR arrays.

Name	Primer 1	Primer 2
First position in pCRRNA-cos		
G20	aaacCCTTCACCTTCACCACGAACAGAGAATTTGgttttagagctatg	aacagcatagctctaaaacCAAATTCTCTGTTCGTGGTGAAGGTGAAGG
G14	aaacCCTTCACCTTGTGGTGGAACAGAGAATTTGgttttagagctatg	aacagcatagctctaaaacCAAATTCTCTGTTCCACCACAAGGTGAAGG
G11	aaacCCTTCACCTTGTGGTGCTTCAGAGAATTTGgttttagagctatg	aacagcatagctctaaaacCAAATTCTCTGAAGCACCACAAGGTGAAGG
G10	aaacCCTTCACCTTGTGGTGCTTGAGAGAATTTGgttttagagctatg	aacagcatagctctaaaacCAAATTCTCTCAAGCACCACAAGGTGAAGG
C	aaacATCGCACATCCTGGTCGCGACATTAAGAGTgttttagagctatg	aacagcatagctctaaaacACTCTTAATGTCGCGACCAGGATGTGCGAT
R20	aaacAGTTTGGCGGTCTGGGTGCCTTCATACGGAgttttagagctatg	aacagcatagctctaaaacTCCGTATGAAGGCACCCAGACCGCCAAACT
R11	aaacAGTTTGGCGGAGACCCACGCTTCATACGGAgttttagagctatg	aacagcatagctctaaaacTCCGTATGAAGCGTGGGTCTCCGCCAAACT
Second position in pCRRNA-cos		
R20	ctgttttgaatggtcccaaaacAGTTTGGCGGTCTGGGTGCCTTCATACGGAg	aaaacTCCGTATGAAGGCACCCAGACCGCCAAACTgttttgggaccattcaa
R18	ctgttttgaatggtcccaaaacAGTTTGGCGGAGTGGGTGCCTTCATACGGAg	aaaacTCCGTATGAAGGCACCCACTCCGCCAAACTgttttgggaccattcaa
R11	ctgttttgaatggtcccaaaacAGTTTGGCGGAGACCCACGCTTCATACGGAg	aaaacTCCGTATGAAGCGTGGGTCTCCGCCAAACTgttttgggaccattcaa
C	ctgttttgaatggtcccaaaacATCGCACATCCTGGTCGCGACATTAAGAGTg	aaaacACTCTTAATGTCGCGACCAGGATGTGCGATgttttgggaccattcaa
Arrays of 3 guide RNAs in pCRRNA-cos		
G20*	aaacCCTTCACCTTCACCACGAACAGAGAATTTGgttttagagctatg	aacagcatagctctaaaacCAAATTCTCTGTTCGTGGTGAAGGTGAAGG
C	ctgttttgaatggtcccaaaacATCGCACATCCTGGTCGCGACATTAAGAGTgttttaga	atagctctaaaacACTCTTAATGTCGCGACCAGGATGTGCGATgttttgggaccattcaa
R20	gctatgctgttttgaatggtcccaaaacAGTTTGGCGGTCTGGGTGCCTTCATACGGAg	aaaacTCCGTATGAAGGCACCCAGACCGCCAAACTgttttgggaccattcaaaacagc
Arrays of 4 guide RNAs in pCRRNA-cos		
G20*	aaacCCTTCACCTTCACCACGAACAGAGAATTTGgttttagagctatg	aacagcatagctctaaaacCAAATTCTCTGTTCGTGGTGAAGGTGAAGG
C (a)	ctgttttgaatggtcccaaaacATCGCACATCCTGGTCGCGACATTAAGAGTgttttagagcta	cagcatagctctaaaacACTCTTAATGTCGCGACCAGGATGTGCGATgttttgggaccattcaa
C (b)	tgctgttttgaatggtcccaaaacATCGCACATCCTGGTCGCGACATTAAGAGTgttttaga	atagctctaaaacACTCTTAATGTCGCGACCAGGATGTGCGATgttttgggaccattcaaaa
R20	gctatgctgttttgaatggtcccaaaacAGTTTGGCGGTCTGGGTGCCTTCATACGGAg	aaaacTCCGTATGAAGGCACCCAGACCGCCAAACTgttttgggaccattcaaaacagc
Single-guide RNA for pAV10		
cat	agcaTATTCTCAATAAACCCTTTA	aaacTAAAGGGTTTATTGAGAATA

*May be replaced with G11 to make pCRRNA-G11-C-C-R20.

Appendix references

Abbas A, Morrissey JP, Marquez PC, Sheehan MM, Delany IR & O'Gara F (2002) Characterization of Interactions between the Transcriptional Repressor PhlF and Its Binding Site at the phlA Promoter in Pseudomonas fluorescens F113. *J. Bacteriol.* **184:** 3008–3016

Baba T, Ara T, Hasegawa M, Takai Y, Okumura Y, Baba M, Datsenko KA, Tomita M, Wanner BL & Mori H (2006) Construction of Escherichia coli K-12 in-frame, single-gene knockout mutants: the Keio collection. *Mol. Syst. Biol.* **2:** 2006.0008

Bendezú FO, Hale CA, Bernhardt TG & de Boer PAJ (2009) RodZ (YfgA) is required for proper assembly of the MreB actin cytoskeleton and cell shape in E. coli. *EMBO J.* **28:** 193–204

Bikard D, Jiang W, Samai P, Hochschild A, Zhang F & Marraffini LA (2013) Programmable repression and activation of bacterial gene expression using an engineered CRISPR-Cas system. *Nucleic Acids Res.* **41:** 7429–7437

Cho H, Wivagg CN, Kapoor M, Barry Z, Rohs PDA, Suh H, Marto JA, Garner EC & Bernhardt TG (2016) Bacterial cell wall biogenesis is mediated by SEDS and PBP polymerase families functioning semi-autonomously. *Nat. Microbiol.* **1:** 16172

Chung CT, Niemela SL & Miller RH (1989) One-step preparation of competent Escherichia coli: transformation and storage of bacterial cells in the same solution. *Proc. Natl. Acad. Sci.* **86:** 2172–2175

Cui L & Bikard D (2016) Consequences of Cas9 cleavage in the chromosome of Escherichia coli. *Nucleic Acids Res.* **44:** 4243–4251

Demarre G, Guérout A-M, Matsumoto-Mashimo C, Rowe-Magnus DA, Marlière P & Mazel D (2005) A new family of mobilizable suicide plasmids based on broad host range R388 plasmid (IncW) and RP4 plasmid (IncPalpha) conjugative machineries and their cognate Escherichia coli host strains. *Res. Microbiol.* **156:** 245–255

Depardieu F, Didier J-P, Bernheim A, Sherlock A, Molina H, Duclos B & Bikard D (2016) A Eukaryotic-like Serine/Threonine Kinase Protects Staphylococci against Phages. *Cell Host Microbe* **20:** 471–481

Jiang Y, Chen B, Duan C, Sun B, Yang J & Yang S (2015) Multigene Editing in the Escherichia coli Genome via the CRISPR-Cas9 System. *Appl. Environ. Microbiol.* **81:** 2506–2514

Lee TK, Tropini C, Hsin J, Desmarais SM, Ursell TS, Gong E, Gitai Z, Monds RD & Huang KC (2014) A dynamically assembled cell wall synthesis machinery buffers cell growth. *Proc. Natl. Acad. Sci. U. S. A.* **111:** 4554–4559

Pósfai G, Kolisnychenko V, Bereczki Z & Blattner FR (1999) Markerless gene replacement in Escherichia coli stimulated by a double-strand break in the chromosome. *Nucleic Acids Res.* **27:** 4409–4415

Qi LS, Larson MH, Gilbert LA, Doudna JA, Weissman JS, Arkin AP & Lim WA (2013) Repurposing CRISPR as an RNA-guided platform for sequence-specific control of gene expression. *Cell* **152:** 1173–1183

Stanton BC, Nielsen AAK, Tamsir A, Clancy K, Peterson T & Voigt CA (2014) Genomic mining of prokaryotic repressors for orthogonal logic gates. *Nat. Chem. Biol.* **10:** 99–105

St-Pierre F, Cui L, Priest DG, Endy D, Dodd IB & Shearwin KE (2013) One-Step Cloning and Chromosomal Integration of DNA. *ACS Synth. Biol.* **2:** 537–541

Chapter 4

The ppppredictor

4.1 Introduction

CRISPR knock-down is a promising tool for fine-tuning the level of one gene of interest, as well as for library works. Unfortunately, it is difficult to know in advance the Passage Probability of Polymerase (PPP, see chapter 3) of a given CRISPR guide. For the quantitative control of gene expression, this remains a major obstacle, as it requires quantification of the target protein, plus a series of trial and error to obtain a satisfying collection of CRISPR guides, as we did in chapter 3. Using fusions to fluorescent reporters is an useful workaround, but it is time-consuming and can create large differences in the baseline expression level of the cassette, even for chromosomal fusions in the native locus (see chapter 5). If one could predict the PPP from the sequence, it would propel CRISPR knock-down beyond being a simple alternative to inducible promoters, and open the way for new approaches in systems biology, especially on the high-throughput side.

For example, it would remove one layer of uncertainty in CRISPR screens: in works like Rousset et al. [87], what is measured is the fitness of a cell with one gene repressed to some undefined low level. By making sure all the guides have roughly the same repression strength, one could have a direct, quantitative measurement of gene essentiality. It would also be possible to perform a competition screen between several expression levels of multiple genes of interest, granting direct access to the relationship between concentration and fitness, similar to what Keren et al. [55] obtained in yeast.

There are some obstacles to the prediction of PPP from the guide's sequence. It cannot be infered easily from the number of mismatches, as the effect of one mismatch can be very different depending on the target (figure 4.1).

PPP also seems to depend on the specific dynamics of the RNAP-dCas9 collision, which is influenced by the structural properties of each complex. As evidence for this, the exact same CRISPR guide sequence can lead to very different PPPs depending on the type of scaffold (crRNA or sgRNA, figure 4.1). In some way, this also means that PPP could be tuned by changing not only the targeting sequence, but also by changing the scaffold or adding some prefixes or suffixes to the guide. This also means that one should be careful when using CRISPR knock-down with a modified version of dCas9, such as a fluorescent protein fusion, as the PPP might not be exactly the same as what

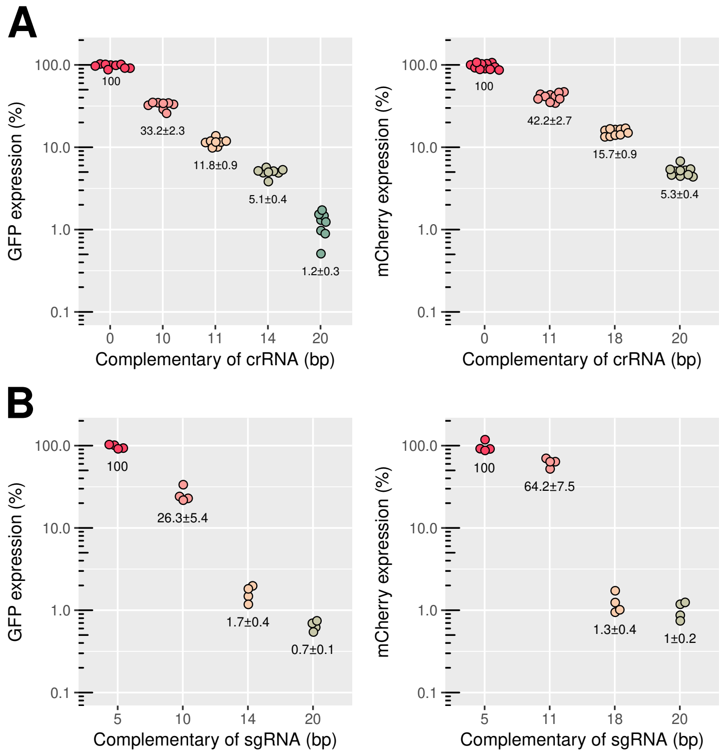

Figure 4.1: Comparison of the same set of guide RNAs, targeting either GFP or mCherry, in the form of crRNA or sgRNA. crRNA are embedded in a CRISPR array in the pcrRNA vector. sgRNA are expressed from the pAV20 vector. 5 bp of complementarity is not enough to produce repression.

we measure on normal dCas9.

To date, no large-scale dataset of sequences and associated PPPs *in vivo* has been reported. There are datasets of binding kinetics *in vitro* [92, 100], which can help finding the parameters that determine dCas9's affinity to its target, and those paramaters may be important for PPP as well, but the outcome of dCas9/RNAP collisions cannot be determined from the kinetic parameters alone. Also, a lot of data exists about cleavage by Cas9, but the cutting probability is very different from the binding affinity, due to the peculiar kinetics of Cas9 cleavage [95, 96].

4.2 Cloning a large number of guide-target pairs

To determine the PPP of CRISPR guides with mismatches between the guide and the target, we must be able to control both sequences simultaneously. Using on-chip oligo synthesis, we synthesize a library of oligos constisting in an assembly prefix, a single-guide RNA sequence, a restriction cloning site, a target sequence with a NGG PAM, and an assembly suffix. This is inserted in a plasmid, which carries a promoter for the sgRNA in 5' upstream of the library insertion site, and a mCherry coding sequence in 3' downstream. After the first cloning step, a round of sequencing will be done to check the integrity of the library, and in particular identify which targets have a defect in the associated CRISPR guides. Thanks to an unique molecular identifier (UMI) in the sequence, individual clones that have an assembly problem can be discarded during the analysis, and the other clones carrying the same sequence can still be exploited. Subsequently, a fragment containing the GFP coding sequence is inserted between the guide and the target, using the restriction site present in the middle of the library's oligos (figure 4.2). This allows to decouple the guide expression cassette from the target, as they would otherwise be very close from each other and likely to interact.

Figure 4.2: **Schematic of the expression cassette used to measure PPPs in high-throughput.** The guide sequence is cloned next to the scaffold, then a cassette with a constitutive promoter and GFP is inserted between the guide and the target. Image courtesy of Alicia Calvo-Villamañan.

This collection of plasmids is then transformed in a strain able to express dCas9. All the strains and plasmids supporting this library were designed and constructed by Alicia Calvo-Villamañan.

4.3 Principle of the measurement

Using this strain library, there are two ways to measure the PPP for each pair of guide and target:

By mRNA sequencing

The most direct measurement of PPP is by extracting the mRNA of the pooled cells, performing reverse-transcription of the mRNA that contains the CRISPR target, then sequencing the cDNA. The number of times each target appears in the sequencing run reflects the number of times the RNAP could displace the dCas9 complex for this particular guide/target pair. This is compared to the number of reads obtained with a control target that does not have a PAM.

By fluorescence-activated cell sorting (FACS)

The intensity of mCherry reflects the amount of transcripts which extend beyond the target site. The cells are sorted into bins of fluorescence intensity, then we sequence the target sites of all cells present in each bin. As each sequence will be found in different proportions in each bin, it will be possible to fit a lognormal distribution and obtain the average mCherry intensity of each sequence. The intensity of GFP can also be used, as it reflects the total amount of transcripts that get initiated. The GFP/mCherry ratio would then be proportional to the PPP. An advantage of using FACS is that we can estimate the noise on gene expression following the repression.

As, in both case, the PPP is determined by sequencing only the target, and not the full guide/target pair, it is essential that the sequence of the guide can be identified using only the target sequence. This can be done by using a limited number of guides, and putting mismatches in the target, rather than in the guide. Therefore, as long as two guides never share the same seed sequence (which is never mismatched in this library), it is possible to know both the sequence of the guide, and the number, nature and position of the mismatches just from the sequence of the target. Thus, there is no need for any barcode.

4.4 General structure of the library

The library consists in 256 different guides of diverse DNA sequence, designed to capture as much information as possible based on the proposed mechanism of dCas9 binding to DNA. For each of these guides, the library will contain a pool of 130 target sequences with different degrees of complementarity with the guide. The length of the complementary region ranges from 20 bp (perfect match) to 8 bp. Below that, we expect that the repression will be very weak. As the number of reads is higher for higher PPP, the weak guide-target pairs will be over-represented in the sequencing results. However such targets are unlikely to produce a large repression, making them less useful for biotechnological applications. Moreover, the more mismatches there are, the higher dCas9's concentration must be to reach saturating conditions. With only 8 matching bases, we might be out of the saturation regime and the results will be harder to interpret. Thus, there is no point in having sequences with less than 8 matching nucleotides in the library. To increase the diversity of the guides that are present in the library, we include an additional 256 guides, that will only have perfectly-matched targets, and no mismatched targets, due to constraints on the library's size.

To account for the potential effects of the guide on cell growth (due to off-targets, bad seed effect or any other unexpected reason), there will also be one "non-target" with a mutated PAM. In the absence of PAM, dCas9 will not bind and there will be no repression, but the guide will still exert its off-target effects. In any case, it is important to make sure none of the guides has a predictable repressive effect on an essential gene, as this would lead to their depletion from the library regardless of their effect on passage probability. Finally, as restriction enzymes are used for cloning the library, the number of restriction sites for corresponding enzymes in the guides or target sequences should be reduced as much as possible. In this particular library, the context around the target is kept constant. Another unrelated library currently in construction in the lab will address this issue.

4.5 Designing the guide RNA pool

For readability, the examples will involve 6 bp mini-gRNA instead of the "real" 20 bp ones.

Maximizing the sequence diversity

Most likely, the bases that make up a gRNA sequence are interacting with each other, and do not affect the PPP in an independent, additive way. For instance, if we know the passage probabilities associated with these 3 guides: `AAAAAG`; `AAAAAT`; `AAAACG` we will not have enough information to predict the PPP of `AAAACT`, because the effect of changing the last G to a T might not always be the same depending on the context (here, A or C in penultimate position).

We make here the assumption that bases that are far away from each other are less likely to interact significantly, and that only the local context should matter for predicting the effect of a given sequence in a given position. For example, if we know the PPP from the following guides: AAAAAG; AAAAAT; CAAAAG, we assume that we have all the required information to compute the PPP of CAAAAT.

In other words, bases separated by more than 4 bases should have independent effects on the passage probability. If we know the separate effect of each 4-gram at each possible position, it should be possible to predict the PPP of virtually any guide. Once the data generated we will attempt to extract the effect of each 4-gram in each position using statistical and machine learning methods.

To this end, we want to design a diverse library that will contain every possible 4-gram (there are $4^4 = 256$) at each position along the guide (there are 17 possible positions for a given 4-gram within a 20 bp guide). Ideally, each 4-gram/position should be present multiple times within different contexts, so we can better distinguish its specific effect (figure 4.3).

Due to constraints from on-chip oligo synthesis, the library should be as small as possible. To generate such a library, we first generate a long sequence that contains all the possible 4-grams once (and only once). Let's call this sequence the "universe". The universe will be, at the minimum, 256 bp long.

Generating the universe sequence is not trivial. One can think of it as a directed graph with 64 vertices (corresponding to all 3-letter words), each connected with 4 other vertices (the 2 last bases of the word + the 4 possible candidates for the next base). Each 4-letter word thus corresponds to one line connecting 2 vertices. The goal is to find a path that goes through each line only once (figure 4.4). As the graph is fully connected and each vertex has an even number of inputs and outputs, such a minimal path has to exist. The nodes AAA, CCC, TTT and GGG are connected to themselves, so that n-grams such as AAAA are also part of the universe.

A naive approach is to start with an arbitrary word (e.g AAAA), then pick the next base so that the newly formed word is never already in the sequence. At some point, there will be no unvisited exit out of a node. In that case, the algorithm picks a line that is not visited yet, and extends from there until coming back to the starting node. This produces another cycle. The two cycles can be fused by swapping two connectors they have in common.

Here is an example of "universe" sequence, generated with the algorithm above, that contains every possible 4-gram only once:
AAAATGATCACAGCCAATTCGCCGGTCGGAGTTTATTACAAACACGCAAGCTCGAAA
GTCAGTGACTGAATCTCTGGATGTGTAGTATCGTCCAGACGGCGGGGACATCCCCGT
TAATAAGATTTTCATAGCATTGTCTTTGGCCTGTTGAGGAAGGGCAGGCTTCTAGGT
ACCATGGTGCGTGGGTTCCGATACTTGCACTAACCGCGCTATATGCTGCCCTACGAC
CCACCTCCTTAGAGCGAGAACTCAACGTAAA

Then, a 20 bp window is slid along this sequence to get a set of 256 20 nucleotides-long words. For the last 20 positions, the universe is extended by taking again the first nucleotides, as if it were a cycle. These 20 nucleotides sequences will be the CRISPR guides that we use in the library. They indeed contain every possible 4-gram, in every possible position along the guide.

From an information theory perspective, if we use only this set of 256 guides, we

```
['ACTGgcttcattaggggccct',
 'ACTGtcacaattgacctgaac',
 'ACTGaactattgtgacaatac',
 'ACTGaagatcgagggtattaa',
 'gCTGTtgaaggtttacccatg',
 'aCTGTcacaattgacctgaac',
 'gCTGTcaccgctaggtatcag',
 'tCTGTttatggcgaaaaccat',
 'cgTGTGagcctcgcgcacgct',
 'caTGTGgggcgaaatcaagga',
 'atTGTGacaatacgatgagat',
 'ttTGTGgattggggagttacg',
 'taaGTGGaaaatcaagatctc',
 'catGTGGggcgaaatcaagga',
 'aacGTGGttaattcggagctt',
 'tttGTGGattggggagttacg',
 'gaacTGGCttcattaggggcc',
 'atgcTGGCtcgtaactcatcg',
 'acccTGGCattttagccggtg',
 'tttaTGGCgaaaaccattccg',
 'gtagaGGCAatagcatcgttc',
 'accgcGGCAaccccgaggtcg',
 'accctGGCAttttagccggtg',
 'taacgGGCAtagcgtgatgta',
 'tatcctGCAGaactggcttca',
 'agcccaGCAGggttcgactac',
 'agaaaaGCAGactgaactatt',
 'gtcgttGCAGgccacgccgta',
 'acacaacCAGCgaccttaacg',
 'ggtagccCAGCagggttcgac',
 'tctcgtcCAGCgaagtctacc',
 'ttcacccCAGCacatgacgat',
 'gaggcaatAGCAtcgttctat',
 'ggtagcccAGCAgggttcgac',
 'tgtagaaaAGCAgactgaact',
 'ttcaccccAGCAcatgacgat',
 'ttgtatcctGCAGaactggct',
 'ggtagcccaGCAGggttcgac',
 'tgtagaaaaGCAGactgaact',
 'agtgtcgttGCAGgccacgcc',
 'caaacacaacCAGCgacctta',
 'gttggtagccCAGCagggttc',
 'cactctcgtcCAGCgaagtct',
 'cttttcacccCAGCacatgac',
 'gtagaggcaatAGCAtcgttc',
 'gttggtagcccAGCAgggttc',
 'acatgtagaaaAGCAgactga',
 'cttttcaccccAGCAcatgac',
 'tgtgagcctcgcGCACgctgt',
 'aacattcagtacGCACtgtca',
 'gggccaagggtcGCACtctcg',
 'cttttcaccccaGCACatgac',
 'attccccgggtgcCACCgtac',
 'gtaactcatcggaCACCgcgg',
 'tagccggtgctgtCACCgcta',
 'ccgtagagcttttCACCccag',
 'aaacacaaccagcgACCTtaa',
 'cactgtcacaattgACCTgaa',
 'aggtatcaggctcaACCTcct',
 'acagtaatcttcggACCTccc',
 'tcgatgatattgtatCCTGca',
 'cactgtcacaattgaCCTGaa',
 'tccagcgaagtctacCCTGgc',
 'actcatcaaataaagCCTGgt',
 'gtgagcctcgcgcacgCTGTt',
 'aaacattcagtacgcaCTGTc',
 'ggcattttagccggtgCTGTc',
 'aaagcctggtccaagtCTGTt']
```

Figure 4.3: **The library contains every 4-gram, in every position, four times.** Example for the CRISPR guide ACTGTGGCAGCAGCACCTGT. This guide itself is not in the library, however the 64 guides above are present in the library, and each of them shares 4 nucleotides with it (in upper case for emphasis). We speculate that knowing the PPP of these 64 guides will allow to make a decent prediction of the PPP of ACTGTGGCAGCAGCACCTGT, using a deep neural network.

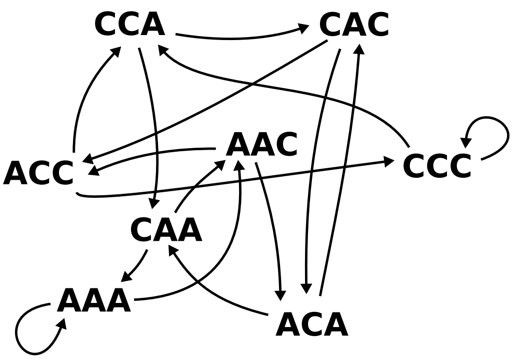

Figure 4.4: **Simplified version of the graph used to generate the "universe".** Here, only two nucleotides are used, so the full graph is small, but the real graph with 4 nucleotides has 64 vertices.

are seriously undersampling: Even under the assumption that there are no interactions between bases separated by more than 4 nucleotide, it is likely that a given 4-gram will have a different effect depending on its position within the guide. Thus, to get the PPP of any perfectly matched guide, there are $256 * 17 = 4352$ degrees of freedom to be measured. In our experiment, each guide gives only one PPP value (in the best case). To have a number of observable matching the number of degrees of freedom, we would need to repeat the process of generating the universe 17 times to get 4352 independent guides. This would make the library too large, so we generated 1024 different guides only (using 4 different universe sequences). This might be sufficient as the effects of each 4-gram in each position are not completely independent: for instance, having the same motif shifted by 1 nucleotide may still produce a similar effect, and very similar 4-grams should also have correlated effects. To account for these potentially complex interactions, we plan to use a deep neural network for the analysis.

Avoid gRNAs with a known toxic effect on the cells

None of the guides in the library should bind to an essential gene with more than 10 bp of complementarity on the PAM-proximal side. Using data from François Rousset's CRISPR screen [87], we make the list of all potential targets in the essential genes of *E. coli*. Then, we only keep the last 10 bp on the 3' side, to make a list of sequences that we never want to find inside a guide from the library. The "universe" sequences are then modified, using a simple cutting and re-assembling algorithm, to eliminate these sequences when they appear.

4.6 Designing the target pool

Using four different "universe" sequences, we obtained 1024 diverse guides with no off-targets in essential genes. For half (512) of these guides, we will design a set of 130 mismatched targets with various complementarities.

According to structural studies, the R-loop extends from the PAM-proximal side to the PAM-distal side [74, 75, 76]. Depending on the number and position of mismatches, the R-loop may not be fully extended at equilibrium, and will rather be extended only up to a certain position along the guide. Thus, a naive model would say that the PPP is determined by the affinity of the part of the guide that is effectively annealed to the DNA at the moment of the collision. This affinity can be determined by multiple things, including the GC-content, the nature of mismatches and the presence of position-specific motifs that could fit more or less well with dCas9's molecular structure.

Among the many ways we could introduce mismatches between the target and the guide, only a few are relevant for biotechnological applications. If the mismatches are spread out along the sequence, the R-loop may be able to overcome them and we expect the PPP of such guides to be quite unpredictable. When mismatches are clustered, on the contrary, it is very unlikely that the R-loop will extend through them. Rather, the R-loop should, in most cases, extend until it reaches the mismatch cluster. If we assume this, it follows that the sequence that comes after a mismatch cluster will never really be interrogated, and therefore should not have a tremendously important effect. For most applications, it is thus preferable to work with guides that comprise a matching region (of variable length, depending on the desired PPP), followed by a mismatch cluster that extends until the end of the guide.

In our library, we vary the 3' complementarity from 8 to 20 bases. It is still possible that the few bases directly following the first mismatch have an effect on PPP, especially if they are matching the target, so we will also investigate their effect. Thus, with N the number of matching bases:

- Base N+1 is mismatched, to each of the 3 other nucleotides (3 combinations)
- Base N+2 is either opposite or matched (2 combinations)
- Base N+3 is either opposite or matched (2 combinations)
- Bases N+4 to 20 are all opposite mismatches (1 combination)

By « opposite » mismatches, we mean that Gs are swapped with Cs, and Ts are swapped with As. By using different ways to select the mismatches, we hope to have more degrees of freedom for guide design rather than just the number of mismatches.

4.7 Planned analysis

Unfortunately, our first attempt at synthesizing this library did not succeed, as the quality of on-chip synthesis was quite poor and the vast majority of the sequences contained errors, rpreventing any exploitation. Another attempt using a more compact design will be done in the future.

In the meantime, the analysis can already be planned. Rather than making assumptions about the additivity, or multiplicativity, of the effects of different motifs, we plan to use a deep neural network such as what was already used in Cui et al. [79]. In addition, a convolutional neural network could be used to identify motifs that influence the PPP regardless of their position within the guide. Using the raw data and the predictions from the model, we can gain mechanistic information about the mechanism of R-loop extension and the outcome of collisions:

- Which features (e.g., GC content) of a motif determine the R-loop transition rates?

- Does the sequence that follow the first mismatch matter for the PPP? Does it depend on the nature of the mismatch?
- Does the transition rate change depending of the position of a motif along the guide?
- Is the degree of R-loop extension at equilibrium a good predictor of PPP?
- Can cleavage efficiency be predicted better using the R-loop transition rates?

On a longer term, it is in principle possible to use this library *in vitro*, for example in a cell extract, similar to what is used in Marshall et al. [93]. This would allow to eliminate all effects of the CRISPR guides on cell growth, and get a cleaner and more direct measurement of the passage probabilities.

Chapter 5

Class A PBPs maintain cell wall homeostasis at an intermediate scale in diderm bacteria

5.1 Introduction

The cylindrical shape of *E. coli* is determined by the peptidoglycan cell wall, a rigid molecule that surrounds the bacterium [53, 145]. This two-dimensional polymer is made of parallel glycan strands organized circumferentially around the cell [36], and peptide cross-links that connect adjactent glycan strands together. Cell wall polymerisation involves two kinds of enzymatic reactions: transglycosylase (TGase) to extend the glycan strands, and transpeptidase (TPase) to create crosslinks between them. These activities are present in two different sets of machineries: the Rod complex and class A PBPs (aPBPs). The Rod complex comprises a variety of proteins (including the essential PBP2 and RodA) that accompany the cytoskeletton MreB in its rotation around the cell [146, 147]. On the other hand, class A PBPs (including the redundantly essential PBP1A and PBP1B) are not known to follow cytoskeletton motion [147]. PBP1A and PBP1B are bifunctional: each of them carry both the TPase and TGase activities. Importantly, PBP1A and 1B need to be activated through the peptidoglycan layer by two outer-membrane lipoprotein cofactors called LpoA and LpoB [53, 148]. Until recently, only aPBPs were known to possess transglycosylase activity and thus were thought to be the main actors of cell wall insertion [149], though it is now known that SEDS proteins (RodA, FtsW) can also perform this activity [150].

While there is evidence for physical interaction and cooperativity between the Rod complex and aPBPs [151, 152, 153], each complex remains partially active upon inhibition of the other one. First, in the absence of aPBP activity, the cytoskeletton protein MreB does not stop its circumferential motion [147], which itself depends on peptidoglycan polymerisation [49]. Second, when Rod complex activity is abolished by the MreB-depolymerizing drug A22, PBP1B remains partially active [147]. Peptidoglycan insertion is then reduced by two thirds.

Combined with the fact that both groups are necessary for cell growth, this suggests that, in spite of catalysing the same chemical reactions, these two categories of peptidoglycan polymerases serve different purposes *in vivo*. Recent work in the monoderm (gram-positive) *B. subtillis* showed that the Rod complex and aPBPs have opposing actions on cell diameter [133], but it is not known whether this holds true for *E. coli*.

On the basis of their subcellular localization and interactions, PBP1A is presumed to be involved primarily in cell wall elongation [154] and PBP1B in cell division [152], although each of them is able to complement for the other when it is deleted. The two paralogs also exhibit different pH sensitivities, suggesting that the presence of two enzymes allows the bacteria to grow over a wider range of pH [**?**]. Yet, the precise function of PBP1A and PBP1B is currently unknown.

The absence of PBP1B causes a few changes in cellular phenotype: First, strains lacking PBP1B have been shown to have greater mechanical plasticity [155]. They are also more sensitive to certain chemicals including D-methionine [156], mecillinam [157] and A22 [158]. Second, the total peptidoglycan insertion rate is lower in the absence of PBP1B [159].

To better understand these properties, we systematically change the levels of PBP1A and PBP1B to well-defined amounts using CRISPR/dCas9 with mismatched guide RNAs. This repression strategy preserves the original noise on gene expression [82], thus facilitating precise gene repression. In addition, it allows observation of cells with a reduced level of the gene(s) of interest during steady-state growth. Compared to depletion experiments, where the concentration of enzymes continuously decreases until cell lysis, steady-state measurements eliminate the effect of transient memory of cell shape, and leave time for enzyme levels to have repercussions on the peptidoglycan. This is particularly relevant in our case, as it is known that aPBP's inactivation only affects cell wall synthesis after a 20 min delay [153].

We examine the phenotype of cells at various concentrations of PBP1AB and show that variations in the level of Rod complex enzymes and aPBPs lead to very different reactions from the cells. Strikingly, the concentration of enzymes from the Rod complex has direct repercussions on cell shape, while the concentration of aPBPs can be changed over a hundred-fold range with virtually no effect on cell shape or growth rate. Below this range, the cells abruptly lyse in an "all-or-nothing" behavior.

It is tempting to think that the mechanical and chemical defects observed in ΔPBP1B are the consequence of a thinner or sparser cell wall, but this has never been verified. Here, we nuance this hypothesis by creating cells with low levels of PBP1AB, that insert peptidoglycan at the normal rate but still exhibit altered mechanical properties. Furthermore, by submitting cells to the depletion of cytoplasmic precursors of the cell wall, we show that PBP1B is important not only to protect cells from subsequent stress, but also to recover from the damage after the stress.

By measuring the motion of single molecules, we show that aPBPs are increasingly immobile with increasing need for cell wall insertion or with increasing LpoAB levels, providing direct quantification of the interplay between the cell wall, aPBPs and their outer-membrane activators LpoA and B.

This suggests that PBP1AB are required to maintain the integrity and structural organization of the peptidoglycan on a local scale.

5.2 Results

Class A PBPs have an "all-or-nothing" behaviour

We constructed a strain with tunable levels of PBP1A and 1B by fusing them to mCherry and GFP respectively, and then controlling their expression level using partial CRISPR knock-down [82] (figure 5.1A). The fusions were expressed from the native promoter, in the native locus, while making sure all the isoforms of PBP1B would still be expressed. By doing so, we expected the concentrations to closely match wild-type (WT) levels. In fact, both fusions were overexpressed compared to the wild-type: quantitative mass spectrometry measurements showed that the levels of the mCherry-PBP1A and GFP-PBP1B fusions were respectively 1300% and 360% of wild-type enzyme levels (table 5.1). While not anticipated, this overexpression was ultimately beneficial since it allowed us to explore aPBP levels ranging from strong repression to strong overexpression in a single strain using only mismatched CRISPR guides as a genetic remote control.

To control the concentration of both GFP-PBP1B and mCherry-PBP1A independently, we used the 5x4 GFP/mCherry crRNA matrix described previously [82]. In addition, we also constructed single-guide RNA (sgRNA) repressors for sfGFP and mCherry to extend the range of possible concentrations (see supplementary information).

By combining mass spectrometry, single-cell fluorescence measurements and SDS-page, we determined the absolute levels of PBP1B when repressed by those different CRISPR guides. Previous estimates of the number of PBP1A and PBP1B molecule per wild-type cell vary between 100-1000 copies [160, 161, 162, 148]. Accordingly, we find the absolute copy number of PBP1B in the wild-type to be 166±26 (table 5.1). To ensure that the repression is effective, bocillin-labeled SDS-page was used to verify that no cryptic, truncated or non-fluorescent form of PBP1AB could be produced to escape the repression (figure 5.5A).

Table 5.1: **Levels of PBP1AB in different strains, measured by mass spectrometry with Data Independent Acquisition (DIA).** Ø: Guide with no target. N.D.: not determined. PRM: Parallel Reaction Monitoring.
*measured by fluorescence microscopy rather than DIA.

Strain	LC69	AV44	AV44	AV51	AV58
Pair of CRISPR guides (bp)	Ø	Ø	14-20	14-Ø	Ø
PBP1A level (%)	100	1337±615	20±2	Deleted	Deleted
PBP1B level (%)	100	367±32	27±2	33±3	1167±17*
Absolute PBP1B (western blot)	N.D.	688±115	40±5.0	67±14	N.D.
Absolute PBP1B (PRM)	166±28	547±52	56±17	56±7	N.D.
Doubling time in M63 (min)	77±3	72±2	77±4	79±2	75±1

Interestingly, the remaining level of GFP-PBP1B after repression is higher than what we would expect from the passage probability of the CRISPR guides we used, as measured by repressing a constitutive GFP reporter (figure 5.6, left). This provides evidence for genetic feedback raising the expression of PBP1B in response to the repression (see also Vigouroux et al. [82]). We did not detect such a feedback for mCherry-PBP1A (figure 5.6, right).

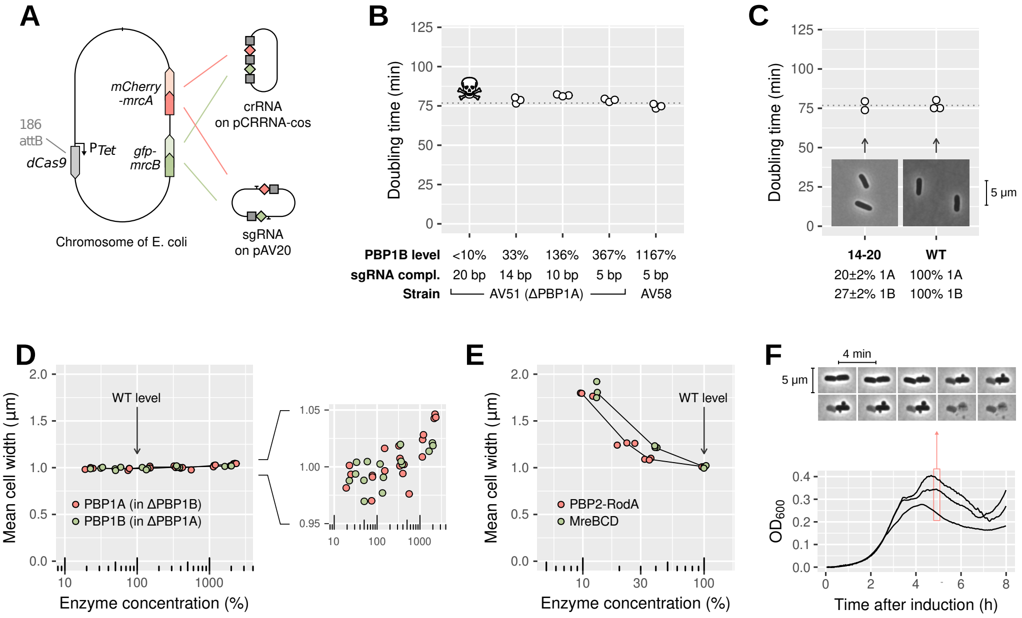

Figure 5.1: **Class A PBPs have an "all-or-nothing" behavior.**
A: Sketch of the strain AV44 with tunable levels of PBP1A and PBP1B. **B:** Doubling times in M63 at 30°C, as a function of PBP1B level in ΔPBP1A. Skull logo: not viable. **C:** Doubling times of WT and the "14-20" strain, and their morphology in phase-contrast microscopy. **D:** Effect of aPBPs' concentration on cell diameter. **E:** Effect of enzymes from the Rod complex on cell diameter. **F:** Growth curve of a strain with PBP1AB repressed to a lethal level, and time-lapse of cell morphology during lysis.
Individual points indicate biological replicates.

As expected from the synthetic lethality of PBP1AB, strains with a strong repression (or deletion) of both PBP1A and PBP1B could not survive. In particular, in a strain lacking PBP1A, a reduction of PBP1B's concentration to about 10% of WT (obtained with a single-guide RNA with 20 bp complementarity), resulted in cell death. However, all the other levels of PBP1B expression, ranging from ≈30% to ≈1200% of WT, were viable in the ΔPBP1A background. For the dual repression of PBP1A and PBP1B, the lowest level we could reach without killing the cells was 27±2% of PBP1B and 20±2% of PBP1A. This was done using sgRNAs with respectively 14 bp and 20 bp of complementarity, thus we nicknamed this strain "14-20".

By examining the phenotype of these surviving strains, we aimed to see the potential repercussions of a perturbed PBP1B level. Surprisingly, the growth rate was completely unaffected: regardless of the level of PBP1B in ΔPBP1A, the cells either grew at the same rate as the wild-type, or died, with no in-between (figure 5.1B). The "14-20" double-repression strain did not have any growth defect either (figure 5.1C).

To measure the impact of PBP1AB levels on cell morphology, we varied the level of each PBP1 from 30 to 1200% in strains lacking the other PBP1. As in *B. subtillis*, we found that repression of either PBP1A or B is associated with a reduction in diameter, while overexpression makes the cells wider (figure 5.1D). While reproducible, this effect is extremely small in magnitude: a 60-fold change in PBP1A or PBP1B concentration leads at most to a 75 nm increase in diameter. For comparison, a mere 10-fold change in PBP2/RodA or MreBCD level using the same method changes the diameter by about 800 nm (figure 5.1E). Our observations are also in stark contrast to *B. subtilis*, where a similar change of the level of the major aPBP PBP1 leads to a 600 nm increase in diameter [133]. As a further control, we used an alternative setup based on the inducible P_{BAD} promoter to check the lack of major shape phenotype at low PBP1AB induction (figure 5.5B and C).

We also examined the terminal phenotype of the strains whose level of PBP1AB is too low for survival. We used timelapse microscopy to monitor single cells at the time of the collapse after induction of our strongest CRISPR plasmid (20 bp of complementarity for each target, leading to a repression below 10% of WT). Contrary to the death by lack of PBP2-RodA, when PBP1AB were repressed the cells abruptly lysed without any further change in cell dimensions compared to the minimum viable expression (figures 5.1F and 5.7). We often observed small bulges on the sides of the cells just before lysis, as previously observed using other methods [53, 163]. These observations suggest that enzymes from the Rod complex are responsible for global rod-like shape, while aPBP are involved in maintenance of peptidoglycan integrity on a smaller scale.

At a critically low level, cells insert as much peptidoglycan as wild-type cells but have different mechanical properties

We then focused on the 14-20 repressed strain, and sought to know if it differed from wild-type cells in any way that is not visible from growth rate and morphology alone.

One possibility is that the density (or thickness) of the peptidoglycan layer is reduced, as it was previously reported for a ΔPBP1B mutant [159]. We therefore measured peptidoglycan insertion rate by recording the incorporation of the radio-labeled cell wall precursor meso-diaminopimelic acid (mDAP) as a function of time [164]. As expected, in ΔPBP1B, peptidoglycan insertion was reduced by about 2-fold, even with a high level of PBP1A (figure 5.2A). This was also the case when using a sgRNA with 20 bp of complementarity, repressing PBP1B to less than 10%. Intriguingly, the strain 14-20, with both PBP1A and PBP1B repressed below 30%, inserted mDAP at the same rate as the non-repressed strain with 1300% PBP1A and 370% PBP1B (figure 5.2A). This means that PBP1AB's concentrations can be varied over a large range without changing the rate of peptidoglycan insertion. It also means that a strain with 20% of PBP1A and 30% of PBP1B inserts more peptidoglycan than a strain with 1300% PBP1A but no PBP1B, further confirming that PBP1A and PBP1B are not equivalent. As a positive control, we also reproduced the finding that 5 mg/ml of D-methionine causes a moderate decrease in peptidoglycan insertion [156].

Furthermore, we measured the chemical composition of the peptidoglycan in these strains by digesting it with mutanolysin and analysing the fragments by HPLC-UV. No large difference was observed in any of the peaks, meaning that the rate of cross-linking is not affected by the repression (figure 5.8B). This indicates that the essential activity of PBP1AB does not take place at the molecular level. Together, these data confirm that PG insertion by the aPBPs is rigorously buffered against variation in their levels, and this buffering holds over a wide range of concentrations.

Previously, it has been reported that cells lacking PBP1B have a more elastic cell wall [155]. As a small amount of PBP1B is enough to completely restore cell wall insertion

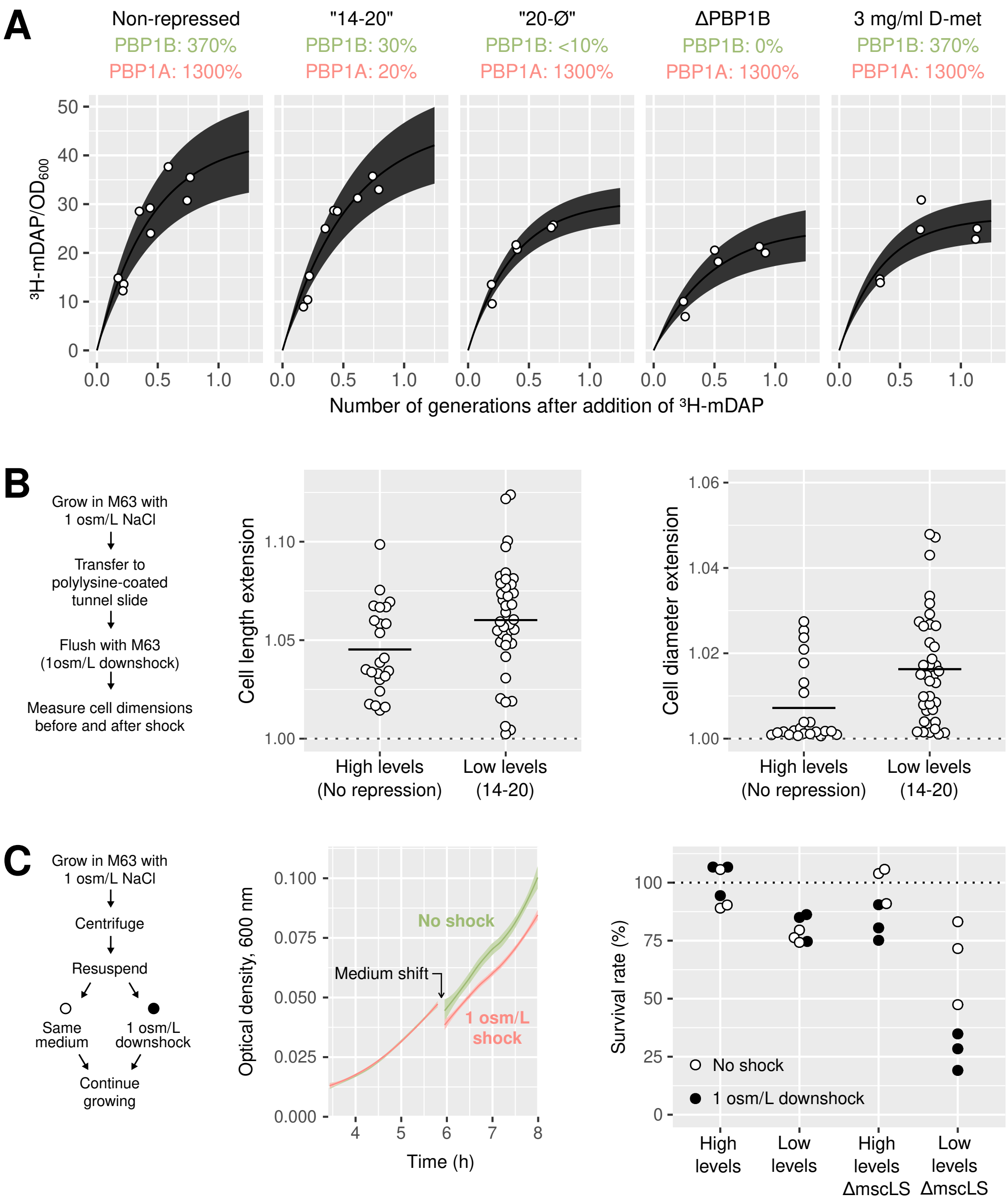

Figure 5.2: **Strong repression of PBP1AB does not change peptidoglycan insertion rate, but changes the mechanical properties of the cell. A:** Amount of incorporated ^{3}H-mDAP per optical density as a function of time (in generations) since ^{3}H-mDAP addition. The solid line and shaded area represent an exponential fit ± standard error on the calculated steady-state value. **B:** Extension of the cell's long axis (*left*) and short axis (*right*) after a 1 osm/L downshock. A value of one corresponds to no extension. **C:** *Left:* Example of growth curves to test osmotic shock resistance. *Right:* Percentage of cells that are lost during the medium replacement, with or without downshock.

rate, we sought to know whether it also restores normal mechanical properties. One method to measure the elasticity of cell surface is to submit the cells to an osmotic downshock. The sudden intake of water causes the cell to expand, and the difference in cell size before and after the shock allows to estimate the rigidity of the cell wall [165]. To make the expansion more visible, we deleted the mechano-sensitive channels *mscS* and *mscL* that normally open after a shock to equilibrate the osmotic pressure. A downshock going from M63 supplemented with 1 osm/L of NaCl, to normal M63 was performed in a "tunnel slide" setup [165]. As the fluorescence from the GFP-PBP1B and mCherry-PBP1A fusions is sufficient to distinguish the non-repressed strain from the repressed one, we pooled both strains in the same tunnel slide and used single-cell fluorescence to identify the two genotypes during analysis. This way, we ensure that the temporal dynamics and magnitude of the osmotic shock were exactly the same for both strain, greatly improving the sensitivity of the measurement. When PBP1A and PBP1B are strongly repressed (strain 14-20), both the axial and circumferential elasticity of the cell are larger than in the non-repressed case, indicating structural differences in the cell wall (figure 5.2B). For both the repressed and non-repressed strains, the expansion along the long axis of the cells was much larger than along the short axis. This is presumably due to the greater elasticity of peptide crosslinks compared to the glycan strands [166].

To rapidly quantify the survival of our strains after an osmotic shock, we developed a simple assay based on optical density in a plate reader: the cells are grown in a high-osmolarity (1 osm/L NaCl) medium up to an optical density of 0.1, then the medium is washed away and replaced either with the same salted medium (no osmotic shock) or with normal medium (1 osm/L downshock). We then continue to monitor growth and estimate the fraction of cells that stopped growing by fitting an exponential curve before and after the shock (figure 5.2C). When both mechanosensitive channels are present, we do not detect any difference between the two resuspension media, meaning that most cells survived the osmotic downshock (black dots *versus* white dots in Fig. 5.2C), even at a low level of PBP1AB. In the Δ*mscLS* strain, however, the osmotic shock caused the death of a large fraction of the cells, especially for the repressed strain, where about two thirds of the cells died due to the shock. In contrast, at high PBP1AB levels, only 20% of the cells died from the shock.

Surprisingly, the 14-20 repressed strain showed some significant mortality even in the absence of any osmotic shock, when the cells were simply pelleted and resuspended in an identical medium (white dots in figure 5.2C). While this washout process had no effect on the strain with high PBP1AB, about 25% of the cells were lost in the repressed case. This suggests that cells with low PBP1AB are more vulnerable to the centrifugation or resuspension step, or have lower adherence. Interestingly, this happened regardless of the presence of the mechano-sensitive channels MscLS.

It is counter-intuitive that cells with normal peptidoglycan insertion rate can have altered mechanical properties. This indicates that, at low PBP1B levels, peptidoglycan polymerization is quantitatively normal, but qualitatively different, in the sense that the structural organization of the peptidoglycan is altered.

PBP1B maintains cell wall integrity and repairs it after stress

The maintenance of cell wall integrity englobes two different tasks: First, PBP1AB could have a preventive effect, making the cell wall more resistant and less likely to break during stress. Second, PBP1AB could have a repair function and help restore peptidoglycan integrity after a damaging event.

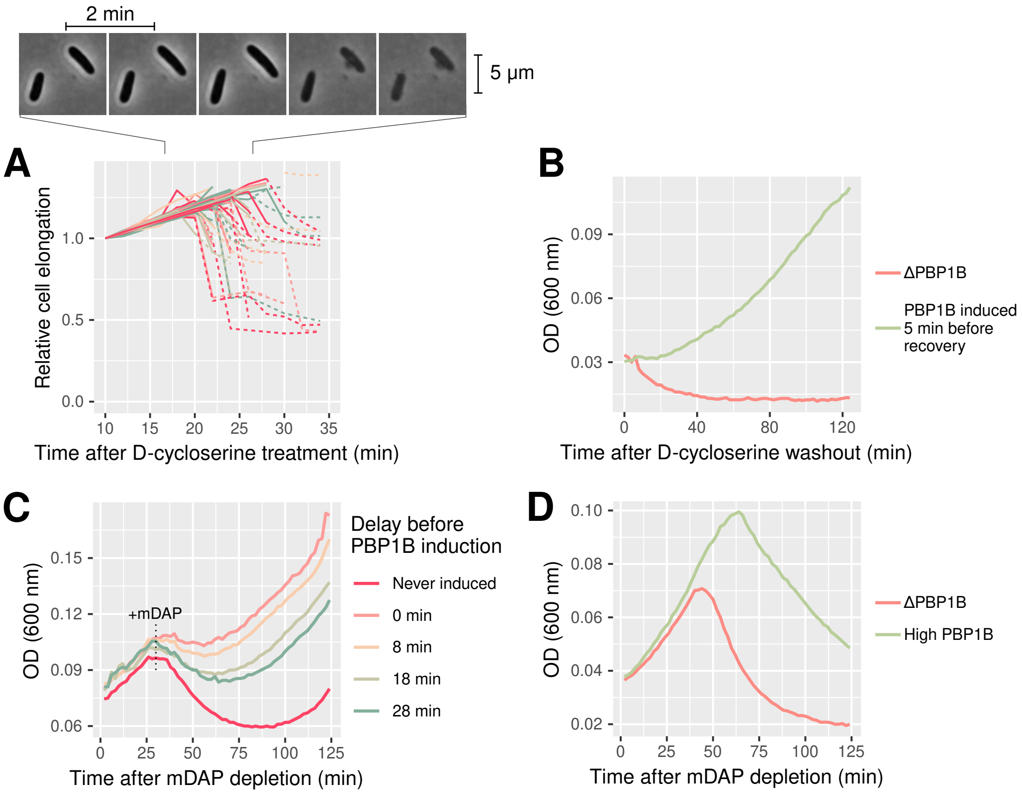

Figure 5.3: **Depletion of peptidoglycan precursors by D-cycloserine.** **A:** Increase of cell length during a timelapse of D-cycloserine treatment, relative to the length on the first frame. Solid lines are living cells, dashed lines are lysed cells. Colors are arbitrary. **B:** Growth curves of recovery after 25 min of D-cycloserine treatment then washout. **C:** Growth curves of recovery after 30 min of mDAP depletion in an auxotrophe. **D:** Growth curves following mDAP depletion in an auxotrophe.

To distinguish between these two roles, we make use of a strain with inducible PBP1B, in combination with D-cycloserine treatment. This antibiotic is an analogue of D-alanine that blocks the synthesis of cell wall precursors in the cytoplasm [167]. Upon treatment with high dose (1 mM) of D-cycloserine, the cells continue to extend during about 15 minutes, before what they brutally lyse (figure 5.3A). Small bulges sometimes appear on the sides of the lysing cells, similarly to cells dying from the lack of PBP1AB.

To measure the ability of PBP1B to repair the damage due to D-cycloserine treatment, cells are grown without PBP1B, then treated with D-cycloserine for 25 min and washed out to allow for recovery. Five minutes before the wash-out, PBP1B is either induced or not. The cells with induced PBP1B recover much better than the cells without it, showing that PBP1B can repair the peptidoglycan after stress (figure 5.3B). The difference in recovery appears almost immediately after induction, so the newly-induced PBP1B did not have time to contribute significantly to cell wall elongation. Thus, the better recovery is probably not due to synthesis of new peptidoglycan, but to repair of the existing cell wall.

We performed a similar experiment using an mDAP auxotrophe. As this strain cannot synthesize mDAP, the culture collapses after about 30 min when it is transfered to a medium without mDAP. If mDAP is supplied again, the culture is able to recover. In figure 5.3C, all the cultures initially lack PBP1B. If PBP1B is induced during the course of mDAP depletion, the recovery is much faster, and the sooner the induction occurs, the better. This suggests that peptidoglycan insertion by PBP1B allowed to use the residual stock of mDAP in a more efficient way, preventing lysis and making the cells more likely to recover. Additionally, we grow the same auxotrophe with or without inducing PBP1B, then transfer them in a medium without mDAP. We find that strains that had initially a high concentration of PBP1B take more time to lyse than strains that were not induced. This demonstrates that the changes in the peptidoglycan due to the lack of PBP1B made the cells more sensitive to mDAP depletion, in other words PBP1B is important for the quality of the cell wall even in normal conditions, before the cells are subjected to any stress (figure 5.3D).

PBP1B and LpoB sense the need for cell wall insertion

Single-molecule tracking of fluorescent protein fusions have shown that PBP1AB can be divided in two populations: one « bound » fraction with a negligible diffusion coefficient, and one « mobile » fraction that is diffusing in two dimensions along the inner membrane [147]. Presumably, the mobile molecules are searching for regions that need polymerization. It is not known whether the interaction with LpoAB alone is able to stop PBP1AB diffusion, or if immobilization is only due to processive peptidoglycan insertion.

To localize individual GFP-PBP1B molecules, we first bleached a large fraction of the molecules in epifluorescence mode. Then, we tracked single GFP-PBP1B molecules in TIRF mode for reduced background fluorescence (figure 5.4B and C). The bound fraction of molecules was then calculated by fitting the observed distribution of single-particle effective diffusion coefficients (Methods).

A lower concentration of PBP1B ($\approx$30% of WT) results in an increased fraction of bound molecules (up to 30% from 10% around wild-type levels, figure 5.4D) while overexpression of PBP1B (to $\approx$370% of WT) decreases the bound fraction (down to 3%). The relative changes in bound fraction seem to mirror the changes in total PBP1B amount, compatible with a constant absolute number of immobile PBP1B molecules per cell.

We measured the bound fraction of PBP1B in a strain with PBP1A either deleted, or overexpressed to 1300%. We kept PBP1B repressed to about 30% in both case. At high PBP1A, the bound fraction is dramatically lower than in ΔPBP1A (figure 5.4E). As PBP1A and PBP1B are not known to communicate directly, it could be that PBP1B's binding is adjusted to the state of the cell wall, possibly mediated by the interaction with LpoAB through the cell wall. In the absence of PBP1A there would be a higher need for cell wall insertion causing more PBP1B immobilization. Another possibility is that PBP1B's binding reflects its activity, which itself reflects the availability of peptidoglycan precursors, so that the deletion of PBP1A redirects the flux of precursors to PBP1B and increases its activity.

In support for the first hypothesis, deleting LpoB makes the bound fraction vanish. On the contrary, overexpressing LpoB from a plasmid causes PBP1B's bound fraction to increase, indicating that the contact with LpoB may be the driving force behind PBP1B's immobilization (figure 5.4F).

We then wondered if the immobilization of PBP1B is due to processive peptidogly-

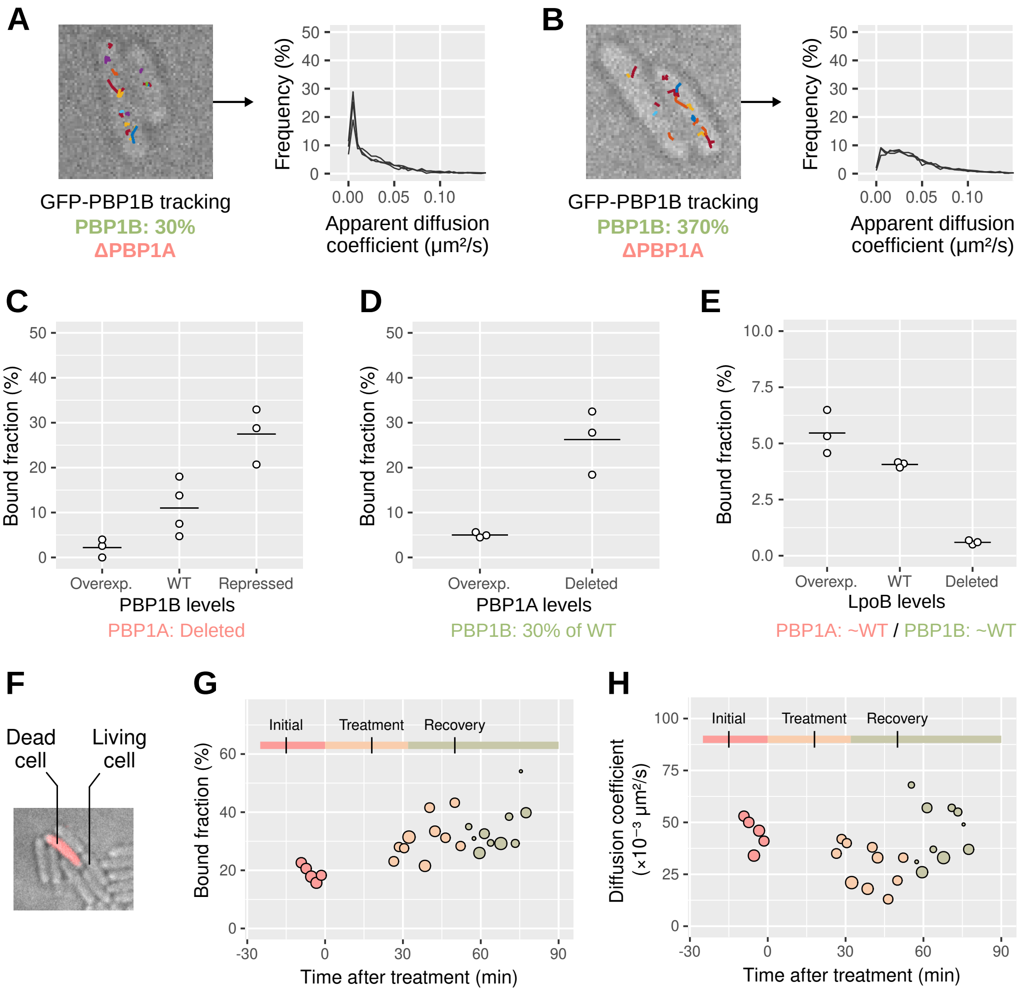

Figure 5.4: **PBP1B's bound fraction adapts to the need for PG synthesis.** **A, B:** Sample tracks of GFP-PBP1B within the cells, and distribution of apparent diffusion coefficients. **C, D, E:** Calculated bound fraction of PBP1B at different levels of PBP1B, PBP1A or LpoB. **F:** Propidium iodide allows to exclude dead cells from the analysis. **G:** Bound fraction and **H:** diffusion coefficient of PBP1B during D-cycloserine treatment. The vertical black ticks are the time when we took samples for microscopy. Circle size reflects the number of tracks per point, ranging from 200 to 1500.

can insertion, or if it simply reflects the demand for cell wall insertion, perhaps through stable interaction with LpoB. We performed single-molecule tracking at three steps of D-cycloserine treatment: before adding the drug, during the treatment and after washing out the antibiotic, all in the absence of PBP1A. As we expected some cells to die because of D-cycloserine, we stained the cells with the vital dye propidium iodide to distinguish living cells from lysed ones (figure 5.3F).

During treatment, the bound fraction of PBP1B goes up to 35-40% compared to 20% for untreated cells (figure 5.3C). This confirms the hypothesis that PBP1B diffusion is governed by the state of the cell wall and not by PBP1's activity or precursor availability, as it is impossible for it to perform cell wall synthesis in the absence of precursors. However, it does not exclude that PBP1B can have some repair activity using just the material already present in the cell wall. At the same time, the diffusion coefficient goes down, from 0.050 to 0.025 $\mu m^2/s$ (figure 5.3D). After washing the D-cycloserine away, the production of lipid II starts again, allowing the cells to recover. During recovery, the bound fraction remains as high as during treatment, however the diffusion coefficient increases again to pre-treatment values.

These observations support the following model: upon precursor depletion, the hydrolases continue to cleave the peptidoglycan for cell wall elongation, uncovering LpoB molecules from the outer membrane. When PBP1B encounters LpoB, it immobilizes. If the D-cycloserine treatment is prolonged, the cells eventually lyse. If it is washed out, newly synthesized precursors can be incorporated and the cell continues to grow, so PBP1B's bound fraction remains high. Such a model would explain why the amount of PBP1B is important for recovery: when cell wall precursors become available again, the demand for cell wall insertion is high and a higher PBP1B concentration allows the cell to catch up quicker.

5.3 Discussion

Using a systematic CRISPR knock-down strategy, we investigated the importance of aPBP's concentration in *E. coli*. Overall, class A PBPs have an "all-or-nothing" behaviour. We estimated the minimum amount of PBP1A and PBP1B for survival to be around 20%. Below this level, the cultures lysed a few hours after induction. All the other levels grew at the same speed as the wild-type. For the surviving strains, we did not find any large variation of cell dimensions. Upon careful examination, the level of PBP1AB is positively correlated with cell diameter, something that was also observed in *B. subtilis* [133], but the magnitude of the effect was much smaller.

Focusing on a strain called "14-20", that expresses critically low amounts of PBP1A (20%) and PBP1B (30%), we find that it inserts as much peptidoglycan as the wild-type but has different mechanical properties. It is more elastic and less resistant to osmotic shocks than wild-type. This indicates that the repression of class A PBPs affects the cell not by reducing peptidoglycan polymerization, but by doing so in a structurally different way. By examining how cells react to the depletion of peptidoglycan precursors, we showed that PBP1B was at the same time capable of making the cell more resistant to future damage, but also to repair the damage once it is done.

In our experiments and others, the deletion of PBP1B resulted in stronger phenotypes than the deletion of PBP1A (in insertion rate, elasticity, antibiotic sensitivity). This could mean that PBP1B is intrinsically more important than PBP1A, but may also depend on the experimental conditions, such as pH [**?**]. Perhaps, in certain ranges of pH, the absence of PBP1A has a larger effect on cell stiffness.

We measured the 2D-diffusion of PBP1B at the single-molecule level, and found that the immobile fraction of PBP1B increases or decreases depending of the total concentration, so that the number of bound molecules is roughly constant. The lack of PBP1A also causes an increase in PBP1B bound fraction, showing that PBP1B's mobility adapts to the need for cell wall insertion. During precursors depletion by D-cycloserine, the bound fraction of PBP1B becomes higher, confirming that it is the state of the cell wall, and not the polymerization activity, that determines immobilization. This change in diffusion dynamics is likely mediated by LpoB, as the deletion of LpoB greatly decreases the immobile fraction of PBP1B.

There are large discrepancies between our single-molecule tracking measurements on PBP1B, and similar measurements from Lee et al. [168]. First, they found that the deletion of PBP1A did not change the diffusion coefficient of single PBP1B molecules, while we find that it causes quite a large increase in bound fraction. Second, they find that removing LpoB did not change PBP1B's diffusion coefficient either. This is surprising, as they observed a large increase in PBP1A's diffusion coefficient when LpoA is deleted. In our measurements, a deletion of LpoB makes PBP1B's bound fraction disappear, so the average diffusion coefficient would be higher. A likely explanation for this discrepancy is that Lee et al. fused the PAmCherry fluorescent protein to PBP1B in its native chromosomal locus, very similarly to the native GFP-PBP1B fusion we use in this study. It is possible that the fusion largely increased the level of PBP1B in their strain, exactly like it did in ours. At a very large level of PBP1B, most molecules are diffusive and it becomes very difficult to see differences in bound fraction, something that we saw ourselves when working with overexpressed GFP-PBP1B. If this explanation is true, then both PBP1A and PBP1B's diffusion are affected by LpoA and LpoB respectively, a result that seems more plausible biologically.

At a critically low level of PBP1AB (in the 14-20 strain), there is no difference with the wild-type in terms of peptidoglycan insertion rate, density of cross-linking, and cell morphology. However, the mechanical properties of the cells are modified. This indicates that class A PBPs maintain the local integrity of the peptidoglycan at an intermediate spatial scale, larger than the molecular scale but smaller than the general rod-shape. The defect in elasticity could come from a difference in length or orientation of glycan strands, or in homogeneity of the cross-linking rate across the cell surface.

When the polymerases from the Rod complex are lacking, the orientation of glycan strands is disorganised [169], something that was also observed in *B. subtilis* [133]. As PBP1AB are not known to co-localize with the rotating cytoskeletton MreB, it seems that PBP1AB insert glycan strands in a random orientation, contrary to the Rod complex which extends glycan strands circumferentially. One can speculate that the aPBPs make homogeneous, but disorganized cell wall, while the Rod complex makes well-aligned cell wall, but does not know where to insert it to have an homogeneous density. Potentially, these two systems could act in a synergistic way, each of them extending or reinforcing strands initiated by the other. This model is compatible with the terminal phenotypes we observe: When there is no class A PBPs, some points in the cell wall become too fragile and bulges appear around the cell (as in figure 5.1F). When there is no Rod complex, the cell wall is resistant and there are no bulges, but there is no large-scale organization, as the class A PBPs are not able to sense the general geometry of the cell.

While aPBPs may not be involved in rod-shape determination, they may still play a role in the sensing of mechanical strain and be important for the straightening of cells after bending [51]. These hypotheses will be interesting to explore in the future.

5.4 Experimental procedures

Strains and media

All the strains and plasmids used in this study are described in the supplementary text. Cloning and strain preparation were done in Luria-Bertani (LB) medium. Unless mentionned otherwise, every measurement was done in M63 minimal medium with 0.2% glucose, 0.1% casaminoacids and 0.5% thiamine. To induce the P_{bad} promoter, we used 0.5% lactose instead of glucose as a carbon source. For single-molecule tracking, the concentration of casaminoacids was reduced to 0.01% to minimize background fluorescence.

As needed, media were supplemented with kanamycine (50 μg/ml), carbenicilline (100 μg/ml), chloramphenicol (25 μg/ml) or spectinomycine (50 μg/ml), all from Sigma-Aldrich. CRISPR repression is induced with 100 ng/ml of anhydro-tetracycline (Acros Organics). For overexpression of PBP1A, PBP1B or LpoB from P_{bad}, 10 mg/ml of arabinose were added to the medium. The concentration of propidium iodide used to reveal dead cells was 0.4 μM.

Biological replicates result from independent cultures grown from separate colonies.

Genetic constructions

All strains used in this study derive from the MG1655 *E. coli* wild-type strain. Table 2 gives the genotypes of all strains used here, with the series of plasmids that were used to modify them. Gene deletions were carried out starting from the Keio collection [129]. P1 phage lysate was prepared from the Keio strain, then used to infect the recipient strain and the cells were plated on kanamycine to select for transducers. After each phage P1 transduction, as well as all “clonetegrations” [170], the kanamycine resistance marker was removed by transforming pE-FLP. Integration of mCherry-PBP1A and GFP-PBP1B in the native locus was done using the allelic exchange procedure described in [82].

The plasmids constructed for this study were assembled by Gibson assembly, from the fragments indicated in table 3. The fragments were obtained either by PCR, or by enzymatic digestion, as described in table 4. Oligonucleotide sequences can be found in table 5.

The CRISPR plasmids are either from the pcrRNA collection described in [82], or were assembled using the pAV20 double-sgRNA vector [133] and oligo pairs mentionned in table 6. In the later case, complementarity oligos (forward and reverse) were phosphorylated with T4 PNK in the presence of T4 ligase buffer (New England Biolabs), then annealed together. A mix containing the pAV20 vector, the two pairs of annealed oligos, the Bsa1 restriction enzyme (New England Biolabs), T4 ligase (New England Biolabs) and ATP was subjected to thermal cycles for digestion, annealing and ligation. The assembly product was subsequently electroporated in DH5α and the resulting plasmids were sequenced. The control guides, producing no repression, still contain the same 5 bp seed sequence as the sfGFP- and mCherry-targeting guides. This is to account for potential mild “bad seed effect” [79].

mDAP incorporation measurement

Overnight cultures of Δ*lysA* strains were grown with induction of the CRISPR system. They were then diluted to $OD_{600} = 0.1$ in M63 Glucose 0.2% with 50 μg/ml of lysine. When OD reached 0.4, ^{3}H-labelled mDAP was added for a final activity of 5 μCi/ml. For each point, 200 μl of culture were transferred to tubes containing 800 μl of boiling 5%SDS. After at least one hour of boiling, the samples were transferred to 0.22 μm GSWP filters. After applying vacuum, the filters were washed twice with 50 ml of hot water. The filters were then moved to 5 ml scintillation vials, treated overnight with 400 μl of 10 mg/ml lysozyme, and dissolved in 5 ml FilterCount cocktail (PerkinElmer) before counting.

The amount of ^{3}H-mDAP per cell was calculated by dividing the total counts by the optical density of the culture, with the assumption that changes in cell shape are negligible (see Fig. 5.1). The number of generations since ^{3}H-mDAP addition was obtained by fitting an exponential to OD_{600} as a function of time, giving the doubling time τ. The number of generations is defined as $G = T/\tau$. To calculate the incorporation rate λ and steady-state value $I_{\max}$, we fit the data with formula $I = I_{\max}(1 - e^{-\lambda G})$ with non-linear least squares (Supplementary Table 1).

Chromatography of peptidoglycan content

The chromatography of mutanolysin-digested peptidoglycan was done on a Shimatzu HPLC system with a hypersil Gold eQ 250x4.6 mm column with 3 μm particle size. The mobile phase was a gradient from water with 0.05% TFA to 50% acetonitrile with 0.05%TFA over 135 min. The flow was set to 0.5 ml/min.

Morphological measurements

Cells were grown to steady-state exponential phase (OD_{600} ≈0.1) and fixed with 4% formaldehyde in phosphate-buffered saline (PBS) during 30 minutes. Fixed cells were transferred to PBS microscopy pads with 1.5% UltraPure Agarose (Invitrogen) and imaged using an inverted microscope (TI-E, Nikon Inc.) equipped with a 100× phase-contrast objective (CFI PlanApo LambdaDM100× 1.4NA, Nikon Inc.), a solid-state light source (Spectra X, Lumencor Inc.), a multiband dichroic (69002bs, Chroma Technology Corp.). GFP and mCherry fluorescence were measured using excitation filters (560/32 and 485/25 resp.) and emission (632/60 and 535/50 resp.) filters. Images were acquired using a sCMOS camera (Orca Flash 4.0, Hamamatsu) with an effective pixel size of 65 nm. The Morphometrics package [171] was used to find cell contours from phase-contrast images. The analysis accounted for background intensity, uneven illumination, and cell auto-fluorescence. Intracellular concentration was obtained by integrating the corrected fluorescence intensity inside cell contours. Total regression was used to find the major axis of the cell. Cell width was defined as the average distance between the cell contour and this axis, excluding the poles. Cell length was calculated as the maximal distance between contour points projected on the cell axis.

Growth measurements

Overnight cultures were diluted 1/500 and grown in a tabletop shaker (Eppendorf) for 90 min to obtain exponential growth. The cultures were then transferred to a flat-bottomed 96-microwell plate (Greiner) and optical density at 600 nm was recorded along growth using a microplate reader (Tecan). To calculate the doubling time, we fit an exponential function to the data points corresponding to the exponential phase. The exponential phase was checked by using Durbin-Watson statistics on the residuals of exponential fit. Optical density at the peak was determined by calculating the first zero of the derivative of OD_{600} after mean-filtering with a bandwidth of 10 min.

Single-particle tracking of PBP1B

Single particle tracking of sfGFP-PBP1B was performed on a custom-designed fluorescence microscope, in a custom-built temperature controlled chamber at 29°C. Prior to imaging the cells were transferred to a pre-heated 1% agarose pad (Invitrogen) then left to dry in the dark for 3 minutes. After covering with a 0.1 mm cover slip, the slide was mounted on the microscope and incubated 5 min to equilibrate sample temperature and minimize drift. The microscope was equipped with a 100x TIRF objective (Apo TIRF, 100x, NA 1.49, Nikon), three laser lines: 405 nm (Obis, Coherent), 488 nm (Sapphire, Coherent), 561 nm (Sapphire, Coherent), a dichroic beamsplitter (Di03-R488/561-t3-25x36, Semrock) and a laser-line filter (NF561-18, Thorlabs). Shuttering of the 488 nm laser was controlled with an acusto optic tunable filter (AA Optoelectronics) or with shutters (Uniblitz, LS3 and TS6B, Vincent Associates). Images were acquired with an EMCCD camera (iXon Ultra, Andor). All components were controlled and synchronized using MicroManager [172]. For high-frequency imaging of sfGFP-PBP1B, images were acquired with exposure time and intervals of 60 ms for a duration of 1 min. To distinguish single molecules, this requires a photo bleaching phase prior to image acquisition. The sample was exposed to 488 nm laser in epifluorescence mode in order not to bias our analysis towards diffusive molecules as exposure to light in TIR mode would dominantly bleach bound PBP1B in the field of view. After photo bleaching, we immediately switched to TIR mode for image acquisition. Bleaching time is adjusted according to the level of PBP1B and varies between 100 ms and 5 s. The analysis pipeline is described in details in the supplementary text.

Quantification of PBP1AB levels

Bocillin-labeling of the PBPs

The bocillin-binding assay used to check the absence of non-fluorescent PBP1AB is similar to what is used in [147, 173]. We prepared exponentially-growing cells at $OD_{600} \approx 0.4$. We washed 1.8 ml of each culture in PBS, resuspended them in 200 µl PBS and kept cultures on ice. We disrupted cells by sonication (FB120, Fisher Scientific) and centrifuged them for 15 min at 4°C (21,000 g). We subsequently resuspended the pellet corresponding to the membrane fraction in 50 µl PBS containing 15 µM fluorescently labelled Bocillin-FL (Invitrogen). Membranes were incubated at 37°C for 30 min and washed once in 1 ml PBS. We centrifuged the membranes for 15 min (21,000 g) and resuspended them in 50 µl PBS. We measured the protein concentration of each sample with a colorimetric assay based on the Bradford method (#5000006, Bio-Rad) and loaded equal amounts of protein mixed with 4X Laemmli buffer onto a 10% polyacrylamide gel. We visualized the labelled proteins with a Typhoon 9000 fluorescence imager (GE Healthcare): excitation at 488 nm and emission at 530 nm. We quantified the relative amounts of PBP2 in each sample by quantifying the grey values of each lane in ImageJ [174].

Content analysis of the peptidoglycan

Extraction of peptidoglycan from exponentially-growing cells was done according to the protocol described in [175]. Mutanolysin digestion was done following the same reference's protocol.

5.5 Acknowledgements

We thank Tom Bernhardt for providing the pHC942 plasmid. The bocillin labelling, SDS-page and growth curves for D-cycloserine treatment and mDAP auxotrophy were done by Baptiste Cordier. The meso-DAP incorporation experiments and osmotic shocks were done with help from Enno Oldewurtel . Thanks to Richard Wheeler for assistance with peptidoglycan extraction and chromatography analysis and to Eva Wollrab for help in the single-molecule tracking.

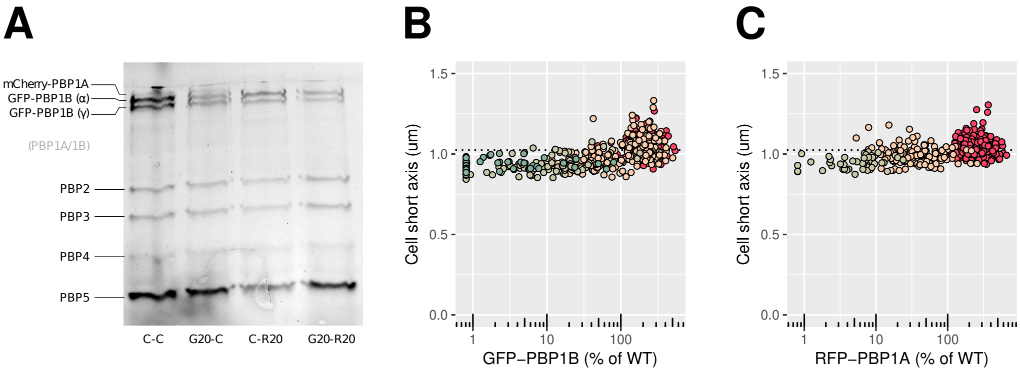

Figure 5.5: **A:** The mCherry-PBP1A fusion (respectively GFP-PBP1B) is the only present form of PBP1A (respectively PBP1B) in the strain AV44 used in this study. The fluorescent bocillin binds specifically to Penicillin Binding Proteins (PBP). The change in band intensity after repression by CRISPR does not reflect the change in fluorescence measured by microscopy for the same conditions, presumably because bocillin only labels active molecules. "C" refers to a control CRISPR spacer (no target). **B and C:** Diameter of single cells at different levels of an inducible GFP-PBP1B fusion (B) or mCherry-PBP1A fusion (C). Different colors indicate different concentrations of arabinose.

5.6 Supplementary information

Single-particle tracking of PBP1B

We first segmented images using the brightfield channel and standard image processing functions. PBP1B spots in fluorescence images were identified as the local maxima of the bandpass filtered images with intensity 3.5 times higher than background (bpass and pkfnd functions from `https://site.physics.georgetown.edu/matlab/code.html`). Sub-pixel resolution was achieved by finding the center of a two-dimensional Gaussian fitted to the intensity profile of each spot. Spots in subsequent frames were then connected into raw trajectories if their distance was below 600 nm [176]. If tracking of a particle lead to a situation where a particle can be connected to more than one possible peak in the next frame we discontinued the tracking for this trajectory.

The effective diffusion constant, D_{eff}, was calculated for the first 4 steps of each track from a linear fit of single-track MSD's according to $\langle x^2(t)\rangle = 4D_{\text{single}}t$. The empirical distribution of D_{eff} values was then compared with the distribution computed from simulated tracks in order to extract the unknown parameters of a 2-state model (diffusion constants $D1$, $D2$ and localization uncertainty σ) based on finding the minimum residual sum of squares (RSS). The population size, p, is extracted by fitting the peak value at $D_{\text{eff}} = 0$ µm^2 to the 2-state model.

For simulating tracks, molecules were generated as either immobile with $D1$ set to 0 µm^2/s or diffusive with diffusion constant $D2$. To account for the localization uncertainties for each population, we subsequently added to all x- and y-coordinates a random displacement drawn from a normal distribution with a mean of 0 nm and standard deviation of σ, repeated 4 times to simulate 4 frames.

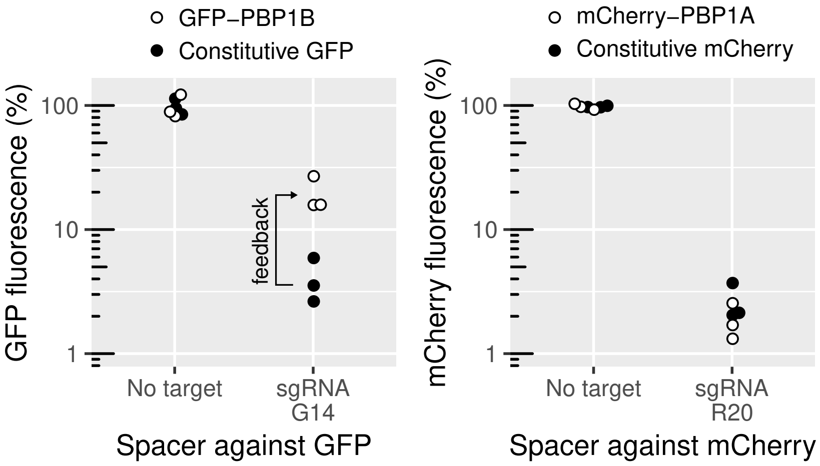

Figure 5.6: **Genetic feedback regulates PBP1B but not PBP1A. Left:** The same CRISPR guides are used to repress either a constitutively-expressed GFP, or the GFP-PBP1B fusion from the native chromosomal locus. The increase of relative residual expression for GFP-PBP1B indicates feedback on gene expression. **Right:** Same measurement comparing constitutively-expressed mCherry and the mCherry-PBP1A fusion, this time showing no evidence of feedback.

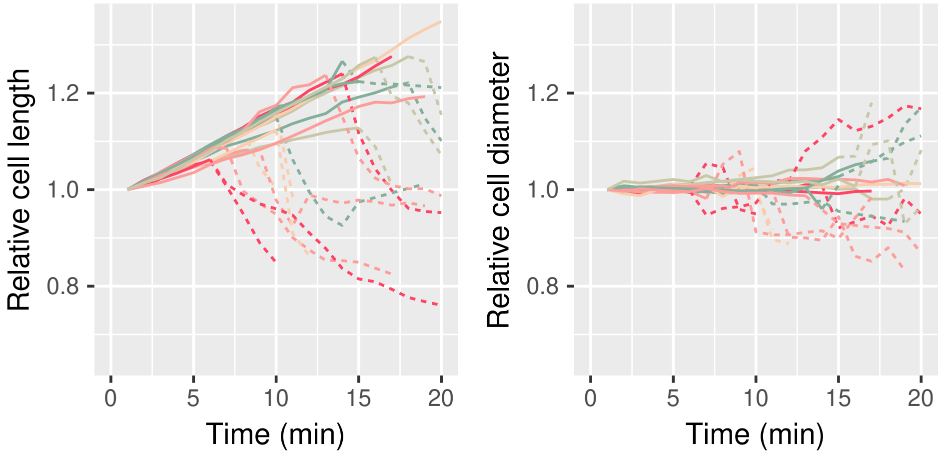

Figure 5.7: **Dimensions of individual cells in the instant before death.** PBP1A and PBP1B are both repressed by single-guide RNAs with perfect complementarity. The film starts 4h45 after the induction of the CRISPR system. Cell length and cell diameter are normalized with respect to the dimensions of the cell in the first frame of the film. Solid lines are living cells, dashed lines are lysed cells (phase-bright and blurry). Colors are arbitrary.

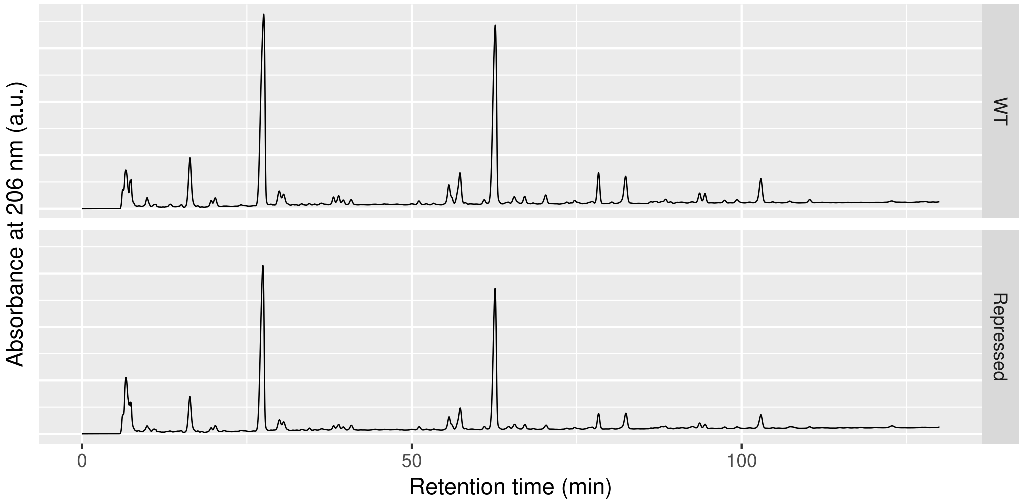

Figure 5.8: **HPLC analysis of the peptidoglycan after digestion by mutanolysin**, in a wild-type strain (WT) and in a repressed strain (14-20).

We performed a 2-step exploration of the parameter space to find values of $D2$ and σ. First, we simultaneously varied $D2$ between 0.0 and 0.1 $\mu m^2/s$ with an interval of 0.005 $\mu m^2/s$ and σ between 0 and 50 nm with an interval of 5 nm. For each parameter set, the RSS between empirical and simulated distributions were calculated, using a bin width of 0.005 $\mu m^2/s$. Using the parameters which gave the lower RSS, we finally determined the bound and mobile fractions.

Table 5.2: **Fit parameters for the mDAP incorporation experiment**. The incorporated ^{3}H-mDAP per cell I is fit with formula $I = I_{\max}(1-e^{-\lambda G})$, where λ is the rate of mDAP incorporation, and $I_{\max}$ is the steady-state mDAP content. Standard errors for the two parameters are also indicated.

Strain	PBP1B (%)	PBP1A (%)	D-methionine	λ	$I_{\max}$
AV44 non-repressed	370	1300	No	2.23±0.86	43.51±9.03
AV44 14-20	30	20	No	1.84±0.59	46.74±8.73
AV44 20-5	<10	1300	No	2.66±0.68	30.72±3.84
AV50 non-repressed	Deleted	1300	No	2.15±1	25.21±5.61
AV44 non-repressed	370	1300	3 mg/ml	2.87±1.41	27.29±4.51

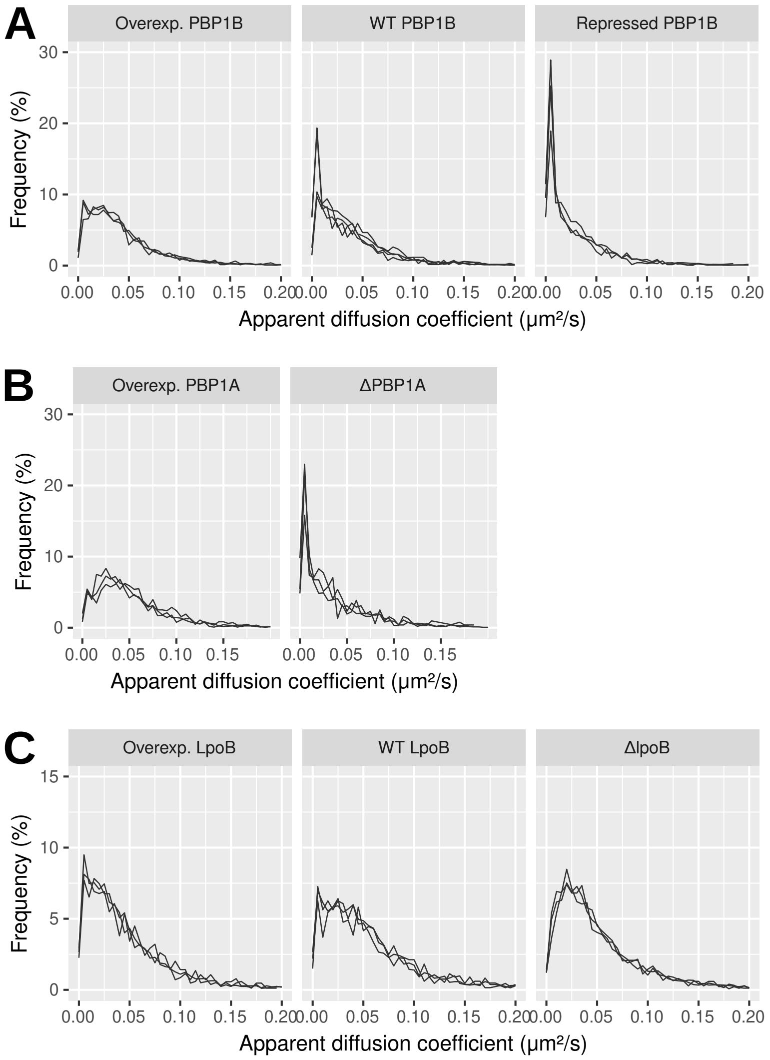

Figure 5.9: **Raw distributions of apparent diffusion coefficients for GFP-PBP1B single-molecule tracking.**
The bound fractions shown in Fig. 5.4 were extracted from the distributions showed here. Each line represents one independent replicate. **A:** Variable PBP1B levels in ΔPBP1A. **B:** Variable PBP1A levels in a strain with PBP1B repressed to 30% of WT level. **C:** Variable LpoB levels in a strain with PBP1A and PBP1B both repressed close to the WT level.

Table 5.3: Strains used in this study.

Strain	Genotype	Construction
LC69	186::P_{Tet}75-dCas9	MG1655→pLC143
AV03	186::P_{Tet}-dcas9, HK022::P_{127}, λ::P_{127}	from [82]
AV04	186::P_{Tet}-dcas9, λ::P_{127}-mcherry	from [82]
AV44	186::P_{Tet}75-dCas9, mrcB::msfgfp-mrcB, mrcA::mcherry-mrcA	LC69→pAV42→pAV43
AV47	186::P_{Tet}75-dcas9, HK022::P_{127}-sfgfp, λ::P_{127}-mcherry	AV03→P1 (pLC143)
AV50	186::P_{Tet}75-dCas9, mrcA::mcherry-mrcA, ΔmrcB	AV44→Keio (ΔmrcB)
AV51	186::P_{Tet}75-dCas9, mrcB::msfgfp-mrcB, ΔmrcA	AV44→Keio (ΔmrcA)
AV58	186::P_{Tet}75-dCas9, mrcB::msfgfp-mrcB, ΔmrcA, HK022::Pbad-sfgfp-mrcB	AV51→pAV71
AV63	186::P_{Tet}75-dCas9, mrcA::mcherry-mrcA, ΔmrcB, HK022::Pbad-mCherry-mrcA	AV50→pAV77
AV80	186::P_{Tet}75-dCas9, mrcB::msfgfp-mrcB, mrcA::mcherry-mrcA, ΔpbpC, ΔmtgA, ΔmscS, ΔmscL	AV44→Keio (ΔmtgA)
AV84	186::P_{Tet}75-dCas9, mrcB::msfgfp-mrcB, mrcA::mcherry-mrcA, ΔpbpC, ΔmtgA, ΔlysA	AV80→Keio (ΔlysA)
AV88	186::P_{Tet}75-dCas9, mreB::sfGFP-mreB	from [133]
AV93	186::P_{Tet}75-dCas9, mrcB::msfgfp-mrcB, mrcA::mcherry-mrcA, ΔpbpC, ΔmtgA, ΔmscS, ΔmscL	AV80→Keio (ΔmscS)
AV100	186::P_{Tet}75-dCas9, ΔmrcA, ΔmrcB, HK022::Pbad-sfgfp-mrcB	AV58→Keio (ΔmrcB)
AV101	186::P_{Tet}75-dCas9, ΔmrcA, ΔmrcB, HK022::Pbad-mCherry-mrcA	AV63→Keio (ΔmrcA)
AV105	186::P_{Tet}75-dCas9, ΔmrcB, mrcA::mcherry-mrcA, ΔpbpC, ΔmtgA, ΔlysA	AV93→Keio (ΔmrcB)
AV109	186::P_{Tet}75-dCas9, mrcB::msfgfp-mrcB, mrcA::mcherry-mrcA, ΔlpoA	AV44→Keio (ΔlpoA)
AV110	186::P_{Tet}75-dCas9, mrcB::msfgfp-mrcB, mrcA::mcherry-mrcA, ΔlpoB	AV44→Keio (ΔlpoB)

Table 5.4: Plasmids used in this study. The fragments "D" are obtained by enzymatic digestions, while the fragments "R" are obtained by PCR amplification. Details about the fragments can be found in table 5.5.

Plasmid	Assembly or reference
pAV10	[82]
pE-FLP	[170]
pAV20	[133]
pLC143	[79]
pAV42	R62 + R63 + R27
pAV43	R64 + R65 + R66 + R23
pHC942	[147]
pAV71	D1+R97+R98
pAV77	D1+R97+R105

Table 5.5: Fragments used to assemble plasmids by Gibson assembly.

Fragment	Enzyme 1	Enzyme 2	Substrate	Reference
D1	EcoR1	PstI	pIT5-KH	[170]

Fragment	Primer 1	Primer 2	Template	Reference
R23	V101	V102	pSW23t	[177]
R27	V109	V110	pSW23t	[177]
R62	V111	V234	MG1655	
R63	V233	V116	pHC942	[147]
R64	V103	V238	MG1655	
R65	V235	V236	AV04	[82]
R66	V237	V108	MG1655	
R97	V317	V318	pBAD30	[178]
R98	V319	V320	AV44	This work
R105	V322	V341	AV44	This work

Table 5.6: Oligonucleotides used to make the fragments in table 5.5.

Oligo	Sequence
V101	TGGTGGCTGGCACAAGTGCCCTCCAGCTTTTGTTCCCTTTAGTGAGGGTTAATTGC
V103	TGATATCGAATTCCTGCAGCCGCGGTAATGCTTGTTGTCAG
V109	AAGGTAAAAGATCTCTCCGGCTCCAGCTTTTGTTCCCTTTAGT
V111	GATATCGAATTCCTGCAGCCCGAAGAGCCGCCACGGAT
V233	GATGACTATGAGGATGAAGAACCGATGAGTAAAGGTGAAGAACTGTTCACCGGTG
V235	ATGAAACTAAATGGGAAATTTCCAGTGGTTTCCAAGGGCGAGGAG
V237	ATGGATGAGCTGTACAAAGGATCCAAGTTCGTAAAGTATTTTTTGATCCTTGCAG
V317	CGCCATAAACTGCCAGGAATTGGGGATCGGGTTACCAATTATGACAACTTGACGGCTAC
V319	TCGCAACTCTCTACTGTTTCTCCATACCCGTGCGGAGAAAAAGCATGGCCGG
V322	AGGCGCCATGCATCTCGAGGCATGCCTGCATAATCAGAACAATTCCTGTGCCTCG

Table 5.7: Oligonucleotides inserted in the pAV20 cloning vector to make plasmids expressing two single-guide RNAs, one against sfGFP and one against mCherry. The capital letters emphasize the sequence of the CRISPR guide.

Oligo	Target	Complementarity	DNA strand	Sequence
V272	sfGFP	20 bp	Forward	ctagtCACCACGAACAGAGAATTTGgt
V273	sfGFP	14 bp	Forward	ctagtGTGGTGGAACAGAGAATTTGgt
V274	sfGFP	10 bp	Forward	ctagtGTGGTGCTTGAGAGAATTTGgt
V275	sfGFP	5 bp	Forward	ctagtGTGGTGCTTGTCTCTATTTGgt
V276	mCherry	20 bp	Forward	tagtTCTGGGTGCCTTCATACGGA
V277	mCherry	18 bp	Forward	tagtAGTGGGTGCCTTCATACGGA
V278	mCherry	11 bp	Forward	tagtAGACCCACGCTTCATACGGA
V279	mCherry	5 bp	Forward	tagtAGACCCACGGAAGTAACGGA
V280	sfGFP	20 bp	Reverse	taaaacCAAATTCTCTGTTCGTGGTGa
V281	sfGFP	14 bp	Reverse	taaaacCAAATTCTCTGTTCCACCACa
V282	sfGFP	10 bp	Reverse	taaaacCAAATTCTCTCAAGCACCACa
V283	sfGFP	5 bp	Reverse	taaaacCAAATAGAGACAAGCACCACa
V284	mCherry	20 bp	Reverse	aaacTCCGTATGAAGGCACCCAGA
V285	mCherry	18 bp	Reverse	aaacTCCGTATGAAGGCACCCACT
V286	mCherry	11 bp	Reverse	aaacTCCGTATGAAGCGTGGGTCT
V287	mCherry	5 bp	Reverse	aaacTCCGTTACTTCCGTGGGTCT

Chapter 6

A CRISPRi screen in *E. coli* reveals sequence-specific toxicity of dCas9

6.1 Impact on the project

When I started to work on changing the levels of class A PBPs, the Bad Seed Effect (BSE, see chapter 2) had not yet been identified. However, in my early experiments on PBP1A and PBP1B, the BSE was already apparent. The fact that it went unnoticed for such a long time is the consequence of several unfortunate choices.

For growth measurements, it was preferable to have all the compared strains in the exact same medium, meaning that all conditions should carry the same antibiotic markers. Also, to avoid potential unexpected effects of dCas9's expression and only measure the effect of gene repression by CRISPR, my initial experiments involved a random CRISPR guide, called "C", that had no target anywhere in *E. coli*'s genome, even when accounting for highly-mismatched potential off-targets. Unfortunately, this control guide produced a mild, non-lethal Bad Seed Effect: any strain expressing dCas9 with the "C" guide would suffer from a slight reduction of growth rate.

A typical experiment would involve a strain with tunable GFP-PBP1A and mCherry-PBP1B, that expressed either the control CRISPR plasmid, or CRISPR arrays against GFP and mCherry to change the levels of the genes. In addition, I usually included a strain without the fusions, but still able to express dCas9 and also carrying the control guide. This is to make sure that the simple presence of GFP- and mCherry- fusions does not affect the measured phenotype in any way.

Due to the bad seed effect of the control guide, the non-repressed strains grew a little slower than the rest. On the contrary, the strains where PBP1A and PBP1B were both repressed did not carry the control guide. As partial repression of PBP1AB does not reduce growth rate (something that was unknown at the time, see chapter 5), all these strains grew at a normal rate and, therefore, faster than the strains carrying the "C" control guide. Thus, in appearance, it was as if the repression of PBP1AB made the cells grow faster (figure 6.1).

To add more confusion, this experiment included strains with either PBP1A or PBP1B deleted, and then a variable level of the remaining one. The CRISPR plasmids contain two guides (one for PBP1A, one for PBP1B). When one of them is deleted, there

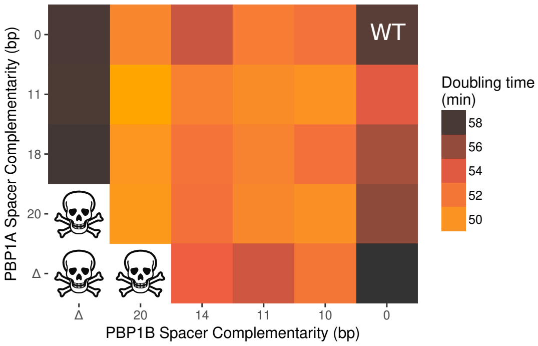

Figure 6.1: Due to the bad seed effect of the “C” guide (0 bp of complementarity), the repression of PBP1A and PBP1B appeared to make the strains grow faster than the wild-type (WT). The doubling times showed here are the averages of three biological replicates. Measured in M63 minimal medium at 30°C.

was no need for a CRISPR guide targeting it, thus I used the “C” guide again. This is why, in the experiment showed in figure 6.1, the row of strains with ΔPBP1B appear to grow at the same rate as the wild-type.

As a result, for a long time, changes in growth rate that were caused by the BSE were mistakenly attributed to changes in PBP1AB concentration. Only when Lun Cui’s CRISPR screen [79] allowed to characterize better the bad seed effect, I could realise that this was an artifact, and thus a major dead-end.

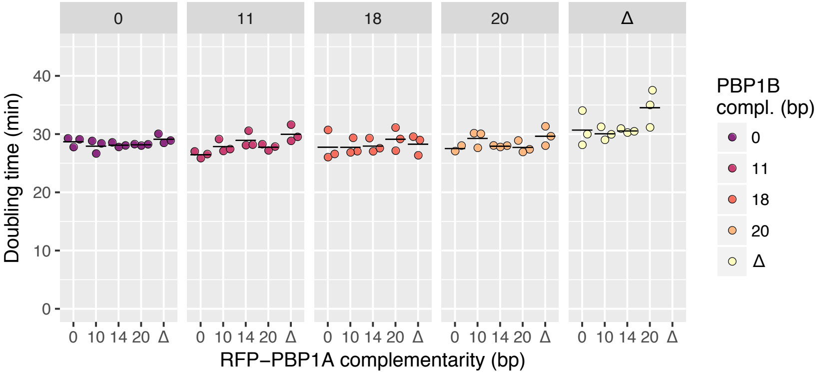

Figure 6.2: **Expressing less dCas9 alleviates the bad seed artifacts.** As AV44 expresses lower amounts of dCas9 than AV34, the bad seed effect of the “C” guide (0 bp) disappears. Each point is one biological replicate. Measured in LB at 30°C.

Building on the mechanistic model presented in chapter 3, we could find a way to alleviate the BSE. While the exact cause of the BSE was (and still is) unknown, the fact that only the first 5 bp of the guide are sufficient to produce an effect suggested that the BSE would behave like a highly-mismatched off-target. A prediction of our model is that, for highly mismatched sequences, the concentration of complex that is necessary to saturate the target becomes higher. Thus, by decreasing dCas9’s concentration, we could find a regime where the well-matched targets would be saturated, but the weak targets would be in the concentration-dependent regime and have attenuated effects. Accordingly, we found a range of expression levels for dCas9 where on-target repression is still efficient, but where the BSE is minimal. Using this new expression system, the mild BSE that we observed for the "C" guide completely vanished, allowing us to pursue the experiments on PBP1AB (figure 6.2).

In the bad seed study, I performed the fluorescence measurements, designed the strains and plasmids used for flow cytometry and constructed most of them.

The next pages are published as:

> Lun Cui, **Antoine Vigouroux**, François Rousset, Hugo Varet, Varun Khanna & David Bikard, A CRISPRi screen in E. coli reveals sequence-specific toxicity of dCas9. *Nature Communications*, 9(1):1912, May 2018, ISSN 2041-1723.
> doi: 10.1038/s41467-018-04209-5.

nature COMMUNICATIONS

ARTICLE

DOI: 10.1038/s41467-018-04209-5 OPEN

A CRISPRi screen in *E. coli* reveals sequence-specific toxicity of dCas9

Lun Cui[1], Antoine Vigouroux[1], François Rousset[1,2], Hugo Varet[3], Varun Khanna[3] & David Bikard[1]

High-throughput CRISPR-Cas9 screens have recently emerged as powerful tools to decipher gene functions and genetic interactions. Here we use a genome-wide library of guide RNAs to direct the catalytically dead Cas9 (dCas9) to block gene transcription in *Escherichia coli*. Using a machine-learning approach, we reveal that guide RNAs sharing specific 5-nucleotide seed sequences can produce strong fitness defects or even kill *E. coli* regardless of the other 15 nucleotides of guide sequence. This effect occurs at high dCas9 concentrations and can be alleviated by tuning the expression of dCas9 while maintaining strong on-target repression. Our results also highlight the fact that off-targets with as little as nine nucleotides of homology to the guide RNA can strongly block gene expression. Altogether this study provides important design rules to safely use dCas9 in *E. coli*.

---

[1] Synthetic Biology Group, Department of Microbiology, Institut Pasteur, Paris 75015, France. [2] Sorbonne Université, Collège Doctoral, Paris F-75005, France. [3] Hub Bioinformatique et Biostatistique, Institut Pasteur - C3BI, USR 3756 IP CNRS, Paris 75015, France. Correspondence and requests for materials should be addressed to D.B. (email: david.bikard@pasteur.fr)

Over the past few years, tools derived from the bacterial immune system known as Clustered Regularly Interspaced Short Palindromic Repeats (CRISPR) and the associated *cas* genes have led to many breakthroughs in genome editing and the control of gene expression[1]. In particular the Cas9 protein has proven to be a very versatile RNA-guided nuclease[2]. Target search goes as follows: Cas9 first scans DNA for the presence of the protospacer adjacent motif (PAM), a small sequence pattern of 2–8 nucleotides (nt)[3,4]. It then initiates the formation of an R-loop by pairing the guide RNA to the target starting from the PAM-proximal region, also known as the seed sequence[5]. The catalytic dead variant of the RNA-guided Cas9 nuclease, known as dCas9, binds to target positions without cleaving DNA[6]. In bacteria, directing dCas9 to bind a promoter region blocks the initiation of transcription, while binding the non-template strand downstream of a promoter efficiently stops elongation of transcription[6,7]. This provides a convenient method to silence genes that has already been used to investigate the role of essential genes in *Bacillus subtilis* and *Streptococcus pneumoniae* via high-throughput screens[8,9].

The action of Cas9 at off-target positions is a major concern for genome-editing applications[10–12], as it could lead to undesired mutations. While extensive binding beyond the seed sequence is required for a conformational shift in Cas9 to occur leading to DNA cleavage[13,14], chromatin immunoprecipitation sequencing experiments have revealed that Cas9 can bind to target positions with as little as 5 nt of homology between the seed region of the guide RNA and the target[15,16], possibly binding hundreds of positions in genomes. These results are also consistent with in vitro assays showing that dCas9 binding to its target remains unaffected by up to 12 mismatches in the PAM-distal region[17], as well as evidence that DNA binding guided by as little as 10 bases can be sufficient for dCas9 to have an effect on transcription in *Escherichia coli*[7]. These results are, however, in sharp contrast to what was reported in a study of dCas9-mediated repression or activation in human cells, where activity was highly sensitive to mismatches[18]. While substantial work has already been conducted to characterize the off-target activity of Cas9 in eukaryotes for genome-editing applications, comparatively little has been done for dCas9 in general and in bacteria in particular.

In this study, we performed a genome-wide pooled dCas9 knockdown screen in *E. coli* with the initial purpose of uncovering the properties and design rules of such screens. This screen confirmed previously reported properties of dCas9 repression in bacteria but revealed the presence of many guides producing unexpectedly strong fitness defects. A combination of machine learning and experimental approaches enabled us to attribute the effect of these guides to two main causes: (i) off-target binding positions that can block the expression of essential or fitness genes with as little as 9 nt of identity in the seed sequence, and (ii) an unexplained sequence-specific toxicity effect that is determined by the 5 PAM-proximal bases and that we refer to as the "bad-seed" effect.

Results

Effect of dCas9-binding position and orientation. We designed a library of ~92,000 unique guide RNAs targeting random positions along the genome of *E. coli* MG1655, with the simple requirement of a "NGG" PAM. The library contains an average of 19 targets per gene. A pool of guide RNAs obtained through on-chip oligo synthesis was cloned under the control of a constitutive promoter on plasmid psgRNA and electroporated in strain LC-E18 carrying the dCas9 gene under the control of a Ptet promoter in the chromosome (Supplementary Fig. 1). The pooled library of cells was then grown in rich medium over 17 generations with anhydrotetracycline (aTc). The effect of each guide on the cell fitness can be measured as the fold change in abundance (log2FC) of the guide RNA in the library during the course of the experiment, as measured through deep sequencing of the library.

In order to investigate the properties of dCas9 repression in *E. coli*, we can analyze the effect of guides targeting essential genes. We expect guides that efficiently block the expression of these genes to be depleted from the library. Previous reports suggested that dCas9 efficiently blocks transcription elongation only when binding the coding strand (non-template strand)[6,7]. As expected guide RNAs targeting essential genes have on average a strong fitness effect when they bind to the coding strand and no fitness effect when they bind to the template strand (Fig. 1a). On the other hand, dCas9 binding in both orientations was reported to efficiently block the initiation of transcription. We analyzed the effect of guides binding the promoter region of a subset of 64 essential genes whose promoter is well defined (Supplementary Data 1). Our results also corroborate these findings (Fig. 1b).

Since dCas9 blocks transcription, we expect that targeting a gene in an operon will also silence all the downstream genes. Guides targeting non-essential genes upstream of essential genes in operons indeed showed a strong fitness defect (see the examples of *cydDC* and *ycaR-kdsB* operons in Fig. 1c). A reverse polar effect was reported in *B. subtilis* where targeting downstream of a gene was seen to block the expression of the upstream gene likely through destabilization of the interrupted transcript[8]. In our screen, we can find many examples where targeting a non-essential gene downstream of an essential gene does not have an impact on the cell fitness (see the examples of *rpoZ-spoT-trmH-recG* and *psd-mscM* operons in Fig. 1d). Opposite examples where targeting the downstream non-essential gene does have an effect can also be found, but in these cases the non-essential gene is typically known to be required for normal growth or is itself followed by another essential gene. These observations suggest that translation can still efficiently occur from mRNAs interrupted by dCas9 in *E. coli*. We did nonetheless observe that guides targeting within ~100 nt after the stop codon of an essential gene sometimes produced a fitness defect. This can, for instance, be seen for a guide in Fig. 1c targeting just after *kdsB*. To study this in a more systematic way, we compiled a list of essential or fitness genes that are not followed by another essential or fitness gene (Supplementary Data 2). Guides targeting within 100 nt of the end of these genes on the coding strand indeed produce a weak but significant fitness defect (Fig. 1e, single sample *t*-test comparison to the mean log2FC of guides targeting the template strand of genes, p-value < 10^{-4}). On the other hand, guides targeting 100–200 nt after the end of these genes did not show a significant effect. A reverse polar effect of dCas9 on the expression of upstream genes thus does seem to exist in *E. coli*, but it is likely short range and weak.

Previous reports suggested that dCas9-mediated repression is negatively correlated with the distance from the beginning of the gene[6]. The same list of genes was used to look at the effect of the relative distance along the gene (Fig. 1f). No effect could be seen: dCas9 efficiency does not seem to correlate with the position inside the gene.

Guides producing unexpected fitness defects. Surprisingly, we observed a high variability of fitness effects between guide RNAs targeting nearby positions in the same orientation (Fig. 2a). These effects are reproducible between three independent experiments, suggesting that they are not the product of experimental noise but a real biological effect. In particular guides, binding to the template strand of non-essential genes are not expected to be

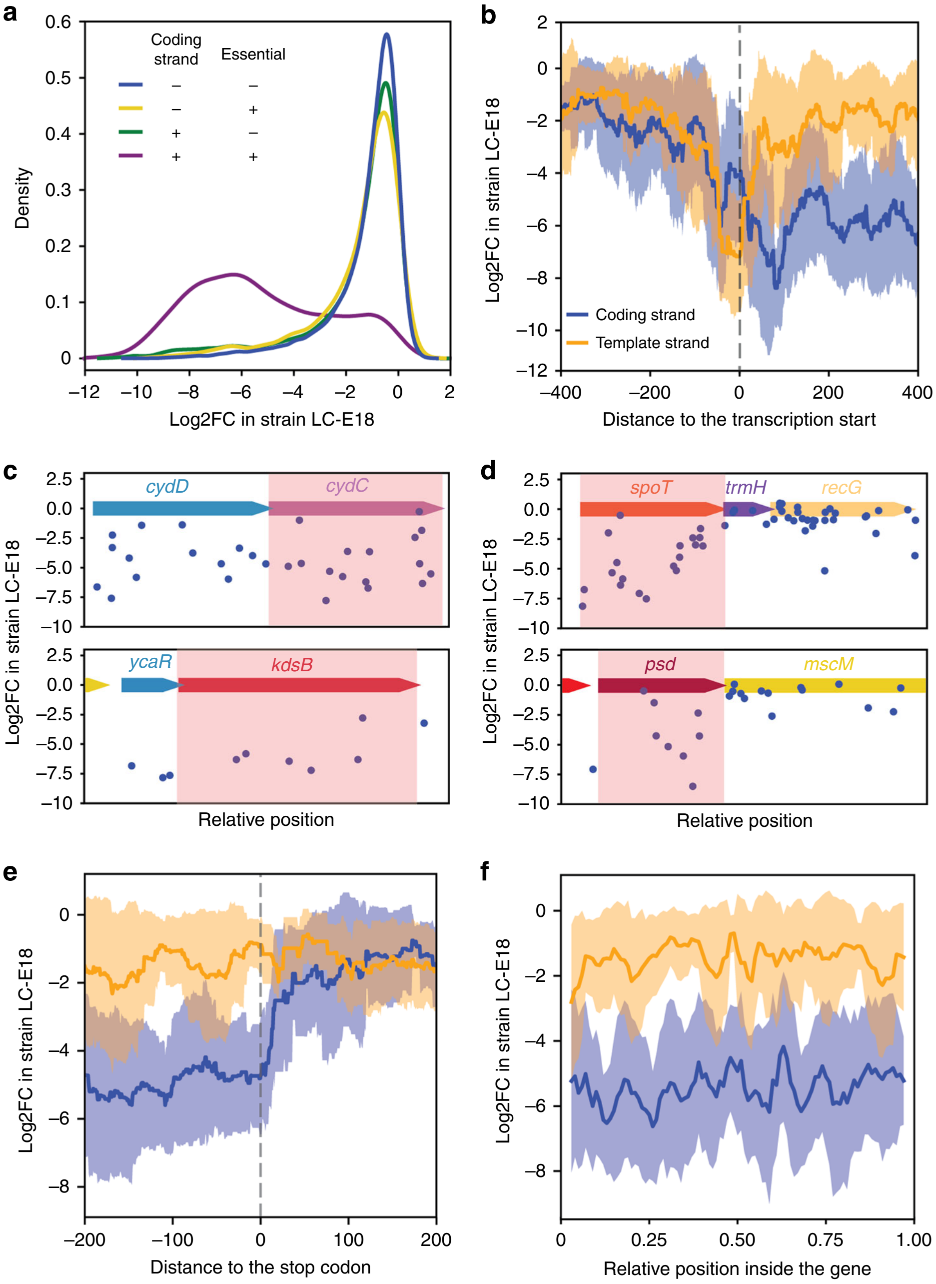

Fig. 1 Effect of dCas9 binding position and orientation. **a** Distribution of the fitness effect of guide RNAs in our library depending on target gene essentiality and target strand. **b** Rolling average of the fitness effect produced by guides targeting the promoter of essential genes in both orientations (rolling window size of 50 bp). **c** Examples of polar effect seen in the *cydDC* and *ycaR-kdsB* operons. Gene *cydC* and *kdsB* highlighted in red are essential but not gene *cydD* and *ycaR*. Guides binding to the coding strand are shown as blue dots. **d** Example of operons containing an essential gene followed by a non-essential gene. Targeting the downstream non-essential gene usually does not produce a fitness defect. **e** Rolling average of the fitness effect produced by guides targeting the end of essential genes (rolling window size of 50 bp). **f** Rolling average of the fitness effect produced by guides along the length of essential genes. Gene start is 0 and gene end is 1 (rolling window size is 5% of the gene length). In all rolling average plots, the shaded area represents the standard deviation

depleted from the library, but in fact 7% of these guides (2499/36,111) produce a strong fitness defect ($\log2FC < -3.5$, see Methods), accounting for 34% of all guides producing a strong fitness defect (Supplementary Table 1).

We arbitrarily decided to further investigate two such guides targeting *lpoB* (T-lpoB) and *hisI* (T-hisI). As a control, for each gene we also analyzed the effect of a nearby guide RNA targeting the coding strand (C-lpoB, C-hisI). Cells carrying T-lpoB or T-hisI only show a small reduction of the target gene transcription but show a markedly reduced plating efficiency when dCas9 is induced, consistently with the screen results (Fig. 2b, c). On the contrary, the C-lpoB and C-hisI guides strongly block the transcription of their target gene but show no defect in plating efficiency. Since a moderate repression of a non-essential gene is very unlikely to cause the death of *E. coli*, we hypothesized that this phenotype results from off-target activity. When looking for putative off-target positions for the T-hisI sgRNA, we identified an 11 base pair (bp) perfect match between the seed region of the guide RNA and a putative off-target in the promoter of the *dnaK-dnaJ* operon. We could measure that the

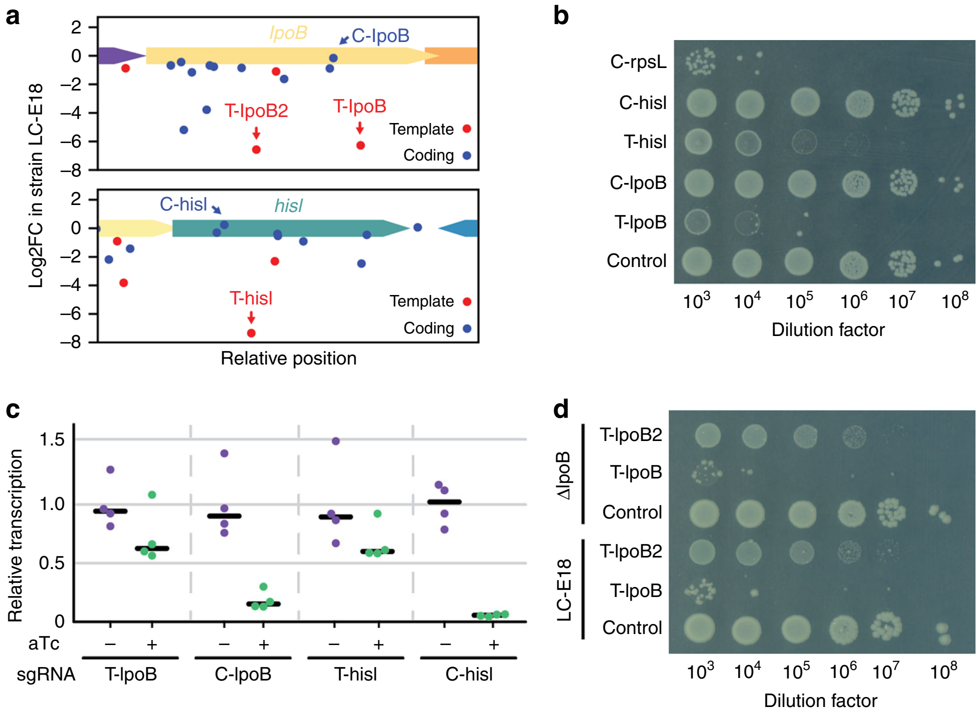

Fig. 2 Analysis of guides producing unexpected fitness defects. **a** Fitness effect of guides targeting the non-essential *lpoB* and *hisI* gene. Guides T-lpoB, T-lpoB2, C-lpoB, T-hisI, and C-hisI are highlighted. **b** The highlighted guides were cloned in plasmid psgRNA and introduced in strain LC-E18 carrying dCas9 under the control of a Ptet promoter in the chromosome. Cells were grown overnight and plated on LB agar with 1 nM of aTc. Representative figure from $p = 4$ independent experiments. **c** Expression levels of *lpoB* and *hisI* when repressed by the T-lpoB, C-lpoB, T-hisI, and C-hisI guide RNAs, as measured by RT-qPCR. Points show biological replicates ($n = 4$), the black bar is the median. **d** Effect of the T-lpoB, T-lpoB2, and control guides on the plating efficiency of LC-E18 and LC-E18ΔlpoB. Cells were grown overnight and plated on LB agar with 1 nM of aTc. Representative figure from $n = 4$ independent experiments

T-hisI guide RNA produces a three-fold repression of the *dnaK-dnaJ* operon. While *dnaK* or *dnaJ* are not essential genes, our screen results show that guides blocking the expression of this operon consistently produce a strong fitness defect (Supplementary Fig. 2). This off-target position thus likely explains the fitness defect produced by T-hisI. To investigate the preponderance of guides with such off-targets, we looked for off-targets that displayed a perfect identity of 9 nt or more between the seed sequence and regions where a strong fitness defect was consistently observed (i.e. essential or fitness genes). We found such off-targets for 24% (600/2499) of the guides that produced an unexpected fitness defect. As a control, we also looked at the proportion of guides with such off-targets among guides that target the same genes in the same orientation but produce no fitness defects. This occurs for 10.7% (3609/33,612) of these guides, giving a measure of the false-positive discovery rate. Guides that produce unexpected fitness defects are thus significantly more likely to have an off-target blocking the expression of a fitness or essential gene (Fisher exact test p-value < 0.001). This enables to provide a conservative estimate that the fitness defect produced by 13% of these guides is due to their off-target activity.

When doing this analysis, it became evident that no obvious off-target positions could be identified for a large majority of guide RNAs producing an unexpectedly strong fitness defect. This is in particular the case of the T-lpoB guide as well as another guide targeting *lpoB* (T-lpoB2), which also produces an unexpected fitness defect. As a definitive proof that the phenotype produced by these two guide RNAs was not due to on-target activity, we deleted the *lpoB* gene in strain LC-E18. This deletion itself produced no growth defect, but the T-lpoB and T-lpoB2 guides still generated a strong fitness defect (Fig. 2d).

Machine-learning approach reveals toxic seed sequences. We then turned to a machine-learning approach to understand whether some sequence features could explain the unexpected fitness defect produced by these guides (Supplementary Fig. 3). We first used a regression tree to predict log2FC using target orientation and position as unique input features in order to locate all the regions where guides consistently produce a fitness defect, i.e., essential and fitness genes. We then analyzed guides targeting outside of these “important” regions. These guides are not expected to produce a fitness defect but ~8% of them show a log2FC < -3.5. We reasoned that some sequence patterns might be predictive of the toxicity of these guides. We used a locally connected neural network to predict the log2FC of guide RNAs using the one-hot-encoded sequence as the only input feature. A first model was trained using an arbitrary 60 nt region around the target and achieved a Pearson correlation coefficient of 0.54 (Root Mean Square Error (RMSE): 0.82) between the measured and predicted fitness on a held-out test set (Fig. 3a). The model thus seems to learn some features explaining the toxicity observed for guide RNAs such as T-lpoB.

To understand what information the model used to make predictions, we performed in silico experiments. We generated a set of 1000 random sequences and measured the effect on the model prediction of mutating each position along the sequence. This revealed that the model uses the whole 20 nt of the guide sequence, and in particular the 5 PAM-proximal bases, but not the surrounding region to make its predictions (Fig. 3b). We thus trained a second model using only the 20 nt of the target sequence. This model performed slightly better (Pearson-r: 0.56, RMSE: 0.81) and was used in the rest of the analysis.

When doing this in silico mutational analysis, one can also see that the effect of individual mutations depends a lot on the

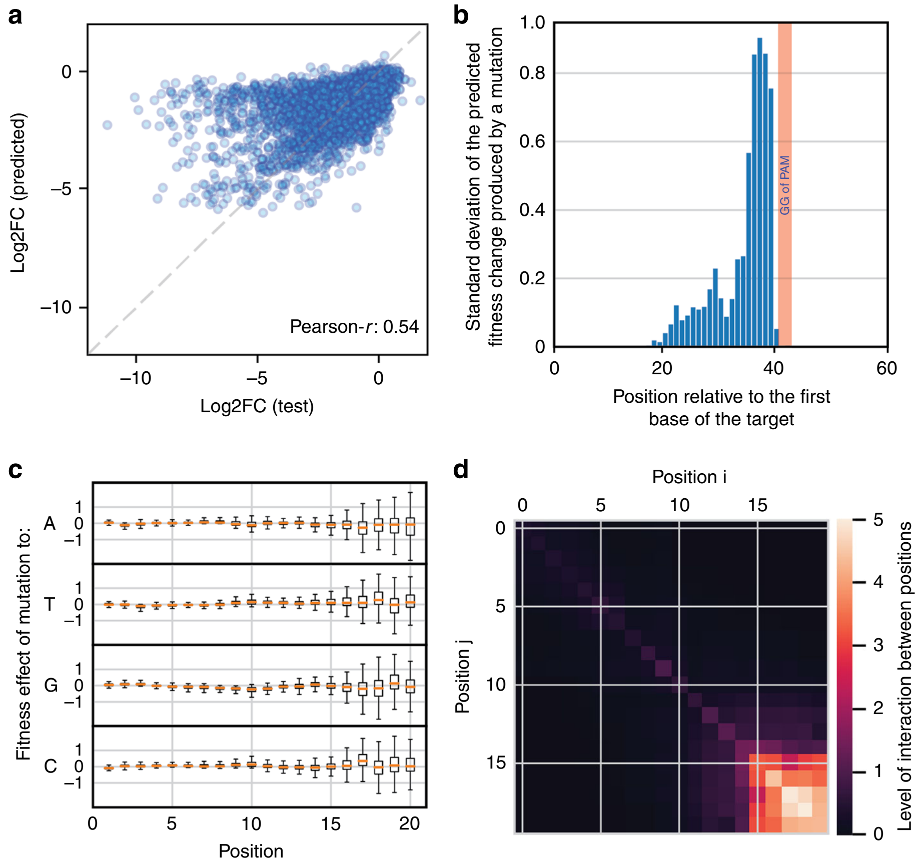

Fig. 3 A machine-learning approach reveals a toxicity effect determined by the seed sequence. **a** A locally connected neural network was trained to predict the fitness effect of guide RNAs that target neutral regions, using the one-hot-encoded 60 nt sequence window around the target. Comparison of predicted and actual log2FC values on a held-out test set. **b** To identify the positions used by the model to make its predictions, we generated a set of 1000 random sequences, mutated each position in silico, and computed the effect of each mutation on the model prediction. The standard deviation of the effect of mutations at each position is plotted. The red bar indicates the position of the GG bases of the PAM. **c** The model was trained again using only the 20 nt of the guide sequence. The box plots show the distribution of the effects that mutations to all possible bases have on the model prediction. One can see that the effect of specific mutations can be either positive or negative, revealing a strong dependence on the rest of the sequence. **d** To measure the level of interaction between positions, we generated all possible pairs of mutations for each sequence in a set of 100 random sequences and compared the effect of individual mutations to that of pairs of mutations. Positions are interacting if the effect of a double mutation (Eij) is different from the sum of the effect of the single mutations (Ei + Ej). The heat map shows the average Euclidean distance between Eij and Ei + Ej for all pairs of positions (see Supplementary Fig. 5). Note the strong network of interacting bases in the 5 nt of the seed sequence

sequence context (Fig. 3c and Supplementary Fig. 4). For instance, a mutation at position 18 to a G can have a positive or a negative impact on the fitness depending on the rest of the sequence. This suggests important interactions between bases. To analyze these interactions, we mutated in silico every pair of bases and compared the effect of individual mutations to that of pairs of mutations. An interaction is observed if the effect of a pair of mutation is not simply the sum of the effects of individual mutations (Supplementary Fig. 5). The analysis revealed a strong network of interaction among the last 5 bases of the target/guide (Fig. 3d and Supplementary Fig. 6).

We observed that the distributions of fitness effects produced by guides with any given five base seed sequence are remarkably narrow. For instance, all guides with an ACCCA seed sequence produce a strong fitness defect regardless of their target position, while all guides with an ATACT seed sequence produce an intermediate fitness defect (Fig. 4a). The T-lpoB and T-lpoB2 guides have an AGTTT and TGGAA seed sequence, which show an average log2FC of −3.2 and −5.1, respectively. All in all, 130 out of the 1024 possible combinations of 5 nucleotides show a significantly reduced fitness compared to the mean (single sample *t*-test, $p < 0.01$ after Bonferroni correction). We then refer to the fitness defect produced by these seed sequences as the "bad-seed" effect. The average fitness effect and standard deviation for all 5 nt seed sequences is given in Supplementary Data 3.

We experimentally validated the effect of three additional guides targeting the template strand of non-essential genes with a TGGAA or ACCCA seed sequence (T-garD, T-yhhX, T-ydeO). We also designed four guides with either the ACCCA or TGGAA seed sequences but where the 15 other nucleotides of the guide were randomized (R1-ACCCA, R2-ACCCA, R1-TGGAA, R2-TGGAA). Guide RNAs were cloned on the psgRNA plasmid, transformed in strain LC-E18, and plated on petri dishes containing aTc. All these guides produced a strong fitness defect, with the ACCCA seed sequence leading to a ~1000× reduction in platting efficiency and the TGGAA seed sequence leading to a small colony phenotype, while the control sgRNA with a TCTCG seed showed no visible phenotype (Fig. 4b). These results are consistent with an action guided by the seed sequence itself regardless of the rest of the guide sequence. As a matter of fact, guides truncated down to 10 bp are still able to kill *E. coli* (Supplementary Fig. 7).

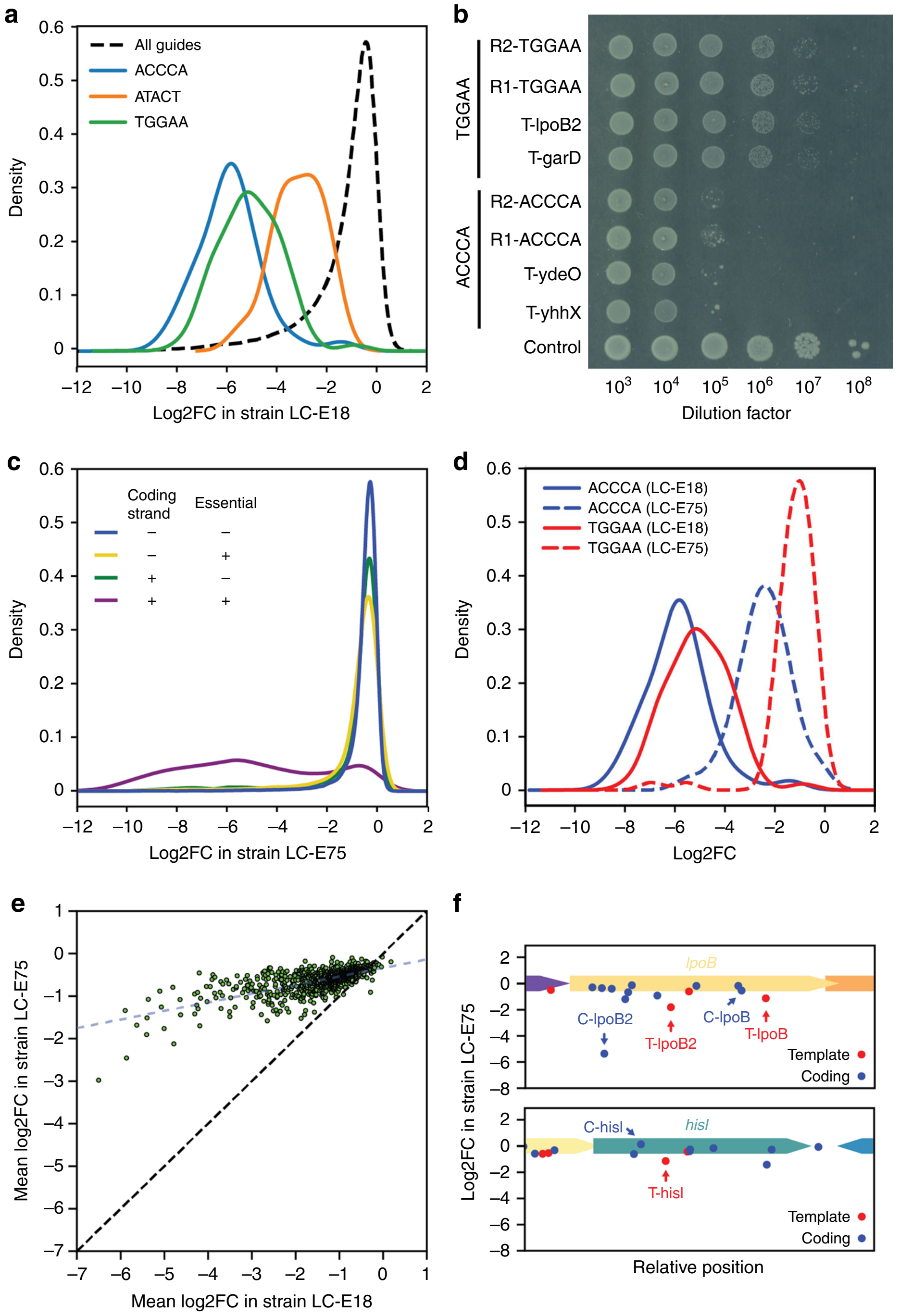

Fig. 4 Specific 5 nt seed sequences produce strong fitness defects that can be alleviated by reducing dCas9 concentration. **a** Distribution of the fitness effect of guide RNAs that share specific 5 nt seed sequences as compared with the distribution of all the guides in the library targeting the template strand of genes. **b** Plasmid psgRNA was programmed with various guide RNAs sharing either the TGGAA seed sequence or the ACCCA seed sequence and introduced in strain LC-E18. Guides named R1 and R2 have sequences that do not match any position in the chromosome of *E. coli*. Cells were grown overnight, serially diluted, and plated on LB agar with 1 nM of aTc. Representative figure from four independent experiments. **c** Distribution of the fitness effect of guide RNAs in our library depending on target gene essentiality and target strand in strain LC-E75, which expresses dCas9 at a lower concentration than strain LC-E18. **d** Distribution of the fitness effect of guide RNAs sharing the ACCCA or TGGAA seed sequences in strain LC-E18 and LC-E75. **e** Average fitness effect of guides sharing specific 5 bp seed sequences in strain LC-E18 (*x* axis) and LC-E75 (*y* axis). The red line shows a linear regression (slope = 0.2, $R^2 = 0.47$). **f** Fitness effect of guides targeting gene *lpoB* and gene *hisI* in strain LC-E75. The strong fitness defect produced by C-lpoB2 can be explained by the presence of an off-target position in the *def* essential gene

The bad-seed effect is alleviated at low dCas9 concentrations. To better understand the mechanism of action of these "bad-seed" sequences, we selected mutants of the LC-E18 strain that could survive killing by the T-yhhX guide (ACCCA seed sequence) while maintaining an efficient repression of a target *rpsL* gene. Six such mutants were obtained, and their genome sequenced. Unexpectedly, they all displayed mutations either in the promoter of dCas9 or frameshift mutations in dCas9 itself (Supplementary Table 2). Note that others have observed the same type of mutations in dCas9, suggesting that they are relatively frequent[19]. The fact that these frameshift mutants still showed efficient *rpsL* repression indicates that they still express dCas9, likely through ribosome slippage, but do so at lower levels. This led us to hypothesize that the bad-seed effect is concentration dependent. A low dCas9 concentration is enough to block the expression of on-target positions, while a high dCas9 concentration is required to observe the bad-seed effect.

We thus designed a novel expression cassette that would reduce the expression level of dCas9 by introducing mutations in the RBS[20] (Supplementary Fig. 8a, b). We screened for the right level of expression by selecting clones that would result in cell death when the essential *rpsL* gene was targeted but that showed normal colony size in the presence of the R1-ACCCA or T-yhhC-ACCCA guide RNAs. The expression level of dCas9 was measured in several strains through western blot and correlated with the strength of the bad-seed effect (Supplementary Fig. 8c, d). The expression cassette selected in this manner displayed an expression level 2.6-time lower than the original strain LC-E18 and was integrated in strain LC-E75. It could repress a target *mCherry* reporter gene 91×, compared to the 167× repression obtained with the dCas9 expression cassette present in strain LC-E18 (Supplementary Fig. 9).

Strain LC-E75 carrying this fine-tuned Ptet-dCas9 cassette was then used to perform a genome-wide dCas9 knockdown screen following the same protocol as the screen previously performed with strain LC-E18. As expected, many guides that produced a strong fitness defect in strain LC-E18 had a weaker or no effect in strain LC-E75, but targets in the coding strand of essential genes still produced a strong fitness defect (Fig. 4c and Supplementary Fig. 10). When plotting the fitness effect of guides sharing a given seed sequence, one can see that the "bad-seed" effect is largely alleviated in strain LC-E75 but not abolished (Fig. 4d, e). Only 14 seed sequences still produced a moderate or weak significant effect (Supplementary Data 3). This new dCas9 expression cassette also makes the general quality of the screen better as the effect of targets within the same gene is now much more consistent (compare Fig. 4f and Fig. 2a; Supplementary Fig. 11). The number of guides producing a strong fitness defect (log2FC < -3.5) while targeting the template strand of non-essential genes dropped from 2499 to 532, due in the most part to the alleviation of the bad-seed effect.

The mechanism of the bad-seed effect described above remains to be elucidated. The binding of dCas9 with only 5 nt of identity between the seed and the target is likely too weak and transient to have a substantial effect on target gene expression. We verified this by targeting the promoter or open-reading frame of a mCherry reporter gene with only 5 nt of identity in the PAM-proximal region (Supplementary Fig. 12). At best, a 14% repression could be observed. Since blocking the expression of any single gene by only 14% is unlikely to stop the growth of *E. coli*, the bad-seed effect is likely due to dCas9 binding at many positions simultaneously or to an entirely different phenomenon. Note that the number of off-targets with a perfect identity of 5 nt in the PAM-proximal region and the fitness defect produced by bad-seed sequences are not correlated (Supplementary Fig. 13).

A 9 nt match to the seed sequence can produce off-target effects. The bad-seed effect is thus a different phenomenon than the off-target effect described above for guides like T-hisI, which block the expression of essential genes. We made the estimate that ~13% of the guides producing an unexpected fitness defects

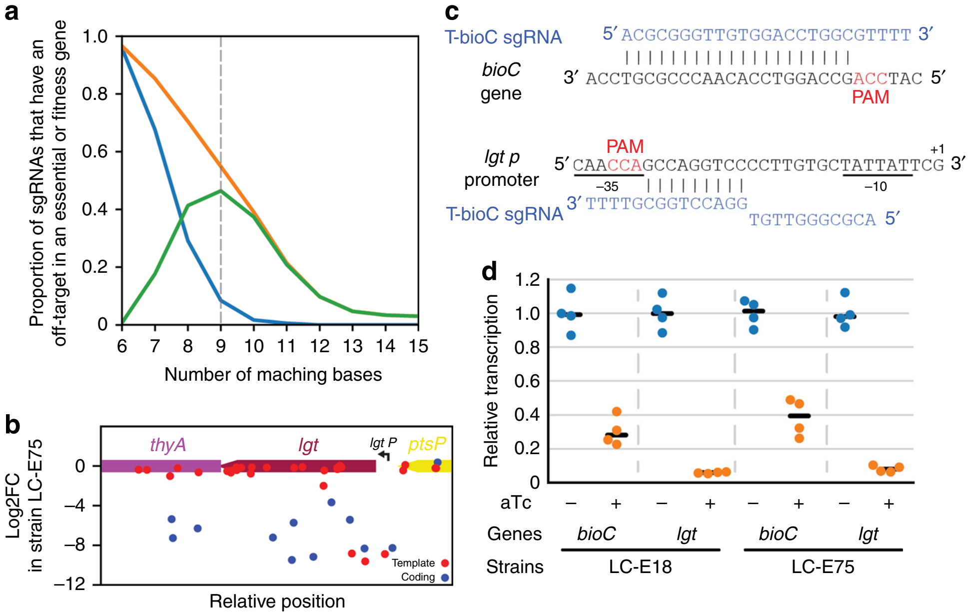

Fig. 5 Off-targets with only 9 nt of identity to the seed sequence can produce strong fitness defects. **a** We plot here the proportion of guide RNAs that have an off-target position in a region where guides consistently produce a strong fitness defect. This proportion is shown for guides that target the template strand of non-essential genes but produce an unexpected fitness defect (orange), as well as for guides in the same genes and orientation but that do not produce a fitness defect (blue). This blue curve can be interpreted as the false-positive rate. The green curve is the difference between the green and blue curves. It can be interpreted as an estimate of the proportion of guides whose fitness defect is due to an off-target effect. The maximum is obtained for a perfect match of 9 nt in the seed sequence, which indicates that 9 nt of identity in the seed sequence is enough to produce a strong fitness defect, but mostly false-positive off-target positions are detected when going down to 8 nt of identity. **b** Fitness effect of guides targeting gene *lgt* in strain LC-E75. The strong fitness defect produced by the T-bioC guide can be explained by the presence of an off-target position in the promoter of essential gene *lgt*. **c** Off-target position of the T-bioC guide in the promoter of *lgt* essential gene. **d** Repression of *bioC and lgt* expression by the T-bioC guide in strains LC-E18 and LC-E75 as measured by RT-qPCR. Points show biological replicates ($n = 4$), the black bar shows the median

in strain LC-E18 have a likely off-target position to an essential or fitness gene, with 9 nt of identity or more to the seed sequence. In the screen performed in strain LC-E75, this number can now be estimated to be 45%. The same analysis was also performed while considering a minimum perfect match in the PAM-proximal region ranging from 6 to 15 bp (Fig. 5a and Supplementary Fig. 14). A seed size of length nine gave the largest difference between the positive detection rate (proportion of guides producing an unexpected fitness defect for which an off-target to an important region is detected) and false-positive detection rate (proportion of guides that do not produce an effect and for which an off-target to an important region is detected), suggesting that 9 nt of identity can be sufficient to block gene expression. We experimentally verified the fitness defect produced by one such guide, T-bioC, which has a candidate off-target position of 9 nt and a proper NGG PAM in the promoter of the essential gene *lgt* (Fig. 5b, c). This guide is indeed able to efficiently block the expression of *lgt* as measured by quantitative PCR (qPCR; Fig. 5d).

Note that, in strain LC-E75, the reduced dCas9 concentration not only alleviated the bad-seed effect but to a lesser extent also limited off-targeting. This can, for instance, be seen for the T-hisI target described above that showed a strong fitness defect in strain LC-E18 and no effect in the new screen (compare Fig. 2a and Fig. 4f). Conversely, the T-bioC off-target effect on *lgt* is still as strong in strain LC-E75 as in strain LC-E18 (Fig. 5d). Another example of a guide that still shows a strong off-target effect can be found at the beginning of the *lpoB* gene (C-lpoB2, Fig. 4f). This guide RNA has a perfect match of 14 bp between its seed sequence and a target on the coding strand of the essential *def* gene.

Discussion

We performed here an unbiased screen of dCas9 effect on the growth of *E. coli*. Our results shed light on important design rules to consider when performing CRISPRi assays:

(i) Targeting promoter regions in both orientations leads to strong silencing, but targeting the coding strand is required to block transcription elongation as described previously[6,7].
(ii) Guides targeting genes in operons block the expression of all the downstream genes, while guides targeting downstream genes do not substantially affect the expression of the upstream genes.
(iii) Guides that have off-targets in the genome with 9 nt of perfect identity or more to the seed sequence should be avoided. Unfortunately, such off-target positions are too frequent to be avoided easily. Guides that target the chromosome of *E. coli* MG1655 have a median of 4 off-targets that carry a perfect match of 9 nt or more with the seed sequence and a NGG PAM motif (see distribution in Supplementary Fig. 15). One can limit the chances that these off-targets will influence the phenotype under study by making sure that they fall in neutral regions, away from regulatory elements, and on the template strand of genes rather than on their coding strand, but researchers should be aware that this could be a confounding factor in their experiments.
(iv) dCas9 concentration needs to be tuned to avoid the “bad-seed” effect while maintaining good on-target repression. Even under such conditions, it is preferable to avoid using guides that carry the strongest “bad seeds” identified here.
(v) For the reasons described above, the effects of genes on a given phenotype should ideally not be inferred from the effect of a single guide but rather from the statistical analyses of several guides.

All in all, the results of the new screen performed with a reduced dCas9 concentration are much more consistent than the initial screen, but there remains a few hundred guide RNAs out of the 84,215 whose fitness effect could not be easily assigned to the bad-seed effect, a polar effect, or an off-target effect. Understanding the effect of these guides on fitness will require further analysis and might reveal interesting biology.

The dataset generated will also likely prove useful in future studies to decipher the determinants of dCas9 repression strength. Indeed, we observed some variability among guides targeting within the same essential gene in the same orientation, suggesting that some guides block expression better than others.

Perhaps the most puzzling question raised by this work is that of the mechanism responsible for the “bad-seed” effect. Others previously reported a dCas9 toxicity at high concentrations, which is likely the same as what we report here[21]. On average, we can find 280 positions in the chromosome of *E. coli* that can be bound by any 5 nt seed sequence with the requirement of a NGG PAM. It is unclear whether weak dCas9 binding at one, a few, or hundreds of positions simultaneously is required for this effect. The fact that it is observed at high dCas9 concentrations and that we were not able to identify mutants that can rescue cells by other means than reducing dCas9 expression suggests that binding to several positions is required. Our work also does not allow excluding the hypothesis that binding to other substrates than DNA might be responsible for the effect. While we further investigate this phenomenon, the results presented here are directly relevant to anyone using dCas9 in bacteria.

Methods

Bacterial strains and media. *E. coli* strain MG1655 was obtained from the laboratory of Didier Mazel, Institut Pasteur. Cells were grown in Luria-Bertani (LB) broth. LB agar 1.5% was used as solid medium. Different antibiotics (20 µg/ml chloramphenicol, 100 µg/ml carbenicillin, 50 µg/ml kanamycin) were used as needed and lower concentrations were used to select for the integration of vectors in the chromosome (10 µg/ml chloramphenicol or 20 µg/ml kanamycin). *E. coli* strain DH5α (New England Biolabs) or MG1655 were used as transformation recipients for plasmid construction.

Plasmid cloning and strain construction. Linear vectors and inserts were generated by digestion with restriction enzymes or PCR and assembled through Gibson assembly[22] as detailed in Supplementary Table 3. Primers and plasmids are listed in Supplementary Tables 4, 5. Guide RNAs were cloned into plasmid psgRNA or psgRNAc by golden gate assembly[23]. The sequence of these plasmids is provided as supplementary Data 4. A list of all guides and corresponding primers is given in Supplementary Table 6.

The pOSIP plasmids[24] were used to integrate genetic elements at phage-attachment sites in the chromosome of *E. coli* K12 (MG1655). All the integrations were verified by PCR, and the backbones were flipped out using the pE-FLP plasmid[24]. Supplementary Table 7 summarizes the construction of strains LCE-18, LCE-75, and AV04.

Deletion of gene *lpoB* was performed using the lambda red recombineering strategy[25]. A linear DNA fragment was generated by PCR using pKD3 as a template with primers LC961 and LC962, followed by electroporation into MG1655 carrying plasmid pKOBEG-A[26]. Colonies resistant to chloramphenicol were selected and the resistance gene was removed using plasmid pE-FLP.

Library construction. The library was designed by randomly choosing targets with a proper NGG PAM around the genome of *E. coli* strain MG1655 (NC_000913.2). A pool of 92,919 oligonucleotides (synthesized by CustomArray) was amplified with primers LC296 and LC297 using the Phusion DNA polymerase (Thermo Scientific) over 18 cycles. The psgRNA backbone was PCR amplified using primers LC293 and LC294. Both the vector backbone and library insert were gel purified, followed by Gibson assembly. To avoid the introduction of bottlenecks in the library, a total of 19 transformation assays were performed each using 0.2 µl of Gibson assembly product and 20 µl of MG1655 electro-competent cells and plated on 12 × 12 cm^2 petri dishes resulting in a total of about 10^7 colonies. Colonies were allowed to grow for only 4–5 h at 37 °C before pooling all the cells together. The plasmid library was then extracted from 5 ml of pooled colonies using a miniprep kit (Macherey-Nagel). The resulting plasmid library DNA was further transferred to strains LC-E18 and LC-E75 by electroporation.

dCas9 knockdown assay. Strain LC-E18 or LC-E75 containing the psgRNA library were grown from 1 ml aliquots frozen at −80 °C into 1000 ml LB until OD600 of 0.2. The expression of dCas9 was then induced by addition of aTc to a final concentration of 1 nM. Cells were grown for 17 generations by diluting the culture 100-fold once it reached OD600 2.2–2.5. This step was repeated twice. The plasmid library was extracted from 50 ml of culture at the beginning of the experiment (OD600 ~0.2) and 5 ml of the culture at the end of the experiment (OD600 ~2.2–2.5). The experiment was performed in triplicates starting from independent aliquots of the library generated from independent electroporation assays.

Library sequencing. A customized Illumina sequencing method was designed to avoid problems arising from low library diversity when sequencing PCR products. Two nested PCR reactions were used to generate the sequencing library with primers described in Supplementary Table 8. The first PCR adds the first index. The second PCR adds the second index and flow cells' attachment sequences. Sequencing is then performed using primer LC609 as a custom read 1 primer. Custom index primers were also used: LC499 reads index 1 and LC610 reads index 2. Sequencing was performed on a NextSeq 500 benchtop sequencer. The first 2 cycles that read bases common to all clusters were set as dark cycles, followed by 20 cycles to read the guide RNA. Using this strategy, we obtained on average 7.5 million and 17 million reads per experimental condition for LC-E18 and LC-E75, respectively.

Fold-change computation. The fold change in abundance of each guide RNA was computed from read counts using DESeq2[27] using data from the three replicates and normalized to the control guide 5′-TGAGACCAGTCTAGGTCTCG-3′. Guides with a total number of reads across samples <20 were discarded from the analysis. A list of all targets with computed fold-change values is provided as Supplementary Data 5.

Machine learning. To model the fitness effect of guide RNAs, a regression tree was first fitted using only two features: the target orientation and position along the genome[28]. This allows the identification of all chromosomal regions that show a consistent fitness effect when targeted in a specific orientation (Supplementary Fig. 3). We were then interested in predicting the fitness effect of guide RNAs targeting regions where the regression tree predicts no substantial fitness defect (log2FC > −3.5).

The dataset was split into training, validation, and test sets. Several network architectures, including dense, sparse, and convolutional, were implemented using Keras and TensorFlow and hyperparameters were manually tuned on the validation set. The dataset used can be found in Supplementary Data 5 and the indices of the rows used for training, validation, and test sets can be found in Supplementary Data 6. The model used in this study consist in a sparsely connected network with 4 layers of size 40, 20, 10, and 5 where each neuron is only connected to the 5 proximal neurons in the previous layer. A tanh activation was used. The network was trained to minimize the mean square error of the log2FC prediction with L2 regularization using the Adam optimizer[29]. Training was interrupted when loss on the validation set ceased do decrease for more than two epochs. Note that we only performed a manual tuning of the architecture and hyperparameters of the model. Better models can likely be built, but this should not affect the conclusions of the study. The machine-learning approach performed here is summarized in Supplementary Figure 3, and the code is available as a jupyter notebook at the following address: https://gitlab.pasteur.fr/dbikard/badSeed_public.

Reverse transcription-qPCR. Overnight cultures were diluted 1:100 in 3 ml of LB, grown 1 h, and induced by addition of aTc. Cells were further grown 2 h followed by RNA extraction from 2 ml of culture using Trizol. All the RNA samples were treated with DNase (Roche) and reverse transcribed into cDNA using the Transcriptor First Strand cDNA Synthesis Kit (Roche). Dual-labeled probes (5'FAM, 3'BHQ1) were used to perform qPCR with the FastStart Essential DNA Probes master mix (Roche) in a LightCycle 96 (Roche). The 5'FAM is a reporter that is quenched by the 3'BHQ1 but released upon amplification of the target DNA. The FastStart Essential DNA Green Master Kit (Roche), which contains DNA Polymerase and double-stranded DNA-specific SYBR Green I dye, was used for the qPCR of bioC off-target effect. The fluorescence signal is directly proportional to the amount of target DNA. Primers and probes used are listed in Supplementary Table 9. Relative gene expression was computed using the ΔΔCq method[30].

dCas9 induction on agar plates. Strain LC-E18 or LC-E75 carrying specific psgRNA plasmids were grown overnight, followed by serial dilutions, and plating of 5 µl spots on LB agar plates with or without aTc (1 nM). Plates were incubated overnight and scanned using an Epson Perfection V550 Photo Color Scanner with a black background.

Selection of mutants surviving the bad-seed effect. An overnight culture of LC-E18 carrying plasmid psgRNAc::T-yhhX was plated on LB agar with 1 nM aTc and Kanamycin. After an overnight incubation at 37 °C, plates showed colonies of different sizes. Twenty-one big colonies were selected. The psgRNA plasmid carrying a guide RNA targeting the essential *rpsL* gene (C-rpsL) was then introduced into these mutants. Clones where dCas9 is still able to efficiently block the expression of *rpsL* are expected to die. We selected 9/21 positive clones that were killed in this assay. As a final confirmation that these clones suppressed the bad-seed effect, we introduced a psgRNA plasmid carrying the R1-ACCCA guide. In all, 6/9 clones tolerated the expression of this sgRNA. The genomes of these 6 clones were sequenced to identify mutations (Supplementary Table 2). Genomic DNA was fragmented using a Covaris E220 ultrasonicator and sequencing libraries were prepared with the NEXTflex PCR-free DNA-Seq Kit (Bioo Scientific Corporation). Sequencing was done on a HiSeq2500 with paired-end reads of 100 bases.

Fine-tuning of dCas9 expression level. A library of RBS sequences was introduced in front of dCas9 to obtain a library of strains producing varying levels of dCas9. Primer LC1088 includes ambiguous positions leading to 64 different variants and was used to amplify and clone dCas9 on plasmid pOSIP-CO-RBS-library-dCas9 (Supplementary Table 3). The plasmid library was integrated into the chromosome of strain MG1655 and individual colonies were screened as follows: the psgRNA:rpsL plasmid was introduced into the cells to identify variants where dCas9 is still expressed at sufficient levels to efficiently block the expression of a target gene. The psgRNA:R1-ACCCA and psgRNA:T-yhhX plasmids were introduced to identify clones that would not produce the bad-seed effect. These plasmids carry a lambda cos site, which facilitated the screen of a large number of clones by enabling their transfer in the recipient strains via transduction with phage lambda as previously described[31]. Finally, 4 candidate colonies were selected from a total of 96 screened colonies. The pOSIP backbone was removed using pE-FLP, and the selected clones were named LC-E69, LC-E70, LC-E71, and LC-E72. Strain LC-E75 was constructed by integrating plasmid pIT5-KL-mcherry into strain LC-E69.

Repression of mCherry by the fine-tuned dCas9 expression cassette. The day before the measurement, cells were grown in 1 ml LB supplemented with 1 nM of aTc and 50 µg/ml of kanamycin at 37 °C using a 96 deep-well plate table-top shaker (Eppendorf). The day of the measurement, cells were diluted 250 times in fresh medium with aTc and kanamycin and grown for 1 h 45 min at 37 °C to reach the exponential phase. Cells were then fixed with 4% formaldehyde and washed with phosphate-buffered saline. A strain without mCherry was used to measure the auto-fluorescence background. Fluorescence of single cells was measured using a Miltenyi MACSquant flux cytometer. Ten thousand cells were measured per replicate. The average fluorescence of each sample was calculated by taking the mean of the single-cell fluorescence values and subtracting the mean fluorescence of the background.

Western blot. Western blot analysis was carried out as previously described[32]. In brief, cells were harvest after 2 h of dCas9 induction in 2× Laemmli sample buffer (with 5% of 2-mercaptoethanol). Samples were run in NuPAGE® Novex® Bis-Tris gels in reducing condition. Proteins were transferred to polyvinylidene difluoride membranes at 15 volts overnight. Rabbit monoclonal antibodies to SpCas9 (ab189380, Abcam, diluted 10,000-fold) and rabbit polyclonal antibody to RecA (ab63797, Abcam, diluted 3,000-fold) were used. Goat anti-rabbit horseradish peroxidase (ab6721, Abcam) was used as secondary antibody to visualize the protein with chemiluminescence (ECL). A Syngene G:box machine was used to acquire the images, which were subsequently analyzed with imageJ. Supplementary Figure 16 shows the uncropped western blot pictures.

Code availability. The code used for the machine-learning approach is available as Jupyter notebooks at the following address: https://gitlab.pasteur.fr/dbikard/badSeed_public.

Data availability. The screen results are provided as Supplementary Data 4. Other relevant data supporting the findings of the study are available in this article and its Supplementary Information files or from the corresponding author upon request.

Received: 4 September 2017 Accepted: 13 April 2018

References

1. Jiang, W. & Marraffini, L. A. CRISPR-Cas: new tools for genetic manipulations from bacterial immunity systems. *Annu. Rev. Microbiol.* **69**, 209–228 (2015).
2. Jinek, M. et al. A programmable dual-RNA-guided DNA endonuclease in adaptive bacterial immunity. *Science* **337**, 816–821 (2012).
3. Sternberg, S. H., Redding, S., Jinek, M., Greene, E. C. & Doudna, J. A. DNA interrogation by the CRISPR RNA-guided endonuclease Cas9. *Nature* **507**, 62–67 (2014).
4. Mojica, F. J. M., Díez-Villaseñor, C., García-Martínez, J. & Almendros, C. Short motif sequences determine the targets of the prokaryotic CRISPR defence system. *Microbiology* **155**, 733–740 (2009).

5. Semenova, E. et al. Interference by clustered regularly interspaced short palindromic repeat (CRISPR) RNA is governed by a seed sequence. *Proc. Natl. Acad. Sci. USA* **108**, 10098–10103 (2011).
6. Qi, L. S. et al. Repurposing CRISPR as an RNA-guided platform for sequence-specific control of gene expression. *Cell* **152**, 1173–1183 (2013).
7. Bikard, D. et al. Programmable repression and activation of bacterial gene expression using an engineered CRISPR-Cas system. *Nucleic Acids Res.* **41**, 7429–7437 (2013).
8. Peters, J. M. et al. A comprehensive, CRISPR-based functional analysis of essential genes in bacteria. *Cell* **165**, 1493–1506 (2016).
9. Liu, X. et al. High-throughput CRISPRi phenotyping identifies new essential genes in *Streptococcus pneumoniae*. *Mol. Syst. Biol.* **13**, 931 (2017).
10. Fu, Y. et al. High-frequency off-target mutagenesis induced by CRISPR-Cas nucleases in human cells. *Nat. Biotechnol.* **31**, 822–826 (2013).
11. Pattanayak, V. et al. High-throughput profiling of off-target DNA cleavage reveals RNA-programmed Cas9 nuclease specificity. *Nat. Biotechnol.* **31**, 839–843 (2013).
12. Hsu, P. D. et al. DNA targeting specificity of RNA-guided Cas9 nucleases. *Nat. Biotechnol.* **31**, 827–832 (2013).
13. Sternberg, S. H., LaFrance, B., Kaplan, M. & Doudna, J. A. Conformational control of DNA target cleavage by CRISPR–Cas9. *Nature* **527**, 110–113 (2015).
14. Jinek, M. et al. Structures of Cas9 endonucleases reveal RNA-mediated conformational activation. *Science* **343**, 1247997 (2014).
15. Kuscu, C., Arslan, S., Singh, R., Thorpe, J. & Adli, M. Genome-wide analysis reveals characteristics of off-target sites bound by the Cas9 endonuclease. *Nat. Biotechnol.* **32**, 677–683 (2014).
16. Wu, X. et al. Genome-wide binding of the CRISPR endonuclease Cas9 in mammalian cells. *Nat. Biotechnol.* **32**, 670–676 (2014).
17. Singh, D., Sternberg, S. H., Fei, J., Doudna, J. A. & Ha, T. Real-time observation of DNA recognition and rejection by the RNA-guided endonuclease Cas9. *Nat. Commun.* **7**, 12778 (2016).
18. Gilbert, L. A. et al. Genome-scale CRISPR-mediated control of gene repression and activation. *Cell* **159**, 647–661 (2014).
19. Zhao, H. et al. Depletion of undecaprenyl pyrophosphate phosphatases disrupts cell envelope biogenesis in *Bacillus subtilis*. *J. Bacteriol.* **198**, 2925–2935 (2016).
20. Farasat, I. et al. Efficient search, mapping, and optimization of multi-protein genetic systems in diverse bacteria. *Mol. Syst. Biol.* **10**, 731 (2014).
21. Nielsen, A. A. & Voigt, C. A. Multi-input CRISPR/Cas genetic circuits that interface host regulatory networks. *Mol. Syst. Biol.* **10**, 763 (2014).
22. Gibson, D. G. et al. Enzymatic assembly of DNA molecules up to several hundred kilobases. *Nat. Methods* **6**, 343–345 (2009).
23. Engler, C., Kandzia, R. & Marillonnet, S. A one pot, one step, precision cloning method with high throughput capability. *PLoS ONE* **3**, e3647 (2008).
24. St-Pierre, F. et al. One-step cloning and chromosomal integration of DNA. *ACS Synth. Biol.* **2**, 537–541 (2013).
25. Sharan, S. K., Thomason, L. C., Kuznetsov, S. G. & Court, D. L. Recombineering: a homologous recombination-based method of genetic engineering. *Nat. Protoc.* **4**, 206–223 (2009).
26. Chaveroche, M.-K., Ghigo, J.-M. & d'Enfert, C. A rapid method for efficient gene replacement in the filamentous fungus *Aspergillus nidulans*. *Nucleic Acids Res.* **28**, e97 (2000).
27. Love, M. I., Huber, W. & Anders, S. Moderated estimation of fold change and dispersion for RNA-seq data with DESeq2. *Genome Biol.* **15**, 550 (2014).
28. Pedregosa, F. et al. Scikit-learn: machine learning in Python. *J. Mach. Learn. Res.* **12**, 2825–2830 (2011).
29. Kingma, D. P. & Ba, J. Adam: a method for stochastic optimization. *arXiv* arXiv:1412.6980 (2014).
30. Schmittgen, T. D. & Livak, K. J. Analyzing real-time PCR data by the comparative CT method. *Nat. Protoc.* **3**, 1101–1108 (2008).
31. Cronan, J. E. Improved plasmid-based system for fully regulated off-to-on gene expression in *Escherichia coli*: application to production of toxic proteins. *Plasmid* **69**, 81–89 (2013).
32. Cinesi, C., Aeschbach, L., Yang, B. & Dion, V. Contracting CAG/CTG repeats using the CRISPR-Cas9 nickase. *Nat. Commun.* **7**, 13272 (2016).

Acknowledgements

We are grateful to Oz Solomon and Zohar Yakhini for helpful discussions, to Christiane Bouchier from the Institut Pasteur sequencing Platform, to Charlotte Cockram and Aimee Wessel for providing experimental assistance, and to Jerome Wong Ng for his assistance with data analysis. *E. coli* mutants were sequenced by the Institut Pasteur Genomics Platform, a member of "France Génomique" consortium (ANR10-INBS-09-08). This work was supported by the European Research Council (ERC) under the Europe Union's Horizon 2020 research and innovation program (grant agreement No. [677823]); the French Government's Investissement d'Avenir program; Laboratoire d'Excellence 'Integrative Biology of Emerging Infectious Diseases' [ANR-10-LABX-62-IBEID]; and the Pasteur-Weizmann consortium and Pasteur-Roux Fellowship to L.C.

Author contributions

L.C. and D.B. designed the study and wrote the manuscript. L.C. performed the experiments. A.V. performed the mcherry fluorescence measurements. D.B., F.R, V.K., H.V. and L.C. analyzed the data.

Additional information

Supplementary Information accompanies this paper at https://doi.org/10.1038/s41467-018-04209-5.

Competing interests: The authors declare no competing interests.

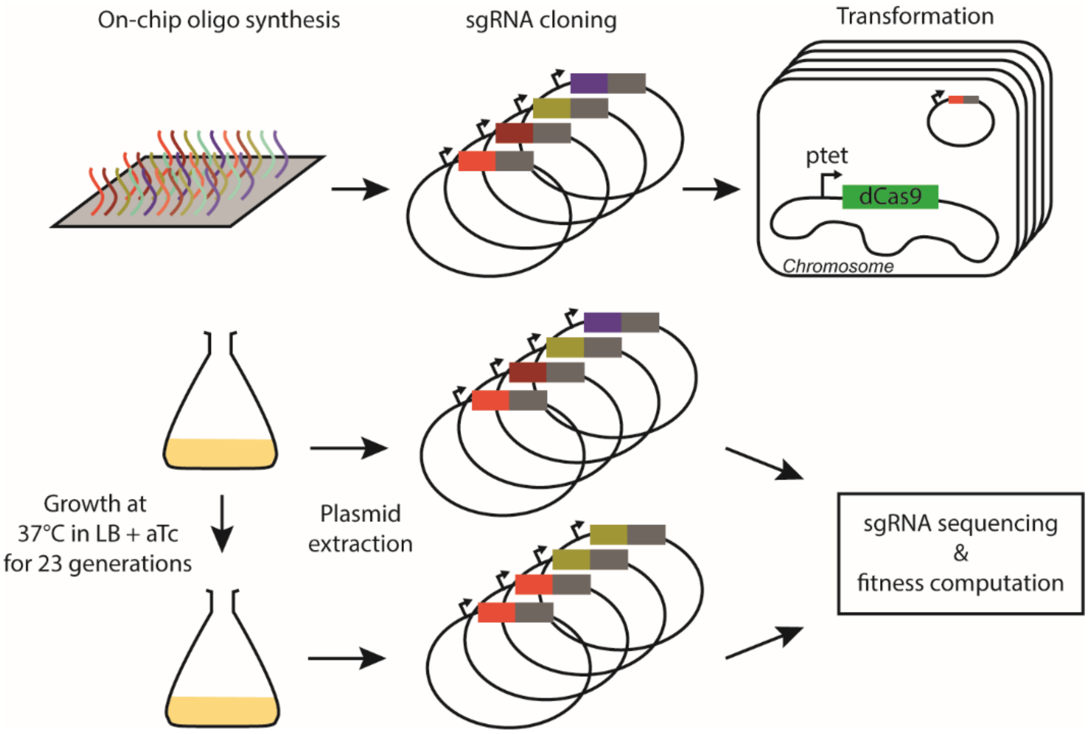

Supplementary Figure 1. Experimental scheme of the CRISPRi screen performed in *E. coli*. Oligonucleotides synthesized on chip were cloned on plasmid psgRNA and electroporated into *E. coli* LC-E18 carrying *dCas9* under the control of a Ptet promoter. Cells were grown at 37°C in LB supplemented with aTc and the psgRNA library was extracted and sequenced at the beginning and at the end of the experiment. Sequencing the guides enables to estimate their relative abundance in the population and to compute their fitness effect on the cell.

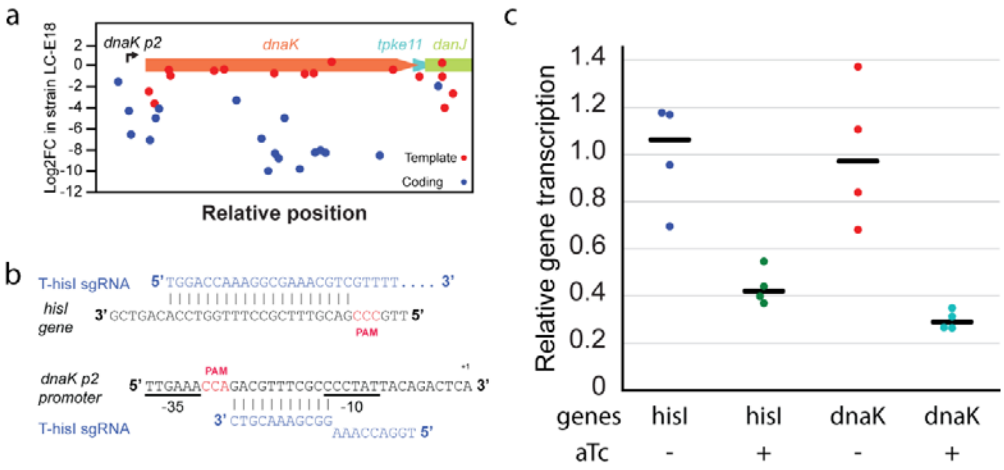

Supplementary Figure 2. The T-hisI guide RNA blocks the expression of the dnaK-dnaJ operon. (a) Fitness effect of guides targeting the dnaK-dnaJ operon (red: template strand, blue: coding strand). (b) There is a 11 bp perfect match between the seed sequence of the T-hisI guide RNA and the dnaK p2 pormoter region. (c) RT-qPCR results showing repression of both *dnaK* and *hisI* by the T-hisI guide RNA, after 2H of growth with and without aTc. n = 4, the black bar shows the median.

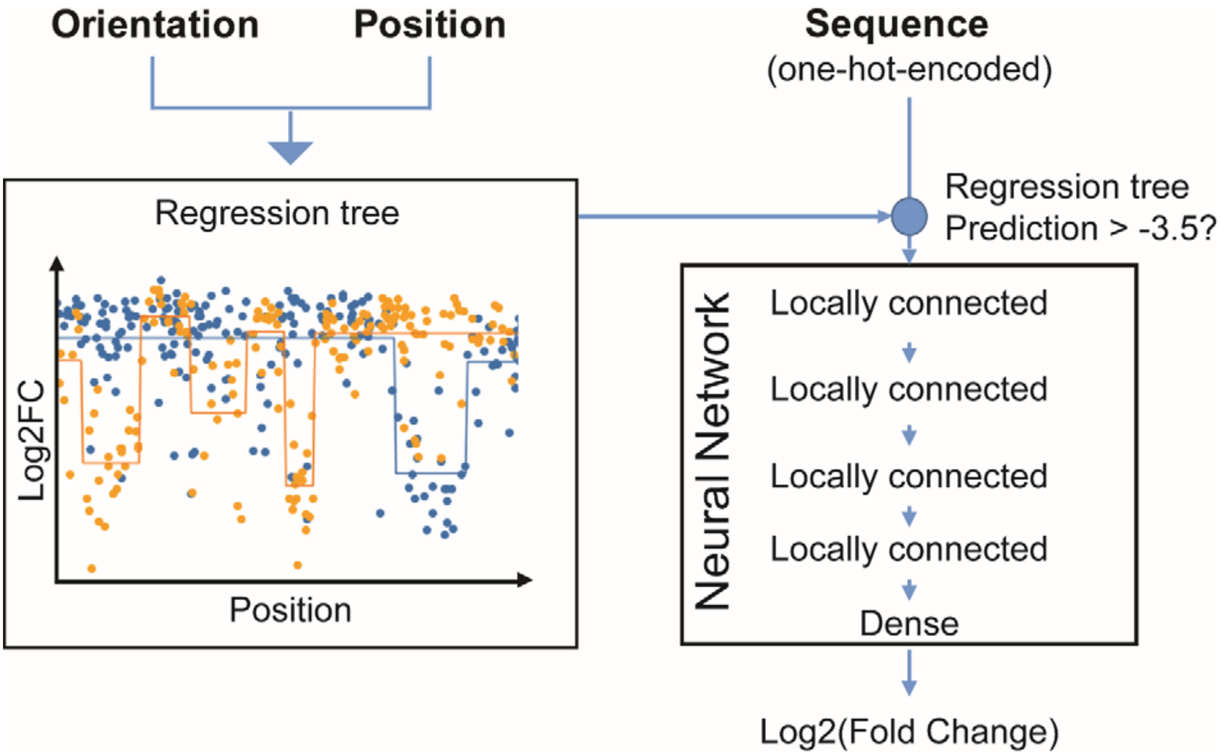

Supplementary Figure 3. Flow chart of machine learning analysis. A regression tree was first fitted using guide orientation and position as the unique features to predict log2FC. This enables to identify regions and orientations were guides consistently produce a fitness defect. The goal of this analysis was then to investigate the fitness defect produced by guides that target in “neutral” regions. In these regions, the log2FC of guides is not consistent and most guides have no effect. We kept guides in genomic regions where the prediction fo the regression tree was greater than -3.5 and then fitted a neural network using the one-hot-encoded sequence as the unique feature to predict the log2FC. The neural network consists in 4 locally connected layers with a kernel size of 5 followed by a dense layer. More details are provided in the methods section.

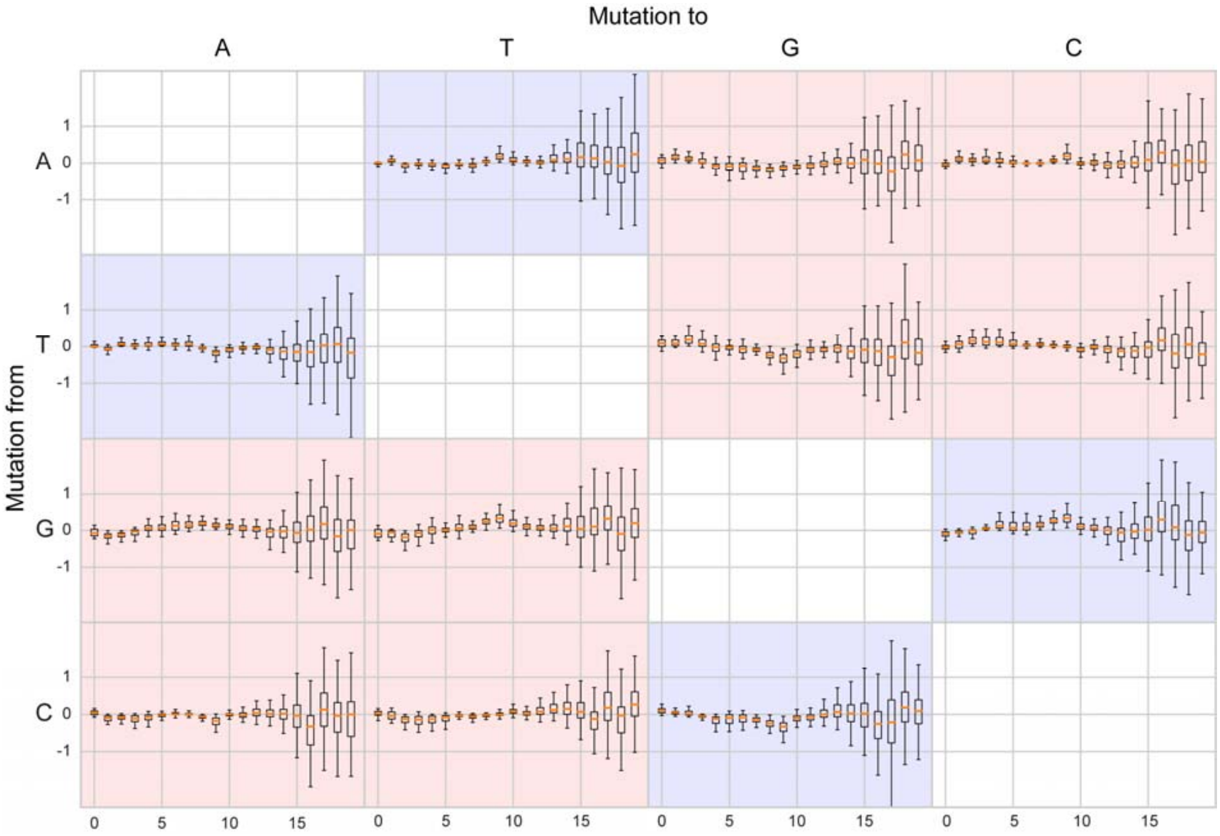

Supplementary Figure 4. Effect of mutations on the model predictions. We generated 1000 random sequences and computed the effect on the model prediction or mutating each base to all possible bases. The distribution of these effects are shown as boxplots for each type of mutation (using the default matplotlib boxplot parameters). The y-axis shows the difference in predicted log2FC between the mutated sequence and the initial sequence (a lower value means that the mutation is predicted to cause a stronger fitness defect). The x-axis shows the position along the guide sequence. Transitions are highlighted in blue and transversions in red.

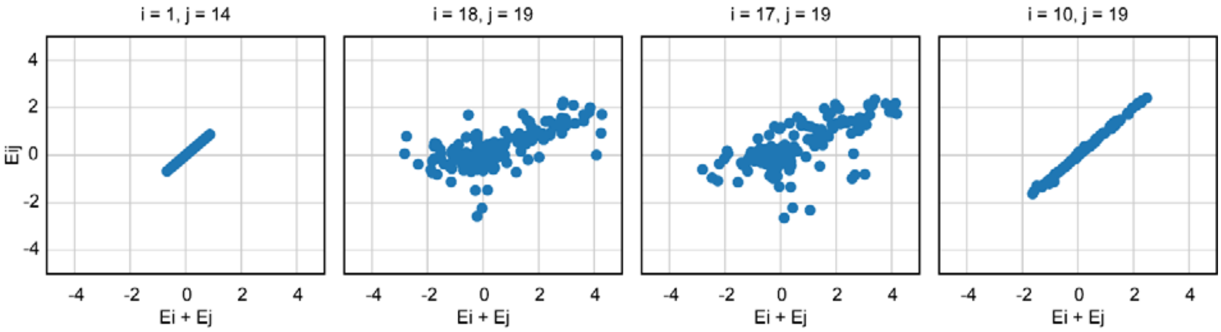

Supplementary Figure 5. Measuring interactions between positions in the model. To measure the level of interaction between positions we generated all possible pairs of mutations for each sequence in a set of 100 random sequences, and compared the effect of individual mutations to that of pairs of mutations. Positions are interacting if the effect of a double mutation (Eij) is different from the sum of the effect of the single mutations (Ei+Ej). As an example we plot Eij vs. Ei+Ej for interacting (i=18,j=19 ; i=17,j=19) and non-interacting positions (i=1,j=14; i=10,j=19).

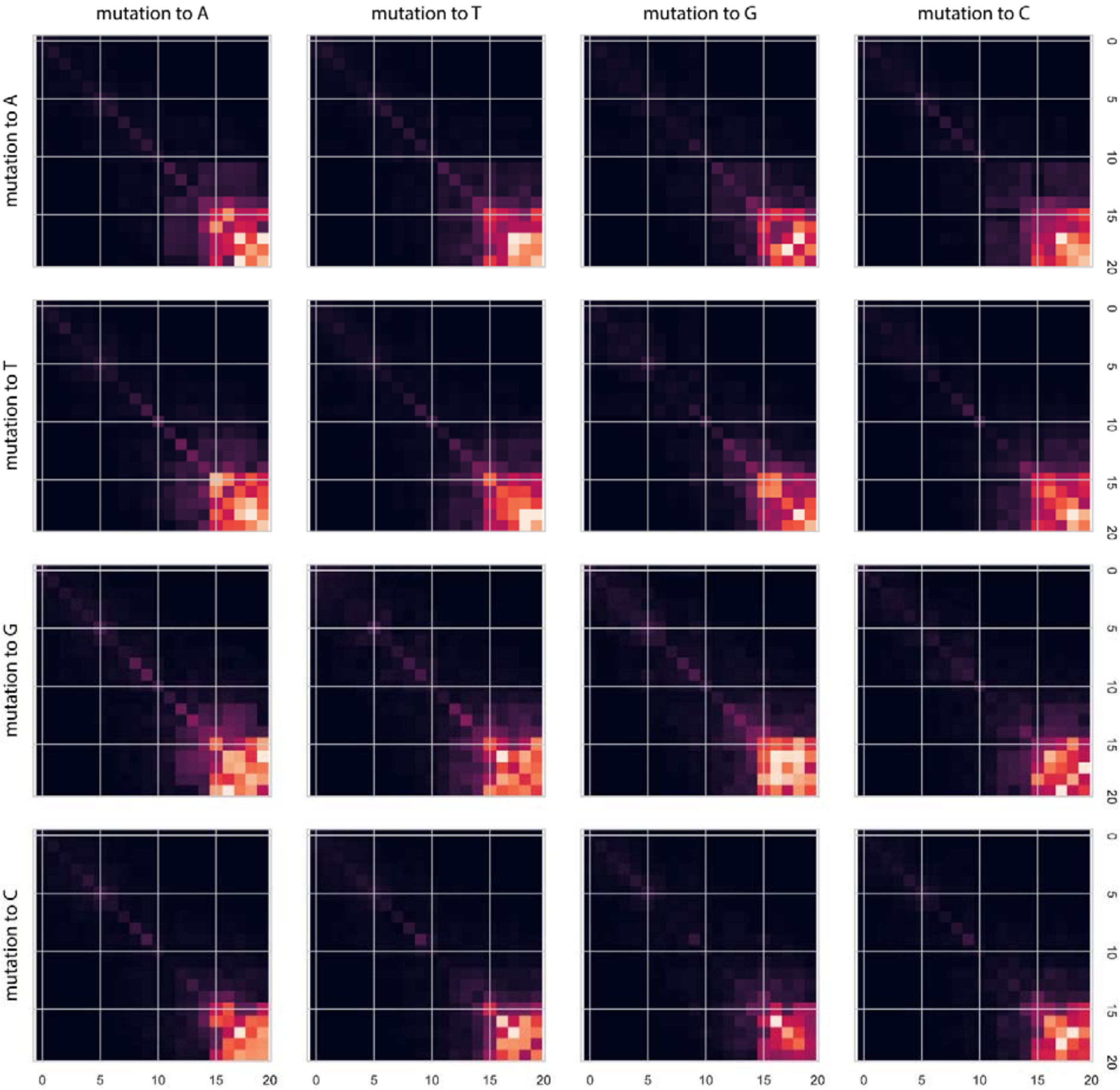

Supplementary Figure 6. Level of interaction predicted by the model for different combinations of mutations. We generated all possible pairs of mutations for each sequence in a set of 100 random sequences, and compared the effect of individual mutations to that of pairs of mutations. The color shows the average Euclidian distance between the effect of a double mutation and the sum of the effect of single mutations (dark: no interaction, white: strong interaction).

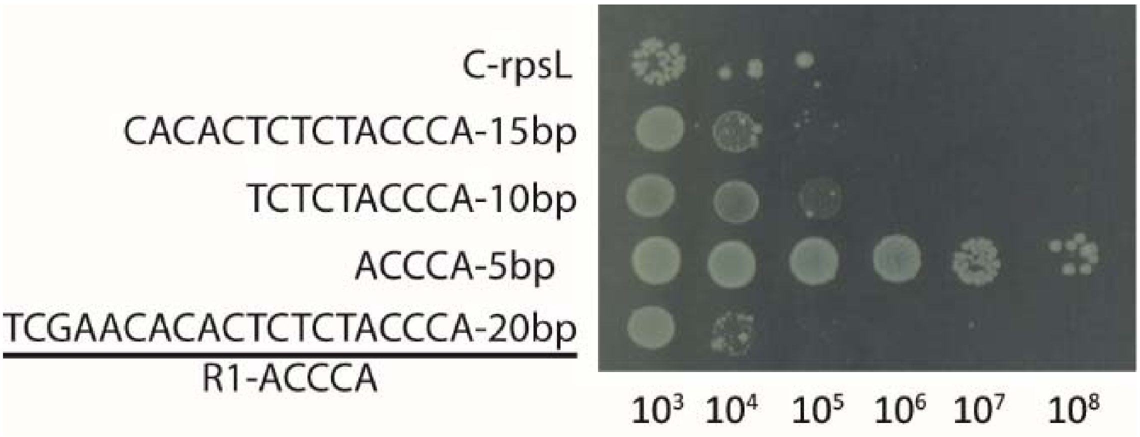

Supplementary Figure 7. Truncated guides with a bad seed sequence can still kill *E. coli*. Truncated single guide RNAs with the ACCCA seed sequence were cloned on plasmid psgRNA and transformed in strain LC-E18. Serial dilutions were then plated on LB supplemented with aTc and kanamycin. The C-rpsL lane shows a positive control where the transcription of *rpsL* essential gene is repressed by dCas9. n = 3.

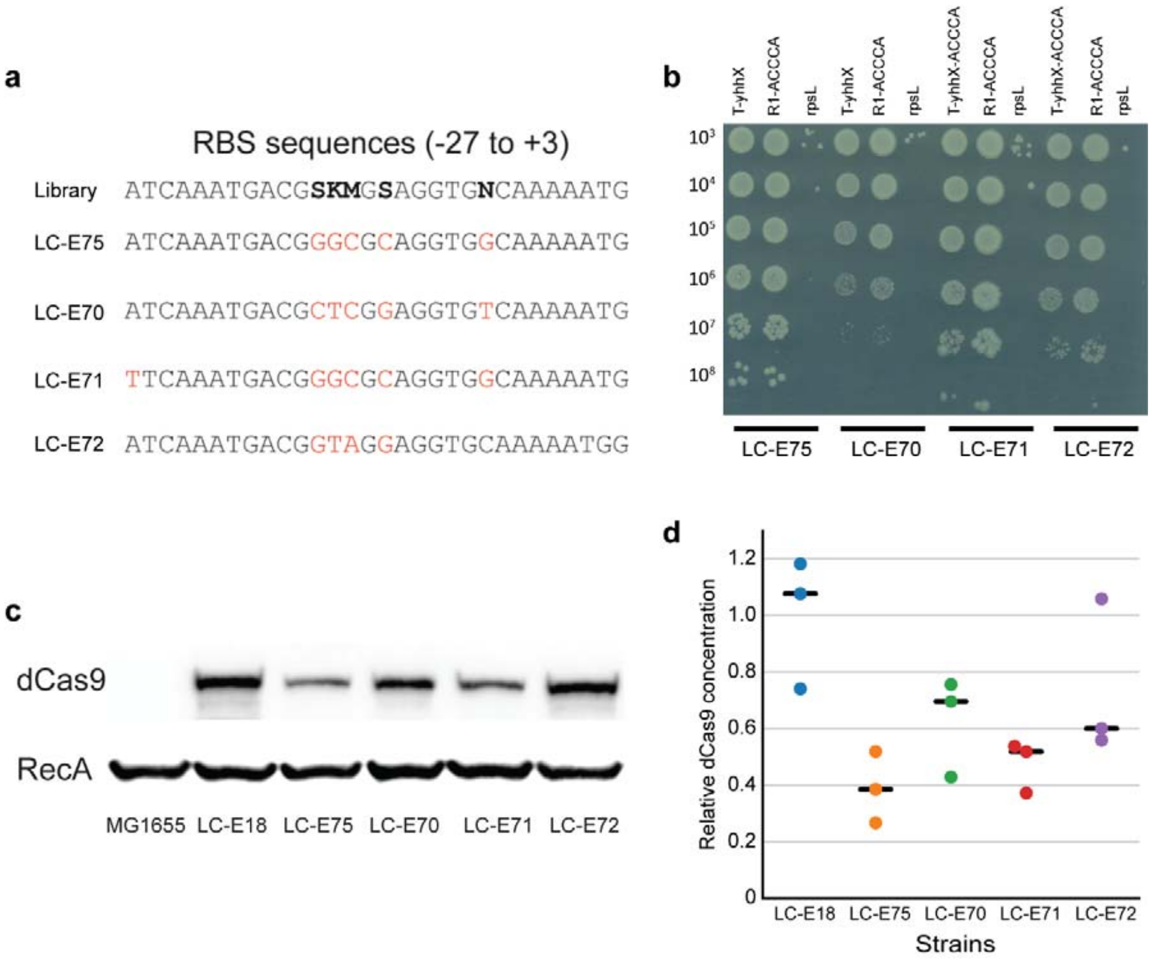

Supplementary Figure 8. The bad seed effect can be alleviated by reducing dCas9 concentration. A library of RBS controlling the expression of dCas9 was generate and clones were selected for their ability to survive the dCas9 expression in the presence of a bad seed sequence while still efficiently blocking the expression of *rpsL* when guided by the C-rpsL sgRNA. Four clones where selected (LC-E70, LC-E71, LC-E72 and LC-E75). (a) RBS sequence of the selected clones. (b) Cells carrying the T-yhhX, R1-ACCCA or C-rpsL guide RNAs were grown overnight, followed by serial dilution and plating with aTc. (c) Western blot image of selected dCas9 strains. (d) quantification results of 3 western blots, the black bar shows the median (Uncorpped photos are shown in Supplementary Figure 16).

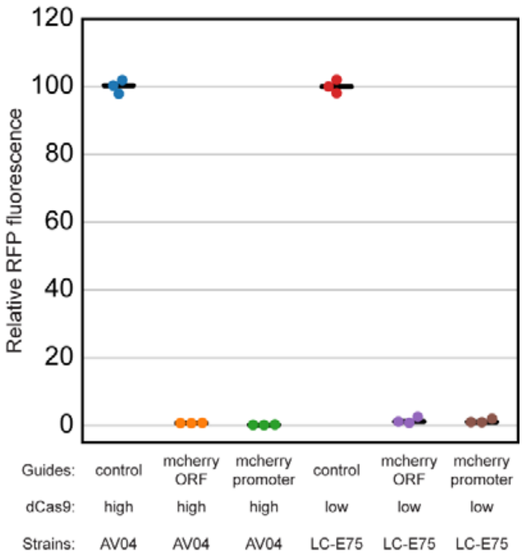

Supplementary Figure 9. The LC-E75 strain efficiently blocks target gene expression. Strain LC-E75 carries an optimized dCas9 expression cassette integrated at the 186 attB site and a constitutively expressed *mcherry* reporter gene at the lambda attB site. Strain AV04 is identical to LC-E75 but carries the stronger un-optimized dCas9 expression cassette from strain LC-E18. Cells carrying plasmids (psgRNA::C-mcherry20orf, psgRNA::C-mcherry20p) or a control psgRNA were grown with aTc overnight. The next morning, the cells were diluted 250 times in fresh medium with 1 nM aTc and kanamycine, and grown for 1.75 hours at 37°C to reach the exponential phase. The cells were fixed and fluorescence was measured using flow cytometry. n = 3.

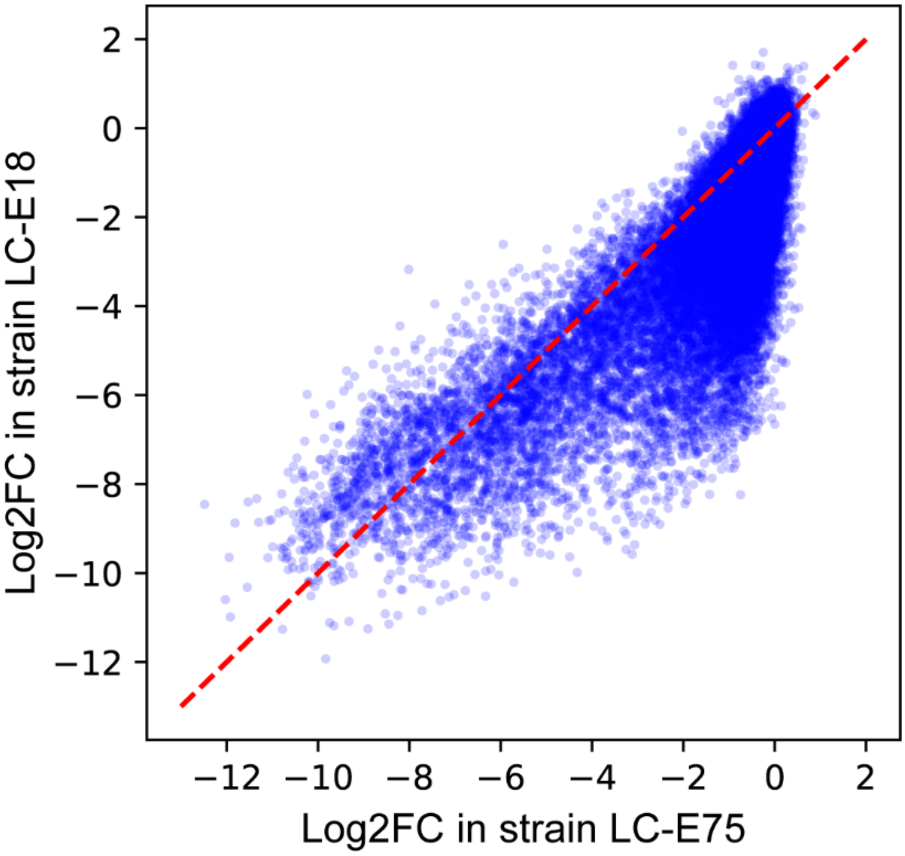

Supplementary Figure 10. Comparision of fitness measurments in strain LC-E18 and LC-E75. Scatter plot of the log2FC value (LC-E18 vs LC-E75) for all the guides in the library.

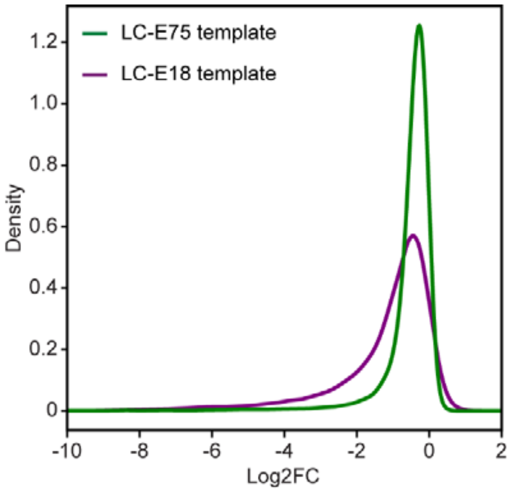

Supplementary Figure 11. Comparison of the fitness effects of sgRNAs targeting the template strand of genes. The log2FC value distribution of guides targeting template strand is much narrower in strain LC-E75, showing that guide RNAs have a more consistent effect in strain LC-E75 than LC-E18.

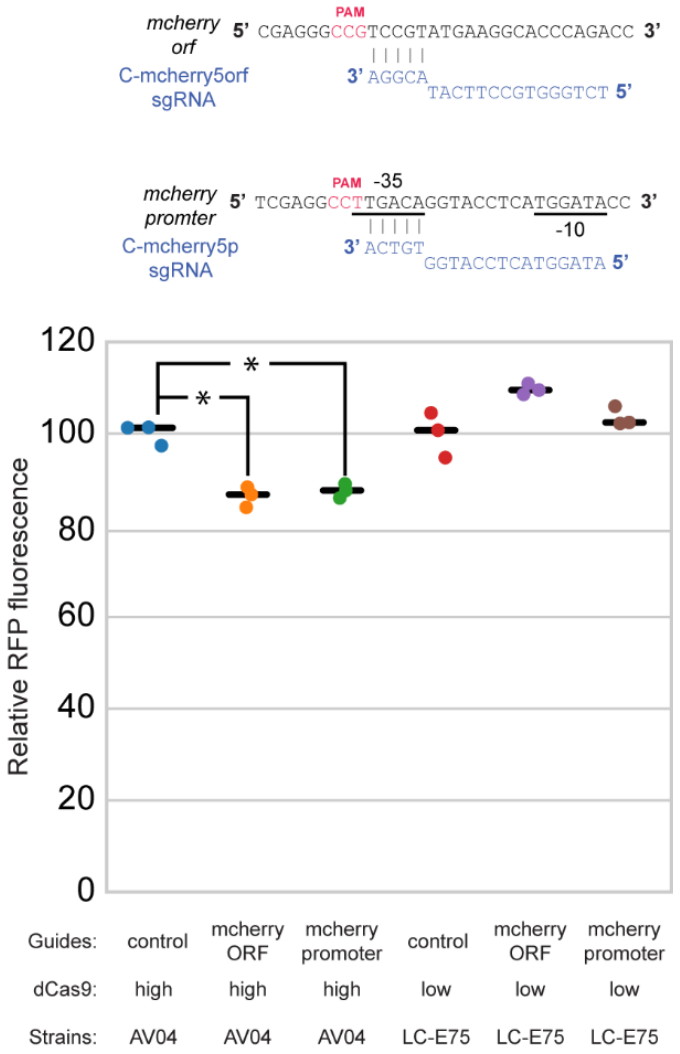

Supplementary Figure 12. A 5 bp of seed match has minimal or no effect on gene transcription. Guides with only 5 bp of identity between the PAM-proximal region and the target where used to target either the mcherry ORF region (C-mcherry5orf) or the promoter region (C-mcherry5p). Strain LC-E75 carries an optimized dCas9 expression cassette integrated at the 186 attB site and a constitutively expressed *mcherry* reporter gene at the lambda attB site. Strain AV04 is identical to LC-E75 but carries the stronger un-optimized dCas9 expression cassette from strain LC-E18. Cells were grown with aTc overnight. The next morning, the cells were diluted 250 times in fresh medium with 1 nM aTc and kanamycine, and grown for 1.75 hours at 37°C to reach the exponential phase. The cells were fixed and fluorescence was measured using flow cytometry. The In the high dCas9 concentraction strain (AV04), 5 bp matches can block transcription by 13.7% and 12.5% when targeting the ORF and promoter region respectively. In the low dCas9 concentraction strain (LC-E75), repression was not significant. “*” indicates a p-test value than 0.05 (double sided t-test with equal variance). n = 3, the black bars show the median.

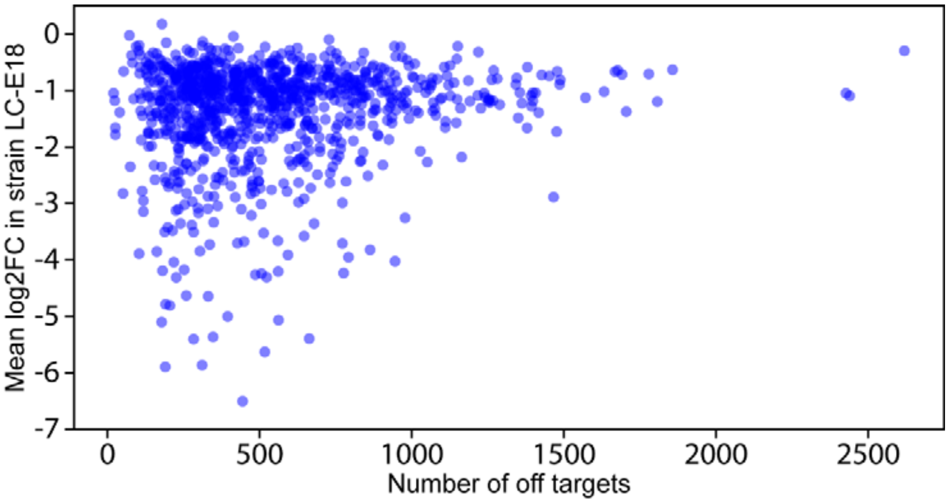

Supplementary Figure 13. The bad seed effect does not correlate with the number of off-targets in the genome. Mean log2FC for guides sharing the same 5nt seed sequence as a function of the number of off-targets in the genome of *E. coli* MG1655 that have a perfect match to these 5nt and a “NGG” PAM.

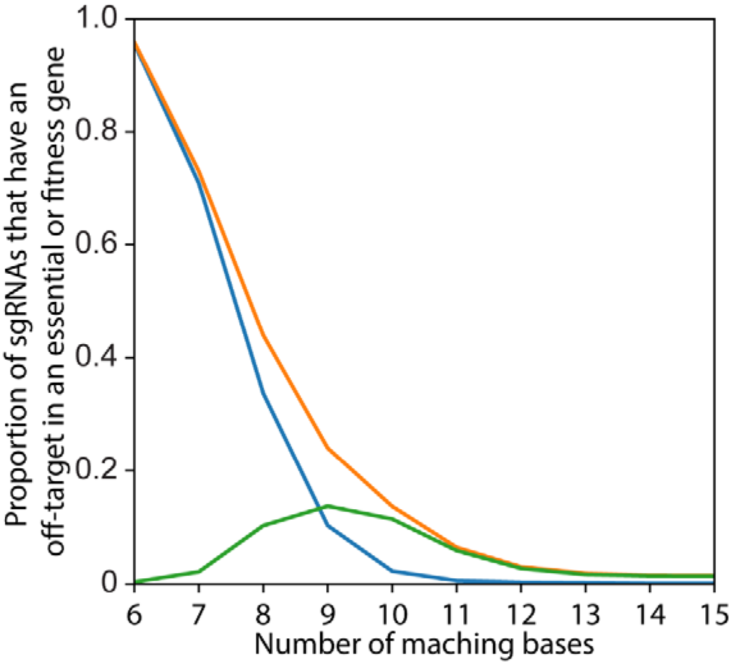

Supplementary Figure 14. Guide RNAs with more than 9nt of perfect identity between the seed sequence and off-target positions can have a strong fitness effect. We plot here the proportion of guide RNAs which have an off-target position in a region where guides consistently produce a strong fitness defect. This proportion is shown for guides that have an unexpectedly strong log2FC (<-3.5) while targeting the template strand of non-essential genes (orange), as well as for guides targeting the same regions but with log2FC>-3.5 (blue), which can be interpreted as the false discovery rate. The green curve is the difference between the green and blue curves. The maximum is at 9nt, which indicates that 9nt of identity in the seed sequence is enough to produce a strong fitness defect, but mostly false positive off-target positions are detected when going down to 8nt of identity.

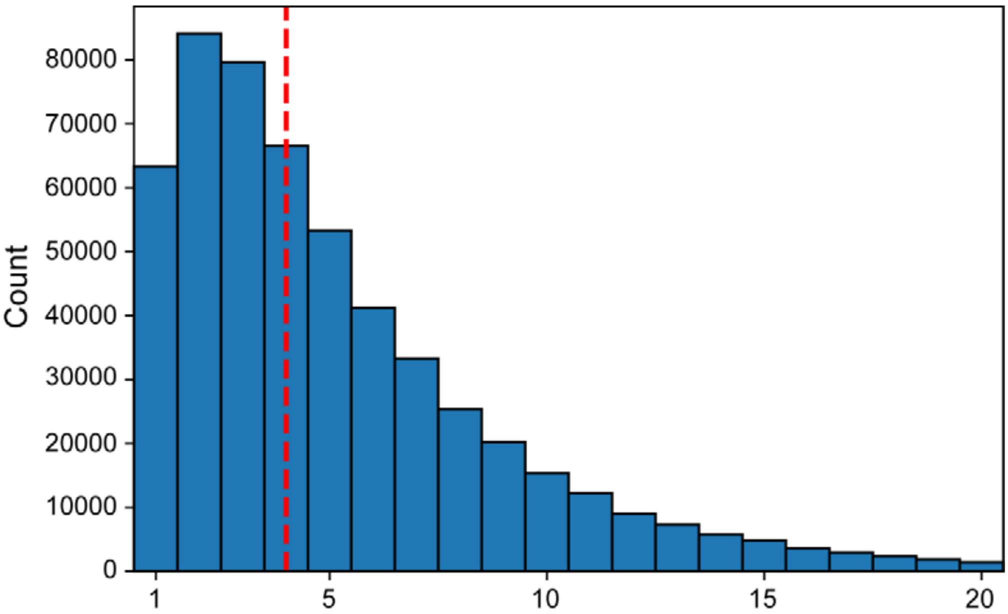

Supplementary Figure 15. Distribution of the number of off-target for guides targeting the chromosome of *E. coli* MG1655. 88.3% of all possible guides with a target in the chromosome of *E. coli* MG1655 have at least one off-target with 9nt of identity in the seed sequence or more. The red dash line is the medium value (4) of the distribution.

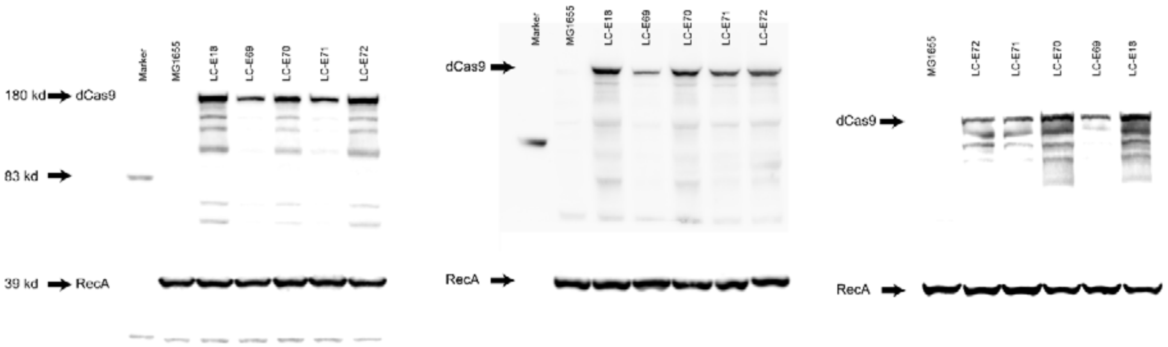

Supplementary Figure 16. Uncropped western blot photos. Uncropped photos of 3 westernblot repeats.

Supplementary Table 1. Repartition of guides according to their fitness effect in strain LCE-18 and binding orientation.

	Template strand		Coding strand		All
Log2FC	**Log2FC>-3.5**	**Log2FC<-3.5**	**Log2FC>-3.5**	**Log2FC<-3.5**	
Essential	2628	351	701	1834	5514
Non-essential	33612	2499	25989	2694	64794
All	36240	2850	26690	4528	70308

Supplementary Table 2. Mutations selected in strain LC-E18 that abolish the fitness defect produced by the T-yhhX-ACCCA guide RNA while maintaining strong repression of *rpsL*. Mutations in samples 1,2,3,4 and 6 led to frameshifts in the *dCas9* gene. The ability of these strains to still efficiently block *rpsL* shows that they still express low levels of dCas9 likely thanks to translational slippage.

Sample ID	Mutation types	Mutations	Consequences
1	Insertion	T inserted between 423 and 424	Frame shift
2	Insertion	T inserted between 1714 and 1715	Frame shift
3	Insertion	T inserted between 1714 and 1715	Frame shift
4	Insertion	T inserted between 1714 and 1715	Frame shift
5	Deletion	Deletion from -27 to +7	Promoter mutated
6	Insertion	T inserted between 1714 and 1715	Frame shift

Supplementary Table 3. Plasmids constructed in this study.

Plasmid name	Backbone			Fragment 1			Fragment 2		
	Template	**Primer 1**	**Primer 2**	**Template**	**Primer 1**	**Primer 2**	**Template**	**Primer 1**	**Primer 2**
pCRRNAcos	pCRRNA digested with AvrII	N/A	N/A	MG1655, lambda lysogen	LC74	LC75	N/A	N/A	N/A
psgRNA*	pCRRNAcos	LC41	LC42	sgRNA_bsaI_gBlock (IDT)	N/A	N/A	N/A	N/A	N/A
psgRNAc*	pCas9	LC89	LC132	psgRNAcos	LC316	LC317	N/A	N/A	N/A
psgRNAcos::R1_ACCCA_5bp	psgRNAcos	LC191	LC1027	psgRNAcos	LC192	LC1028	N/A	N/A	N/A
psgRNAcos::R1_ACCCA_10bp	psgRNAcos	LC191	LC1029	psgRNAcos	LC192	LC1030	N/A	N/A	N/A
pOSIP-KL-sulA-GFP	pOSIP-KL digested with EcoRI and PstI	N/A	N/A	pZA31-sulA-GFP	LC245	LC246	N/A	N/A	N/A
pOSIP-KL-mcherry	pOSIP-KL digested with EcoRI and PstI	N/A	N/A	pDB127	V1	V40	pFB262	V38	V39
pOSIP-KH-RBS2-dCas9	pOSIP-KH digested with EcoRI and PstI	N/A	N/A	pDB275	LC100	LC283	pdCas9-bacteria	LC284	LC285
pOSIP-KO-RBS2-dCas9	pOSIP-KO digested with EcoRI and PstI	N/A	N/A	pOSIP-KH-RBS2-dCas9	LC124	LC125	N/A	N/A	N/A
pOSIP-CO-RBS-library-dCas9	pOSIP-CO digested with BamHI and PstI	N/A	N/A	pDB275	LC653	LC1090	pdCas9-bacteria	LC1088	LC285

* Sequence provided in Supplementary Data 4

Plasmids and strains were deposited in Addgene.

Supplementary Table 4. Primers used for cloning.

Name	Sequence (5’ to 3’)
LC41	TGCAGCGCGATCGTAATCAGGATCCCATGGTACGCGT
LC42	ACAGAACTTAATGGGCCCGAAGACGAAAGGGCCTCGT
LC74	TGAACGCTCTCCTGAGTAGGACAAATCCGCCGCCCTAGACCCTCCACGCACGTTGTGATATG
LC75	CCTTTGAGTGAGCTGATACCGCTCGCCGCAGCCGAACGCCCCAAAAAGCCTCGCTTTCAGC
LC89	CAGGTGCTACATTTGAAGAGAT
LC100	GCAGGACGCCCGCCATAAACTGCCAGGAATTGGGGATCGGTTAAGACCCACTTTCACATTTAAG
LC124	CTGCCAGGAATTGGGGATC
LC125	CAGTTTAGGTTAGGCGCCAT
LC132	GGGGAGAGCCTGAGCAAA
LC191	GTCTAGGGCGGCGGATTTG
LC192	CGCTCTCCTGAGTAGGACAAAT
LC245	GACGCCCGCCATAAACTGCCAGGAATTGGGGATCGGATCGGTATTCAATTGTGCCCA
LC246	TAGGTTAGGCGCCATGCATCTCGAGGCATGCCTGCATTATTTGTATAGTTCATCCATGCCA
LC283	TCCATTTTTGCCTCCTAACTAGGTCATTTGATATGCCTCC
LC284	CCTAGTTAGGAGGCAAAAATGGATAAGAAATACTCAATAGGC
LC285	AGTTTAGGTTAGGCGCCATGCATCTCGAGGCATGCCTGCAATGCCTGGAGATCCTTACTC
LC293	GTTTTAGAGCTAGAAATAGCAAGTTAA
LC294	ACTAGTATTATACCTAGGACTGAGCTA
LC296	TATATTTTAGGAATTCTAAAGATCTTTGACAGCTAGCTCAGTCCTAGGTATAATACTAGT
LC297	ACTTTTTCAAGTTGATAACGGACTAGCCTTATTTTAACTTGCTATTTCTAGCTCTAAAAC
LC316	CAAATGCCTGAGGCCAGTTTGCTCAGGCTCTCCCCCCTGATTACGATCGCGCTG
LC317	TTCAGTGCAATTTATCTCTTCAAATGTAGCACCTGGCTAGGAGGTGACTGAAGT
LC499	GATCGGAAGAGCACACGTCTGAACTCCAGTCAC
LC609	GCACGCCCGTCGCTCAGTCCTAGGTATAATACTA
LC610	TATTATACCTAGGACTGAGCGACGGGCGTGC
LC653	GGAATTGGGGATCGGAATTCGAGCTCGGTACCCGGGGGTTAAGACCCACTTTCACATT
LC961	GCACAAAGTCAGACTTTATCTATATTTGTAAGGGGTGAATCTTGATGACAACATGGGAATTAGCCATGGTCC
LC962	TGTAGGGTCGGAGCGTTAACGTTGCCAGAGGCGCTGGAGTACAGCACGTAGTGTAGGCTGGAGCTGCTTC
LC1027	TAATACTAGTTCTCTACCCAGTTTTAGAGCTAGAAATAGCAAG
LC1028	CTAGCTCTAAAACTGGGTAGAGAACTAGTATTATACCTAGGACTGAGCTA
LC1029	TAATACTAGTACCCAGTTTTAGAGCTAGAAATAGCAAG
LC1030	CTAGCTCTAAAACTGGGTACTAGTATTATACCTAGGACTGAGCTA
LC1088	TGATAGAGTGATATCCGGAGGCATATCAAATGACGSKMGSAGGTGNCAAAAATGGATAAGAAATACTCAATAGGCTTAGCT
LC1090	CATTTGATATGCCTCCGGATATCACTCTATCA
V1	CGCCATAAACTGCCAGGAATTGGGGATCGGCCTATGAACTGTCGACTCGAGG
V38	GGAGAAATCTAGATGGTTTCCAAGGGCGAGGAGGAT
V39	TTAGGCGCCATGCATCTCGAGGCATGCCTGCATTATTTGTACAGCTCATCCATGCC
V40	ATCCTCCTCGCCCTTGGAAACCATCTAGATTTCTCCTCTTTAAAGGAATTCC

Supplementary Table 5. Plasmids used in this study.

Plasmids from other studies	**Addgene Catalog # (or References)**
pCRRNAcos	Plasmid #78493
pCas9	Plasmid #42876
pOSIP-KH	Plasmid #45983
pOSIP-KL	Plasmid #45984
pOSIP-KO	Plasmid #45985
pOSIP-CO	Ref[1]
pZA31-sulA-GFP	Plasmid #78492
pDB127	Ref[2]
pDB275	Ref[3]
pdCas9-bacteria	Plasmid #44249
pE-FLP	Plasmid #45978
pKD3	Plasmid #45604
pKOBEG-A	Ref[4]
pFB262	Ref[5]

Supplementary Table 6. sgRNA guide sequences and corresponding primers

Target name	Target sequences	Forward primer	Reverse primer
T-lpoB	TTGTCGCCGCAGGACAGTTT	TAGTTTGTCGCCGCAGGACAGTTT	AAACAAACTGTCCTGCGGCGACAA
T-lpoB2	ATTCGCCATTATGACTGGAA	TAGTATTCGCCATTATGACTGGAA	AAACTTCCAGTCATAATGGCGAAT
C-lopB	CGCCATCGACAGTTGCTGGG	TAGTCGCCATCGACAGTTGCTGGG	AAACCCCAGCAACTGTCGATGGCG
T-hisI	TGGACCAAAGGCGAAACGTC	TAGTTGGACCAAAGGCGAAACGTC	AAACGACGTTTCGCCTTTGGTCCA
C-hisI	GGTGACTTTGCCGCTTTCGA	TAGTGGTGACTTTGCCGCTTTCGA	AAACTCGAAAGCGGCAAAGTCACC
C-rpsL	AGCGCGGAGTTCGGTTTTTT	TAGTAGCGCGGAGTTCGGTTTTTT	AAACAAAAAACCGAACTCCGCGCT
R1-ACCCA	TCGAACACACTCTCTACCCA	TAGTTCGAACACACTCTCTACCCA	AAACTGGGTAGAGAGTGTGTTCGA
R1-ACCCA	GCTACCTTAACGCCTACCCA	GCTACCTTAACGCCTACCCA	AAACTGGGTAGGCGTTAAGGTAGC
T-yhhX	TTGTATCAAACCATCACCCA	TAGTTTGTATCAAACCATCACCCA	AAACTGGGTGATGGTTTGATACAA
T-ydeO	ACATGAAGCCGGCGCACCCA	TAGTACATGAAGCCGGCGCACCCA	AAACTGGGTGCGCCGGCTTCATGT
R1-TGGAA	CCGCTATGTCAGGCGTGGAA	TAGTCCGCTATGTCAGGCGTGGAA	AAACTTCCACGCCTGACATAGCGG
R2-TGGAA	GTCAGTCATATTAACTGGAA	TAGTGTCAGTCATATTAACTGGAA	AAACTTCCAGTTAATATGACTGAC
T-garD	TGAGCGCCTGCTGACTGGAA	TAGTTGAGCGCCTGCTGACTGGAA	AAACTTCCAGTCAGCAGGCGCTCA
R1-ACCCA_15bp	CACACTCTCTACCCA	TAGTCACACTCTCTACCCA	AAACTGGGTAGAGAGTGTG
T-bioC	ACGCGGGTTGTGGACCTGGC	TAGTACGCGGGTTGTGGACCTGGC	AAACGCCAGGTCCACAACCCGCGT
C-mcherry20orf	TCTGGGTGCCTTCATACGGA	TAGTTCTGGGTGCCTTCATACGGA	AAACTCCGTATGAAGGCACCCAGA
C-mcherry20p	TATCCATGAGGTACCTGTCA	TAGTTATCCATGAGGTACCTGTCA	AAACTGACAGGTACCTCATGGATA
C-mcherry5orf	AGACCCACGGAAGTAACGGA	TAGTAGACCCACGGAAGTAACGGA	AAACTCCGTTACTTCCGTGGGTCT
c-mcherry5p	ATAGGTACTCCATGGTGTCA	TAGTATAGGTACTCCATGGTGTCA	AAACTGACACCATGGAGTACCTAT

Supplementary Table 7. Strains made using the OSIP system.

Strain Name	Original strain	Integration at lambda attB	Integration at primary 186 attB	Integration at HK022 attB
LC-E18	MG1655	pOSIP-KL-sulA-GFP	N/A	pOSIP-KH-RBS2-dCas9
LC-E75	MG1655	pOSIP-KL-mcherry	pOSIP-CO-RBS-library-dCas9 (2-3)*	N/A
AV04	MG1655	pOSIP-KL-mcherry	pOSIP-KO-RBS2-dCas9	N/A

*The number in the parentheses is corresponding to the selected colony number.

Supplementary Table 8. Primers and corresponding indexes used to prepare the sequencing libraries.

Primer name	Index	primer sequences	PCR function
LC606	AGAT	TTCCCTACACGACGCTCTTCCGATCTTAGANNNNGCACGCCCGTCGCTCAGTCCTAGGTATAATACTA	1st PCR forward
LC607	TCTC	TTCCCTACACGACGCTCTTCCGATCTCTCTNNNNGCACGCCCGTCGCTCAGTCCTAGGTATAATACTA	1st PCR forward
LC608	CTTA	TTCCCTACACGACGCTCTTCCGATCTATTCNNNNGCACGCCCGTCGCTCAGTCCTAGGTATAATACTA	1st PCR forward
LC863	N/A	GTGACTGGAGTTCAGACGTGTGCTCTTCCGATCTNNNNNNAAAGGACCCGTAAAGTGATAATGAT	1st PCR reverse
LC415	N/A	AATGATACGGCGACCACCGAGATCTACACTCTTTCCCTACACGACGCT	2nd PCR forward
LC416	CGAGTAAT	CAAGCAGAAGACGGCATACGAGATCGAGTAATGTGACTGGAGTTCAGACG	2nd PCR reverse
LC417	TCTCCGGA	CAAGCAGAAGACGGCATACGAGATTCTCCGGAGTGACTGGAGTTCAGACG	2nd PCR reverse
LC420	TTCTGAAT	CAAGCAGAAGACGGCATACGAGATTTCTGAATGTGACTGGAGTTCAGACG	2nd PCR reverse
LC421	ACGAATTC	CAAGCAGAAGACGGCATACGAGATACGAATTCGTGACTGGAGTTCAGACG	2nd PCR reverse

Supplementary Table 9. qPCR primers and probes.

Targeted gene	**rrsA**	**hisI**	**lpoB**	**bioC**	**lgt**
Forward primer (5'----- 3')	GGATAACTACTGGAAACGGTAGC	CAGTGGCTGTTCCTGTATCAA	CGCTCATTACGTGCTGTACT	GATATCGAATCCCTGCCGTTAG	GCCACCCATCACAGCTTTA
Reverse primer (5'----- 3')	CTAATCCCATCTGGGCACATC	ATACAGTTTGGCGGTGTAGG	CCAGATAATTTCGCCCGTCT	CGGAGTGCCGTGGATAAAT	GCCGTAACCAATCAGGAACA
Probe (5'----- 3')	FAM -- TACCGCATAACGTCGCAAGACCAA -- BHQ1	FAM -- CGCAAATCTGCCGATCCGGAAAC-- BHQ1	FAM -- TAACGCTCCGACCCTACAAATGCA-- BHQ1	N/A	N/A

Supplementary References:

1. St-Pierre, F. *et al.* One-Step Cloning and Chromosomal Integration of DNA. *ACS Synth. Biol.* **2,** 537–541 (2013).
2. Jiang, W., Bikard, D., Cox, D., Zhang, F. & Marraffini, L. A. RNA-guided editing of bacterial genomes using CRISPR-Cas systems. *Nat. Biotechnol.* **31,** 233–239 (2013).
3. Depardieu, F. *et al.* A Eukaryotic-like Serine/Threonine Kinase Protects Staphylococci against Phages. *Cell Host Microbe* **20,** 471–481 (2016).
4. Chaveroche, M.-K., Ghigo, J.-M. & d'Enfert, C. A rapid method for efficient gene replacement in the filamentous fungus Aspergillus nidulans. *Nucleic Acids Res.* **28,** e97 (2000).
5. Teeffelen, S. van *et al.* The bacterial actin MreB rotates, and rotation depends on cell-wall assembly. *Proc. Natl. Acad. Sci.* **108,** 15822–15827 (2011).

Chapter 7

Subcellular localization of class A PBPs changes in response to stress

7.1 Introduction

The motion of membrane molecules along the bacterial envelope is not fully understood. In *E. coli*, the envelope comprises three layers: the inner lipidic membrane, the peptidoglycan and the outer lipidic membrane. Peptidoglycan synthesis enzymes are usually linked to the inner or outer membrane, either by having a fragment embedded in the membrane (like PBP2, PBP1AB or RodA) or by using an anchor (like LpoA or LpoB). Therefore, their diffusion is restricted to 2-dimensional motion along the envelope. However, this diffusion is subject to many constraints : many interactions have been found between the different enzymes, which may form large macromolecular complexes with other proteins [179] or with themselves [180]. Such interactions often span from one membrane to the other [181, 148]. Some geometry-sensing systems like MinCDE or Tol-Pal can also affect the localization of various membrane proteins [182, 24, 183].

In addition, peptidoglycan construction reacts to extrinsic stimuli. For instance, external mechanical constraints affect peptidoglycan synthesis so that cells retain their deformation when the constraint is removed [47, 46]. The molecular components of the envelope are therefore in complex interaction with their environment, rather than simply building new cells in a blind manner. The outer membrane itself is important for the mechanical properties of the cell, a role that has been neglected for a long time [184].

The peptidoglycan synthesis enzymes PBP1A and PBP1B were previously reported to have different roles in cell wall synthesis, despite their relatedness and their very similar activities. When both PBP1 enzymes are present, PBP1B is supposed to have a preference for cell division [152], and PBP1A a preference for elongation [154]. Accordingly, PBP1B localizes preferentially at the poles [154], but little is known about the robustness and origin of this localization. There is also evidence that PBP1A and PBP1B are not equivalent, as their deletions produce slightly different phenotypes: when PBP1B is missing, the strain is more sensitive to certain chemicals [185, 156, 157, 158], inserts less cell wall [159] and has reduced stiffness [155] (see also chapter 5).

For the first time, we explore the reaction of PBP1A and PBP1B's localization to various stimuli, including genetic modifications, mechanical shocks and osmotic pressure. Most of the work presented here has been done using the strain AV44, or its derivatives, which expresses a GFP-PBP1B fusion to ≈370%, and a mCherry-PBP1A fusion to ≈1300% of wild-type level. This is a potential confounding factor, as most molecules would now be inactive and it is hard to tell whether their localization is influenced by their concentration.

Nevertheless, we provide evidence that PBP1AB localization is not random and confirm that PBP1A and PBP1B have different patterns consistent with their alleged preferences of activity. As each of the class A PBPs is able to replace the other one when it is deleted, we investigate whether the localization patterns change when one or the other is deleted. This preliminary data show that subcellular localization of PBP1AB is directly related to their activities.

We then submit the cells to osmotic down-shocks as well as steady-state growth at different osmotic pressures and find that these stimuli exacerbate the patterns. In addition to polar and midcell localization, we also find that both enzymes can form patches on the sides of the cells under certain conditions. By overexpressing the cell wall hydrolase MepS, expecting to stimulate peptidoglycan cleavage and the need for more synthesis, we also find that the localization patterns of PBP1AB are amplified. Combined with growth measurement, this provides an interesting lead for better understanding the role of MepS, the activity of PBP1AB and the forces driving their localization.

Finally, as we previously found that the outer-membrane lipoprotein LpoB has a large effect on the single-molecule dynamics of PBP1B (Chapter 5), we looked at the localization patterns in the absence of either LpoA or LpoB. To our surprise, we find that some part of the patterns are independent of the presence of LpoAB, suggesting that the observed localization is the result of multiple superimposed phenomena.

7.2 Results

PBP1A and PBP1B have different sub-cellular localization

As PBP1A and B are inner-membrane proteins, they appear on the contour of the cell when imaged in epifluorescence with the focal plane in the middle (figure 7.1A). Both PBP1A and PBP1B have a marked tendency to localize at cell poles, but this tendency is stronger for PBP1B (figure 7.1B). PBP1A tend to be distributed more evenly around the cell. There is also a peak of intensity in the middle of the cell. This only occurs in larger cells, as seen in the demographs of figure 7.1C, indicating that mid-cell localization is linked to the formation of the new septum. However, this central peak of localization could often be seen before any constriction was visible in phase contrast.

We therefore sought to know whether the different localization of PBP1A and B were related to their difference in function. Even if the two enzymes have preferences for division or elongation, they are both capable to compensate for the loss of the other one. Thus, we deleted either PBP1A or PBP1B and measured if the sub-cellular localization of the other one is affected by the deletion. In the absence of PBP1A, PBP1B's localization to cell poles is less marked, and there is more signal on cell sides and at mid-cell (figure 7.1D). This confirms that the localization patterns that we see are reflecting the function of the enzymes in the cell, and reinforces the hypothesis that PBP1A and 1B have preferential roles for cell elongation and division, respectively.

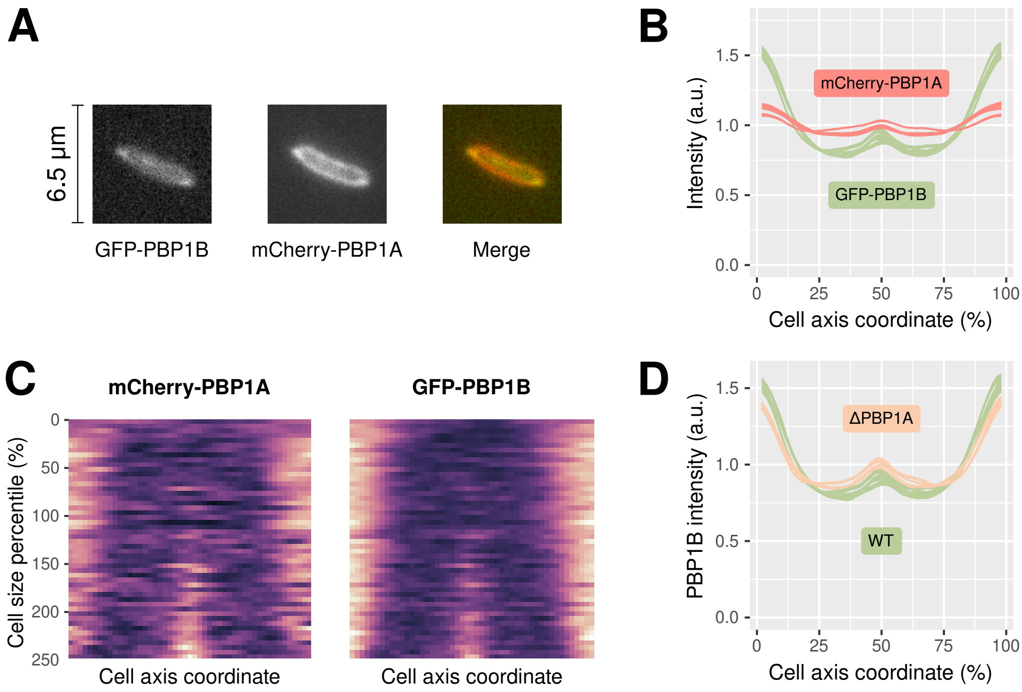

Figure 7.1: **Different localization for PBP1A and PBP1B. A:** Sample images of the PBP1AB fusions. **B:** Mean density of PBP1A (left) and PBP1B (right) along cell contour (0% and 100% are poles). **C:** Demographs of PBP1AB cell contour, sorted by area. Lighter pixels correspond to higher fluorescence. **C:** Mean density of PBP1B along cell contour, with or without PBP1A.

PBP1AB localization patterns are amplified after osmotic shocks

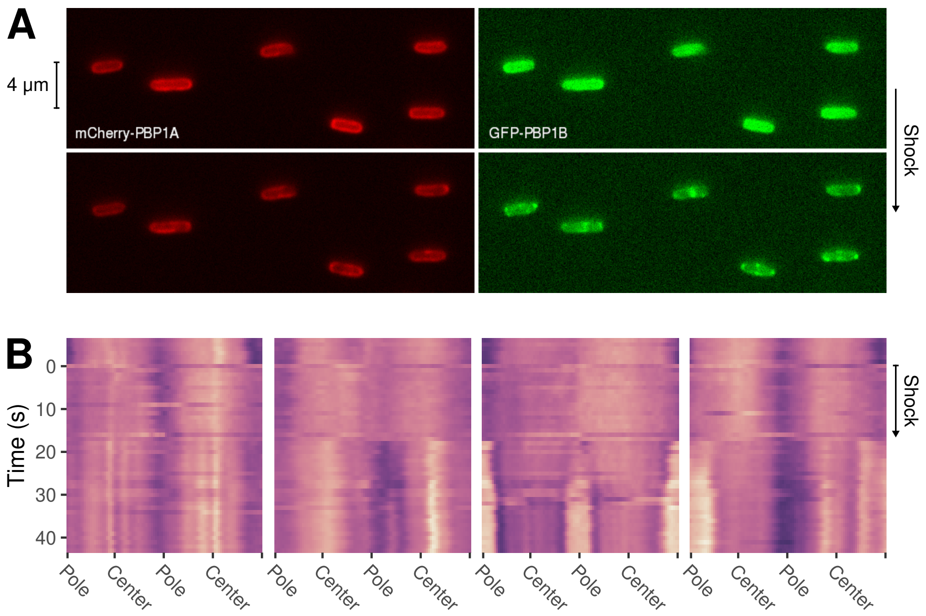

Figure 7.2: **Localization of PBP1AB during an osmotic downshock. A:** Fluorescence images of representative cells before and after a 1 osm/L osmotic downshock. **B:** Kymographs of PBP1A localization of a few cells during a 1 osm/L osmotic downshock. Lighter pixels correspond to a higher density of mCherry-PBP1A.

When measuring the elasticity of cells by trapping them in polylysine-coated tunnel slides [165], we noticed that sharp patterns of fluorescence appear during osmotic downshock (figure 7.2A and B). As the cells expand due to the drop in osmotic pressure, both GFP-PBP1B and mCherry-PBP1A relocalize to the poles and to the middle of the cell quickly after the shock. The localization to mid-cell was observed in most cells after shock, even in cells without any sign of constriction. This indicates that the cause of PBP1AB localization is already present at a very early stage of cell division. The change of localization appeared within seconds of the osmotic downshock, narrowing down the kind of cellular processes that could explain the pattern. For example, it is unlikely that any mechanism involving genetic control is involved. Asymmetric patches also appear frequently on the sides of the cells (figure 7.2B, first cell from the left).

This is reminiscent of a previous study in *C. crescentus* where PBP2 was found to localize at the poles after an osmotic shift [186]. In *E. coli*, the localization of PBP2 is more heterogenous than PBP1AB, possibly due to its association with MreB [146, 147], making it harder to follow its motion after an osmotic shock (figure 7.3).

As the osmotic downshock produces a sudden expansion of the cell, there may be large perturbations in the peptidolycan as well as the membranes. Many phenomena could give rise to the patterns we observed, however when doing a similar osmotic downshock on cells labelled with the outer-membrane dye FM4-64 (figure 7.4), the pattern of FM4-64 fluorescence remained uniform, meaning that simple movement of the outer membrane is not enough to account for the observed patterns.

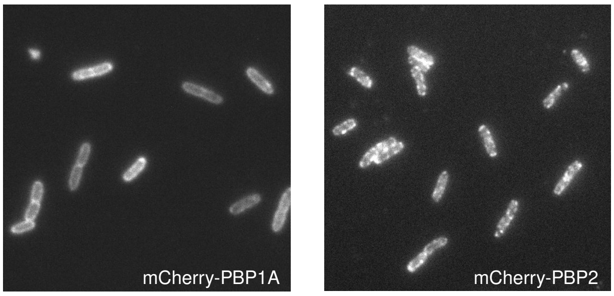

Figure 7.3: The distribution of PBP2 (right) is not as smooth as PBP1A (left).

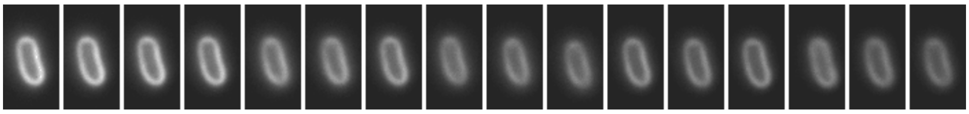

Figure 7.4: **FM4-64 localization during an osmotic downshock.** Each frame corresponds to 10 seconds. The fluorescence intensity decreases after each frame due to photobleaching.

Polar localization increases with medium osmolarity

Due to the relative brutality of osmotic downshocks, cells are subject to potentially complicated changes after the shock. Thus, we sought to establish the relationship between PBP1AB localization and osmotic pressure during steady-state growth. This way, we expect our observations to be easier to interpret. We grew cells in a range of osmolarities, by adding up to 600 mM of sodium chloride to the medium. During exponential growth, the cells were fixed with 4% formaldehyde then imaged. As *E. coli* possesses mechano-sensitive channels (including MscS and MscL), it is able to regulate its internal pressure in response to changes in external osmolarity [165]. We thus performed this experiment in parallel in a wild-type strain, and in a strain without the MscS and MscL channels.

The polar localization of both PBP1A and PBP1B tends to intensify as the salt concentration increases (figure 7.5A and B). However, this effect is much more marked in the absence of *mscSL*. In that case, there is a clear, monotonic relationship between the osmolarity of the medium and the fraction of PBP1A or PBP1B fluorescence that is found at the poles (figure 7.5A and B). Cell dimensions are not dramatically affected by the different salt concentration, so the shift in localization is not due to a change in cell size.

In addition to polar and mid-cell localization, we frequently found foci on the sides of the cells. Such patches usually (but not always) appear at the same exact location for PBP1A and PBP1B (figure 7.5C).

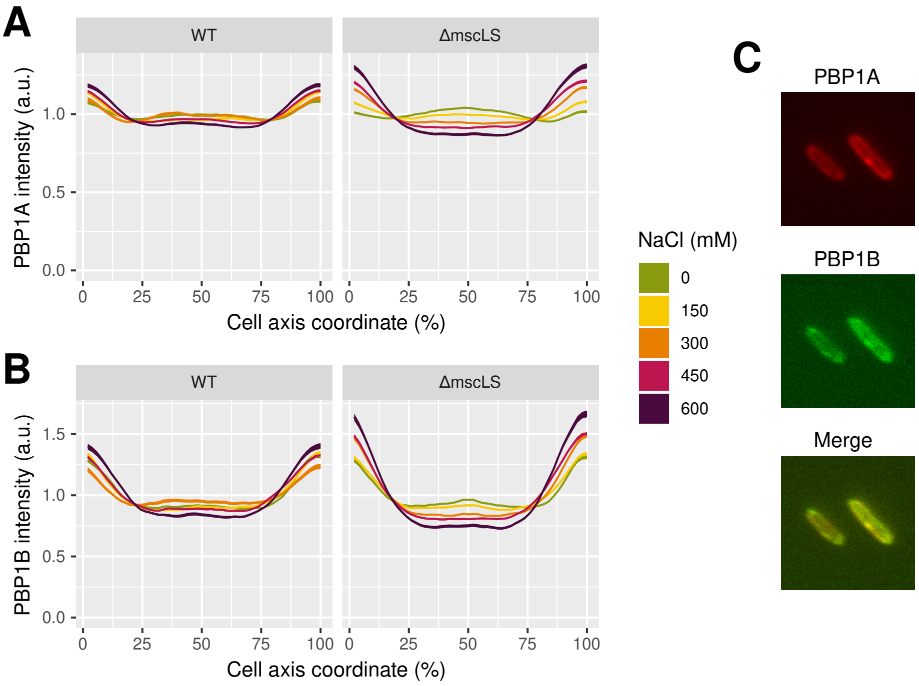

Figure 7.5: **Steady-state localization depends on osmotic pressure. A:** Density of PBP1A along cell contour of fixed cells, at different salt concentrations. **B:** Idem for PBP1B. **C:** Patches tend to be present in the same place for both PBP1A and PBP1B.

The peptidoglycan hydrolase MepS enhances the localization pattern

MepS is one of the three redundantly essential hydrolases of the cell wall. In standard M63 minimal medium, overexpression of MepS does not affect growth rate, though it lowers the maximum optical density reached by the culture by a small margin (figure 7.6A). When the osmolarity of the medium is increased, however, the overexpression of MepS causes a sharp decrease in growth rate compared to wild-type cells.

This effect was observed at all tested osmolarities, but its magnitude is variable and non-monotonic, with a minimum at intermediate osmotic pressures (figure 7.6B).

Localization patterns do not require LpoAB

We then tried to see if these patterns persisted in the absence of the outer-membrane proteins LpoA and LpoB, which are known to interact through the cell wall with PBP1A and 1B [148] and activate them. As we determined (chapter 5), deletion of LpoB abolishes the immobilization of PBP1B molecules, which then appear to diffuse randomly. It could be that the patches that we observed at the poles and on the sides of the cells are breaking points of the cell wall, exposing LpoAB molecules and causing a rush of PBP1AB in order to repair them.

However, the deletion of LpoB and LpoA does not abolish the localization patterns of PBP1B and PBP1A respectively. In fact, the re-localization of PBP1B to the poles due to MepS overexpression is even higher in ΔLpoB than with LpoB (figure 7.7). This suggests

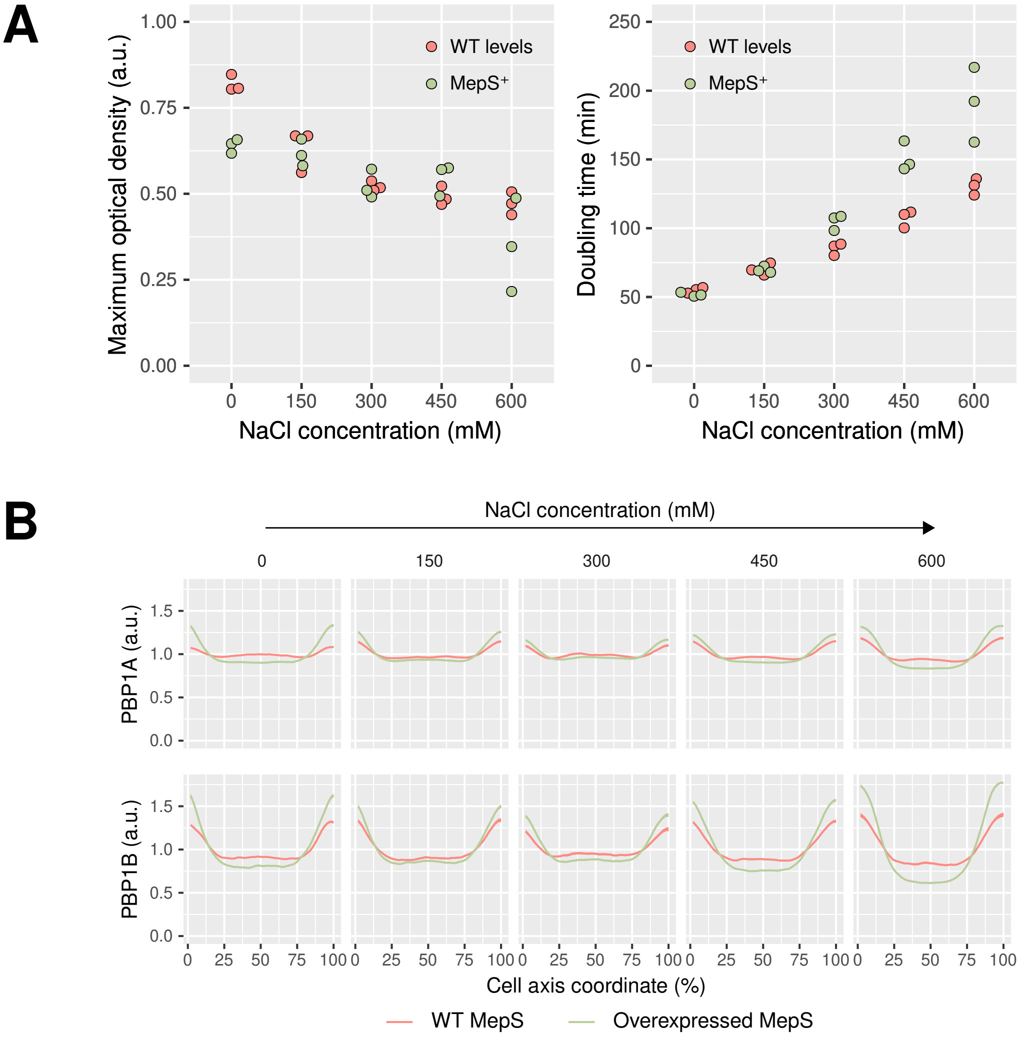

Figure 7.6: **MepS overexpression enhances PBP1AB patterns. A:** In Δ*mscLS*, MepS overexpression only has an effect on growth at high osmotic pressure. **B:** Density of PBP1AB along cell contour depending on MepS overexpression and salt concentration.

that the change of subcellular localization of PBP1AB upon MepS overexpression is not mediated by LpoAB.

7.3 Discussion

As, in the absence of LpoB, PBP1B molecules are all inactive and in a diffusive state, it seems that the large-scale pattern of polar localization is the "natural" localization of PBP1B, where it tends to go when it is not immobilized by LpoB.

Perhaps the polar preference is just determined by the enzyme's biophysical properties, independent on the state of the peptidoglycan and polymerization activity. It could be that the enzyme accumulates predominantly in regions where the cell wall is

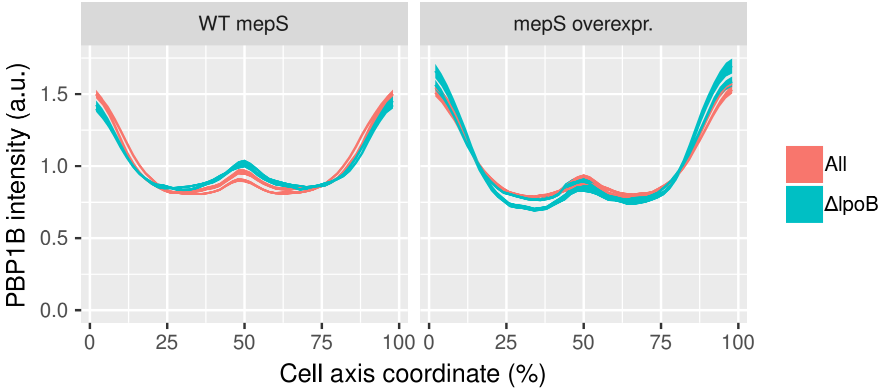

Figure 7.7: **The deletion of LpoB does not suppress patterns of PBP1B.** When MepS is overexpressed, the pattern is in fact stronger without LpoB.

the densest, and, depending on the internal pressure, the thickness of the peptidoglycan is different at the poles and on the sidewalls. Likewise, the volume of periplasmic space, or the distance between the inner membrane and the cell wall, may also be important factors in PBP1AB localization. It is likely that osmotic pressure causes some change in the thickness of the periplasm. Due to differences in mechanical strain, or due to the different proteins that link the inner membrane to the cell wall, the size of this spacing may be affected differently at the poles and on the sides of the cell. The observation that LpoB attenuates PBP1B's polar localization during MepS overexpression could be explained by the fact that, as it immobilizes PBP1B molecules, it maintains them in their lateral positions, where cell wall synthesis is needed, and prevents them from diffusing back to the poles. It can be speculated that the preference of PBP1A and PBP1B for elongation and division respectively is due to this difference in localization, and not due to differences in biochemical activity. However, experimental evidence, possibly *in vitro*, would be required to back up this hypothesis.

To understand PBP1AB's function, it may not be enough to look at their local interaction with LpoAB and with the cell wall (chapter 5), and the global pattern due to other local cues might play an equally important role.

Chapter 8

Interaction between D-aminoacids and cell wall synthesis

8.1 Introduction

The mirror images of L-aminoacids, D-aminoacids, are extremely rare in the biological world. However, some of them, such as D-methionine and D-leucine, are known to be synthesized endogenously by diverse bacterial phyla. They may be inserted occasionally in the peptidoglycan, where they are thought to play a regulatory role in stationary phase remodeling and biofilm formation [187, 188].

At high doses, typically higher than 10 g/L, D-methionine is toxic for *E. coli*. The mechanism of toxicity is unclear, but may be due to the insertion of D-methionine in the peptidoglycan, which could create imperfections in the cell wall or prevent further cross-linking. It is also not excluded that D-methionine directly inhibits transpeptidases by competitively binding to their active site.

The deletion of PBP1B was previously reported to increase the sensitivity of *E. coli* to high concentrations of D-methionine [185]. Yet, it is not known why the two class A PBPs would have different reactions to D-aminoacid treatment. Understanding the effect of D-methionine could help understand both the physiological role of D-aminoacids and the function of the redundantly essential PBP1A and PBP1B.

8.2 Results

At low aPBPs concentration, cells become highly sensitive to D-aminoacids

To better understand how this difference in sensitivity comes about, we grew strains lacking either PBP1A, PBP1B, or having both of them repressed strongly (using the strain 14-20 from chapter 5), in the presence of different concentrations of D-methionine. We calculated the growth rate and the maximum optical density reached by the culture (figure 8.1A).

As expected, the ΔPBP1A strain is not affected, while the ΔPBP1B strain is more sensitive and could not grow with more than 1 mg/ml of D-methionine. Quite surprisingly, the 14-20 repressed strain is extremely sensitive to D-methionine treatment, with

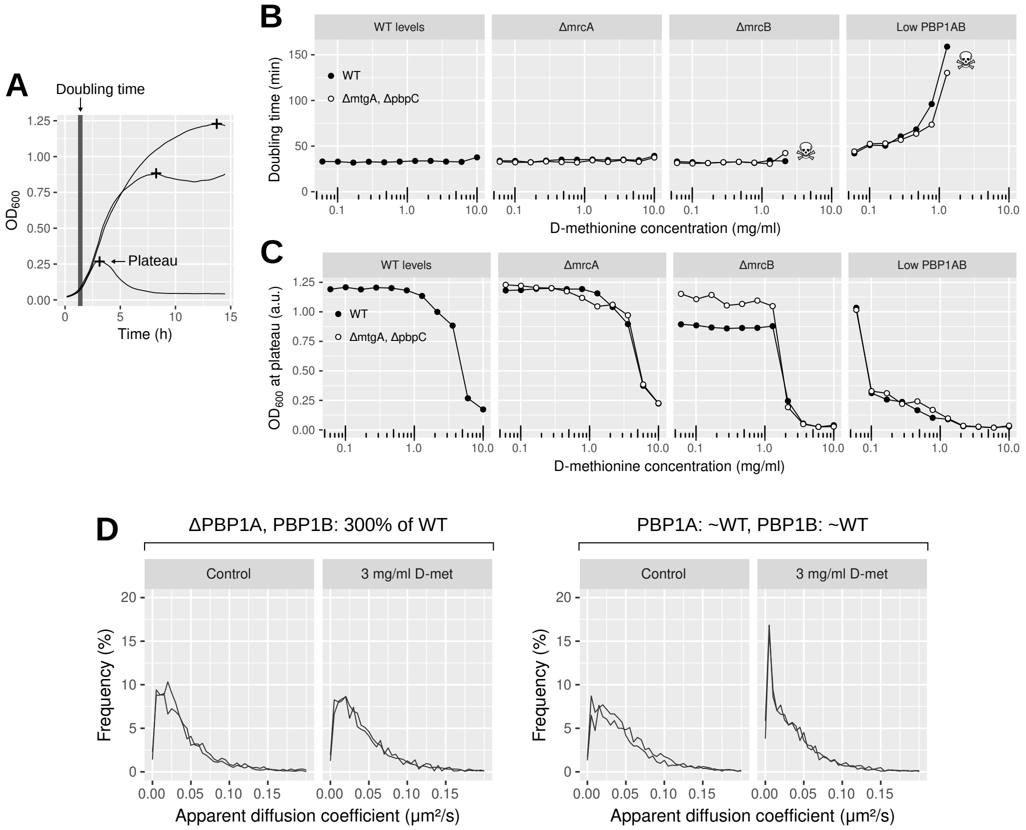

Figure 8.1: **Strong repression of the class A PBPs increases sensitivy to D-methionine.**
A: Schematic of the two parameters extracted from growth curves to quantify fitness. **B:** Doubling times of strains with class A PBPs either deleted or repressed, as a function of D-methionine concentration. The skull logo indicates than no exponential growth was observed. **C:** Optical density reached by the same strains at the plateau, as shown in panel A. **D:** Distribution of PBP1B's apparent diffusion coefficient when treated with 3 mg/ml of D-methionine. *Left* is from a strain with high PBP1B and no PBP1A ; *right* is in a strain where PBP1A and PBP1B are at wild-type level. Each line represent one biological replicate.

a minimum inhibitory concentration (MIC) at least 20 times lower than in ΔPBP1B (figure 8.1B and C), and 40 times lower than the wild-type. Contrary to the wild-type or ΔPBP1B, which does not exhibit any slow-down of growth at sublethal concentrations of D-methionine, the repressed strain's growth rate seems to reflect directly the concentration of D-methionine (figure 8.1B). Interestingly, the strain lacking PBP1B reaches a lower OD plateau than the other strains, regardless of D-methionine concentration, and this effect disappears when the non-essential class A PBPs MtgA and PBP1C are deleted (figure 8.1C).

To estimate the minimal amount of PBP1AB needed to grant resistance to D-methionine, we repressed PBP1A and PBP1B to 25 different combinations of levels, using the crRNA matrix from Vigouroux et al. [82]. We then grew this matrix in the presence of 1 mg/ml of D-methionine (enough to kill 14-20 but not ΔPBP1B). Overall,the doubling times were not drastically affected, and only the repression of one PBP1 combined with the deletion of the other one produced an effect on maximal OD (figure 8.2), confirming that the increased sensitivity only appears at critically low levels of PBP1AB.

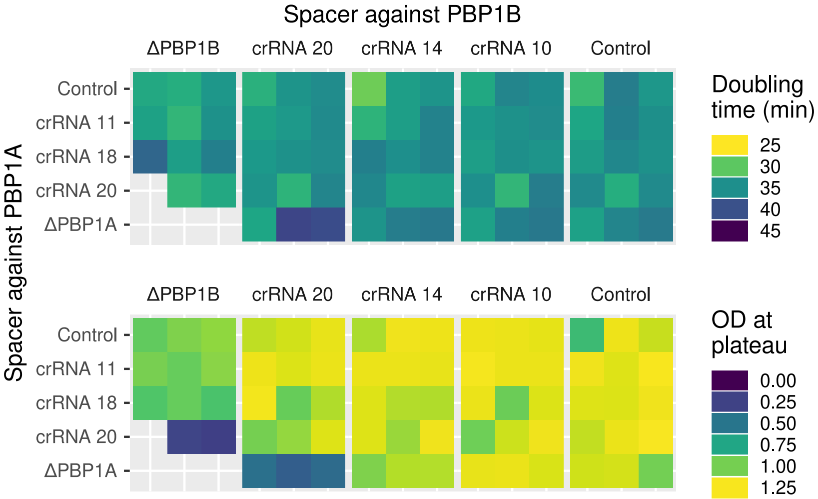

Figure 8.2: **D-methionine sensitivity at different levels of PBP1A and PBP1B.**
The matrix of CRISPR spacers used in this experiment is described in [82]. The indicated crRNA numbers are the number of matching base pairs between the guide and the target. We estimate that the strain with crRNA 10 for PBP1B and crRNA 14 for PBP1A is repressed to levels close to wild-type. Top: doubling time, bottom: maximum optical density. "Control" refers to a non-targeting spacer. Each square represents one replicate (3 per conditions).

D-methionine prevents PBP1A activity, much more than PBP1B

To gain more insight into D-methionine's mode of action, we measured single-molecule PBP1B diffusion in presence of 3 mg/ml of D-methionine. According to our growth experiments (figure 8.1BC), this concentration of D-methionine has no effect in ΔPBP1A but would result in cell death in ΔPBP1B. In the presence of PBP1A at wild-type level, the bound fraction of PBP1B is greatly increased by D-methionine treatment, similarly to what we obtained when PBP1A is deleted (figure 8.1D, right). In a ΔPBP1A strain, the bound fraction of PBP1B is mostly unaffected by to D-methionine treatment, and may in fact become lower (figure 8.1D, left). This contradicts the idea that PBP1B repairs damage in the cell wall due to D-methionine, as PBP1B activity would be expected to increase. This suggests that D-methionine inhibits PBP1A, directly or not, thus giving more work for PBP1B and explaining why a strain lacking PBP1B is more sensitive.

D-methionine treatment is more severe when MepS is over-expressed

While the exact effect of D-methionine on *E. coli* is not clear, we previously found that it interferes with PBP1A's activity and provokes cell lysis if the level of PBP1AB is not sufficient. The peptidoglycan-hydrolase MepS, that we use extensively in chapter 7, also seems related to D-methionine treatment in some way: the deletion of *nlpI*, an outer-membrane protein the negatively regulates MepS, also makes the strain more sensitive to D-methionine [189], but only if MepS is present. This negative regulation presumably relies on the protease Prc, that uses NlpI as an adaptator to degrade MepS [190, 191]. Using a strain expressing MepS from an inducible promoter, we found that overexpression of MepS itself also made cells more vulnerable to D-methionine treatment (figure 8.3).

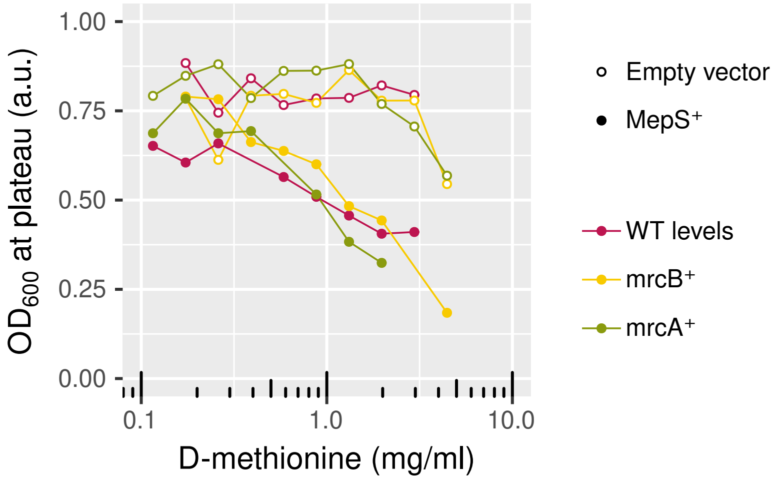

Figure 8.3: **The over-expression of the hydrolase MepS makes cells more sensitive to D-methionine.** "+" means that the enzyme in question is over-expressed from an inducible promoter. When MepS is overexpressed, the minimal inhibitory concentration of MepS become lower. The cells are still able to grow to some extent, but the population collapses before reaching a high optical density. The over-expression of PBP1A or PBP1B does not seem to compensate this effect in a major way.

Genome-wide CRISPR screen identifies processes related to D-methionine

As many processes seem to be interlinked and there is a lot of uncertainty about the function of each part, we decided to scale up and find if other genes are affected by D-methionine treatment. For this, we used the CRISPR library presented in [79] in a variety of deletion strains, either in the presence or absence of a sublethal concentration of D-methionine. The library is transfered to each strain by cosmid transduction, then the pooled collection of strains are induced and grown in competition. Finally, high-throughput sequencing of the CRISPR guides in the population allows to find the fitness of each strain.

Among the strains tested here, there were strains lacking PBP1A, PBP1B, MepS, MtgA, PBP1C and others. We also included a strain that over-expresses MepS. The screening itself (competition and sequencing) was done by Lun Cui. Unfortunately, the sequence coverage was very limited, and a lot of guides had zero reads and therefore cannot be analyzed accurately. It made it especially difficult to compare different strains, however we could use the few strains that had a good coverage to investigate D-methionine sensitivity.

Thus, we compared the fitness cost of repressing each gene, either in LB, or in LB with 2 mg/ml of D-methionine. Among the expected results, we could confirm that the repression of NlpI, Prc, PBP1B and LpoB increased D-methionine sensitivity, as did MepS over-expression. In addition, we found that members of the Tol-Pal system (*tolA*, *tolB*, *tolR*, *pal*) also greatly increased the sensitivity to D-methionine, as well as *ftsB* and *envC*, two proteins involved in cell division (figure 8.4, left).

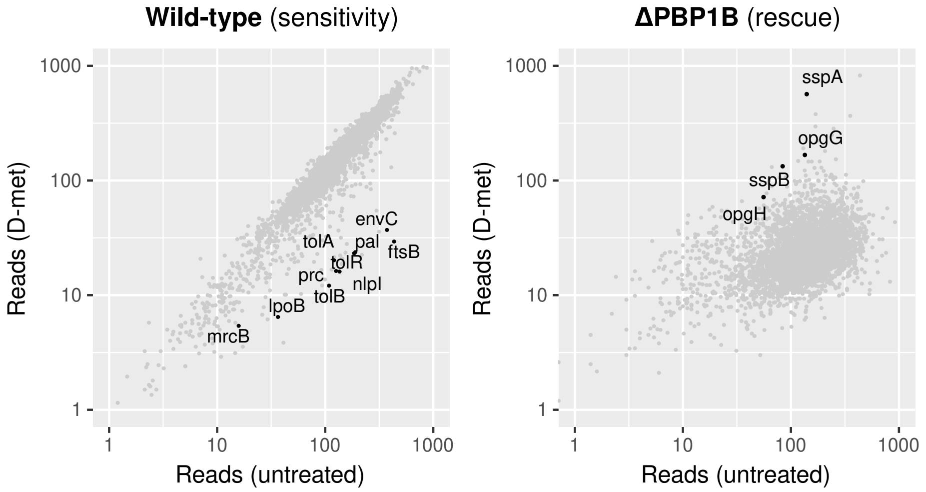

Figure 8.4: **CRISPR screen identify genes that affect D-methionine treatment.** The plots show the number of reads obtained in LB, or in LB with 2 mg/ml of D-methionine. Each point represents the average of all the guides from the library that target one gene. **Left:** Points that stand below the diagonal show that repressing this gene increases sensitivity to D-methionine. **Right:** In a ΔPBP1B background, points that are above the diagonal show that this gene rescues the over-sensitivity to D-methionine due to ΔPBP1B.

Interestingly, a few genes would consistently rescue a ΔPBP1B strain from D-methionine sensitivity (figure 8.4, right). Among them were the stress-response regulators *sspA* and *sspB*, and the glucan synthesis enzymes *opgG* and *opgH*.

Before further investigation of these results, we sought to validate the potential D-methionine rescue by deletion mutants. Using strains from the Keio collection [129] as donnors, we made strains with repressible PBP1AB and a deletion of either *sspA* or *opgG*. These strains were grown in the presence of 2 mg/ml of D-methionine, with the levels of PBP1AB set to either wild-type level, or strongly repressed with the "14-20" pair of guides (see chapter 5).

This experiment confirmed that these two genes abolished the extra sensitivity of a strain with low PBP1AB to D-methionine (figure 8.5). In a strain lacking *sspA*, the re-

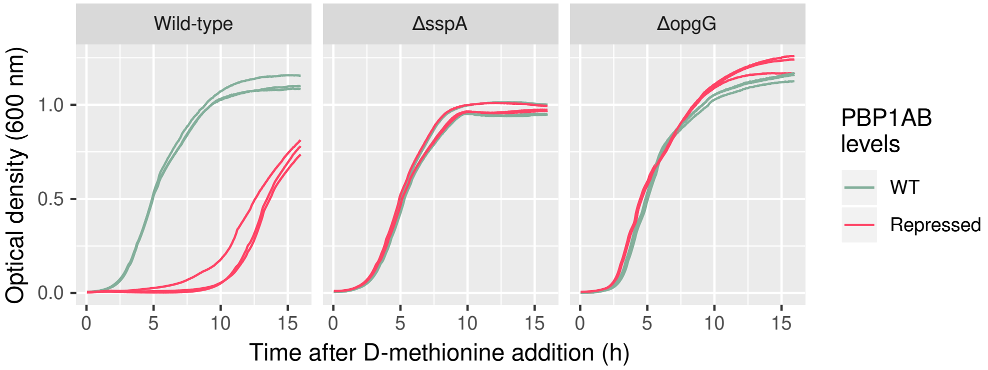

Figure 8.5: **Validating the hits from the CRISPR screens** Growth curves of strains with PBP1AB either at WT level, or strongly repressed, in 2 mg/ml of D-methionine. The repressed strain is very sensitive to D-methionine, but this disappears when *sspA* or *opgG* are deleted. After about seven hours, the repressed wild-type strain starts growing again. This is likely due to the selections of mutants where CRISPR repression is not efficient anymore.

pression of PBP1AB had no effect on growth in 2 mg/ml of D-methionine. As *sspAB* are involved in stringent starvation response and interact directly with the RNA polymerase [192], they might be related to the genetic feedback we observed on PBP1B (chapter 5) and it is possible that their deletion raised levels of PBP1B, explaining the rescue. This remains to be investigated. One possible way Δ*opgG* could rescue D-methionine hypersensitivity is through its effect on periplasm thickness [193], as this could stimulate aPBP's activity by making the Lpo/PBP1 interaction easier. In the strain lacking *opgG*, interestingly, the repression of PBP1AB made the cells grow to a higher maximal optical density than at wild-type levels. Further experiments will be required to elucidate the origin of this somewhat paradoxical phenomenon. As optical density measurements are influenced not only by the number of cells, but also by cell morphology, it is possible that the repression of PBP1AB starts to have a noticeable effect on cell shape when *opgG* is absent.

Related to cell constriction [194] and the maintenance of outer-membrane integrity [195, 183], the Tol-Pal complex has also be shown to enable polar localization of other proteins, in conjunction to membrane curvature [182]. The glucans synthesis genes *opgGH* are also interesting, as glucans are major regulators of the pressure in the periplasm, and are known to affect the thickness of periplasmic space [196]. All together, these provides a new lead to investigate the complex interaction between class A PBPs, hydrolases, osmotic pressure and D-aminoacids.

Chapter 9

More CRISPR exploration

9.1 Genetic regulation of the *mreBCD* operon

In chapter 5 and [133], we used CRISPR to change the level of a GFP-MreB fusion. When the concentration of MreB becomes lower, the cell diameter increases but the growth rate is not dramatically affected until very low levels. However, it quickly appeared that the repression was not as strong as expected, hinting at the possibility of a negative feedback on MreB's expression. As the *mreB* gene is part of an operon that also contains *mreC* and *mreD*, that would mean that the three proteins are affected by the feedback loop.

At first, we sought to use fluorescence microscopy to measure the strength of the potential feedback, but to quantify the number of GFP proteins per generation, we would need to find the total amount of GFP per cell. This is made difficult by the large changes in shape that the cells undergo, especially as the cells become spherical and thus a larger part of it may escape the focal plane. Rather than using the microscope, we used flow cytometry instead. In that case, the fluorescence signal is recorded by a photo-multiplier, without any focal plane, so we can make a less biased measurement of the total amount of GFP by integrating the area under the fluorescence peak.

This way, we confirmed the presence of a strong feedback loop on the level of GFP-MreB (figure 9.1), as the same CRISPR guides would produce a much weaker repression on $\mathrm{P}_{\mathrm{mreB}}$-*gfp-mreBCD* than on the constitutive P_{127}-*gfp*. To investigate the origin and mechanism of this feedback, we performed the same experiment in a mutant lacking *bolA*. BolA was shown to regulate MreB's expression [197], as well as other enzymes related to cell wall synthesis. In the absence of *bolA*, the strength of the feedback on MreB was attenuated, but not quite suppressed (figure 9.1, right). This suggests that BolA is implicated in the negative feedback on MreB's expression level. However, the exact genetic network is likely to be complex and tightly linked to cell wall synthesis and growth, as multiple cell wall carboxpeptidases (PBP5, PBP6) are also regulated by BolA [198], and their function is not well understood.

This experiment demonstrates that CRISPR knock-down can be used easily to discover genetic regulations and to find genes that are responsible for such genetic control.

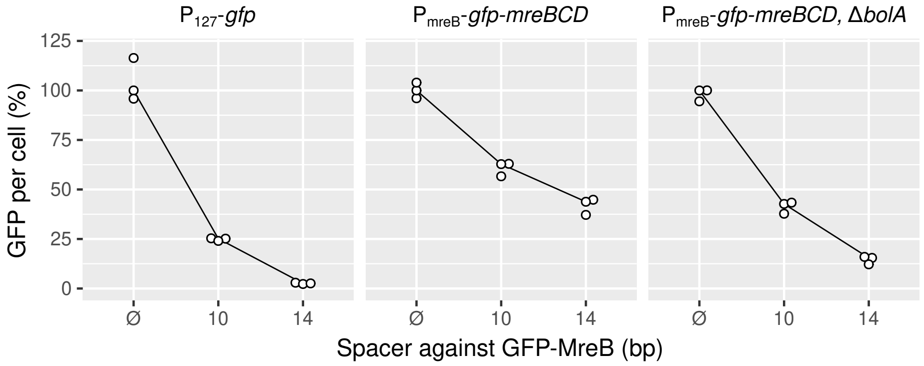

Figure 9.1: **Strong genetic feedback regulates MreBCD expression.** The same CRISPR guides with 10 bp or 14 bp of complementarity, are used on either a constitutive GFP or GFP-MreB in native locus. MreB's expression is subject to negative feedback, that disappears when *bolA* is deleted. Points are independent replicates.

9.2 Anti-CRISPR proteins to reverse the repression

Due to the long-term binding of dCas9 to its target, combined with the low concentration of effector that is necessary to maintain strong repression (see chapter 2), it can take a long time for the expression of the target to recover after one washes away dCas9's inducer [66, 109]. To make this system truly reversible, a possibility would be to use one of the antagonists of dCas9 that are found in nature. Anti-CRISPR proteins are widely found in phages' genome, as a counter-attack against the CRISPR immune systems. The mechanisms discovered so far work primarily by preventing interaction between CRISPR effectors and the PAM next to the target [199]. We thus decided to use the small anti-CRISPR protein AcrIIA4, as it was shown to work on SpCas9 [200]. First, a strain expressing mCherry and a CRISPR guide against mCherry was grown overnight with induction of dCas9, in order to get a population of cells that are already repressed. This strain also carried a plasmid with an inducible *acrIIA4* cassette, though this was not induced yet. As a control, we also had the same strain with an empty vector without *acrIIA4*, and a strain with a non-targeting CRISPR spacer to know what the original expression is. Figure 9.2 shows a timecourse, measured with a fluorimeter and spectrophotometer, of these three strains after the anti-CRISPR is induced. The fluorescence per cell is calculated by dividing the total fluorescence by the OD_{600} of the culture.

After the anti-CRISPR is induced, the level of mCherry returns to a non-repressed level after a few hours. This shows that, when both a dCas9 complex and an anti-CRISPR are expressed, the anti-CRISPR is dominant and there is no repression. However, the recovery of expression took about 5 hours. To explain this slow behaviour, one needs to consider that AcrII4A is not able to displace the dCas9 complex once it is bound to the DNA. The guide we used here, a sgRNA with 20 matching nucleotide on mCherry, produces a very strong repression and only about 1% of the collisions with the RNAP are able to kick dCas9 out of the DNA. Thus, even if the anti-CRISPR can bind to dCas9 once it has been kicked out, and prevent a re-binding, many transcription

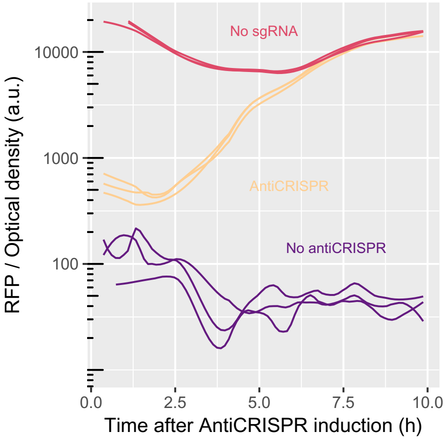

Figure 9.2: **Anti-CRISPR proteins can be used to restore expression after knock-down by dCas9.** Here the small anti-CRISPR protein AcrIIA4 is expressed in a population where the RFP reporter was already repressed, causing the expression of the reporter to increase back to non-repressed levels. Lines are independent replicates.

events are necessary to clear the target from the repressors.

Chapter 10

Discussion

10.1 Summary of the results

Bacteria exhibit a vast range of possible shapes, yet each species maintains its own shape with a great precision. It is an important characteristic, that has been selected through evolution and is passed on from generation to generation using specific instructions from the genome. In the case of bacteria, the relationship between the DNA sequence and the shape of the whole organism is very complex, as there is no construction plan and no cell-wide cytoskeleton to use as a canvas. Rather, the shape information is spread out within many enzymes that continuously construct and remodel the peptidoglycan. Together, these enzymes form a dynamical system with many essential parts. To understand what the different parts do, we constructed modified strains with various concentrations of each components, and looked at the resulting organisms.

To gain control over the concentration of these enzymes, we used the ability of CRISPR effectors to knock-down bacterial genes. The first part of this project was to characterize the properties and mechanism of this method on a toy model that expresses two fluorescent proteins. We showed that RNAP can transcribe targets even when they are occupied by dCas9, by actively kicking dCas9 out with a probability that depends on guide/target complementarity. If dCas9 is saturating the target, the relative repression depends only of the passage probability of the polymerase (PPP), and is independent of the target gene's transcription rate. If dCas9 is not saturating the target, relative repression depends on promoter strength, and we developed a mathematical model to predict the resulting expression level. Based on this model, we found interesting properties of CRISPR knock-down that could be harnessed as a technology.

In particular, mismatched guides allow to repress the target without addition of noise. CRISPR knockdown can also be used to uncover and characterize genetic feedback, as the change in protein level affects the transcription rate from the promoter. This situation turned out to be very frequent. We found a strong genetic feedback on PBP1B expression (chapter 5), that was, curiously, not found on PBP1A. The genes *sspA* and *sspB*, identified in the D-methionine CRISPR screen (chapter 7), could be involved in this feedback, and future measurements on deletion strains will confirm or dismiss this hypothesis. MreB was also found to be involved in a negative feedback loop (chapter 9).

Currently, the main limitation of CRISPR knock-down is that the relationship between the guide's sequence and the PPP is quite unpredictable. To address this issue, we designed an experiment to provide a clean data set of guide RNAs, target sequences and associated PPPs, that will in future works be used to build predictive models of PPP from the target sequence information.

Armed with this tool, we perturbed the concentration of the different enzymes that polymerize the cell wall and play an important role in determining cell shape.

First, by repressing the *mrdAB* operon, we could show that below wild-type level, stochastic fluctuations of PBP2/RodA levels created morphological diversity in the population. In an echo to this work, another laboratory showed that the stoichiometry of PBP2 and RodA must be tightly regulated [44], hightlighting the advantage of acting on genes in their native operon with a low-noise method.

We then used dCas9 to change the levels of the redundantly-essential cell wall polymerases PBP1A and PBP1B. We estimated the minimum amount of PBP1A and PBP1B for survival to be around 20%. Below this level, the cultures lysed a few hours after induction. At all the other levels, the cells grew at the same speed as the wild-type and we did not find a large variation of cell dimensions. Upon careful examination, the level of PBP1AB is positively correlated with cell diameter, something that was also observed in *B. subtilis* [133], but the magnitude of the effect is much smaller. Overall, class A PBPs have an "all-or-nothing" behaviour.

Focusing on a strain called "14-20", that expresses low amounts of PBP1A (20%) and PBP1B (30%), we found that it inserts as much peptidoglycan as the wild-type but has different mechanical properties: cell elasticity is increased and it is less resistant to osmotic shocks. This indicates that the repression of class A PBPs affects the cell not by reducing peptidoglycan polymerization, but by doing so in a structurally different way. By looking at the 2D-diffusion of PBP1B, we found that the immobile fraction of PBP1B increases or decreases depending of the total concentration, so that the number of bound molecules is roughly constant. The lack of PBP1A also causes an increase in PBP1B bound fraction, showing that PBP1B's mobility adapts to the need for cell wall insertion. This change in diffusion dynamics is likely mediated by LpoB, as the deletion of LpoB greatly decreases the immobile fraction of PBP1B. Finally, by examining resistance and recovery to D-cycloserine treatment and to mDAP depeletion, we showed that PBP1B was useful for maintaining cell wall integrity, thus making it more resistant to future stress, and also for repairing it after stress.

Within the cell, PBP1A and PBP1B have different sub-cellular localization. Both tend to be enriched at the poles, but this pattern is stronger for PBP1B. When one of them is deleted, the localization of the other changes to compensate, showing that the localization patterns are related to the enzyme's function. After an osmotic downshock, PBP1AB localization patterns are amplified and patches often appear on the sides of the cell. Polar localization is also magnified by high osmotic pressures. As a further demonstration of the link between peptidoglycan state and PBP1AB localization, we showed that an over-expression of the hydrolase MepS enhances the localization pattern. Interestingly, this happened even in the absence of outer-membrane activators, suggesting that the localization is not due to LpoAB sensing the state of the peptidoglycan, but rather to a more indirect phenomenon, possibly involving periplasmic volume or membrane dynamics.

When PBP1A and PBP1B are low, cells become highly sensitive to D-methionine, even more so that a ΔPBP1B strain. It is likely that D-methionine impairs PBP1A's activity, as our single-molecule tracking data suggests. We performed a series of genome-wide CRISPR screens to find which other processes are associated with D-methionine sensitivity and resistance, and found a link with the stringent starvation response and to the synthesis of periplasmic glucans.

Finally, in addition to the work presented in this thesis, I also contributed to other projects, for example by designing and constructing strains with tunable levels of various genes.

10.2 Status of the projects

Publications

Antoine Vigouroux, Enno Oldewurtel, Lun Cui, David Bikard, and Sven van Teeffelen, Tuning dCas9's ability to block transcription enables robust, noiseless knockdown of bacterial genes. *Molecular Systems Biology*, 14(3):e7899, March 2018, ISSN-1744-4292. `doi:10.15252/msb.20177899.`

Lun Cui, **Antoine Vigouroux**, François Rousset, Hugo Varet, Varun Khanna & David Bikard, A CRISPRi screen in E. coli reveals sequence-specific toxicity of dCas9. *Nature Communications*, 9(1):1912, May 2018, ISSN 2041-1723. `doi:10.1038/s41467-018-04209-5.`

Michael Dion*, Mrinal Kapoor*, Yingjie Sun*, Sean Wilson, Joel Ryan, **Antoine Vigouroux**, Sven van Teeffelen, Rudolf Oldenbourg, Ethan C Garner, Bacillus subtilis cell diameter is determined by the opposing actions of two distinct cell wall synthetic systems. *Nature Microbiology*, accepted, 2019.

Manuscripts

Antoine Vigouroux, Baptiste Cordier, Enno Oldewurtel, François Simon, Gizem Özbaykal, David Bikard & Sven van Teeffelen, Class A PBPs maintain cell wall homeostasis at an intermediate scale in diderm bacteria *Submitted.*

Eva Wollrab*, Gizem Özbaykal*, **Antoine Vigouroux**, Baptiste Cordier, Francois Simon, Enno Oldewurtel, David Bikard, and Sven van Teeffelen, Binding of the major transpeptidase PBP2 determines localization of rod-complex formation independently of cell-envelope curvature. *Submitted.*

Ongoing projects

The ppppredictor: designing CRISPR guides with defined polymerase passage probability. *Experimental part coming soon.*

Sub-cellular localization of class A PBPs changes in response to stress.
Requires verification at wild-type levels of PBP1AB expression.

Interaction between D-aminoacids and cell wall synthesis.
Still in exploration.

* Equal contribution.

10.3 Future work

Mistakes and dead ends

On the way to understand cell wall synthesis, there were many dead ends and artifacts, and there will continue to be. The extensive use of fusions with fluorescent tags is a common source of artifacts in the field of microscopy-heavy molecular biology. For about ten years, it was believed that MreB formed a spiral cytoskeleton within *B. subtillis*'s cells, a structure that was in fact created artificially by the presence of the yellow fluorescent protein on the N-terminus of MreB. In my case, fusing mCherry and GFP to PBP1A and PBP1B caused a dramatic change in their expression levels. This was unfortunate, given that the main goal of the fusions was to study the concentration of these enzymes. The fact that overexpression of PBP1AB did not produce any obvious phenotype, something that was not known at the time, helped this accidental overexpression go unnoticed. In addition, it is likely that the difference of expression happens at the translational level, making it impossible to detect by quantitative PCR. We even performed absolute quantification of GFP-PBP1B, using GFP fluorescence and an anti-GFP antibody, without noticing the over-expression as all these measurements relied on GFP. Only mass spectrometry allowed us to compare directly the levels of the fusions to the levels of the wild-type enzymes.

Another major impediment for this work was the Bad Seed Effect. While still unexplained, we ended up finding a workaround and the CRISPR method could still be used, after a few weeks of reconstructing every strain. Further work is currently being undertaken in the lab to identify the cause of the Bad Seed Effect. More generally, this kind of unpredictable problem is hard to avoid, aside from systematically testing every part separately to find potential effects of allegedly innocuous vectors. Fortunately, this happened in the context of fundamental research, and I hope nothing similar ever happens to the people using CRISPR to edit human embryos.

Technological improvements

Among the countless technologies that are flourishing in the field of molecular biology, a few seem particularly promising, especially when they allow to have more confidence in experimental results.

The rise of large-scale proteomics, and their increasing accessibility, will be beneficial for all studies concerned about gene expression levels. Data-Independent Acquisition (DIA), as we used in chapter 5, allows to quantify proteins without any label. Thus, it is one of the best tools to check the level of protein fusions. It also does not require antibodies specific to the protein of interest, although specific fragmentation peptides are necessary for absolute quantification. Moreover, it directly measures the amount of protein, so translational effects can be accounted for. This is not the case with quantitative PCR or RNA-sequencing, for example, as they only count the number of mRNA transcripts. As it is proteome-wide, we can also monitor changes in the expression levels of other genes in the cell, which may be a way to explain puzzling results that would be confusing otherwise.

When preparing strains for molecular biology, we usually sequence only some parts of the plasmids we construct, typically the insert, by Sanger sequencing. In addition, strain construction often requires to grow the cells over multiple nights, making mutations inevitable. As high-throughput sequencing becomes more widely available, researchers should be able to check the full genome of their working strains more often and avoid many non-reproducible results.

The use of fluorescent fusions for single-molecule tracking opens the way for more direct measurements of the dynamics of cell-wall synthesis. As new tags and dyes are being developed, a lot of work is still required to make sure they give the expected results in bacteria. For example, a tag that binds a fluorescent molecule with a fast turnover can be used to circumvent the problem of photo-bleaching [201]. To bypass the need for fusions, an interesting perspective can be found in genetically recoded organisms [202, 203]. In the genome of these organisms, all TAG stop codons have been replaced by TAA, and the release factor RF1 is deleted. This turns the TAG stop codon into a regular codon that can code for an aminoacid as long as a corresponding tRNA is provided. This way, it is possible to incorporate unnatural aminoacids in proteins, and possibly fluorescent dyes. This should minimize the effect of the tagging on protein's function and localization and hopefully help to avoid artifacts.

Another rapidly improving technology is electron microscopy, as well as atomic-force microscopy (AFM) [204]. As these methods achieve better resolution, they should allow to analyse the state of the bacterial cell wall in more detail and distinguish structural features that cannot be seen by optical microscopy. For instance, AFM has already been used to see individual glycan strands from the peptidoglycan of *E. coli* [169]. This information will be valuable to understand whether the pre-existing features of the cell wall, such as the glycan strands that are already present, play a role in determining where the polymerases are going to insert new material. It is possible, for example, that the motion of MreB filaments is in part influenced by the position and orientation of the previous generation of glycan strands. As it allows to see the structure of peptidoglycan at an intermediate scale between the molecular level and the global cell shape, AFM, could help knowing why a strain with a low level of PBP1A and PBP1B is more elastic than normal, despite having the same amount of peptidoglycan (chapter 5).

Next steps

More research will be required to clarify some points that remain unclear in this work.

The CRISPR-based method to control the levels of genes still has room for improvement, in particular regarding the predictability of repression. When succesfully synthesized, the “pppppredictor” CRISPR library should allow to understand better the sequence determinants of repression, to identify potential off-target binding sites and to design tailored CRISPR guides to get a range of repression on new targets, without the need for fusions. This big dataset should require a large amount of bio-informatics to exploit it as much as possible. In the best case, the model could bring valuable information on the mechanism of R-loop extension and RNAP/dCas9 collisions.

Our experiments on the role of PBP1AB in cell wall synthesis brought new information and allowed to exclude some previous hypothesis, but they also revealed that this machinery has many interacting parts. In particular, we observed many unexplained relationships between the class A PBPs, the hydrolase MepS, D-aminoacids, osmotic pressure and the subcellular organization of membrane proteins. All these elements appear to be connected, and step by step progress on the characterization of each part should hopefully allow to solve this puzzle. Another interesting point is whether PBP1AB can repair damage in the peptidoglycan without relying on new cell wall synthesis, meaning that they can bring together material that is already in the cell wall without the need for new precursors. One way to address this question would be to deplete cell wall precursors using D-cycloserine, then measure cell wall elasticity as a proxy for repair. As many time-sensitive parameters need to be adjusted, this kind of experiment is difficult to perform. It is likely that *in vitro* studies will be necessary before this question can be solved *in vivo*. It would also be interesting to look at the TPase and TGase activities of PBP1AB separately, by using site-specific mutants.

Another research direction is to investigate the apparition of blebs on the sides of the cell in response to D-cycloserine or D-methionine or to PBP1AB depletion. We previously sought to know whether PBP1AB would localize at the spots where these blebs appear, but this is difficult to do as blebs can be anywhere around the cell, not necessarily in the focal plane, so 3D-imaging has to be used. Moreover, the fact that patches of PBP1AB still appear in the absence of LpoA or LpoB makes this hypothesis less attractive.

Finally, a mutant of PBP1B, PBP1B(E313D), was reported to insert cell wall without the need for activation by LpoB [205]. We previously attempted to work with this mutant, including a sfGFP-PBP1B(E313D) fusion, as it could provide insight on the differences between *E. coli* and *B. subtilis* control of diameter. However, our preliminary work involved strains with numerous chromosomal modifications and many scars from genome editing. As these strains gave very variable results, this part of the project was set aside. Making a new, simpler strain would be useful to study the importance of LpoB as a sensing mechanism, and to know the effects of processive cell-wall insertion on PBP1B(E313D)'s diffusion. Now that we know more about this protein, a new set of experiments involving the mutant could be undertaken. By changing the level of this mutant, we could see if its concentration has a larger effect on cell morphology than wild-type PBP1B, maybe more similar to what is seen in *B. subtilis* [133]. It would also be possible to look at the mechanical properties of the cell with such a mutant, to know whether the lack of sensing by LpoB leads to a cell wall of lower quality and thus to less mechanical resistance. As a caveat, it is not clear whether the rate of peptidoglycan insertion by this mutant is identifical to the wild-type protein. In particular, as the need for activation by LpoB no longer limits insertion, the E313D mutant may insert much more peptidoglycan than the wild-type. In addition, LpoB may still be able to increase the activity of the mutant, so it is preferable to work in a strain lacking LpoB. Finally, by using a fluorescent fusion to this hyper-active mutant, we could perform single-molecule tracking to know if it immobilizes, and which factors this depends on.

The project to understand PBP1AB's subcellular localization is still in an early phase. With the revelation that the strains used in these experiment are over-expressing class A PBPs, the biological significance of our previous results is to be examined. When expressing a high level of a fusion protein, it is possible that its localization is altered and that excess proteins form aggregation bodies. While some of the results seem independent from over-expression (especially the change in one aPBP's localization when the other is removed), most of the experiments from chapter 7 should be reproduced using wild-type levels of the fusions.

To better understand the importance of LpoB in localization, one could repress PBP1B to a non-lethal level in ΔPBP1A (or the opposite), with or without LpoB, and see if the change in localization due to 1A repression requires LpoB.

It is also possible that the patterns we see are not specific to PBP1AB, but are common for inner-membrane proteins. Using an artificial membrane protein with no biological function could help understand the dynamics of freely-diffusing proteins in the inner membrane. The Min system [24] and the Tol-Pal system [182] have also been reported to change the localization of membrane proteins. Their relationship with PBP1AB could also be investigated.

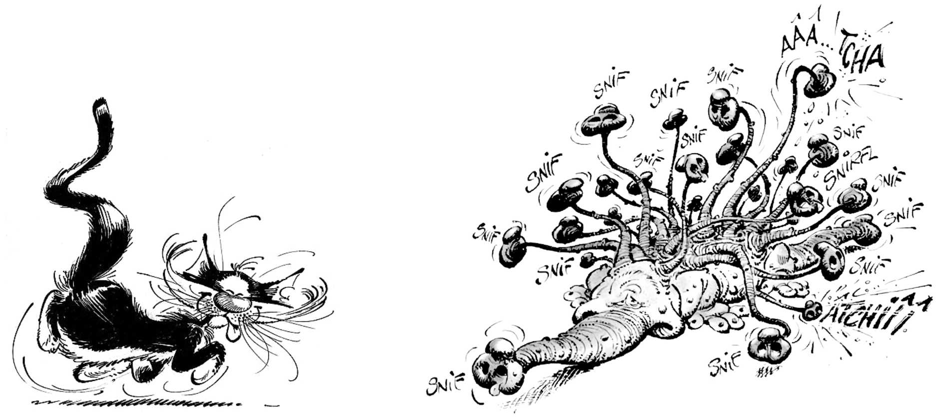

Figure 10.1: **Left:** Allegorical depiction of the experiments that worked and made it to this thesis. **Right:** Allegorical depiction of all the other experiments I attempted to do. Drawings by André Franquin.

Bibliography

[1] E. B. Lewis. A gene complex controlling segmentation in Drosophila. *Nature*, 276(5688):565, December 1978. ISSN 1476-4687. doi: 10.1038/276565a0. URL `https://www.nature.com/articles/276565a0`.

[2] Ron Milo & Ron Philips. » How big is the "average" protein? URL `http://book.bionumbers.org/how-big-is-the-average-protein/`.

[3] Waldemar Vollmer and Stephen J. Seligman. Architecture of peptidoglycan: more data and more models. *Trends in Microbiology*, 18(2):59–66, February 2010. ISSN 0966-842X. doi: 10.1016/j.tim.2009.12.004. URL `http://www.sciencedirect.com/science/article/pii/S0966842X09002601`.

[4] M.-T. Sung, Y.-T. Lai, C.-Y. Huang, L.-Y. Chou, H.-W. Shih, W.-C. Cheng, C.-H. Wong, and C. Ma. Crystal structure of the membrane-bound bifunctional transglycosylase PBP1b from Escherichia coli. *Proceedings of the National Academy of Sciences*, 106(22):8824–8829, June 2009. ISSN 0027-8424, 1091-6490. doi: 10.1073/pnas.0904030106. URL `http://www.pnas.org/cgi/doi/10.1073/pnas.0904030106`.

[5] Geoffrey M. Cooper. Structure and Organization of Actin Filaments. *The Cell: A Molecular Approach. 2nd edition*, 2000. URL `https://www.ncbi.nlm.nih.gov/books/NBK9908/`.

[6] Kohei Koyama, Ken Yamamoto, and Masayuki Ushio. A lognormal distribution of the lengths of terminal twigs on self-similar branches of elm trees. *Proceedings. Biological Sciences*, 284(1846), 2017. ISSN 1471-2954. doi: 10.1098/rspb.2016.2395.

[7] Geoffrey B. West, James H. Brown, and Brian J. Enquist. The Fourth Dimension of Life: Fractal Geometry and Allometric Scaling of Organisms. *Science*, 284(5420):1677–1679, June 1999. ISSN 0036-8075, 1095-9203. doi: 10.1126/science.284.5420.1677. URL `http://science.sciencemag.org/content/284/5420/1677`.

[8] Richard S. Smith, Soazig Guyomarc'h, Therese Mandel, Didier Reinhardt, Cris Kuhlemeier, and Przemyslaw Prusinkiewicz. A plausible model of phyllotaxis. *Proceedings of the National Academy of Sciences of the United States of America*, 103(5):1301–1306, January 2006. ISSN 0027-8424. doi: 10.1073/pnas.0510457103.

[9] Tyler M. Reese, Antoni Brzoska, Dylan T. Yott, and Daniel J. Kelleher. Analyzing self-similar and fractal properties of the C. elegans neural network. *PloS One*, 7 (10):e40483, 2012. ISSN 1932-6203. doi: 10.1371/journal.pone.0040483.

[10] Tohey Matsuyama and Mitsugu Matsushita. Fractal Morphogenesis by a Bacterial Cell Population. *Critical Reviews in Microbiology*, 19(2):117–135, January 1993. ISSN 1040-841X. doi: 10.3109/10408419309113526. URL `https://doi.org/10.3109/10408419309113526`.

[11] Eugene Presnov, Valeria Isaeva, and Nikolay Kasyanov. Topological determination of early morphogenesis in Metazoa. *Theory in Biosciences*, 129(4):259–270, December 2010. ISSN 1611-7530. doi: 10.1007/s12064-010-0103-y. URL `https://doi.org/10.1007/s12064-010-0103-y`.

[12] F. W. Cummings. A model of morphogenetic pattern formation. *Journal of Theoretical Biology*, 144(4):547–566, June 1990. ISSN 0022-5193. doi: 10.1016/S0022-5193(05)80089-X. URL `http://www.sciencedirect.com/science/article/pii/S002251930580089X`.

[13] Yuting Zhao, Jianglan Liu, Changsong Yang, Benjamin R. Capraro, Tobias Baumgart, Ryan P. Bradley, N. Ramakrishnan, Xiaowei Xu, Ravi Radhakrishnan, Tatyana Svitkina, and Wei Guo. Exo70 Generates Membrane Curvature for Morphogenesis and Cell Migration. *Developmental Cell*, 26(3):266–278, August 2013. ISSN 1534-5807. doi: 10.1016/j.devcel.2013.07.007. URL `http://www.sciencedirect.com/science/article/pii/S1534580713004152`.

[14] Patrick Müller, Katherine W. Rogers, Ben M. Jordan, Joon S. Lee, Drew Robson, Sharad Ramanathan, and Alexander F. Schier. Differential Diffusivity of Nodal and Lefty Underlies a Reaction-Diffusion Patterning System. *Science*, 336(6082): 721–724, May 2012. ISSN 0036-8075, 1095-9203. doi: 10.1126/science.1221920. URL `http://science.sciencemag.org/content/336/6082/721`.

[15] Rolando Rivera-Pomar and Herbert Jăckle. From gradients to stripes in Drosophila embryogenesis: filling in the gaps. *Trends in Genetics*, 12(11): 478–483, November 1996. ISSN 0168-9525. doi: 10.1016/0168-9525(96)10044-5. URL `http://www.sciencedirect.com/science/article/pii/0168952596100445`.

[16] Martin J .Cohn and Cheryll Tickle. Developmental basis of limblessness and axial patterning in snakes. *Nature*, 399(6735):474–479, June 1999. ISSN 1476-4687. doi: 10.1038/20944. URL `https://www.nature.com/articles/20944`.

[17] Satoshi Toda, Lucas R. Blauch, Sindy K. Y. Tang, Leonardo Morsut, and Wendell A. Lim. Programming self-organizing multicellular structures with synthetic cell-cell signaling. *Science*, page eaat0271, May 2018. ISSN 0036-8075, 1095-9203. doi: 10.1126/science.aat0271. URL `http://science.sciencemag.org/content/early/2018/05/30/science.aat0271`.

[18] Larissa B. Patterson, Emily J. Bain, and David M. Parichy. Pigment cell interactions and differential xanthophore recruitment underlying zebrafish stripe reiteration and *Danio* pattern evolution. *Nature Communications*, 5:5299, November 2014. doi: 10.1038/ncomms6299. URL `https://www.nature.com/articles/ncomms6299`.

[19] Volkening Alexandria and Sandstede Björn. Modelling stripe formation in zebrafish: an agent-based approach. *Journal of The Royal Society Interface*, 12 (112):20150812, November 2015. doi: 10.1098/rsif.2015.0812. URL `https://royalsocietypublishing.org/doi/10.1098/rsif.2015.0812`.

[20] Martin Loose, Elisabeth Fischer-Friedrich, Jonas Ries, Karsten Kruse, and Petra Schwille. Spatial Regulators for Bacterial Cell Division Self-Organize into Surface Waves in Vitro. *Science*, 320(5877):789–792, May 2008. ISSN 0036-8075, 1095-9203. doi: 10.1126/science.1154413. URL `http://science.sciencemag.org/content/320/5877/789`.

[21] Martin Loose, Elisabeth Fischer-Friedrich, Christoph Herold, Karsten Kruse, and Petra Schwille. Min protein patterns emerge from rapid rebinding and membrane interaction of MinE. *Nature Structural & Molecular Biology*, 18(5):577–583, May 2011. ISSN 1545-9985. doi: 10.1038/nsmb.2037. URL `https://www.nature.com/articles/nsmb.2037`.

[22] Dominik Thalmeier, Jacob Halatek, and Erwin Frey. Geometry-induced protein pattern formation. *Proceedings of the National Academy of Sciences of the United States of America*, 113(3):548–553, January 2016. ISSN 1091-6490. doi: 10.1073/pnas.1515191113.

[23] Jakob Schweizer, Martin Loose, Mike Bonny, Karsten Kruse, Ingolf Mönch, and Petra Schwille. Geometry sensing by self-organized protein patterns. *Proceedings of the National Academy of Sciences*, 109(38):15283–15288, September 2012. ISSN 0027-8424, 1091-6490. doi: 10.1073/pnas.1206953109. URL `https://www.pnas.org/content/109/38/15283`.

[24] Beatrice Ramm, Philipp Glock, Jonas Mücksch, Philipp Blumhardt, Daniela A. García-Soriano, Michael Heymann, and Petra Schwille. The MinDE system is a generic spatial cue for membrane protein distribution in vitro. *Nature Communications*, 9(1):3942, 2018. ISSN 2041-1723. doi: 10.1038/s41467-018-06310-1.

[25] David T. Kysela, Amelia M. Randich, Paul D. Caccamo, and Yves V. Brun. Diversity Takes Shape: Understanding the Mechanistic and Adaptive Basis of Bacterial Morphology. *PLOS Biology*, 14(10):e1002565, October 2016. ISSN 1545-7885. doi: 10.1371/journal.pbio.1002565. URL `https://journals.plos.org/plosbiology/article?id=10.1371/journal.pbio.1002565`.

[26] Amelia M. Randich and Yves V. Brun. Molecular mechanisms for the evolution of bacterial morphologies and growth modes. *Frontiers in Microbiology*, 6, 2015. ISSN 1664-302X. doi: 10.3389/fmicb.2015.00580. URL `https://www.frontiersin.org/articles/10.3389/fmicb.2015.00580/full`.

[27] Richard A. Daniel and Jeff Errington. Control of Cell Morphogenesis in Bacteria: Two Distinct Ways to Make a Rod-Shaped Cell. *Cell*, 113(6):767–776, June 2003. ISSN 0092-8674. doi: 10.1016/S0092-8674(03)00421-5. URL `http://www.sciencedirect.com/science/article/pii/S0092867403004215`.

[28] Kevin D. Young. The Selective Value of Bacterial Shape. *Microbiology and Molecular Biology Reviews*, 70(3):660–703, September 2006. ISSN 1092-2172. doi: 10.1128/MMBR.00001-06. URL `https://www.ncbi.nlm.nih.gov/pmc/articles/PMC1594593/`.

[29] Chao Jiang, Paul D. Caccamo, and Yves V. Brun. Mechanisms of bacterial morphogenesis: Evolutionary cell biology approaches provide new insights. *BioEssays*, 37(4):413–425, April 2015. ISSN 0265-9247. doi: 10.1002/bies.201400098. URL https://onlinelibrary.wiley.com/doi/full/10.1002/bies.201400098.

[30] Dennis J. Horvath, Birong Li, Travis Casper, Santiago Partida-Sanchez, David A. Hunstad, Scott J. Hultgren, and Sheryl S. Justice. Morphological plasticity promotes resistance to phagocyte killing of uropathogenic Escherichia coli. *Microbes and Infection*, 13(5):426–437, May 2011. ISSN 1769-714X. doi: 10.1016/j.micinf.2010.12.004.

[31] Leigh K. Harris and Julie A. Theriot. Relative Rates of Surface and Volume Synthesis Set Bacterial Cell Size. *Cell*, 165(6):1479–1492, June 2016. ISSN 1097-4172. doi: 10.1016/j.cell.2016.05.045.

[32] Michaela E Sharpe, Philippe M Hauser, Robert G Sharpe, and Jeffery Errington. Bacillus subtilis Cell Cycle as Studied by Fluorescence Microscopy: Constancy of Cell Length at Initiation of DNA Replication and Evidence for Active Nucleoid Partitioning. *J. BACTERIOL.*, 180:9, 1998.

[33] Robert D. Turner, Alexander F. Hurd, Ashley Cadby, Jamie K. Hobbs, and Simon J. Foster. Cell wall elongation mode in Gram-negative bacteria is determined by peptidoglycan architecture. *Nature Communications*, 4(1), December 2013. ISSN 2041-1723. doi: 10.1038/ncomms2503. URL http://www.nature.com/articles/ncomms2503.

[34] Waldemar Vollmer, Didier Blanot, and Miguel A. De Pedro. Peptidoglycan structure and architecture. *FEMS Microbiology Reviews*, 32(2):149–167, March 2008. ISSN 0168-6445. doi: 10.1111/j.1574-6976.2007.00094.x. URL https://academic.oup.com/femsre/article/32/2/149/2683904.

[35] V. Braun and H. Wolff. Attachment of lipoprotein to murein (peptidoglycan) of Escherichia coli in the presence and absence of penicillin FL 1060. *Journal of Bacteriology*, 123(3):888–897, September 1975. ISSN 0021-9193.

[36] Lu Gan, Songye Chen, and Grant J. Jensen. Molecular organization of Gram-negative peptidoglycan. *Proceedings of the National Academy of Sciences*, 105(48): 18953–18957, December 2008. ISSN 0027-8424, 1091-6490. doi: 10.1073/pnas.0808035105. URL https://www.pnas.org/content/105/48/18953.

[37] E. F. Bi and J. Lutkenhaus. FtsZ ring structure associated with division in Escherichia coli. *Nature*, 354(6349):161–164, November 1991. ISSN 0028-0836. doi: 10.1038/354161a0.

[38] H. P. Erickson. FtsZ, a prokaryotic homolog of tubulin? *Cell*, 80(3):367–370, February 1995. ISSN 0092-8674.

[39] F. van den Ent, L. A. Amos, and J. Löwe. Prokaryotic origin of the actin cytoskeleton. *Nature*, 413(6851):39–44, September 2001. ISSN 0028-0836. doi: 10.1038/35092500.

[40] Laura J. F. Jones, Rut Carballido-López, and Jeffery Errington. Control of Cell Shape in Bacteria: Helical, Actin-like Filaments in Bacillus subtilis. *Cell*, 104 (6):913–922, March 2001. ISSN 0092-8674. doi: 10.1016/S0092-8674(01) 00287-2. URL `http://www.sciencedirect.com/science/article/pii/S0092867401002872`.

[41] Matthew T. Swulius and Grant J. Jensen. The helical MreB cytoskeleton in Escherichia coli MC1000/pLE7 is an artifact of the N-Terminal yellow fluorescent protein tag. *Journal of Bacteriology*, 194(23):6382–6386, December 2012. ISSN 1098-5530. doi: 10.1128/JB.00505-12.

[42] Nikolay Ouzounov, Jeffrey P. Nguyen, Benjamin P. Bratton, David Jacobowitz, Zemer Gitai, and Joshua W. Shaevitz. MreB Orientation Correlates with Cell Diameter in Escherichia coli. *Biophysical Journal*, 111(5):1035–1043, September 2016. ISSN 0006-3495. doi: 10.1016/j.bpj.2016.07.017. URL `http://www.sciencedirect.com/science/article/pii/S000634951630580X`.

[43] Cyrille Billaudeau, Arnaud Chastanet, Zhizhong Yao, Charlène Cornilleau, Nicolas Mirouze, Vincent Fromion, and Rut Carballido-López. Contrasting mechanisms of growth in two model rod-shaped bacteria. *Nature Communications*, 8: 15370, 2017. ISSN 2041-1723. doi: 10.1038/ncomms15370.

[44] Patricia D. A. Rohs, Jackson Buss, Sue I. Sim, Georgia R. Squyres, Veerasak Srisuknimit, Mandy Smith, Hongbaek Cho, Megan Sjodt, Andrew C. Kruse, Ethan C. Garner, Suzanne Walker, Daniel E. Kahne, and Thomas G. Bernhardt. A central role for PBP2 in the activation of peptidoglycan polymerization by the bacterial cell elongation machinery. *PLOS Genetics*, 14(10):e1007726, October 2018. ISSN 1553-7404. doi: 10.1371/journal.pgen.1007726. URL `https://journals.plos.org/plosgenetics/article?id=10.1371/journal.pgen.1007726`.

[45] Lam T. Nguyen, James C. Gumbart, Morgan Beeby, and Grant J. Jensen. Coarse-grained simulations of bacterial cell wall growth reveal that local coordination alone can be sufficient to maintain rod shape. *Proceedings of the National Academy of Sciences*, 112(28):E3689–E3698, July 2015. ISSN 0027-8424, 1091-6490. doi: 10.1073/pnas.1504281112. URL `https://www.pnas.org/content/112/28/E3689`.

[46] Shoji Takeuchi, Willow R. DiLuzio, Douglas B. Weibel, and George M. Whitesides. Controlling the Shape of Filamentous Cells of Escherichia Coli. *Nano letters*, 5(9): 1819–1823, September 2005. ISSN 1530-6984. doi: 10.1021/nl0507360. URL `https://www.ncbi.nlm.nih.gov/pmc/articles/PMC2519610/`.

[47] Ariel Amir, Farinaz Babaeipour, Dustin B. McIntosh, David R. Nelson, and Suckjoon Jun. Bending forces plastically deform growing bacterial cell walls. *Proceedings of the National Academy of Sciences*, 111(16):5778–5783, April 2014. ISSN 0027-8424, 1091-6490. doi: 10.1073/pnas.1317497111. URL `http://www.pnas.org/content/111/16/5778`.

[48] Tristan S. Ursell, Jeffrey Nguyen, Russell D. Monds, Alexandre Colavin, Gabriel Billings, Nikolay Ouzounov, Zemer Gitai, Joshua W. Shaevitz, and Kerwyn Casey Huang. Rod-like bacterial shape is maintained by feedback between cell curvature

and cytoskeletal localization. *Proceedings of the National Academy of Sciences*, 111 (11):E1025–E1034, March 2014. ISSN 0027-8424, 1091-6490. doi: 10.1073/pnas.1317174111. URL https://www.pnas.org/content/111/11/E1025.

[49] Sven van Teeffelen, Siyuan Wang, Leon Furchtgott, Kerwyn Casey Huang, Ned S. Wingreen, Joshua W. Shaevitz, and Zemer Gitai. The bacterial actin MreB rotates, and rotation depends on cell-wall assembly. *Proceedings of the National Academy of Sciences*, 108(38):15822–15827, September 2011. ISSN 0027-8424, 1091-6490. doi: 10.1073/pnas.1108999108. URL https://www.pnas.org/content/108/38/15822.

[50] Ethan C. Garner, Remi Bernard, Wenqin Wang, Xiaowei Zhuang, David Z. Rudner, and Tim Mitchison. Coupled, Circumferential Motions of the Cell Wall Synthesis Machinery and MreB Filaments in B. subtilis. *Science*, 333(6039):222–225, July 2011. ISSN 0036-8075, 1095-9203. doi: 10.1126/science.1203285. URL http://science.sciencemag.org/content/333/6039/222.

[51] Felix Wong, Lars D. Renner, Gizem Özbaykal, Jayson Paulose, Douglas B. Weibel, Sven van Teeffelen, and Ariel Amir. Mechanical strain sensing implicated in cell shape recovery in *Escherichia coli*. *Nature Microbiology*, 2(9):17115, September 2017. ISSN 2058-5276. doi: 10.1038/nmicrobiol.2017.115. URL https://www.nature.com/articles/nmicrobiol2017115.

[52] Saman Hussain, Carl N. Wivagg, Piotr Szwedziak, Felix Wong, Kaitlin Schaefer, Thierry Izoré, Lars D. Renner, Matthew J. Holmes, Yingjie Sun, Alexandre W. Bisson-Filho, Suzanne Walker, Ariel Amir, Jan Löwe, and Ethan C. Garner. MreB filaments align along greatest principal membrane curvature to orient cell wall synthesis. *eLife*, 7:e32471, February 2018. ISSN 2050-084X. doi: 10.7554/eLife.32471. URL https://elifesciences.org/articles/32471.

[53] Athanasios Typas, Manuel Banzhaf, Bart van den Berg van Saparoea, Jolanda Verheul, Jacob Biboy, Robert J. Nichols, Matylda Zietek, Katrin Beilharz, Kai Kannenberg, Moritz von Rechenberg, Eefjan Breukink, Tanneke den Blaauwen, Carol A. Gross, and Waldemar Vollmer. Regulation of Peptidoglycan Synthesis by Outer-Membrane Proteins. *Cell*, 143(7):1097–1109, December 2010. ISSN 0092-8674. doi: 10.1016/j.cell.2010.11.038. URL http://www.sciencedirect.com/science/article/pii/S0092867410013607.

[54] David Bikard, Wenyan Jiang, Poulami Samai, Ann Hochschild, Feng Zhang, and Luciano A. Marraffini. Programmable repression and activation of bacterial gene expression using an engineered CRISPR-Cas system. *Nucleic Acids Research*, 41(15):7429–7437, August 2013. ISSN 0305-1048. doi: 10.1093/nar/gkt520. URL https://academic.oup.com/nar/article/41/15/7429/2411254/Programmable-repression-and-activation-of.

[55] Leeat Keren, Jean Hausser, Maya Lotan-Pompan, Ilya Vainberg Slutskin, Hadas Alisar, Sivan Kaminski, Adina Weinberger, Uri Alon, Ron Milo, and Eran Segal. Massively Parallel Interrogation of the Effects of Gene Expression Levels on Fitness. *Cell*, 166(5):1282–1294.e18, August 2016. ISSN 0092-8674. doi: 10.1016/j.cell.2016.07.024. URL http://www.sciencedirect.com/science/article/pii/S009286741630931X.

[56] Yolanda Schaerli, Alba Jiménez, José M. Duarte, Ljiljana Mihajlovic, Julien Renggli, Mark Isalan, James Sharpe, and Andreas Wagner. Synthetic circuits reveal how mechanisms of gene regulatory networks constrain evolution. *Molecular Systems Biology*, 14(9):e8102, September 2018. ISSN 1744-4292, 1744-4292. doi: 10.15252/msb.20178102. URL `http://msb.embopress.org/content/14/9/e8102`.

[57] Daniel L. Jones, Robert C. Brewster, and Rob Phillips. Promoter architecture dictates cell-to-cell variability in gene expression. *Science (New York, N.Y.)*, 346(6216): 1533–1536, December 2014. ISSN 1095-9203. doi: 10.1126/science.1255301.

[58] Luise Wolf, Olin K Silander, and Erik van Nimwegen. Expression noise facilitates the evolution of gene regulation. *eLife*, 4:e05856, June 2015. ISSN 2050-084X. doi: 10.7554/eLife.05856. URL `https://doi.org/10.7554/eLife.05856`.

[59] Mark Mimee, Phillip Nadeau, Alison Hayward, Sean Carim, Sarah Flanagan, Logan Jerger, Joy Collins, Shane McDonnell, Richard Swartwout, Robert J. Citorik, Vladimir Bulović, Robert Langer, Giovanni Traverso, Anantha P. Chandrakasan, and Timothy K. Lu. An ingestible bacterial-electronic system to monitor gastrointestinal health. *Science*, 360(6391):915–918, May 2018. ISSN 0036-8075, 1095-9203. doi: 10.1126/science.aas9315. URL `http://science.sciencemag.org/content/360/6391/915`.

[60] Mark Mimee, Alex C. Tucker, Christopher A. Voigt, and Timothy K. Lu. Programming a Human Commensal Bacterium, Bacteroides thetaiotaomicron, to Sense and Respond to Stimuli in the Murine Gut Microbiota. *Cell systems*, 1 (1):62–71, July 2015. ISSN 2405-4712. doi: 10.1016/j.cels.2015.06.001. URL `https://www.ncbi.nlm.nih.gov/pmc/articles/PMC4762051/`.

[61] George L. Sen and Helen M. Blau. A brief history of RNAi: the silence of the genes. *The FASEB Journal*, 20(9):1293–1299, July 2006. ISSN 0892-6638. doi: 10.1096/fj.06-6014rev. URL `https://www.fasebj.org/doi/abs/10.1096/fj.06-6014rev`.

[62] Y. Ji, B. Zhang, S. F. Van, null Horn, P. Warren, G. Woodnutt, M. K. Burnham, and M. Rosenberg. Identification of critical staphylococcal genes using conditional phenotypes generated by antisense RNA. *Science (New York, N.Y.)*, 293(5538): 2266–2269, September 2001. ISSN 0036-8075. doi: 10.1126/science.1063566.

[63] R. Allyn Forsyth, Robert J. Haselbeck, Kari L. Ohlsen, Robert T. Yamamoto, Howard Xu, John D. Trawick, Daniel Wall, Liangsu Wang, Vickie Brown-Driver, Jamie M. Froelich, Kedar G. C, Paula King, Melissa McCarthy, Cheryl Malone, Brian Misiner, David Robbins, Zehui Tan, Zhan-yang Zhu Zy, Grant Carr, Deborah A. Mosca, Carlos Zamudio, J. Gordon Foulkes, and Judith W. Zyskind. A genome-wide strategy for the identification of essential genes in Staphylococcus aureus. *Molecular Microbiology*, 43(6):1387–1400, March 2002. ISSN 0950-382X.

[64] Nobutaka Nakashima, Tomohiro Tamura, and Liam Good. Paired termini stabilize antisense RNAs and enhance conditional gene silencing in Escherichia coli. *Nucleic Acids Research*, 34(20):e138, 2006. ISSN 1362-4962. doi: 10.1093/nar/gkl697.

[65] Wenyan Jiang, David Bikard, David Cox, Feng Zhang, and Luciano A. Marraffini. RNA-guided editing of bacterial genomes using CRISPR-Cas systems. *Nature Biotechnology*, 31(3):233, March 2013. ISSN 1546-1696. doi: 10.1038/nbt.2508. URL `https://www.nature.com/articles/nbt.2508`.

[66] Lei S. Qi, Matthew H. Larson, Luke A. Gilbert, Jennifer A. Doudna, Jonathan S. Weissman, Adam P. Arkin, and Wendell A. Lim. Repurposing CRISPR as an RNA-Guided Platform for Sequence-Specific Control of Gene Expression. *Cell*, 152(5):1173–1183, February 2013. ISSN 0092-8674. doi: 10.1016/j.cell.2013.02.022. URL `http://www.sciencedirect.com/science/article/pii/S0092867413002110`.

[67] N. Nakashima and T. Tamura. Gene silencing in Escherichia coli using antisense RNAs expressed from doxycycline-inducible vectors. *Letters in Applied Microbiology*, 56(6):436–442, June 2013. ISSN 1472-765X. doi: 10.1111/lam.12066.

[68] Dokyun Na, Seung Min Yoo, Hannah Chung, Hyegwon Park, Jin Hwan Park, and Sang Yup Lee. Metabolic engineering of Escherichia coli using synthetic small regulatory RNAs. *Nature Biotechnology*, 31(2):170–174, February 2013. ISSN 1546-1696. doi: 10.1038/nbt.2461.

[69] James M. Carothers, Jonathan A. Goler, Darmawi Juminaga, and Jay D. Keasling. Model-driven engineering of RNA devices to quantitatively program gene expression. *Science (New York, N.Y.)*, 334(6063):1716–1719, December 2011. ISSN 1095-9203. doi: 10.1126/science.1212209.

[70] Nobutaka Nakashima and Tomohiro Tamura. Conditional gene silencing of multiple genes with antisense RNAs and generation of a mutator strain of Escherichia coli. *Nucleic Acids Research*, 37(15):e103, August 2009. ISSN 0305-1048. doi: 10.1093/nar/gkp498. URL `https://www.ncbi.nlm.nih.gov/pmc/articles/PMC2731896/`.

[71] Eugene V. Koonin, Kira S. Makarova, and Feng Zhang. Diversity, classification and evolution of CRISPR-Cas systems. *Current Opinion in Microbiology*, 37:67–78, June 2017. ISSN 1879-0364. doi: 10.1016/j.mib.2017.05.008.

[72] John G. Doench, Nicolo Fusi, Meagan Sullender, Mudra Hegde, Emma W. Vaimberg, Katherine F. Donovan, Ian Smith, Zuzana Tothova, Craig Wilen, Robert Orchard, Herbert W. Virgin, Jennifer Listgarten, and David E. Root. Optimized sgRNA design to maximize activity and minimize off-target effects of CRISPR-Cas9. *Nature Biotechnology*, 34(2):184–191, February 2016. ISSN 1546-1696. doi: 10.1038/nbt.3437. URL `https://www.nature.com/articles/nbt.3437`.

[73] Seong Keun Kim, Haseong Kim, Woo-Chan Ahn, Kwang-Hyun Park, Eui-Jeon Woo, Dae-Hee Lee, and Seung-Goo Lee. Efficient Transcriptional Gene Repression by Type V-A CRISPR-Cpf1 from Eubacterium eligens. *ACS synthetic biology*, 6(7):1273–1282, 2017. ISSN 2161-5063. doi: 10.1021/acssynbio.6b00368.

[74] Fuguo Jiang, Kaihong Zhou, Linlin Ma, Saskia Gressel, and Jennifer A. Doudna. STRUCTURAL BIOLOGY. A Cas9-guide RNA complex preorganized for target DNA recognition. *Science (New York, N.Y.)*, 348(6242):1477–1481, June 2015. ISSN 1095-9203. doi: 10.1126/science.aab1452.

[75] Yibei Xiao, Min Luo, Robert P. Hayes, Jonathan Kim, Sherwin Ng, Fang Ding, Maofu Liao, and Ailong Ke. Structure Basis for Directional R-loop Formation and Substrate Handover Mechanisms in Type I CRISPR-Cas System. *Cell*, 170 (1):48–60.e11, June 2017. ISSN 00928674. doi: 10.1016/j.cell.2017.06.012. URL `https://linkinghub.elsevier.com/retrieve/pii/S0092867417306955`.

[76] Mark D. Szczelkun, Maria S. Tikhomirova, Tomas Sinkunas, Giedrius Gasiunas, Tautvydas Karvelis, Patrizia Pschera, Virginijus Siksnys, and Ralf Seidel. Direct observation of R-loop formation by single RNA-guided Cas9 and Cascade effector complexes. *Proceedings of the National Academy of Sciences of the United States of America*, 111(27):9798–9803, July 2014. ISSN 1091-6490. doi: 10.1073/pnas.1402597111.

[77] Michelle L. Luo, Adam S. Mullis, Ryan T. Leenay, and Chase L. Beisel. Repurposing endogenous type I CRISPR-Cas systems for programmable gene repression. *Nucleic Acids Research*, 43(1):674–681, January 2015. ISSN 1362-4962. doi: 10.1093/nar/gku971.

[78] Jason M. Peters, Alexandre Colavin, Handuo Shi, Tomasz L. Czarny, Matthew H. Larson, Spencer Wong, John S. Hawkins, Candy H. S. Lu, Byoung-Mo Koo, Elizabeth Marta, Anthony L. Shiver, Evan H. Whitehead, Jonathan S. Weissman, Eric D. Brown, Lei S. Qi, Kerwyn Casey Huang, and Carol A. Gross. A Comprehensive, CRISPR-based Functional Analysis of Essential Genes in Bacteria. *Cell*, 165(6): 1493–1506, June 2016. ISSN 1097-4172. doi: 10.1016/j.cell.2016.05.003.

[79] Lun Cui, Antoine Vigouroux, François Rousset, Hugo Varet, Varun Khanna, and David Bikard. A CRISPRi screen in E. coli reveals sequence-specific toxicity of dCas9. *Nature Communications*, 9(1):1912, May 2018. ISSN 2041-1723. doi: 10.1038/s41467-018-04209-5. URL `https://www.nature.com/articles/s41467-018-04209-5`.

[80] Chensi Miao, Huiwei Zhao, Long Qian, and Chunbo Lou. Systematically investigating the key features of the DNase deactivated Cpf1 for tunable transcription regulation in prokaryotic cells. *Synthetic and Systems Biotechnology*, 4(1):1–9, November 2018. ISSN 2405-805X. doi: 10.1016/j.synbio.2018.11.002. URL `https://www.ncbi.nlm.nih.gov/pmc/articles/PMC6251280/`.

[81] Jakub Wiktor, Christian Lesterlin, David J. Sherratt, and Cees Dekker. CRISPR-mediated control of the bacterial initiation of replication. *Nucleic Acids Research*, 44(8):3801–3810, May 2016. ISSN 0305-1048. doi: 10.1093/nar/gkw214. URL `https://academic.oup.com/nar/article/44/8/3801/2467335/CRISPR-mediated-control-of-the-bacterial`.

[82] Antoine Vigouroux, Enno Oldewurtel, Lun Cui, David Bikard, and Sven van Teeffelen. Tuning dCas9's ability to block transcription enables robust, noiseless knockdown of bacterial genes. *Molecular Systems Biology*, 14(3):e7899, March 2018. ISSN 1744-4292, 1744-4292, 1744-4292. doi: 10.15252/msb.20177899. URL `http://msb.embopress.org/lookup/doi/10.15252/msb.20177899`.

[83] Tianmin Wang, Changge Guan, Jiahui Guo, Bing Liu, Yinan Wu, Zhen Xie, Chong Zhang, and Xin-Hui Xing. Pooled CRISPR interference screening en-

ables genome-scale functional genomics study in bacteria with superior performance. *Nature Communications*, 9(1):2475, June 2018. ISSN 2041-1723. doi: 10.1038/s41467-018-04899-x. URL https://www.nature.com/articles/s41467-018-04899-x.

[84] K. C. Keiler, P. R. Waller, and R. T. Sauer. Role of a peptide tagging system in degradation of proteins synthesized from damaged messenger RNA. *Science (New York, N.Y.)*, 271(5251):990–993, February 1996. ISSN 0036-8075.

[85] Jason M. Peters, Byoung-Mo Koo, Ramiro Patino, Gary E. Heussler, Cameron C. Hearne, Jiuxin Qu, Yuki F. Inclan, John S. Hawkins, Candy H. S. Lu, Melanie R. Silvis, M. Michael Harden, Hendrik Osadnik, Joseph E. Peters, Joanne N. Engel, Rachel J. Dutton, Alan D. Grossman, Carol A. Gross, and Oren S. Rosenberg. Enabling genetic analysis of diverse bacteria with Mobile-CRISPRi. *Nature Microbiology*, 4(2):244–250, February 2019. ISSN 2058-5276. doi: 10.1038/s41564-018-0327-z.

[86] Jia Meng, Gregory Kanzaki, Diane Meas, Christopher K. Lam, Heather Crummer, Justina Tain, and H. Howard Xu. A genome-wide inducible phenotypic screen identifies antisense RNA constructs silencing Escherichia coli essential genes. *FEMS microbiology letters*, 329(1):45–53, April 2012. ISSN 1574-6968. doi: 10.1111/j.1574-6968.2012.02503.x.

[87] François Rousset, Lun Cui, Elise Siouve, Christophe Becavin, Florence Depardieu, and David Bikard. Genome-wide CRISPR-dCas9 screens in E. coli identify essential genes and phage host factors. *PLOS Genetics*, 14(11): e1007749, November 2018. ISSN 1553-7404. doi: 10.1371/journal.pgen.1007749. URL https://journals.plos.org/plosgenetics/article?id=10.1371/journal.pgen.1007749.

[88] Yi Wang, Zhong-Tian Zhang, Seung-Oh Seo, Patrick Lynn, Ting Lu, Yong-Su Jin, and Hans P. Blaschek. Gene transcription repression in Clostridium beijerinckii using CRISPR-dCas9. *Biotechnology and Bioengineering*, 113(12):2739–2743, 2016. ISSN 1097-0290. doi: 10.1002/bit.26020.

[89] Daniel Dar and Rotem Sorek. Extensive reshaping of bacterial operons by programmed mRNA decay. *PLOS Genetics*, 14(4):e1007354, April 2018. ISSN 1553-7404. doi: 10.1371/journal.pgen.1007354. URL https://journals.plos.org/plosgenetics/article?id=10.1371/journal.pgen.1007354.

[90] Nan Hao, Adam C. Palmer, Alexandra Ahlgren-Berg, Keith E. Shearwin, and Ian B. Dodd. The role of repressor kinetics in relief of transcriptional interference between convergent promoters. *Nucleic Acids Research*, 44(14):6625–6638, August 2016. ISSN 0305-1048. doi: 10.1093/nar/gkw600. URL https://academic.oup.com/nar/article/44/14/6625/2468218.

[91] Iman Farasat and Howard M. Salis. A Biophysical Model of CRISPR/Cas9 Activity for Rational Design of Genome Editing and Gene Regulation. *PLoS computational biology*, 12(1):e1004724, January 2016. ISSN 1553-7358. doi: 10.1371/journal.pcbi.1004724.

[92] Evan A. Boyle, Johan O. L. Andreasson, Lauren M. Chircus, Samuel H. Sternberg, Michelle J. Wu, Chantal K. Guegler, Jennifer A. Doudna, and William J. Greenleaf. High-throughput biochemical profiling reveals sequence determinants of dCas9 off-target binding and unbinding. *Proceedings of the National Academy of Sciences of the United States of America*, 114(21):5461–5466, May 2017. ISSN 1091-6490. doi: 10.1073/pnas.1700557114.

[93] Ryan Marshall, Colin S. Maxwell, Scott P. Collins, Thomas Jacobsen, Michelle L. Luo, Matthew B. Begemann, Benjamin N. Gray, Emma January, Anna Singer, Yonghua He, Chase L. Beisel, and Vincent Noireaux. Rapid and Scalable Characterization of CRISPR Technologies Using an E. coli Cell-Free Transcription-Translation System. *Molecular cell*, 69(1):146–157.e3, January 2018. ISSN 1097-2765. doi: 10.1016/j.molcel.2017.12.007. URL https://www.ncbi.nlm.nih.gov/pmc/articles/PMC5976856/.

[94] Brady F. Cress, J. Andrew Jones, Daniel C. Kim, Quentin D. Leitz, Jacob A. Englaender, Shannon M. Collins, Robert J. Linhardt, and Mattheos A. G. Koffas. Rapid generation of CRISPR/dCas9-regulated, orthogonally repressible hybrid T7-lac promoters for modular, tuneable control of metabolic pathway fluxes in Escherichia coli. *Nucleic Acids Research*, 44(9):4472–4485, May 2016. ISSN 1362-4962. doi: 10.1093/nar/gkw231.

[95] Namita Bisaria, Inga Jarmoskaite, and Daniel Herschlag. Lessons from Enzyme Kinetics Reveal Specificity Principles for RNA-Guided Nucleases in RNA Interference and CRISPR-Based Genome Editing. *Cell Systems*, 4(1):21–29, January 2017. ISSN 2405-4712. doi: 10.1016/j.cels.2016.12.010. URL http://www.sciencedirect.com/science/article/pii/S2405471216304203.

[96] Misha Klein, Behrouz Eslami-Mossallam, Dylan Gonzalez Arroyo, and Martin Depken. Hybridization Kinetics Explains CRISPR-Cas Off-Targeting Rules. *Cell Reports*, 22(6):1413–1423, February 2018. ISSN 2211-1247. doi: 10.1016/j.celrep.2018.01.045. URL https://www.cell.com/cell-reports/abstract/S2211-1247(18)30077-9.

[97] Isabel Strohkendl, Fatema A. Saifuddin, James R. Rybarski, Ilya J. Finkelstein, and Rick Russell. Kinetic Basis for DNA Target Specificity of CRISPR-Cas12a. *Molecular Cell*, 71(5):816–824.e3, September 2018. ISSN 1097-4164. doi: 10.1016/j.molcel.2018.06.043.

[98] Johnny H. Hu, Shannon M. Miller, Maarten H. Geurts, Weixin Tang, Liwei Chen, Ning Sun, Christina M. Zeina, Xue Gao, Holly A. Rees, Zhi Lin, and David R. Liu. Evolved Cas9 variants with broad PAM compatibility and high DNA specificity. *Nature*, 556(7699):57–63, 2018. ISSN 1476-4687. doi: 10.1038/nature26155.

[99] Mikihiro Shibata, Hiroshi Nishimasu, Noriyuki Kodera, Seiichi Hirano, Toshio Ando, Takayuki Uchihashi, and Osamu Nureki. Real-space and real-time dynamics of CRISPR-Cas9 visualized by high-speed atomic force microscopy. *Nature Communications*, 8(1):1430, November 2017. ISSN 2041-1723. doi: 10.1038/s41467-017-01466-8. URL https://www.nature.com/articles/s41467-017-01466-8.

[100] Samuel H. Sternberg, Sy Redding, Martin Jinek, Eric C. Greene, and Jennifer A. Doudna. DNA interrogation by the CRISPR RNA-guided endonuclease Cas9. *Nature*, 507(7490):62–67, March 2014. ISSN 1476-4687. doi: 10.1038/nature13011.

[101] Viktorija Globyte, Seung Hwan Lee, Taegeun Bae, Jin-Soo Kim, and Chirlmin Joo. CRISPR/Cas9 searches for a protospacer adjacent motif by lateral diffusion. *The EMBO Journal*, page e99466, December 2018. ISSN 0261-4189, 1460-2075. doi: 10.15252/embj.201899466. URL `http://emboj.embopress.org/content/early/2018/12/20/embj.201899466`.

[102] Yongmoon Jeon, You Hee Choi, Yunsu Jang, Jihyeon Yu, Jiyoung Goo, Gyejun Lee, You Kyeong Jeong, Seung Hwan Lee, In-San Kim, Jin-Soo Kim, Cherlhyun Jeong, Sanghwa Lee, and Sangsu Bae. Direct observation of DNA target searching and cleavage by CRISPR-Cas12a. *Nature Communications*, 9(1):2777, July 2018. ISSN 2041-1723. doi: 10.1038/s41467-018-05245-x. URL `https://www.nature.com/articles/s41467-018-05245-x`.

[103] Daniel Lawson Jones, Prune Leroy, Cecilia Unoson, David Fange, Vladimir Ćurić, Michael J. Lawson, and Johan Elf. Kinetics of dCas9 target search in Escherichia coli. *Science*, 357(6358):1420–1424, September 2017. ISSN 0036-8075, 1095-9203. doi: 10.1126/science.aah7084. URL `http://science.sciencemag.org/content/357/6358/1420`.

[104] Xin-Tian Li, Yonggun Jun, Michael J. Erickstad, Steven D. Brown, Adam Parks, Donald L. Court, and Suckjoon Jun. tCRISPRi: tunable and reversible, one-step control of gene expression. *Scientific Reports*, 6:39076, December 2016. ISSN 2045-2322. doi: 10.1038/srep39076.

[105] Jason Fontana, Chen Dong, Jennifer Y. Ham, Jesse G. Zalatan, and James M. Carothers. Regulated Expression of sgRNAs Tunes CRISPRi in E. coli. *Biotechnology Journal*, 13(9):1800069, 2018. ISSN 1860-7314. doi: 10.1002/biot.201800069. URL `https://onlinelibrary.wiley.com/doi/abs/10.1002/biot.201800069`.

[106] Fangwei Si, Dongyang Li, Sarah E. Cox, John T. Sauls, Omid Azizi, Cindy Sou, Amy B. Schwartz, Michael J. Erickstad, Yonggun Jun, Xintian Li, and Suckjoon Jun. Invariance of Initiation Mass and Predictability of Cell Size in Escherichia coli. *Current Biology*, 27(9):1278–1287, May 2017. ISSN 0960-9822. doi: 10.1016/j.cub.2017.03.022. URL `http://www.sciencedirect.com/science/article/pii/S0960982217302919`.

[107] Chunyu Liao, Fani Ttofali, Rebecca A. Slotkowski, Steven R. Denny, Taylor D. Cecil, Ryan T. Leenay, Albert J. Keung, and Chase L. Beisel. One-step assembly of large CRISPR arrays enables multi-functional targeting and reveals constraints on array design. *bioRxiv*, page 312421, May 2018. doi: 10.1101/312421. URL `https://www.biorxiv.org/content/10.1101/312421v1`.

[108] Balwina Koopal, Aleksander J. Kruis, Nico J. Claassens, Franklin L. Nobrega, and John van der Oost. Incorporation of a Synthetic Amino Acid into dCas9 Improves Control of Gene Silencing. *ACS Synthetic Biology*, January 2019. doi: 10.1021/acssynbio.8b00347. URL `https://doi.org/10.1021/acssynbio.8b00347`.

[109] Young Je Lee, Allison Hoynes-O'Connor, Matthew C. Leong, and Tae Seok Moon. Programmable control of bacterial gene expression with the combined CRISPR and antisense RNA system. *Nucleic Acids Research*, 44(5):2462–2473, March 2016. ISSN 1362-4962. doi: 10.1093/nar/gkw056.

[110] Chen Dong, Jason Fontana, Anika Patel, James M. Carothers, and Jesse G. Zalatan. Synthetic CRISPR-Cas gene activators for transcriptional reprogramming in bacteria. *Nature Communications*, 9, June 2018. ISSN 2041-1723. doi: 10.1038/s41467-018-04901-6. URL https://www.ncbi.nlm.nih.gov/pmc/articles/PMC6021436/.

[111] Z. Lu, S. Yang, X. Yuan, Y. Shi, L. Ouyang, S. Jiang, L. Yi, and G. Zhang. CRISPR-assisted multi-dimensional regulation for fine-tuning gene expression in Bacillus subtilis. *Nucleic acids research*, February 2019. ISSN 0305-1048. doi: 10.1093/nar/gkz072. URL http://europepmc.org/abstract/MED/30767015.

[112] Rodolphe Barrangou and Luciano A. Marraffini. CRISPR-Cas Systems: Prokaryotes Upgrade to Adaptive Immunity. *Molecular Cell*, 54(2):234–244, April 2014. ISSN 1097-2765. doi: 10.1016/j.molcel.2014.03.011. URL http://www.sciencedirect.com/science/article/pii/S1097276514002160.

[113] Heng Zhao, Yingjie Sun, Jason M. Peters, Carol A. Gross, Ethan C. Garner, and John D. Helmann. Depletion of Undecaprenyl Pyrophosphate Phosphatases Disrupts Cell Envelope Biogenesis in Bacillus subtilis. *Journal of Bacteriology*, 198 (21):2925–2935, 2016. ISSN 1098-5530. doi: 10.1128/JB.00507-16.

[114] Xiaochun Zhang, Jingman Wang, Qiuxiang Cheng, Xuan Zheng, Guoping Zhao, and Jin Wang. Multiplex gene regulation by CRISPR-ddCpf1. *Cell Discovery*, 3: 17018, 2017. ISSN 2056-5968. doi: 10.1038/celldisc.2017.18.

[115] Brady F. Cress, Ö Duhan Toparlak, Sanjay Guleria, Matthew Lebovich, Jessica T. Stieglitz, Jacob A. Englaender, J. Andrew Jones, Robert J. Linhardt, and Mattheos A. G. Koffas. CRISPathBrick: Modular Combinatorial Assembly of Type II-A CRISPR Arrays for dCas9-Mediated Multiplex Transcriptional Repression in E. coli. *ACS synthetic biology*, 4(9):987–1000, September 2015. ISSN 2161-5063. doi: 10.1021/acssynbio.5b00012.

[116] Dipti D. Nayak and William W. Metcalf. Cas9-mediated genome editing in the methanogenic archaeon Methanosarcina acetivorans. *Proceedings of the National Academy of Sciences*, 114(11):2976–2981, March 2017. ISSN 0027-8424, 1091-6490. doi: 10.1073/pnas.1618596114. URL https://www.pnas.org/content/114/11/2976.

[117] Levi G. Lowder, Aimee Malzahn, and Yiping Qi. Plant Gene Regulation Using Multiplex CRISPR-dCas9 Artificial Transcription Factors. In L. Mark Lagrimini, editor, *Maize: Methods and Protocols*, Methods in Molecular Biology, pages 197–214. Springer New York, New York, NY, 2018. ISBN 978-1-4939-7315-6. doi: 10.1007/978-1-4939-7315-6_12. URL https://doi.org/10.1007/978-1-4939-7315-6_12.

[118] Tang Hai, Fei Teng, Runfa Guo, Wei Li, and Qi Zhou. One-step generation of knockout pigs by zygote injection of CRISPR/Cas system. *Cell Research*, 24(3):

372–375, March 2014. ISSN 1748-7838. doi: 10.1038/cr.2014.11. URL https://www.nature.com/articles/cr201411.

[119] S. G. McInally, K. D. Hagen, C. Nosala, J. Williams, K. Nguyen, J. Booker, K. Jones, and Scott C. Dawson. Robust and stable transcriptional repression in Giardia using CRISPRi. *Molecular Biology of the Cell*, 30(1):119–130, January 2019. ISSN 1939-4586. doi: 10.1091/mbc.E18-09-0605.

[120] Christina S. Nødvig, Jakob B. Nielsen, Martin E. Kogle, and Uffe H. Mortensen. A CRISPR-Cas9 System for Genetic Engineering of Filamentous Fungi. *PLOS ONE*, 10(7):e0133085, July 2015. ISSN 1932-6203. doi: 10.1371/journal.pone.0133085. URL https://journals.plos.org/plosone/article?id=10.1371/journal.pone.0133085.

[121] Sue Zanne Tan, Christopher R. Reisch, and Kristala L. J. Prather. A Robust CRISPR Interference Gene Repression System in Pseudomonas. *Journal of Bacteriology*, 200(7), 2018. ISSN 1098-5530. doi: 10.1128/JB.00575-17.

[122] Aleš Berlec, Katja Škrlec, Janja Kocjan, Maria Olenic, and Borut Štrukelj. Single plasmid systems for inducible dual protein expression and for CRISPR-Cas9/CRISPRi gene regulation in lactic acid bacterium Lactococcus lactis. *Scientific Reports*, 8(1):1009, 2018. ISSN 2045-2322. doi: 10.1038/s41598-018-19402-1.

[123] Jaehyun Park, Hyojung Shin, Sun-Mi Lee, Youngsoon Um, and Han Min Woo. RNA-guided single/double gene repressions in Corynebacterium glutamicum using an efficient CRISPR interference and its application to industrial strain. *Microbial Cell Factories*, 17(1):4, January 2018. ISSN 1475-2859. doi: 10.1186/s12934-017-0843-1.

[124] Yusuke Sato'o, Junzo Hisatsune, Liansheng Yu, Tetsushi Sakuma, Takashi Yamamoto, and Motoyuki Sugai. Tailor-made gene silencing of Staphylococcus aureus clinical isolates by CRISPR interference. *PloS One*, 13(1):e0185987, 2018. ISSN 1932-6203. doi: 10.1371/journal.pone.0185987.

[125] Ioannis Mougiakos, Prarthana Mohanraju, Elleke F. Bosma, Valentijn Vrouwe, Max Finger Bou, Mihris I. S. Naduthodi, Alex Gussak, Rudolf B. L. Brinkman, Richard van Kranenburg, and John van der Oost. Characterizing a thermostable Cas9 for bacterial genome editing and silencing. *Nature Communications*, 8(1):1647, November 2017. ISSN 2041-1723. doi: 10.1038/s41467-017-01591-4. URL https://www.nature.com/articles/s41467-017-01591-4.

[126] Alec AK Nielsen and Christopher A. Voigt. Multi-input CRISPR/Cas genetic circuits that interface host regulatory networks. *Molecular Systems Biology*, 10(11):763, November 2014. ISSN 1744-4292, 1744-4292. doi: 10.15252/msb.20145735. URL http://msb.embopress.org/content/10/11/763.

[127] Suhyung Cho, Donghui Choe, Eunju Lee, Sun Chang Kim, Bernhard Ø. Palsson, and Byung-Kwan Cho. High-level dCas9 expression induces abnormal cell morphology in Escherichia coli. *ACS Synthetic Biology*, March 2018. doi: 10.1021/acssynbio.7b00462. URL https://cdn-pubs.acs.org/doi/abs/10.1021/acssynbio.7b00462.

[128] Shuyi Zhang and Christopher A. Voigt. Engineered dCas9 with reduced toxicity in bacteria: implications for genetic circuit design. *Nucleic Acids Research*, 2018. doi: 10.1093/nar/gky884. URL https://academic.oup.com/nar/advance-article/doi/10.1093/nar/gky884/5115820.

[129] Tomoya Baba, Takeshi Ara, Miki Hasegawa, Yuki Takai, Yoshiko Okumura, Miki Baba, Kirill A Datsenko, Masaru Tomita, Barry L Wanner, and Hirotada Mori. Construction of Escherichia coli K-12 in-frame, single-gene knockout mutants: the Keio collection. *Molecular Systems Biology*, 2:2006.0008, February 2006. ISSN 1744-4292. doi: 10.1038/msb4100050. URL http://www.ncbi.nlm.nih.gov/pmc/articles/PMC1681482/.

[130] Byoung-Mo Koo, George Kritikos, Jeremiah D. Farelli, Horia Todor, Kenneth Tong, Harvey Kimsey, Ilan Wapinski, Marco Galardini, Angelo Cabal, Jason M. Peters, Anna-Barbara Hachmann, David Z. Rudner, Karen N. Allen, Athanasios Typas, and Carol A. Gross. Construction and Analysis of Two Genome-Scale Deletion Libraries for Bacillus subtilis. *Cell Systems*, 4(3):291–305.e7, March 2017. ISSN 2405-4712. doi: 10.1016/j.cels.2016.12.013.

[131] Kelly M. Wetmore, Morgan N. Price, Robert J. Waters, Jacob S. Lamson, Jennifer He, Cindi A. Hoover, Matthew J. Blow, James Bristow, Gareth Butland, Adam P. Arkin, and Adam Deutschbauer. Rapid Quantification of Mutant Fitness in Diverse Bacteria by Sequencing Randomly Bar-Coded Transposons. *mBio*, 6(3): e00306–15, July 2015. ISSN 2150-7511. doi: 10.1128/mBio.00306-15. URL https://mbio.asm.org/content/6/3/e00306-15.

[132] Morgan N. Price, Kelly M. Wetmore, R. Jordan Waters, Mark Callaghan, Jayashree Ray, Hualan Liu, Jennifer V. Kuehl, Ryan A. Melnyk, Jacob S. Lamson, Yumi Suh, Hans K. Carlson, Zuelma Esquivel, Harini Sadeeshkumar, Romy Chakraborty, Grant M. Zane, Benjamin E. Rubin, Judy D. Wall, Axel Visel, James Bristow, Matthew J. Blow, Adam P. Arkin, and Adam M. Deutschbauer. Mutant phenotypes for thousands of bacterial genes of unknown function. *Nature*, 557(7706): 503, May 2018. ISSN 1476-4687. doi: 10.1038/s41586-018-0124-0. URL https://www.nature.com/articles/s41586-018-0124-0.

[133] Michael Dion, Mrinal Kapoor, Yingjie Sun, Sean Wilson, Joel Ryan, Antoine Vigouroux, Sven van Teeffelen, Rudolf Oldenbourg, and Ethan C. Garner. Cell Diameter in Bacillus subtilis is Determined by the Opposing Actions of Two Distinct Cell Wall Synthetic Systems. *bioRxiv*, page 392837, August 2018. doi: 10.1101/392837. URL https://www.biorxiv.org/content/10.1101/392837v3.

[134] Yuchen Liu, Jinghong Han, Zhicong Chen, Hanwei Wu, Hongsong Dong, and Guohui Nie. Engineering cell signaling using tunable CRISPR–Cpf1-based transcription factors. *Nature Communications*, 8, December 2017. ISSN 2041-1723. doi: 10.1038/s41467-017-02265-x. URL https://www.ncbi.nlm.nih.gov/pmc/articles/PMC5727435/.

[135] Henry H. Lee, Nili Ostrov, Brandon G. Wong, Michaela A. Gold, Ahmad S. Khalil, and George M. Church. Functional genomics of the rapidly replicating bacterium Vibrio natriegens by CRISPRi. *Nature Microbiology*, page 1, April 2019. ISSN 2058-5276. doi: 10.1038/s41564-019-0423-8. URL https://www.nature.com/articles/s41564-019-0423-8.

[136] Michael J. Lawson, Daniel Camsund, Jimmy Larsson, Özden Baltekin, David Fange, and Johan Elf. In situ genotyping of a pooled strain library after characterizing complex phenotypes. *Molecular Systems Biology*, 13(10):947, October 2017. ISSN 1744-4292, 1744-4292. doi: 10.15252/msb.20177951. URL `http://msb.embopress.org/content/13/10/947`.

[137] Francesca Ceroni, Alice Boo, Simone Furini, Thomas E. Gorochowski, Olivier Borkowski, Yaseen N. Ladak, Ali R. Awan, Charlie Gilbert, Guy-Bart Stan, and Tom Ellis. Burden-driven feedback control of gene expression. *Nature Methods*, 15(5):387–393, May 2018. ISSN 1548-7105. doi: 10.1038/nmeth.4635.

[138] Alexander Schmidt, Karl Kochanowski, Silke Vedelaar, Erik Ahrné, Benjamin Volkmer, Luciano Callipo, Kèvin Knoops, Manuel Bauer, Ruedi Aebersold, and Matthias Heinemann. The quantitative and condition-dependent Escherichia coli proteome. *Nature Biotechnology*, 34(1):104–110, January 2016. ISSN 1087-0156, 1546-1696. doi: 10.1038/nbt.3418. URL `http://www.nature.com/articles/nbt.3418`.

[139] Nan Hao, Keith E. Shearwin, and Ian B. Dodd. Programmable DNA looping using engineered bivalent dCas9 complexes. *Nature Communications*, 8(1):1628, 2017. ISSN 2041-1723. doi: 10.1038/s41467-017-01873-x.

[140] Andrea Mückl, Matthaeus Schwarz-Schilling, Katrin Fischer, and Friedrich C. Simmel. Filamentation and restoration of normal growth in Escherichia coli using a combined CRISPRi sgRNA/antisense RNA approach. *PLOS ONE*, 13(9):e0198058, September 2018. ISSN 1932-6203. doi: 10.1371/journal.pone.0198058. URL `https://journals.plos.org/plosone/article?id=10.1371/journal.pone.0198058`.

[141] Tian Tian, Jing Wei Kang, Aram Kang, and Taek Soon Lee. Redirecting Metabolic Flux via Combinatorial Multiplex CRISPRi-Mediated Repression for Isopentenol Production in Escherichia coli. *ACS synthetic biology*, February 2019. ISSN 2161-5063. doi: 10.1021/acssynbio.8b00429.

[142] Suhyung Cho, Jongoh Shin, and Byung-Kwan Cho. Applications of CRISPR/Cas System to Bacterial Metabolic Engineering. *International Journal of Molecular Sciences*, 19(4), April 2018. ISSN 1422-0067. doi: 10.3390/ijms19041089.

[143] Dina Elhadi, Li Lv, Xiao-Ran Jiang, Hong Wu, and Guo-Qiang Chen. CRISPRi engineering E. coli for morphology diversification. *Metabolic Engineering*, 38:358–369, 2016. ISSN 1096-7184. doi: 10.1016/j.ymben.2016.09.001.

[144] Songyuan Li, Christian Bille Jendresen, Alexander Grünberger, Carlotta Ronda, Sheila Ingemann Jensen, Stephan Noack, and Alex Toftgaard Nielsen. Enhanced protein and biochemical production using CRISPRi-based growth switches. *Metabolic Engineering*, 38:274–284, 2016. ISSN 1096-7184. doi: 10.1016/j.ymben.2016.09.003.

[145] Waldemar Vollmer and Ute Bertsche. Murein (peptidoglycan) structure, architecture and biosynthesis in Escherichia coli. *Biochimica et Biophysica Acta (BBA) - Biomembranes*, 1778(9):1714–1734, September 2008. ISSN 0005-2736. doi: 10.1016/j.bbamem.2007.06.007. URL `http://www.sciencedirect.com/science/article/pii/S0005273607002210`.

[146] Timothy K. Lee, Carolina Tropini, Jen Hsin, Samantha M. Desmarais, Tristan S. Ursell, Enhao Gong, Zemer Gitai, Russell D. Monds, and Kerwyn Casey Huang. A dynamically assembled cell wall synthesis machinery buffers cell growth. *Proceedings of the National Academy of Sciences of the United States of America*, 111(12): 4554–4559, March 2014. ISSN 1091-6490. doi: 10.1073/pnas.1313826111.

[147] Hongbaek Cho, Carl N. Wivagg, Mrinal Kapoor, Zachary Barry, Patricia D. A. Rohs, Hyunsuk Suh, Jarrod A. Marto, Ethan C. Garner, and Thomas G. Bernhardt. Bacterial cell wall biogenesis is mediated by SEDS and PBP polymerase families functioning semi-autonomously. *Nature Microbiology*, 1:16172, September 2016. ISSN 2058-5276. doi: 10.1038/nmicrobiol.2016.172. URL `http://www.nature.com/articles/nmicrobiol2016172`.

[148] Catherine Paradis-Bleau, Monica Markovski, Tsuyoshi Uehara, Tania J. Lupoli, Suzanne Walker, Daniel E. Kahne, and Thomas G. Bernhardt. Lipoprotein Cofactors Located in the Outer Membrane Activate Bacterial Cell Wall Polymerases. *Cell*, 143(7):1110–1120, December 2010. ISSN 0092-8674. doi: 10.1016/j.cell.2010.11.037. URL `http://www.sciencedirect.com/science/article/pii/S0092867410013590`.

[149] Jun-ichi Nakagawa and Michio Matsuhashi. Molecular divergence of a major peptidoglycan synthetase with transglycosylase - transpeptidase activities in Escherichia coli — Penicillin-binding protein 1bs. *Biochemical and Biophysical Research Communications*, 105(4):1546–1553, April 1982. ISSN 0006-291X. doi: 10.1016/0006-291X(82)90964-0. URL `http://www.sciencedirect.com/science/article/pii/0006291X82909640`.

[150] Alexander J. Meeske, Eammon P. Riley, William P. Robins, Tsuyoshi Uehara, John J. Mekalanos, Daniel Kahne, Suzanne Walker, Andrew C. Kruse, Thomas G. Bernhardt, and David Z. Rudner. SEDS proteins are a widespread family of bacterial cell wall polymerases. *Nature*, 537(7622):634–638, September 2016. ISSN 0028-0836. doi: 10.1038/nature19331. URL `http://www.nature.com/nature/journal/v537/n7622/full/nature19331.html`.

[151] Sophie Leclercq, Adeline Derouaux, Samir Olatunji, Claudine Fraipont, Alexander J. F. Egan, Waldemar Vollmer, Eefjan Breukink, and Mohammed Terrak. Interplay between Penicillin-binding proteins and SEDS proteins promotes bacterial cell wall synthesis. *Scientific Reports*, 7:43306, 2017. ISSN 2045-2322. doi: 10.1038/srep43306.

[152] Ute Bertsche, Thomas Kast, Benoît Wolf, Claudine Fraipont, Mirjam E. G. Aarsman, Kai Kannenberg, Moritz von Rechenberg, Martine Nguyen-Distèche, Tanneke den Blaauwen, Joachim-Volker Höltje, and Waldemar Vollmer. Interaction between two murein (peptidoglycan) synthases, PBP3 and PBP1b, in Escherichia coli. *Molecular Microbiology*, 61(3):675–690, August 2006. ISSN 0950-382X. doi: 10.1111/j.1365-2958.2006.05280.x.

[153] F. B. Wientjes and N. Nanninga. On the role of the high molecular weight penicillin-binding proteins in the cell cycle of Escherichia coli. *Research in Microbiology*, 142(2):333–344, January 1991. ISSN 0923-2508. doi: 10.1016/0923-2508(91)90049-G. URL `http://www.sciencedirect.com/science/article/pii/092325089190049G`.

[154] Manuel Banzhaf, Bart van den Berg van Saparoea, Mohammed Terrak, Claudine Fraipont, Alexander Egan, Jules Philippe, André Zapun, Eefjan Breukink, Martine Nguyen-Distèche, Tanneke den Blaauwen, and Waldemar Vollmer. Cooperativity of peptidoglycan synthases active in bacterial cell elongation. *Molecular Microbiology*, 85(1):179–194, July 2012. ISSN 1365-2958. doi: 10.1111/j.1365-2958.2012.08103.x.

[155] George K. Auer, Timothy K. Lee, Manohary Rajendram, Spencer Cesar, Amanda Miguel, Kerwyn Casey Huang, and Douglas B. Weibel. Mechanical Genomics Identifies Diverse Modulators of Bacterial Cell Stiffness. *Cell Systems*, 2(6):402–411, June 2016. ISSN 2405-4712. doi: 10.1016/j.cels.2016.05.006. URL `http://www.sciencedirect.com/science/article/pii/S2405471216301818`.

[156] M Caparrós, A G Pisabarro, and M A de Pedro. Effect of D-amino acids on structure and synthesis of peptidoglycan in Escherichia coli. *Journal of Bacteriology*, 174(17):5549–5559, September 1992. ISSN 0021-9193, 1098-5530. doi: 10.1128/jb.174.17.5549-5559.1992. URL `http://jb.asm.org/lookup/doi/10.1128/jb.174.17.5549-5559.1992`.

[157] F. García del Portillo and M. A. de Pedro. Penicillin-binding protein 2 is essential for the integrity of growing cells of Escherichia coli ponB strains. *Journal of Bacteriology*, 173(14):4530–4532, July 1991. ISSN 0021-9193.

[158] Robert J. Nichols, Saunak Sen, Yoe Jin Choo, Pedro Beltrao, Matylda Zietek, Rachna Chaba, Sueyoung Lee, Krystyna M. Kazmierczak, Karis J. Lee, Angela Wong, Michael Shales, Susan Lovett, Malcolm E. Winkler, Nevan J. Krogan, Athanasios Typas, and Carol A. Gross. Phenotypic landscape of a bacterial cell. *Cell*, 144(1):143–156, January 2011. ISSN 1097-4172. doi: 10.1016/j.cell.2010.11.052.

[159] Marta Caparrós, JoséCarlos Quintela, and Miguel A. de Pedro. Variability of peptidoglycan surface density in Escherichia coli. *FEMS Microbiology Letters*, 121(1):71–76, August 1994. ISSN 1574-6968. doi: 10.1111/j.1574-6968.1994.tb07077.x. URL `https://onlinelibrary.wiley.com/doi/abs/10.1111/j.1574-6968.1994.tb07077.x`.

[160] T. J. Dougherty, K. Kennedy, R. E. Kessler, and M. J. Pucci. Direct quantitation of the number of individual penicillin-binding proteins per cell in Escherichia coli. *Journal of Bacteriology*, 178(21):6110–6115, November 1996. ISSN 0021-9193, 1098-5530. doi: 10.1128/jb.178.21.6110-6115.1996. URL `https://jb.asm.org/content/178/21/6110`.

[161] Yuichi Taniguchi, Paul J. Choi, Gene-Wei Li, Huiyi Chen, Mohan Babu, Jeremy Hearn, Andrew Emili, and X. Sunney Xie. Quantifying E. coli proteome and transcriptome with single-molecule sensitivity in single cells. *Science (New York, N.Y.)*, 329(5991):533–538, July 2010. ISSN 1095-9203. doi: 10.1126/science.1188308.

[162] Jacek R. Wiśniewski and Dariusz Rakus. Quantitative analysis of the Escherichia coli proteome. *Data in Brief*, 1:7–11, December 2014. ISSN 2352-3409. doi: 10.1016/j.dib.2014.08.004. URL `http://www.sciencedirect.com/science/article/pii/S2352340914000079`.

[163] Hak Suk Chung, Zhizhong Yao, Nathan W. Goehring, Roy Kishony, Jon Beckwith, and Daniel Kahne. Rapid -lactam-induced lysis requires successful assembly of the cell division machinery. *Proceedings of the National Academy of Sciences*, 106 (51):21872–21877, December 2009. ISSN 0027-8424, 1091-6490. doi: 10.1073/pnas.0911674106. URL https://www.pnas.org/content/106/51/21872.

[164] F. B. Wientjes, C. L. Woldringh, and N. Nanninga. Amount of peptidoglycan in cell walls of gram-negative bacteria. *Journal of Bacteriology*, 173(23):7684–7691, December 1991. ISSN 0021-9193, 1098-5530. doi: 10.1128/jb.173.23.7684-7691.1991. URL https://jb.asm.org/content/173/23/7684.

[165] Renata Buda, Yunxiao Liu, Jin Yang, Smitha Hegde, Keiran Stevenson, Fan Bai, and Teuta Pilizota. Dynamics of Escherichia coli's passive response to a sudden decrease in external osmolarity. *Proceedings of the National Academy of Sciences of the United States of America*, 113(40):E5838–E5846, 2016. ISSN 1091-6490. doi: 10.1073/pnas.1522185113.

[166] X. Yao, M. Jericho, D. Pink, and T. Beveridge. Thickness and Elasticity of Gram-Negative Murein Sacculi Measured by Atomic Force Microscopy. *Journal of Bacteriology*, 181(22):6865–6875, November 1999. ISSN 0021-9193, 1098-5530. URL http://jb.asm.org/content/181/22/6865.

[167] Mary P. Lambert and Francis C. Neuhaus. Mechanism of d-Cycloserine Action: Alanine Racemase from Escherichia coli W1. *Journal of Bacteriology*, 110(3):978–987, June 1972. ISSN 0021-9193. URL https://www.ncbi.nlm.nih.gov/pmc/articles/PMC247518/.

[168] Timothy K. Lee, Kevin Meng, Handuo Shi, and Kerwyn Casey Huang. Single-molecule imaging reveals modulation of cell wall synthesis dynamics in live bacterial cells. *Nature Communications*, 7:13170, 2016. ISSN 2041-1723. doi: 10.1038/ncomms13170.

[169] Robert D. Turner, Stéphane Mesnage, Jamie K. Hobbs, and Simon J. Foster. Molecular imaging of glycan chains couples cell-wall polysaccharide architecture to bacterial cell morphology. *Nature Communications*, 9(1):1263, 2018. ISSN 2041-1723. doi: 10.1038/s41467-018-03551-y.

[170] François St-Pierre, Lun Cui, David G. Priest, Drew Endy, Ian B. Dodd, and Keith E. Shearwin. One-Step Cloning and Chromosomal Integration of DNA. *ACS Synthetic Biology*, 2(9):537–541, September 2013. doi: 10.1021/sb400021j. URL http://dx.doi.org/10.1021/sb400021j.

[171] Tristan Ursell, Timothy K. Lee, Daisuke Shiomi, Handuo Shi, Carolina Tropini, Russell D. Monds, Alexandre Colavin, Gabriel Billings, Ilina Bhaya-Grossman, Michael Broxton, Bevan Emma Huang, Hironori Niki, and Kerwyn Casey Huang. Rapid, precise quantification of bacterial cellular dimensions across a genomic-scale knockout library. *BMC Biology*, 15(1):17, February 2017. ISSN 1741-7007. doi: 10.1186/s12915-017-0348-8. URL https://doi.org/10.1186/s12915-017-0348-8.

[172] Arthur Edelstein, Nenad Amodaj, Karl Hoover, Ron Vale, and Nico Stuurman. Computer Control of Microscopes Using µManager. *Current Protocols in Molecular Biology*, 92(1):14.20.1–14.20.17, 2010. ISSN 1934-3647. doi: 10.1002/0471142727.mb1420s92. URL https://currentprotocols.onlinelibrary.wiley.com/doi/abs/10.1002/0471142727.mb1420s92.

[173] Ozden Kocaoglu, Bryan Lanning, Loralyn Cozy, Rebecca Calvo, Daniel Kearns, and Erin E. Carlson. Activity-Based Probes for Penicillin-Binding Protein Imaging. *The FASEB Journal*, 26(1_supplement):1000.1–1000.1, April 2012. ISSN 0892-6638. doi: 10.1096/fasebj.26.1_supplement.1000.1. URL https://www.fasebj.org/doi/abs/10.1096/fasebj.26.1_supplement.1000.1.

[174] Caroline A. Schneider, Wayne S. Rasband, and Kevin W. Eliceiri. NIH Image to ImageJ: 25 years of image analysis. *Nature Methods*, 9:671–675, June 2012. ISSN 1548-7105. doi: 10.1038/nmeth.2089. URL https://www.nature.com/articles/nmeth.2089.

[175] Richard Wheeler, Frédéric Veyrier, Catherine Werts, and Ivo Gomperts Boneca. PeptidoglycanPeptidoglycanand Nod Receptor. In Tamao Endo, Peter H. Seeberger, Gerald W. Hart, Chi-Huey Wong, and Naoyuki Taniguchi, editors, *Glycoscience: Biology and Medicine*, pages 1–10. Springer Japan, Tokyo, 2021. ISBN 978-4-431-54836-2. doi: 10.1007/978-4-431-54836-2_147-1. URL https://doi.org/10.1007/978-4-431-54836-2_147-1.

[176] John C. Crocker and David G. Grier. Methods of Digital Video Microscopy for Colloidal Studies. *Journal of Colloid and Interface Science*, 179(1):298–310, April 1996. ISSN 00219797. doi: 10.1006/jcis.1996.0217. URL http://linkinghub.elsevier.com/retrieve/pii/S0021979796902179.

[177] Gaëlle Demarre, Anne-Marie Guérout, Chiho Matsumoto-Mashimo, Dean A. Rowe-Magnus, Philippe Marlière, and Didier Mazel. A new family of mobilizable suicide plasmids based on broad host range R388 plasmid (IncW) and RP4 plasmid (IncPalpha) conjugative machineries and their cognate Escherichia coli host strains. *Research in Microbiology*, 156(2):245–255, March 2005. ISSN 0923-2508. doi: 10.1016/j.resmic.2004.09.007.

[178] L. M. Guzman, D. Belin, M. J. Carson, and J. Beckwith. Tight regulation, modulation, and high-level expression by vectors containing the arabinose PBAD promoter. *Journal of Bacteriology*, 177(14):4121–4130, July 1995. ISSN 0021-9193.

[179] Athanasios Typas, Manuel Banzhaf, Carol A. Gross, and Waldemar Vollmer. From the regulation of peptidoglycan synthesis to bacterial growth and morphology. *Nature Reviews Microbiology*, 10(2):123–136, February 2012. ISSN 1740-1526. doi: 10.1038/nrmicro2677. URL http://www.nature.com/nrmicro/journal/v10/n2/full/nrmicro2677.html.

[180] C. A. Zijderveld, M. E. Aarsman, and N. Nanninga. Differences between inner membrane and peptidoglycan-associated PBP1b dimers of Escherichia coli. *Journal of Bacteriology*, 177(7):1860–1863, April 1995. ISSN 0021-9193, 1098-5530. doi: 10.1128/jb.177.7.1860-1863.1995. URL https://jb.asm.org/content/177/7/1860.

[181] Patrice Rassam, Kathleen R. Long, Renata Kaminska, David J. Williams, Grigorios Papadakos, Christoph G. Baumann, and Colin Kleanthous. Intermembrane crosstalk drives inner-membrane protein organization in Escherichia coli. *Nature Communications*, 9(1):1082, 2018. ISSN 2041-1723. doi: 10.1038/s41467-018-03521-4.

[182] Terrens N. V. Saaki, Henrik Strahl, and Leendert W. Hamoen. Membrane Curvature and the Tol-Pal Complex Determine Polar Localization of the Chemoreceptor Tar in Escherichia coli. *Journal of Bacteriology*, 200(9), May 2018. ISSN 1098-5530. doi: 10.1128/JB.00658-17.

[183] Yi-Chun Yeh, Luis R. Comolli, Kenneth H. Downing, Lucy Shapiro, and Harley H. McAdams. The caulobacter Tol-Pal complex is essential for outer membrane integrity and the positioning of a polar localization factor. *Journal of Bacteriology*, 192(19):4847–4858, October 2010. ISSN 1098-5530. doi: 10.1128/JB.00607-10.

[184] Enrique R. Rojas, Gabriel Billings, Pascal D. Odermatt, George K. Auer, Lillian Zhu, Amanda Miguel, Fred Chang, Douglas B. Weibel, Julie A. Theriot, and Kerwyn Casey Huang. The outer membrane is an essential load-bearing element in Gram-negative bacteria. *Nature*, 559(7715):617, July 2018. ISSN 1476-4687. doi: 10.1038/s41586-018-0344-3. URL `https://www.nature.com/articles/s41586-018-0344-3`.

[185] M. Caparrós, J. L. M. Torrecuadrada, and M. A. de Pedro. Effect of D-amino acids on Escherichia coli strains with impaired penicillin-binding proteins. *Research in Microbiology*, 142(2):345–350, January 1991. ISSN 0923-2508. doi: 10.1016/0923-2508(91)90050-K. URL `http://www.sciencedirect.com/science/article/pii/092325089190050K`.

[186] Jason Hocking, Richa Priyadarshini, Constantin N. Takacs, Teresa Costa, Natalie A. Dye, Lucy Shapiro, Waldemar Vollmer, and Christine Jacobs-Wagner. Osmolality-dependent relocation of penicillin-binding protein PBP2 to the division site in Caulobacter crescentus. *Journal of Bacteriology*, 194(12):3116–3127, June 2012. ISSN 1098-5530. doi: 10.1128/JB.00260-12.

[187] Felipe Cava, Hubert Lam, Miguel A. de Pedro, and Matthew K. Waldor. Emerging knowledge of regulatory roles of D-amino acids in bacteria. *Cellular and molecular life sciences: CMLS*, 68(5):817–831, March 2011. ISSN 1420-9071. doi: 10.1007/s00018-010-0571-8.

[188] Hubert Lam, Dong-Chan Oh, Felipe Cava, Constantin N. Takacs, Jon Clardy, Miguel A. de Pedro, and Matthew K. Waldor. D-Amino Acids Govern Stationary Phase Cell Wall Remodeling in Bacteria. *Science*, 325(5947):1552–1555, September 2009. ISSN 0036-8075, 1095-9203. doi: 10.1126/science.1178123. URL `http://science.sciencemag.org/content/325/5947/1552`.

[189] Carmen Schwechheimer, Daniel L Rodriguez, and Meta J Kuehn. NlpI-mediated modulation of outer membrane vesicle production through peptidoglycan dynamics in Escherichia coli. *MicrobiologyOpen*, 4(3):375–389, June 2015. ISSN 2045-8827. doi: 10.1002/mbo3.244. URL `https://www.ncbi.nlm.nih.gov/pmc/articles/PMC4475382/`.

[190] Ming-Yuan Su, Nilanjan Som, Chia-Yun Wu, Shih-Chieh Su, Yi-Ting Kuo, Lu-Chu Ke, Meng-Ru Ho, Shiou-Ru Tzeng, Ching-Hao Teng, Dominique Mengin-Lecreulx, Manjula Reddy, and Chung-I. Chang. Structural basis of adaptor-mediated protein degradation by the tail-specific PDZ-protease Prc. *Nature Communications*, 8(1):1516, November 2017. ISSN 2041-1723. doi: 10.1038/s41467-017-01697-9. URL https://www.nature.com/articles/s41467-017-01697-9.

[191] Akiko Tadokoro, Hidemi Hayashi, Toshihiko Kishimoto, Yasutaka Makino, Shingo Fujisaki, and Yukinobu Nishimura. Interaction of the Escherichia coli Lipoprotein NlpI with Periplasmic Prc (Tsp) Protease. *The Journal of Biochemistry*, 135(2):185–191, February 2004. ISSN 0021-924X. doi: 10.1093/jb/mvh022. URL https://academic.oup.com/jb/article/135/2/185/800433.

[192] Anne-Marie Hansen, Yu Qiu, Norman Yeh, Frederick R. Blattner, Tim Durfee, and Ding Jun Jin. SspA is required for acid resistance in stationary phase by downregulation of H-NS in Escherichia coli. *Molecular Microbiology*, 56(3):719–734, May 2005. ISSN 0950-382X. doi: 10.1111/j.1365-2958.2005.04567.x.

[193] J. V. Höltje, W. Fiedler, H. Rotering, B. Walderich, and J. van Duin. Lysis induction of Escherichia coli by the cloned lysis protein of the phage MS2 depends on the presence of osmoregulatory membrane-derived oligosaccharides. *The Journal of Biological Chemistry*, 263(8):3539–3541, March 1988. ISSN 0021-9258.

[194] Matthew A. Gerding, Yasuyuki Ogata, Nicole D. Pecora, Hironori Niki, and Piet A. J. de Boer. The trans-envelope Tol-Pal complex is part of the cell division machinery and required for proper outer-membrane invagination during cell constriction in E. coli. *Molecular Microbiology*, 63(4):1008–1025, February 2007. ISSN 0950-382X. doi: 10.1111/j.1365-2958.2006.05571.x.

[195] J. C. Lazzaroni, P. Germon, M. C. Ray, and A. Vianney. The Tol proteins of Escherichia coli and their involvement in the uptake of biomolecules and outer membrane stability. *FEMS microbiology letters*, 177(2):191–197, August 1999. ISSN 0378-1097. doi: 10.1111/j.1574-6968.1999.tb13731.x.

[196] Sébastien Bontemps-Gallo, Jean-Pierre Bohin, and Jean-Marie Lacroix. Osmoregulated Periplasmic Glucans. *EcoSal Plus*, 7(2), 2017. ISSN 2324-6200. doi: 10.1128/ecosalplus.ESP-0001-2017.

[197] Patrick Freire, Ricardo Neves Moreira, and Cecília Maria Arraiano. BolA Inhibits Cell Elongation and Regulates MreB Expression Levels. *Journal of Molecular Biology*, 385(5):1345–1351, February 2009. ISSN 0022-2836. doi: 10.1016/j.jmb.2008.12.026. URL http://www.sciencedirect.com/science/article/pii/S0022283608015350.

[198] Jorge M. Santos, Mónica Lobo, António P. A. Matos, Miguel A. De Pedro, and Cecilia M. Arraiano. The gene bolA regulates dacA (PBP5), dacC (PBP6) and ampC (AmpC), promoting normal morphology in Escherichia coli. *Molecular Microbiology*, 45(6):1729–1740, 2002. ISSN 1365-2958. doi: 10.1046/j.1365-2958.2002.03131.x. URL https://onlinelibrary.wiley.com/doi/abs/10.1046/j.1365-2958.2002.03131.x.

[199] April Pawluk, Alan R. Davidson, and Karen L. Maxwell. Anti-CRISPR: discovery, mechanism and function. *Nature Reviews. Microbiology*, 16(1):12–17, January 2018. ISSN 1740-1534. doi: 10.1038/nrmicro.2017.120.

[200] Chuan Dong, Ge-Fei Hao, Hong-Li Hua, Shuo Liu, Abraham Alemayehu Labena, Guoshi Chai, Jian Huang, Nini Rao, and Feng-Biao Guo. Anti-CRISPRdb: a comprehensive online resource for anti-CRISPR proteins. *Nucleic Acids Research*, 46 (D1):D393–D398, January 2018. ISSN 0305-1048. doi: 10.1093/nar/gkx835. URL `https://academic.oup.com/nar/article/46/D1/D393/4191329`.

[201] Saumya Saurabh, Adam M. Perez, Colin J. Comerci, Lucy Shapiro, and W. E. Moerner. Super-resolution Imaging of Live Bacteria Cells Using a Genetically Directed, Highly Photostable Fluoromodule. *Journal of the American Chemical Society*, 138(33):10398–10401, 2016. ISSN 1520-5126. doi: 10.1021/jacs.6b05943.

[202] Marc J. Lajoie, Alexis J. Rovner, Daniel B. Goodman, Hans-Rudolf Aerni, Adrian D. Haimovich, Gleb Kuznetsov, Jaron A. Mercer, Harris H. Wang, Peter A. Carr, Joshua A. Mosberg, Nadin Rohland, Peter G. Schultz, Joseph M. Jacobson, Jesse Rinehart, George M. Church, and Farren J. Isaacs. Genomically Recoded Organisms Expand Biological Functions. *Science*, 342(6156):357–360, October 2013. ISSN 0036-8075, 1095-9203. doi: 10.1126/science.1241459. URL `http://science.sciencemag.org/content/342/6156/357`.

[203] Daniel J. Mandell, Marc J. Lajoie, Michael T. Mee, Ryo Takeuchi, Gleb Kuznetsov, Julie E. Norville, Christopher J. Gregg, Barry L. Stoddard, and George M. Church. Biocontainment of genetically modified organisms by synthetic protein design. *Nature*, 518(7537):55–60, February 2015. ISSN 1476-4687. doi: 10.1038/nature14121. URL `https://www.nature.com/articles/nature14121`.

[204] Robert D. Turner, Jamie K. Hobbs, and Simon J. Foster. Atomic Force Microscopy Analysis of Bacterial Cell Wall Peptidoglycan Architecture. *Methods in Molecular Biology (Clifton, N.J.)*, 1440:3–9, 2016. ISSN 1940-6029. doi: 10.1007/978-1-4939-3676-2_1.

[205] Monica Markovski, Jessica L. Bohrhunter, Tania J. Lupoli, Tsuyoshi Uehara, Suzanne Walker, Daniel E. Kahne, and Thomas G. Bernhardt. Cofactor bypass variants reveal a conformational control mechanism governing cell wall polymerase activity. *Proceedings of the National Academy of Sciences of the United States of America*, 113(17):4788–4793, April 2016. ISSN 1091-6490. doi: 10.1073/pnas.1524538113.

Chapter 11

Appendix

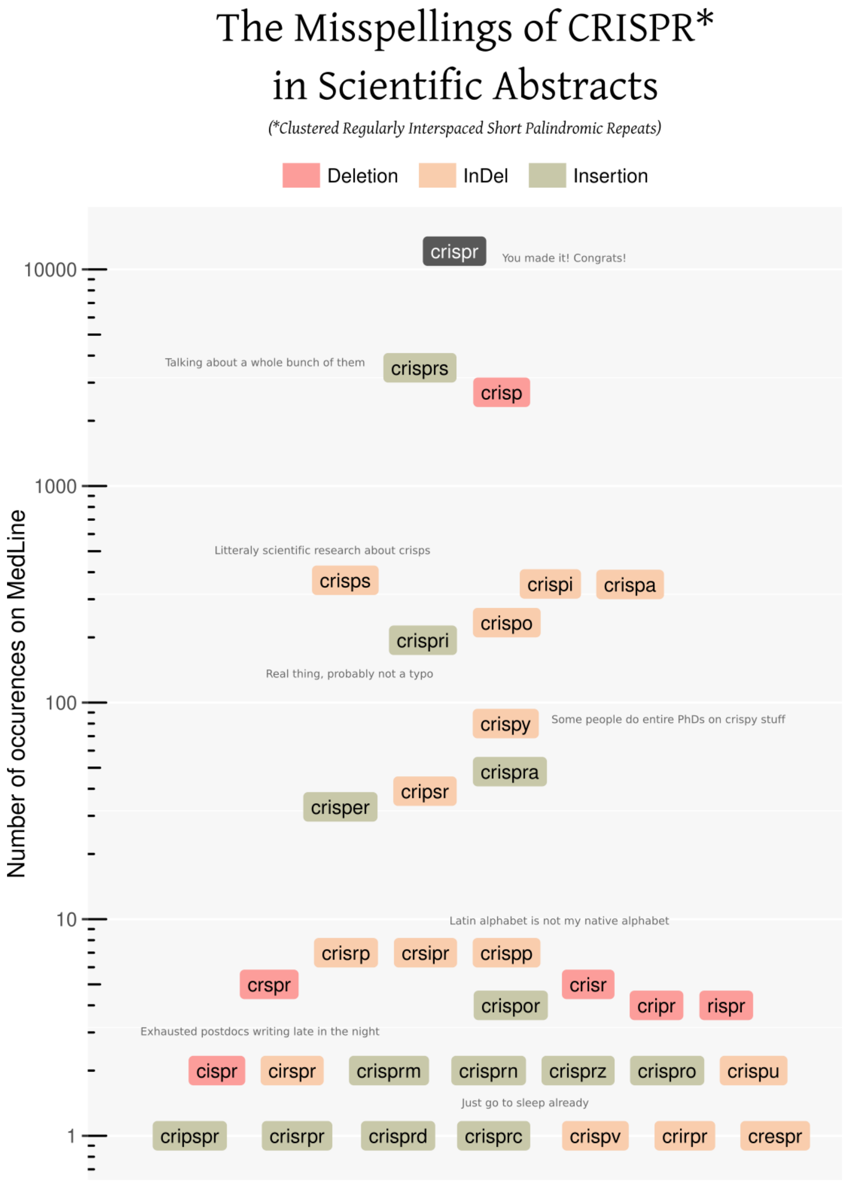

Figure 11.1: Random mutagenesis was applied to the word CRISPR, then the number of occurrences in abstracts on the MedLine database was counted for each of them.

Figure 11.2: Current state of my bench. I will come back in 10 years and check that nothing has moved.